Evaluation of the Effects of Microporous Layer Characteristics and Assembly Parameters on the Performance and Durability of a Planar PEM Fuel Cell

Patrick Hiroshi Burand

Thesis submitted to the faculty of
Virginia Polytechnic Institute and State University
in partial fulfillment of the requirements for the degree of

Master of Science
In
Mechanical Engineering

Committee Members:

Michael W. Ellis – Chair, ME
Douglas J. Nelson – ME
David A. Dillard – ESM

September 3, 2009
Blacksburg, Virginia

Keywords: PEMFC, Planar Fuel Cell, Ribbon Fuel Cell, Microporous Layer

Evaluation of the Effects of Microporous Layer Characteristics and Assembly Parameters on the Performance and Durability of a Planar PEM Fuel Cell

Patrick Hiroshi Burand

Abstract

In recent years a significant portion of proton exchange membrane fuel cell (PEMFC) work has been focused on understanding and optimizing the functions of the microporous layer (MPL). Researchers have found that including this layer, composed of carbon black and Teflon^{TM} (PTFE), between the gas diffusion layer (GDL) and catalyst layer (CL) of PEMFCs improves performance. The major benefit of the MPL in conventional fuel cells is that it improves water management and reduces contact resistances between cell layers. Although the functions of the MPL in conventional PEMFCs are well understood, the essential functions and optimal formulation of the layer in planar PEMFCs which operate without stack compression, are for the most part unknown. This work determines the essential functions and optimal composition, loading and sintering pressure of the MPL in a planar fuel cell design called a Ribbon Fuel Cell. Adhesion as well as performance data were gathered to determine the essential functions and formulation of the MPL which leads to high performance and durability in Ribbon Fuel Cells. Statistical models were created based on performance data of cells constructed with various MPLs; and a MPL composed of 45 wt% PTFE, loaded at 3.5 mg/cm^2 and sintered between 20 and 40 psi was found to exhibit optimal performance and durability. The reason why such a high PTFE content yields optimal results is because it strengthens the MPL, allowing it to successfully join various cell layers together, a function that is essential in Ribbon Cells which operate without external stack compression.

Acknowledgements

This research could not have been completed without the help and encouragement of a number of people. I would like to thank Dr. Michael Ellis, my advisor and committee chairperson, for guiding me through the sometimes arduous but ultimately rewarding research and thesis process. Thanks to you my knowledge of fuel cells and more importantly of the research process, has improved tremendously since beginning my graduate education. I want to express my appreciation to my other committee members, Dr. David Dillard and Dr. Doug Nelson for their support in completing my thesis. I would also like to thank Charles Strickler for his time and financial support of my research on Ribbon Fuel Cells. Lastly, I want to thank my family for their support not only during my graduate study here at Virginia Tech, but throughout my entire education; I couldn't have done it without you.

Dedication

To my family, for their unwavering love and support of all my pursuits in life.

Table of Contents

List of Figures

List of Tables

Nomenclature and Acronyms

Acronym	*Definition*
BPP	Bipolar Plate
CCC	Circumscribed Central Composite Design
CCD	Central Composite Design
CCF	Face Centered Central Composite Design
CCI	Inscribed Central Composite Design
CL	Catalyst Layer
EDF	Extended Depth of Field
EIS	Electrochemical Impedance Spectroscopy
ESL	Energy Systems Laboratory
FEP	Perflourinated Ethylene-Propelyene
GDL	Gas Diffusion Layer
HFR	High Frequency Resistance
IPA	Isopropyl Alcohol
MEA	Membrane Electrode Assembly
MPL	Microporous Layer
ORR	Oxygen Reduction Reaction
PEMFC	Proton Exchange Membrane Fuel Cell
PTFE	Teflon™
TGA	Thermogravimetric Analyzer
VI	Virtual Instrument

Symbol	*Definition*
$wt\%_{PTFE}$	Weight percentage of PTFE
m_{GDL}	Mass of bare GDL without sizing or PTFE
m_{PTFE}	Mass of PTFE in either the GDL or MPL
m_{GDL_Total}	Total mass of GDL after hydrophobic treatment
m_{CB}	Mass of carbon black in MPL

L_{MPL}	Average MPL loading in mg/cm^2
$m_{GDL+MPL}$	Mass of the MPL coated GDL
G_C	Apparent fracture energy for peel test samples
F_{AVG}	Average de-bond force for peel test samples
l	Bond length for peel test samples
w	Bond width for peel test samples
D_{GRIPS}	Distance traveled by microtester^{TM} grips during peel test

List of Equations

1. Introduction

The dramatic rise in global oil prices over the past decade has made Americans increasingly aware of the effect of energy on the economic well being of their country as well as their individual lives. In the last few years, gasoline prices have fluctuated wildly and reached record high levels; the cost to heat and power homes has increased and even the price of many consumer goods has risen with the elevated energy costs. These new financial hardships have opened the country's eyes to the fact that its well being and the well being of its citizens are closely tied to the price of energy. Due to America's dependence on foreign oil, the price of much of this energy is out of our control; and unfortunately, conflict in the Middle East coupled with the depletion of cheap oil reserves, make it almost certain that the cost of energy will continue to increase in the years to come.

Policy makers are acutely aware of how energy prices can bolster or suppress economic growth. They know that our continued reliance on foreign oil to meet domestic energy needs will only result in future economic hardships for the country. A promising solution to this problem is the further implementation of domestic alternative energy sources such as solar, wind, nuclear power systems, along with the development of other efficient energy conversion systems such as fuel cells.

Proton exchange membrane fuel cells (PEMFCs) are one type of energy conversion system that is particularly promising due to its high efficiency, ultra-low emissions and relatively low operating temperature. Since their invention in the early 1960's by General Electric [4], significant investments have been made to develop and implement PEMFCs into the country's energy infrastructure. Potential applications for

PEMFCs include everything from providing power for residential housing, to powering automobiles to smaller portable applications such as powering a laptop. Because of the numerous applications for PEMFCs, companies which specialize in manufacturing PEMFCs, such as Ballard Power Systems, Hydrogenics and UTC Power have emerged in recent decades. Despite the enthusiasm and great potential of PEMFCs, their widespread commercialization has yet to be realized; however, with further improvements in power density and lower material costs, PEMFCs could become an integral part the country's energy infrastructure and our everyday lives.

This chapter will first explain the electrochemistry of a single PEMFC. The following section will discuss the basic components of a PEMFC and their arrangement in a conventional fuel cell stack. Next, a unique fuel cell architecture, called a Ribbon Fuel Cell, will be presented, and finally the research objectives of this work will be outlined.

1.1 Proton Exchange Membrane Fuel Cell (PEMFC) Operation

At the most basic level, a proton exchange membrane fuel cell can be thought of as a black box that uses hydrogen and oxygen to produce electricity, water and heat. Inside the black box, one will see a symmetrical layered assembly of materials as shown in Figure 1.1.

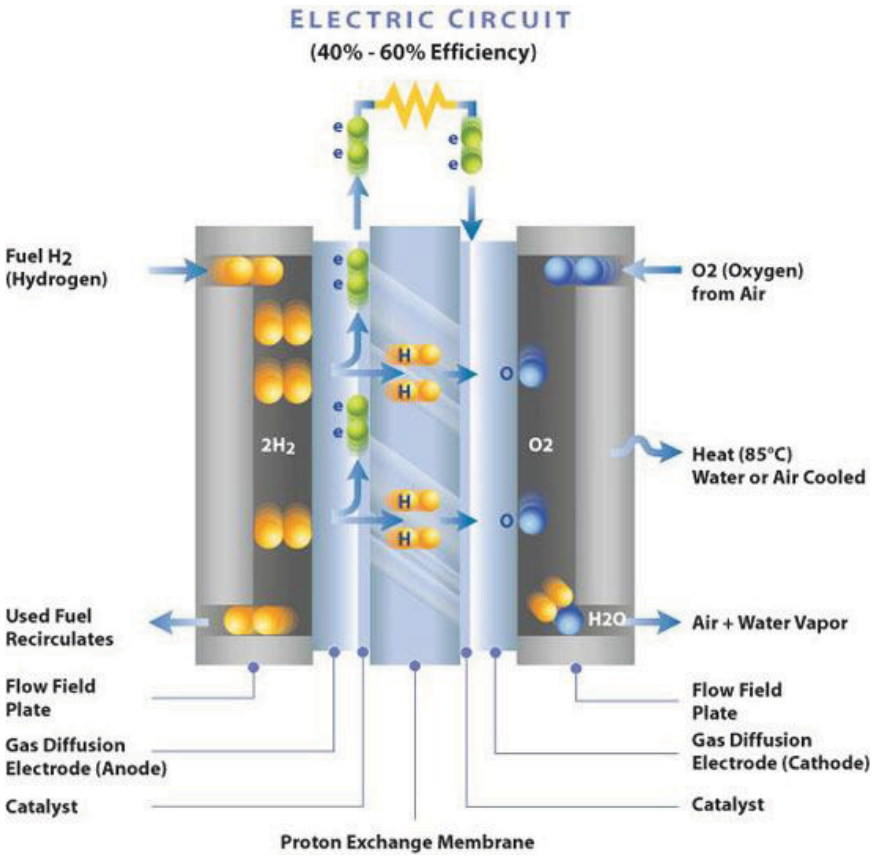

Figure 1-1. Basic architecture of a conventional PEMFC [1]

On one side of the fuel cell, hydrogen (H_2) is supplied through flow channels of the bipolar plate (BPP). This side of the fuel cell is referred to as the anode, while the opposite side is referred to as the cathode. From the flow channels, hydrogen diffuses through the gas diffusion layer (GDL) and microporous layer (MPL) until it reaches the surface of a catalyst coated polymer electrolyte membrane. In almost all cases, this membrane is made of Nafion® which is permeable to protons, but not electrons. Once hydrogen reaches the electrolyte, if it is in contact with an electron conductor (typically carbon black in the catalyst layer), catalyst and the aforementioned proton conducting electrolyte, a chemical reaction will take place in which the protons and electrons of the hydrogen molecule are separated. Locations where these three materials (carbon, catalyst

and electrolyte) are adjacent to one another are called triple phase zones, and the anode oxidation reaction which occurs there is shown in equation 1-1.

$$2H_2 \longrightarrow 4H^+ + 4e- \quad (1\text{-}1)$$

After separating from the hydrogen protons, newly separated electrons travel through the conductive MPL and GDL, then through an external circuit connected to the cathode. This flow of electrons constitutes an electrical current, and is utilized to perform work. The oxidized protons travel through the electrolyte to the cathode side of the fuel cell. On the cathode BPP, oxygen (O_2) or air is fed through flow channels where it diffuses through the cathode GDL and MPL to another triple phase zone in the cathode catalyst layer. Here, the oxygen molecules contact with the oxidized proton and the electron that has traveled through the external circuit, and the cathode reduction reaction occurs as shown in equation 1-2.

$$O_2 + 4H^+ + 4e^- \longrightarrow 2H_2O \quad (1\text{-}2)$$

The overall reaction for a PEMFC is as follows:

$$2H_2 + O_2 \longrightarrow 2H_2O \quad (1\text{-}3)$$

In summary, a PEMFC requires the input of hydrogen and oxygen (or air) to create electrical current, while producing water and heat as byproducts. The following

section will further explain the composition and function of each of the layers in a PEMFC.

1.2 PEMFC Components

The major components of a PEMFC are: bipolar plates (BPPs), gas diffusion layers (GDLs), microporous layers (MPLs), catalyst layers (CLs) and an electrolyte. As mentioned in the previous section, the architecture of PEMFCs is symmetrical around the electrolyte, with both anode and cathode sides containing each of the component layers listed above.

Bipolar plates are made of electrically conductive material, typically carbon in the form of graphite, and have a number of functions. The first of the two main functions of the BPP is to provide a conductive medium for electron travel between the anode and cathode. The second function is to provide a pathway which efficiently delivers reactant gasses to catalyst sites on the electrolyte, while at the same time removing product water on the cathode. It is critical to have an effective flow channel design because the shape, size and pattern of the channels can significantly affect performance [2]. Poorly designed flow fields can cause liquid water buildup on the cathode side of the cell, blocking gas reaction sites in the GDL and CL, ultimately lowering cell performance. There are three flow channel patterns commonly used in PEMFC, parallel, serpentine and interdigitated as shown in Figure 1-2.

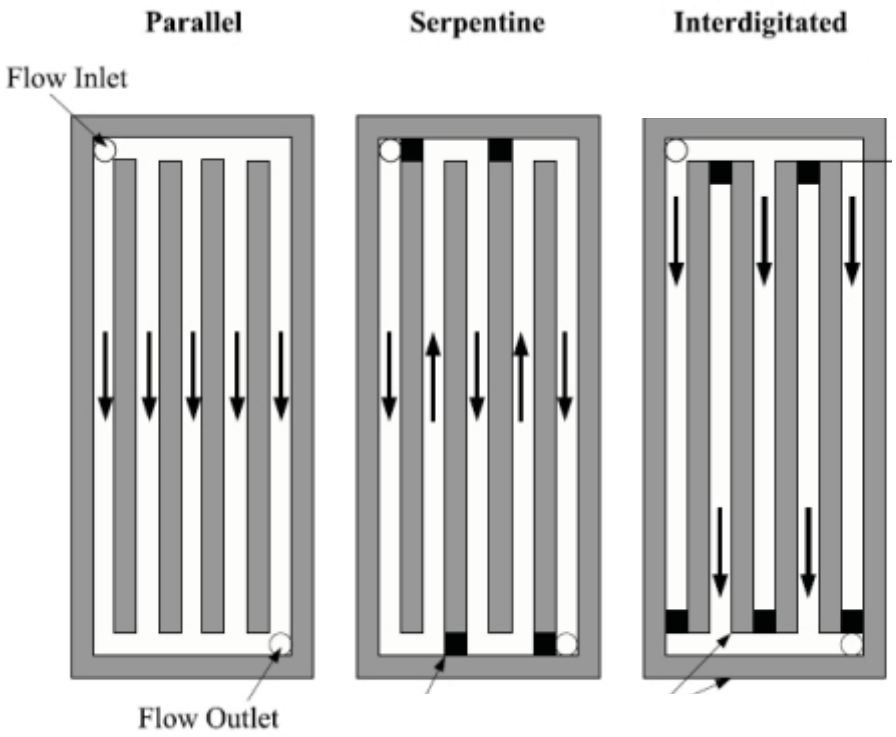

Figure 1-2. Parallel, serpentine and interdigitated flow field designs [3]

The benefit of a parallel flow field design, is that there is a low overall pressure drop between the gas inlet and outlet; therefore less power is needed to supply reactant gasses. A major drawback of this design is that the flow distribution in each channel may be non-uniform, and some channels may experience water buildup, lowering local performance. The most commonly used flow field design is the serpentine pattern. Since only one flow path exists from inlet to outlet, liquid water is forced to exit the channel outlet, resulting in superior water removal ability. A disadvantage of the serpentine pattern is that in cells with large active areas, there is a significant pressure drop between the inlet and outlet ports. In the interdigitated designs, dead-ended inlet flow channels force reactant gases through the GDL to an exit flowchannel, resulting in excellent water

management capabilities. As with the serpentine design, improved water management comes at the price of a large pressure drop between the flow field inlet and outlet.

Adjacent to the BPP is the GDL which must be electrically conductive and gas permeable, as well as be able to withstand acidic environments. Carbon cloths and carbon papers are two materials that satisfy these conditions and are commonly used for GDLs in PEMFCs. These papers and cloths are gas permeable so that reactant gasses can easily diffuse through them to the CL, and are electrically conductive in order to transport electrons from reaction sites on the CL to the BPP without significant losses. A third requirement for the GDL is that it must be able to remove water from the cathode CL to the flow channels of the BPP. To enhance its water removal capabilities, the GDL is often coated with a hydrophobic agent, usually Teflon™ (PTFE). There are a number of commercially available GDLs, the most common being ELAT™ and Toray™.

A relatively recent addition to the PEMFC architecture is the microporous layer. This thin layer is made of carbon black particles and a flouropolymer, usually PTFE. Research has found that the addition of this thin layer between the GDL and CL of the anode and cathode, greatly improves water management in the cell, leading to higher power outputs. There are a number of different techniques for applying the MPL to the GDL such as screen printing, spraying and rolling. The advantages and disadvantages of each method, along with a detailed explanation of exactly how the MPL improves water management will be discussed in more detail in following sections.

The catalyst layer is located between the MPL and the electrolyte, and plays an essential role in the operation of every PEMFC. Its main function is to facilitate the half-reactions at the anode and cathode by lowering their activation barriers. It is especially

important for the cathode CL to be effective, because the slow reaction kinetics of the oxygen reduction reaction (ORR) can result in major performance penalties. The most common catalyst for PEMFCs is platinum, which in the early years contributed to much of the cost of the cell assembly, due to its high loading. This high platinum loading made PEMFCs extremely expensive and far from economically competitive with other energy producing technologies. However, over the past few decades great strides have been made in reducing the required platinum loading, which has gone from 28 mg/cm^2 [4] down to around 0.4 mg/cm^2 on the cathode, and 0.05 mg/cm^2 on the anode [5]. The architecture of the CL consists of platinum particles supported on larger carbon particles, mixed with a proton conducting electrolyte, in most cases Nafion®. This mixture is then applied either directly to the electrolyte membrane, or to the GDL/MPL assembly. Application methods include painting, spraying or hot pressing. Once the CL is applied to both sides of the electrolyte, the assembly is referred to as a membrane electrode assembly (MEA).

The final component of a PEMFC is the electrolyte, which is found at the center of the assembly, separating the anode and cathode. For a PEMFC to function correctly, the electrolyte must be ionically conductive, impermeable to electrons and have stability in both oxidizing and reducing environments. A polymer which satisfies the above requirements and is most commonly used in PEMFCs is Nafion®, which has a chemical backbone structure similar to PTFE with sulfonic acid (HSO_3) side chains [2]. Nafion's® unique composition makes its proton conductivity highly dependent on its water content. When the membrane is dry, fuel cell performance will drop significantly due to the large resistive losses associated with its reduced conductivity. To keep the Nafion® from

drying during operation, reactant gasses are often humidified, and components of the fuel cell such as the MPL and GDL are constructed to optimize the water content in the membrane.

1.3 PEMFC Conventional Stack Architecture

The previous section described the components and construction of a single PEMFC. Single cells can provide a relatively large range of current depending on the size of the area over which cathode and anode reactions are occurring, referred to as the active area. However, single cells typically only yield a maximum voltage of 1.0 V, and operate typically between 0.7 – 0.4 V. The most common way to scale up voltage output is to electrically connect single cells in series, forming a configuration referred to as a fuel cell stack. This stack configuration can be seen in Figure 1-3. In a conventional stack configuration, the cathode collector plate of one cell serves as the anode collector plate of the adjacent cell. End plates are placed at each end of the stack and connected using tie rods, which apply a pressure throughout the stack. There exists an optimal stack pressure for each stack design which is the result of certain tradeoffs that will be discussed in a later section.

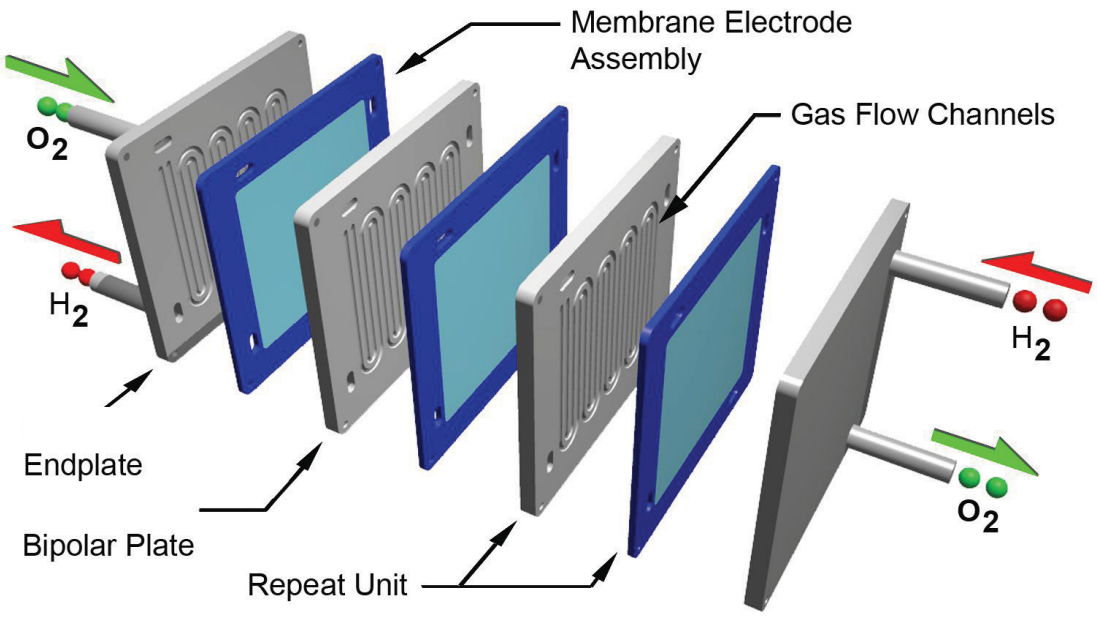

Figure 1-3. Conventional PEMFC stack architecture [6].

Stacking is an efficient way to assemble cells because the stacks exhibit extremely low ohmic losses due to the large electrical contact area between cells [2]. A drawback to this configuration is that each BPP in the stack must be machined to have flowchannels for hydrogen on the anode and for air/oxygen on the cathode. The machining of these flowchannels into both sides of the graphite plates is time consuming and expensive, often contributing to 50% of the total system cost [2]. A second drawback to the stack configuration is that in order to prevent reactant gasses from leaking through the porous electrodes and mixing, robust gaskets are needed around the edge every cell. If a single gasket fails in the stack, that particular cell will not be able to produce current. Since all the cells are connected in series, the failed cell becomes an open circuit, preventing current flow through the entire stack, rendering the stack useless.

A number of system level components are needed for a PEMFC stack to operate efficiently, the most significant having to do with heat and water management. Without proper management, heat generated from the ORR will raise the temperature of the stack to well above its optimal operating temperature of 80 °C. In smaller stacks air cooling is sufficient, while in larger stacks more extensive cooling systems are required. Since the efficiency of each cell depends on the water content of its electrolyte, a humidification system is often necessary to add moisture to reactant gasses. These system level components can contribute to a significant amount of parasitic power draw from the stack, reducing the system's net power output.

1.4 PEMFC Ribbon Assembly Architecture

An alternative option for assembling multiple cells together in series is a planar configuration where current flows from cell to cell in a plane parallel to the electrode surface. One such planar design which was proposed and developed by the Energy Systems Laboratory (ESL) at Virginia Polytechnic Institute and State University is the Ribbon Fuel Cell design [7] shown in Figure 1-4. In a Ribbon Cell stack, current is conducted in-plane along a highly conductive GDL to adjacent cells, instead of through the plane of the GDL as in conventional stacks.

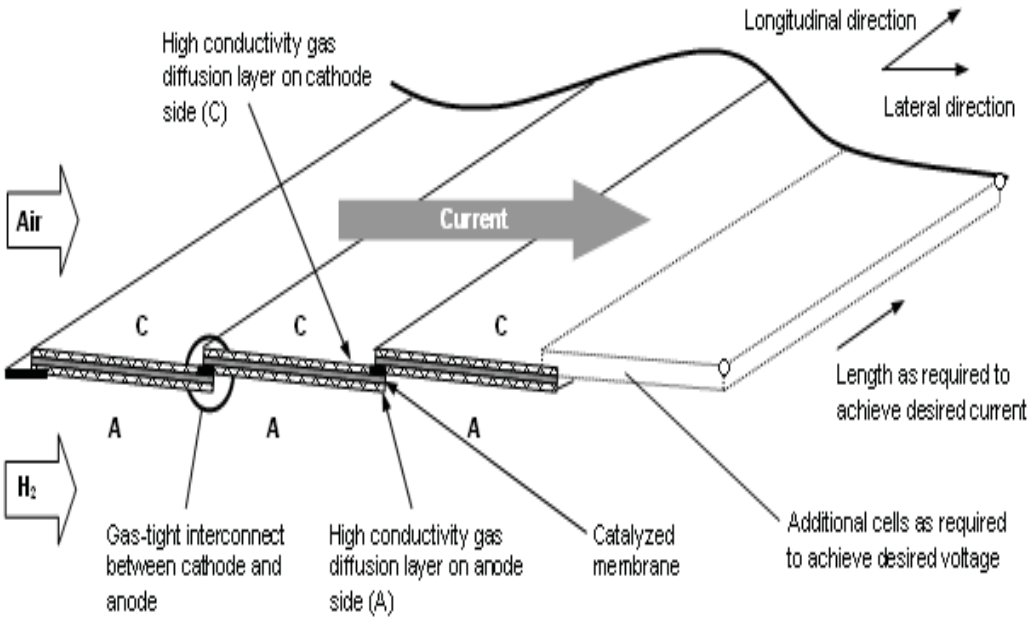

Figure 1-4. Ribbon Cell stack architecture [7].

The advantages of the Ribbon Cell stack stem from its in-plane current conduction, which eliminates the need for bipolar plates. Because of the high cost associated with the precision machining of bipolar plates, Ribbon Cells have the potential for reduced material and assembly costs. Their planar configuration also lends itself well to a streamlined manufacturing process using modern laminating equipment, which would reduce cost even further. The elimination of bipolar plates has a second major benefit in that it reduces the weight of a fuel cell stack, a characteristic which is extremely important for automotive and other portable power applications. Lastly, the planar configuration of a Ribbon Cell stack lends itself well to applications such as powering a laptop, where the shape and volume of conventional stacks make their use impractical.

As with any novel design, the advantages of the Ribbon Fuel Cell architecture are accompanied by disadvantages when compared to conventional PEMFC stacks. In order for Ribbon Cells to operate efficiently, they must have GDLs which are highly conductive to counteract the increased electron travel path. Remember, that instead of having to travel on the order of 0.25 mm through the GDL thickness, electrons in Ribbon Cells must travel nearly 25.4 mm along the cell to reach adjacent cells. Thus, in order to produce similar power as a conventional stack, Ribbon Cell GDLs must have conductivities that are two orders of magnitude higher than their conventional counterparts. The ESL has been able to achieve this highly conductive GDL by weaving high conductivity pitch based carbon fibers with PAN based fibers into a carbon cloth. Although this GDL is much more conductive than those made from conventional carbon cloths or papers, the long conduction length associated with the planar design of Ribbon Cells still makes them slightly less efficient than conventional cells.

A second difference between conventional PEMFCs and Ribbon Cells, is that Ribbon Cells operate without stack compression[1]. Conventional stacks use tie rods or other methods to apply a uniform compression throughout the stack. This compression holds the different fuel cell components close together, greatly reducing contact resistance between layers in the cells. Compression also helps to prevent delamination of the electrolyte from the GDL, which results in an extremely large local contact resistance. Without external compression, Ribbon Cell assemblies must rely on the MPL to provide

[1] Operation without stack compression is the preferred design of Ribbon Cells, however some options exists for applying light surface compression to the assemblies using various foams. Even if these foam options prove to be functional and feasible, the resulting surface compression would be far smaller than the compression found in conventional PEMFC stacks.

adhesion between GDL and electrolyte layers. *If the MPL fails to provide adequate adhesion, cell performance will drop dramatically.*

Although the ESL at Virginia Tech has been able to construct Ribbon Cell assemblies with a highly conductive GDL, and a MPL which provides some adhesion between GDL and electrolyte, the power of Ribbon Cells is not yet competitive with conventional PEMFC stacks. Currently, Ribbon Cell assemblies produce around 0.15 W/cm^2 operating at 50 °C with a cathode open to ambient air, while conventional stacks operating under the same conditions but with cathode air flow, achieve power densities of between 0.25 and 0.5 W/cm^2. The sustainability of power output over numerous on/off or wet/dry operating cycles is also an issue in Ribbon Cells. It has been observed that power output declines slightly each time the cell is turned on and off. This power drop is likely due to the delamination of electrolyte from GDL, which occurs when the electrolyte swells and shrinks as its moisture content changes. *Delamination is a durability concern in conventional stacks, however, the problem is exacerbated in Ribbon Cells due to their lack of compression.* In summary, Ribbon Fuel Cells are a promising portable power source due to their lightweight planar design; however, their efficiency and durability must be improved before their commercialization can be realized.

1.5 Research Objectives

The overall goal of this research is to determine the MPL parameters and assembly techniques which lead to optimal performance and durability in Ribbon Fuel

Cell assemblies. In this work, durability is defined as the sustainability of performance after multiple wet/dry operating cycles. The major objectives of this work are:

- Determine which MPL and Assembly parameters have the most influence on Ribbon Cell performance.
- Determine the level of each parameter that leads to optimal initial performance at various operating conditions.
- Determine the levels of each parameter that leads to optimal durability, or performance after multiple wet/dry operating cycles.
- Explain the failure mechanism that is causing Ribbon Cells to exhibit poor durability.
- Explain the influence of each factor and why the optimal levels found lead to high performance.

The following section will briefly discuss other planar PEMFC configurations and outline the work which has already been performed regarding optimization of the MPL. Next, the experimental procedures used to achieve the above goals will be described. The following section will present and discuss the findings of this work, and finally overall conclusions and recommendations for future Ribbon Cell work will be presented.

2. Literature Review

The focus of this work is on optimizing the MPL for Ribbon Fuel Cells, therefore this chapter will summarize previous work on other novel planar PEMFC configurations and will review research over the past decade regarding optimization of the MPL for specific PEMFC applications. Specifically, conclusions related to the function of the MPL, its composition, loading and application will be reviewed.

2.1 Planar PEMFC Designs

One of the first planar PEMFC designs which utilized lateral current conduction was developed by Heinzel et al. [8] in 1998. In their design, shown in Figure 2-1, current is conducted in-plane along the cathode GDL, through an interconnect to the anode of the adjacent cell. In Figure 2-1, this structure is repeated four times to create a four cell planar assembly.

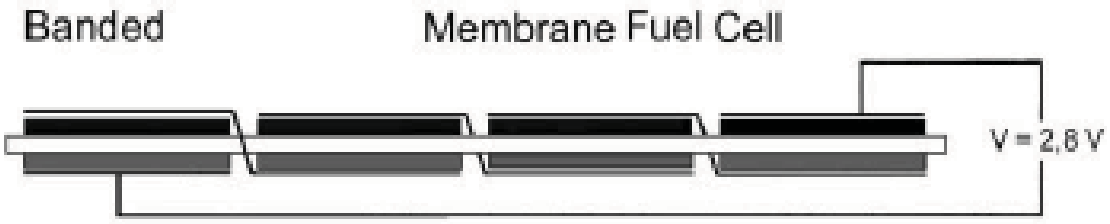

Figure 2-1. 4-Cell banded assembly developed by Heinzel [8].

The authors do not specify the exact design of the electrical connections that bridge adjacent anodes and cathodes; however, there are only two feasible ways to make the connection [2]. The first is to make the connection around the edge of the membrane at the perimeter of the assembly through conductive edge tabs. Although robust, this connection places constraints on the width of each cell because the electrons must travel an additional distance equal to the width of the cell to reach reaction sites of the adjacent cell, see Figure 2-2. In addition to limiting the size of each cell, the long conduction paths introduce greater resistive losses in the assembly. A second way to make the cell to cell electrical connections is to rout some conductive material through the membrane (also shown in Figure 2-2). This breach method creates a shorter electron path, but for the assembly to be functional, the area around the connection must be sealed to prevent reactant gasses from mixing. Sealing around the breach interconnection is especially difficult with Nafion® as it swells drastically with water content. Since the authors do not describe their electrical connections in detail it is impossible to know which connection they used.

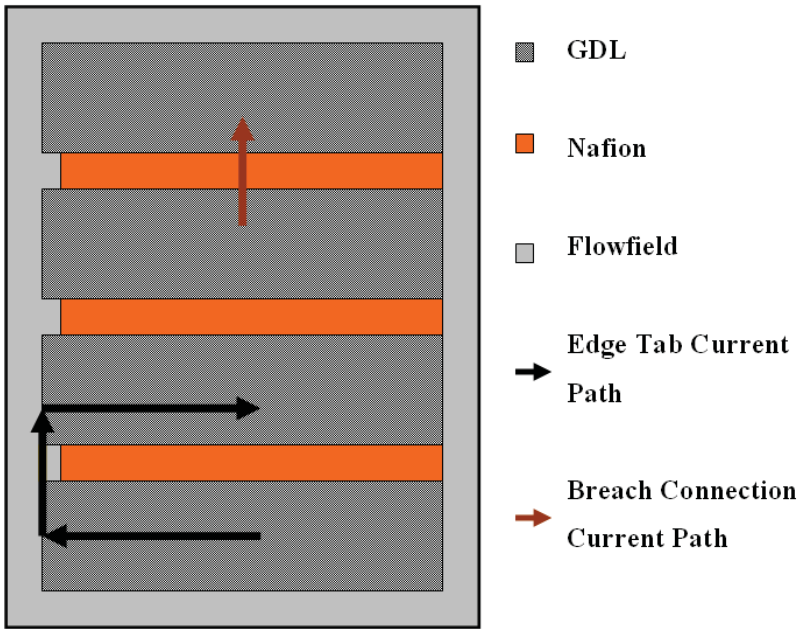

Figure 2-2. Top view of banded assembly showing current path around membrane edge and through membrane.

With the 4-cell banded assembly shown in Figure 2-1, Heinzel was able to achieve a current density of 0.23 A/cm^2 at a voltage of 0.5 V while operating with air on the cathode and at a cell temperature of 25 °C. The humidities of the reactant gasses were not given. The authors were able to achieve sufficient conductivity in their GDL by using Toray Carbon Paper impregnated with carbon particles. Impregnating the GDL pore space with conductive particles improved through-plane conductivity of the carbon paper by nearly 20%. After the initial success of the 4-cell assembly, Heinzel scaled up his prototype to include five banded structure membrane layers with five cells each similar to that shown in Figure 2-3. This hybrid method of assembling planar cells in a stack configuration was able to achieve a power output of between 15-20W. Unfortunately, the authors did not provide the active area of the assembly, so calculation of area specific power density is impossible. It is important to note that although this

banded structure is very similar to Ribbon Cell architecture, all tests were performed using end plates to apply compression throughout the assembly.

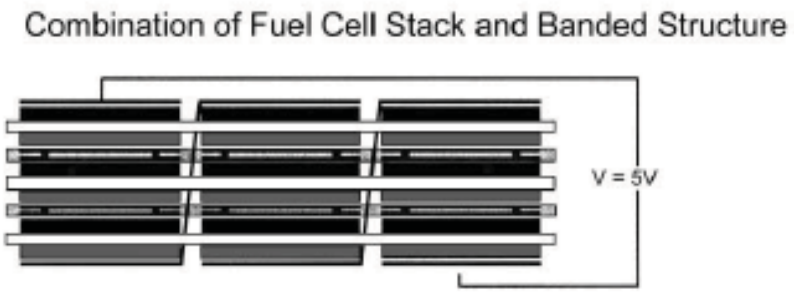

Figure 2-3. Multiple banded structure assemblies in a stack configuration.

A configuration which is even more similar to the Ribbon Cell design than the banded structure, is the monopolar strip stack developed by Jiang and Chu [9] shown in Figure 2-4. As with the banded structure design, current is conducted in plane from the cathode of one cell to the anode of the adjacent cell. The difference is that the electrolyte membrane is not continuous between cells. To verify the functionality of their design, a ten-cell 190 cm^2 stack was constructed and tested under various temperatures and anode relative humidities, while leaving the cathode open to ambient air. Jiang and Chu were able to achieve a sustained power density of 0.048 W/cm^2 at a cell temperature of 21 °C and 100% anode RH. The authors attribute this low power output to large resistive losses in the GDL associated with the lengthy current conduction path in the design. Despite the low power per unit area, the monopolar strip stack had a higher power density by mass than a conventional BPP stack constructed by the authors.

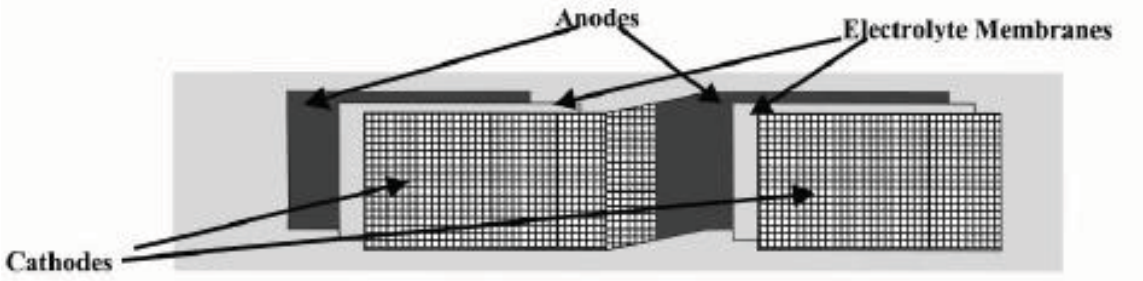

Figure 2-4. Two cell monopolar strip stack [9].

2.2 MPL Functions

The MPL is a key component of the Ribbon Cell design. While considerable research has been undertaken to understand the functions of the MPL in conventional cells, there has been little effort toward optimizing the MPL for a planar cell design. It is thought that the MPL of a Ribbon Cell performs all of the functions of the MPL in a conventional cell, but in addition plays the critical role of joining the GDL to the MEA. The relative importance of these conventional functions compared the additional adhesion role of Ribbon Cell MPLs is an unanswered question which will be explored in this work. Before this relative importance can be determined however, the conventional functions of the MPL will be described in this subsection.

Much of the recent work with conventional PEMFCs has been focused on improving the electrolyte or the GDL; however research has found that optimization of the MPL can improve cell performance by over 140% [10]. This increase in power is the result of a well formed MPL which 1) reduces the contact resistance between the CL and GDL, 2) prevents CL penetration into the GDL, 3) enhances the diffusion of gasses to reactant sites and most importantly 4) improves water management in the cell.

One function of the MPL that is commonly overlooked is its ability to prevent CL particles from penetrating into the GDL. Weber and Newman [10] believe that when compression is applied to the cell, catalyst layers may become entrenched in the GDL far from the electrolyte, thus lowering the number of triple phase zones in both the anode and cathode of the cell. They also write that the MPL acts as a buffer, preventing GDL fibers from piercing the electrolyte upon cell compression. This buffer effect can be seen in Figure 2-5, where the MPL is referred to as the catalyst supporting layer.

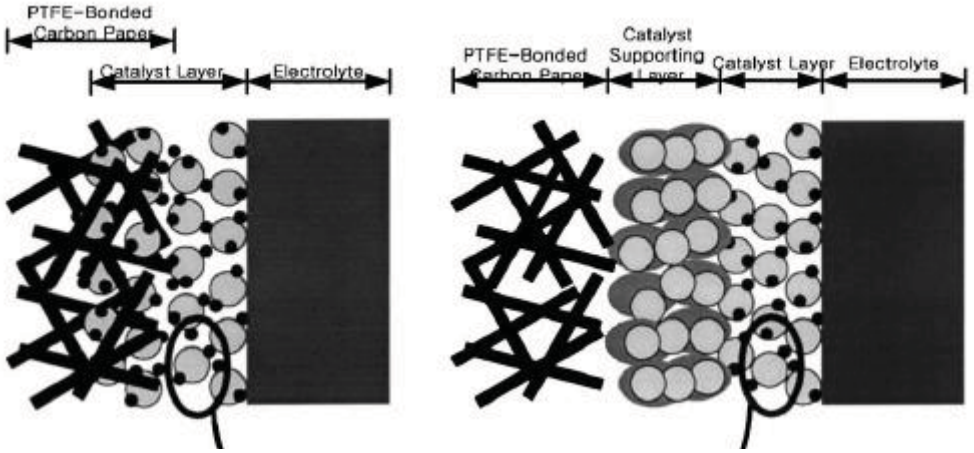

Figure 2-5. Buffer effect of MPL [18].

One of the more tangible benefits of the MPL is that it reduces ohmic losses in the fuel cell by reducing contact resistance between the CL and the GDL. Nitta et al. [11] found that when a MPL was not present, the contact resistance between the GDL and CL was more than an order of magnitude larger than the contact resistance between the GDL and BPP. The contact resistance was even comparable to the ionic resistance of the electrolyte, which usually dominates losses in PEMFCs! Chen-Yang et al. [12] explain that the surface roughness of the GDL leads to poor overall contact with the CL resulting

in very high CR values for PEMFCs without a MPL. They believe that the addition of a MPL reduces interfacial resistance by forming a flat and uniform layer on the GDL surface which provides better contact with the CL. In addition to providing more contact surface, Weber and Newman [10] believe that contact resistance is further reduced by the MPL because it provides better adhesion between layers of the fuel cell.

Perhaps the most essential function of the MPL in conventional fuel cells is to assist in cathode water management. Effective water management is most essential on the cathode because that is where the majority of liquid water is present. Two factors contribute to the cell's cathode side having higher water content than the anode. The first is the formation of product water during the ORR, and the second is the movement of water from anode to cathode by electro-osmotic drag. When air is used as the oxidant rather than oxygen, cathode water management becomes even more important. Since the partial pressure of oxygen in air is reduced, the oxygen diffuses more slowly through the GDL to catalyst sites. Therefore, it is essential to keep the cathode GDL permeability high by preventing liquid water from blocking its pores. Figure 2-6 shows the drop in performance associated with flooding of the cathode.

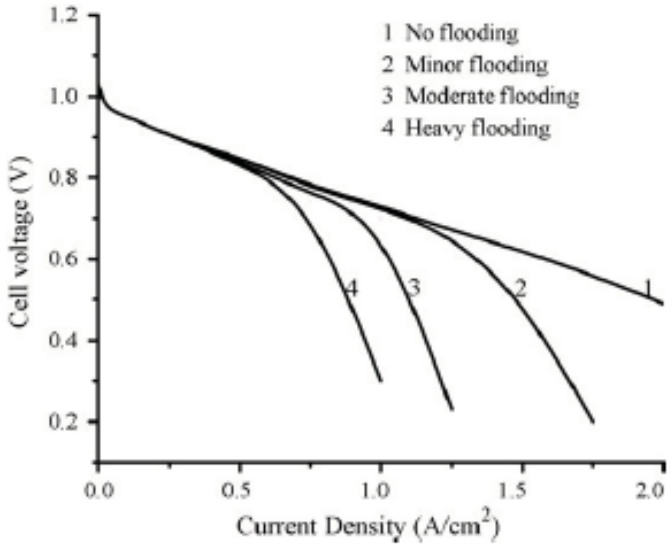

Figure 2-6. Polarization curves illustrating the effect of cathode flooding on cell performance [13].

In addition to lowering permeability by blocking GDL pores, flooding can drastically lower performance by blocking reaction sites in the CL. Li et al. [13] believe that the MPL wicks liquid water away from the CL and into the GDL where it eventually makes its way to flowchannels and out of the cell. Qi and Kaufman [14] have an opposite theory as to how the MPL reduces CL flooding. They believe that the cathode MPL acts as a barrier that forces water away from the cathode CL and back through the membrane to the anode side of the cell.

As discussed previously, the MPL helps to assist in diffusion of reactant gasses to CL sites; and although there is widespread agreement that diffusion is enhanced by the MPL, the exact mechanism for that enhancement is under discussion. Kong et al. [15] performed a study where they used various pore forming agents to control the pore size distribution and permeability of the MPL. They concluded that the distribution of macropores (5-20 μm) versus micropores (0.03-0.06 μm) is responsible for enhanced gas

diffusion through the GDL and MPL. The authors argue that micropores become filled with water before macropores because their diameters are smaller than the critical pore size, causing water to condense before reaching its saturation pressure. This leaves macropores void of liquid water and able to provide clear pathways for reactant gas diffusion. Passalacaqua et al. [16] also agree with Kong that the distribution of pore size is what improves the diffusion characteristics of the MPL, however, their reasoning is very different. They believe that macropores flood first, while the micropores remain dry and provide unrestricted pathways for reactant gas diffusion.

In their analytical model of water distribution in various fuel cell layers, Weber and Newman [10], found that the MPL reduced GDL flooding dramatically. They argue that since the MPL has smaller pores than the GDL, it can withstand higher liquid water pressures before flooding than can the macroporous GDL. The resistance to water flow caused by the MPL acts to increase the water pressure at the GDL/CL interface and force water back through the electrolyte instead of allowing it to flood the cathode GDL pores. Figure 2-7 shows the water saturation and pressure across different layers of a fuel containing no MPL (shown on the left) and one with a cathode MPL (shown on the right).

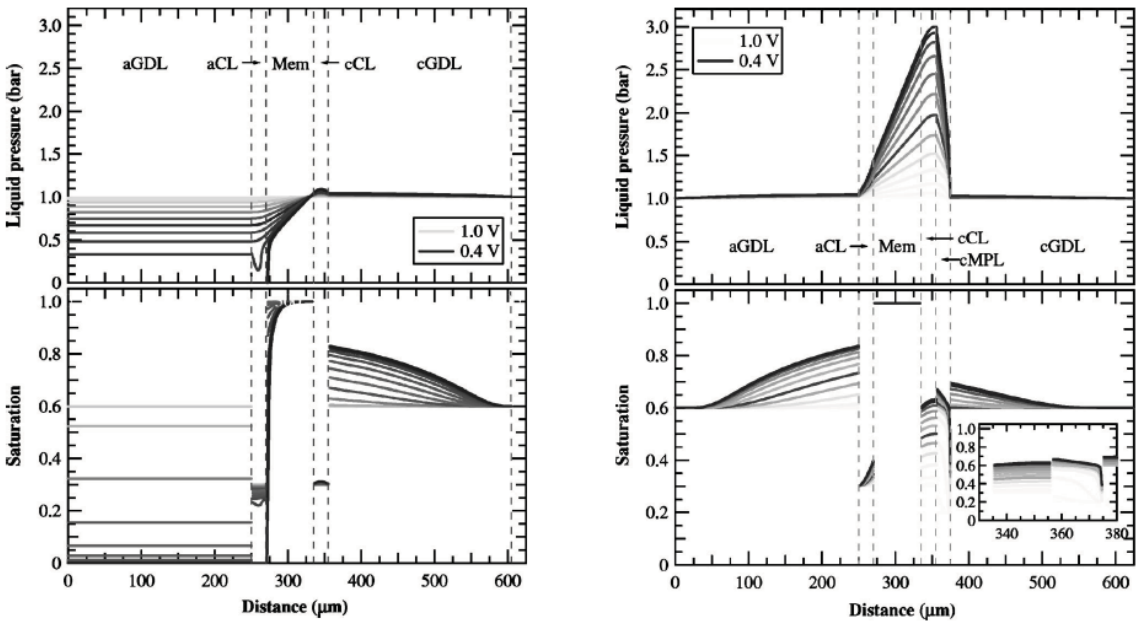

Figure 2-7. Saturation and liquid water pressure across a PEMFC with no MPL (left) and with a cathode MPL (right) [10].

In addition to reducing GDL flooding, Weber and Newman [10] believe that the MPL is essential in keeping the moisture content of the electrolyte high. They write that when no cathode MPL is present, the porosity of the membrane is too high to force back diffusion of water through the membrane. Instead of moisturizing the electrolyte, water flows out through the cathode GDL, leaving the membrane dry and highly resistive. Figure 2-7 shows the difference in membrane moisture content with and without the presence of a MPL. With a MPL, the membrane is completely saturated throughout its entire thickness, while the membrane without the MPL is below saturation near the anode side.

In summary, the MPL performs many functions in a conventional PEMFC such as preventing catalyst particles from penetrating into the GDL and providing a smooth surface for contact with the CL, which reduces interfacial resistance. The most important

function of the MPL in a conventional PEMFC however, is managing water on the cathode side of fuel cell. It keeps the moisture content of the electrolyte high, while preventing the cathode GDL from flooding and becoming impermeable to oxygen. It is believed that in addition to the functions described above, the MPL of a Ribbon Cell joins the GDL and MEA, preventing delamination between these layers. Unfortunatley, this theory cannot be verified through a review of relevant literature because there has been little, if any, exploration into the functions of the MPL in a planar PEMFC that operates without external compression. A major goal of this work is to determine if adhesion between GDL and MEA is an essential function of a Ribbon Cell MPL, and if so, how important is this function relative to the conventional MPL functions. The next few sections will outline research that has been performed on how the MPL composition, loading and application affect conventional cell performance.

2.3 MPL composition

The MPL is composed of a fluoropolymer and a carbon filler, with the most common formulations containing PTFE and carbon black. In some cases perflourinated ethylene-propylene (FEP) is used in the place of PTFE, however this is rare and it is more common to see variation in the type of carbon filler used. The most commonly used carbon fillers are Vulcan XC-72R which is a fine carbon powder, and Vulcan XC-72, which is composed of small carbon pellets. Despite the material options available, most of the work concerning the optimization of MPL composition focuses on the ratio, not the type of flouropolymer and carbon filler. Since the MPL consists of only two materials,

composition is usually expressed as the weight percentage of one of the components; in this work composition will be expressed as the weight percent of Teflon (wt% PTFE).

One study which did examine the effect of various materials in the MPL was performed by Jordan et al. [17]. They compared the performance of PEMFCs using Acetylene Black versus Vulcan XC-72R as the carbon filler of the MPL. It was found that cells containing Acetylene Black performed 15% better than those with the more common XC-72R. The improved performance was attributed to the lower pore volume and smaller pore size of the Acetylene Black MPL. The authors speculated that lower porosity and smaller pore volume kept more water at the CL instead of in the MPL and GDL where it would block reactant gas pathways.

Numerous studies have attempted to find the optimal ratio of PTFE to carbon black in the MPL, however there is little agreement among their findings. Giorgi et al. [19] varied the weight percent of PTFE from 10% to 60% in a MPL which contained 2 mg/cm^2 of carbon and found 10% yielded the highest power output. As the percentage of PTFE was increased, they found that cell resistance increased and MPL porosity decreased from 94% to 76%. This decrease in porosity caused a decrease in the amount of oxygen at catalyst sites, resulting in lower performance, especially at high current densities. Increasing the PTFE content also caused the formation of large cracks on the MPL surface, which are undesirable because they are believed to increase contact resistance. The authors speculated that although their lowest PTFE value performed the best, there is a minimum amount of PTFE needed in the MPL to bond carbon particles together and combat cathode flooding.

Velayutham et al. [20] varied the PTFE content in both their GDL and MPL. AvCarb P50 carbon paper was used as the GDL, and Vulcan XC-72 and PTFE composed the MPL. The MPL PTFE content was varied from 10% to 32%, with 20% giving the best cell performance. The authors noted the tradeoff between charge transfer resistance and permeability that must be reached when finding the optimal composition. If the PTFE content is too high, charge transfer resistance will increase as seen by the Nyquist plot in Figure 2-8. The benefit is that this MPL will manage water effectively and maintain high permeability in the GDL and MPL itself. If the PTFE content is too low, the opposite effects will be seen; charge transfer resistance will decrease, but permeability will suffer.

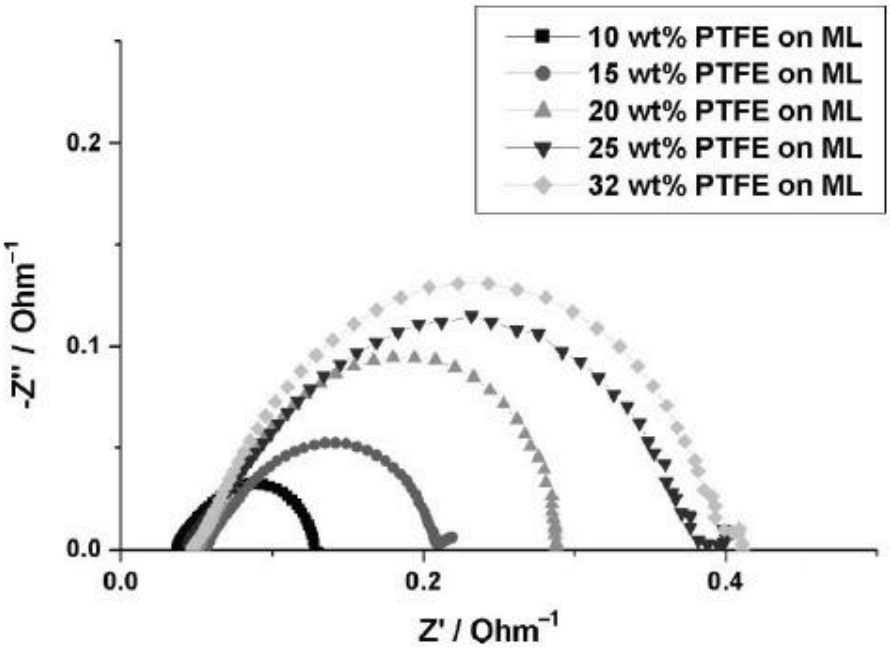

Figure 2-8. Nyquist plot illustrating the increase in charge transfer resistance with increasing PTFE content [20].

Park et al.[12] also found that a MPL composition consisting of 20% PTFE yielded the best performance, however their reasoning for why this value was optimal is slightly different. SGL 10CA carbon paper was used as the GDL, and Acetylene Black and PTFE composed the MPL. Carbon loading was kept constant at 2.0 mg/cm^2 and PTFE content was varied from 10% to 40% by weight. Using mercury porosimetry to characterize the porous structure of the MPL, the authors found that increasing PTFE content decreased the porosity of the MPL. Increasing PTFE content also created a higher number of hydrophobic pores in the layer. The authors speculated that at high PTFE levels, both these effects combine to greatly impede the flow of water from the CL through the MPL and into the GDL, causing flooding of the CL and reducing performance. Their hypothesis was validated when they measured the threshold pressure of liquid water versus PTFE content and found that there was a positive linear correlation. The results of their threshold pressure experiments are shown in Figure 2-9.

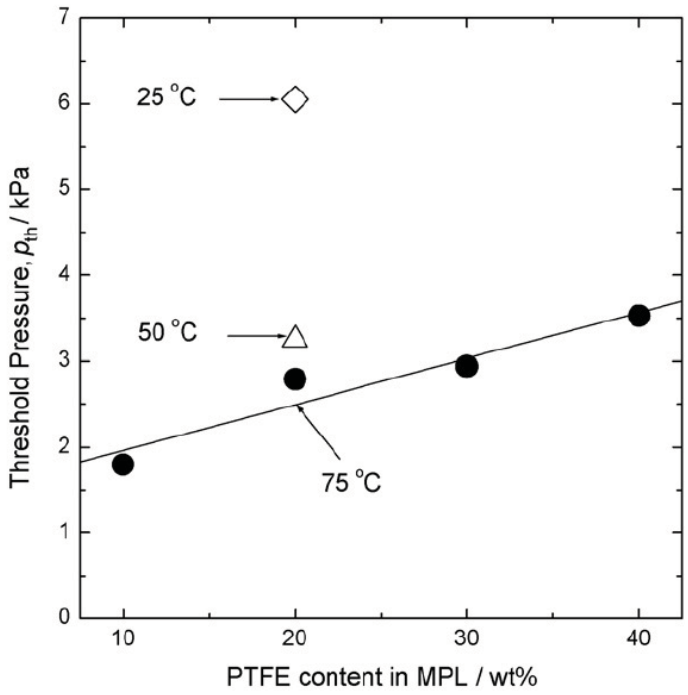

Figure 2-9. Plot of threshold pressure for liquid water versus PTFE content in MPL [12].

The major conclusion of Park et al. was that PTFE in the MPL acts as a water distributor, balancing liquid water between the CL and GDL. If the PTFE content is too high, the majority of the water will remain adjacent to the CL, flooding it and blocking reaction sites. If the PTFE content is too low, most of the liquid water will exist in the GDL, blocking its pores and lowering its effective permeability. Both situations result in lower than optimal performance. Figure 2-10 shows the performance of a cell with optimal PTFE levels, and cells with PTFE levels higher and lower than optimal. Weber and Newman [10] used an analytical model to asses the effect of PTFE content in the MPL. They reached the same conclusion as Park et al., that the percentage of PTFE in the MPL controls the distribution of water between the CL and GDL.

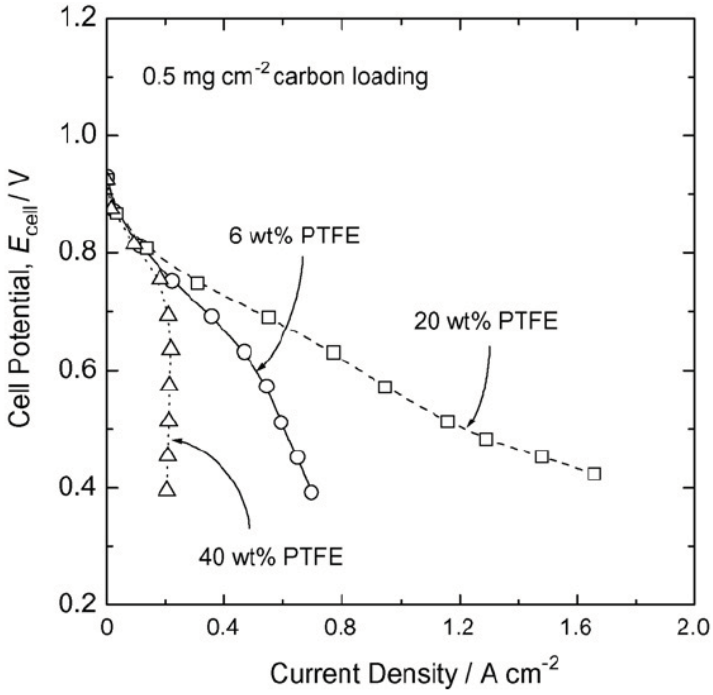

Figure 2-10. Polarization curves of PEMFC with varying PTFE contents in MPL [12].

2.4 MPL Loading

MPL loading is most commonly quantified by weight per area in units of mg/cm^2. In some cases, thickness of the layer is used to characterize loading, however this measurement is somewhat ambiguous because it does not factor in the density of the MPL, which can vary dramatically depending on the application technique and PTFE content of the layer. Also, sometimes the MPL is compacted onto the GDL by hot pressing or rolling, which can change the thickness of the layer. For these reasons it is almost impossible to correlate the two measurement techniques, making comparison of MPL loading studies difficult. Even among studies where the same loading measurement

method is used, there is little agreement on the exact value of MPL loading which gives peak performance.

In addition to varying the composition of their MPLs, Qi and Kaufman [14] investigated the effect of loading on performance. Using carbon paper for the GDL, MPL loading was varied from 0.57 mg/cm^2 to 4.04 mg/cm^2. They found that the optimal thickness of the MPL was dependent on the operating conditions of the cell. When only the hydrogen stream was humidified, a loading of 3.28 mg/cm^2 gave the best performance; and when both reactant streams were humidified a loading of only 0.96 mg/cm^2 yielded peak power. The authors also noted that there was some interaction between loading and composition. The exact interactions were difficult to extract, except that at higher PTFE contents, loading has less of an affect on performance than it did at lower PTFE values.

Weber and Newman [10] also varied both loading and composition of the MPL in their analytical study where they characterized loading by thickness of the MPL. A loading which gave a thickness of 20 μm gave the best performance. The authors believe that this thickness was large enough to manage water effectively and keep the GDL from flooding, while not being too thick as to limit gas permeability. Their reasoning is that as the MPL becomes thicker, reactant gas pathways through the layer become longer and more convoluted, introducing mass transport limitations. A layer that is too thick also introduces ohmic losses in the form of increased resistance through the thickness of the layer. This effect can be significant because of the fact that the MPL is less conductive than the GDL. On the opposite extreme, a thin layer will not be able to hold sufficient

water adjacent to the electrolyte, lowering back-diffusion and drying the membrane, thus reducing membrane conductivity.

Jordan et al. [17] also agree that an intermediate MPL loading is optimal. They used TPG-H-120 carbon paper and a MPL with 10% PTFE by weight. Loadings were varied between 0.7 and 2.5 mg/cm^2, with loadings of 1.9 and 1.25 mg/cm^2 giving the best performance. They observed that high loadings performed worst, due to poor gas diffusion through a thicker layer. It was theorized that low loadings performed poorly because there was not enough MPL to provide a non-permeable support for the CL. As a result some of the CL permeated into the GDL far away from the electrolyte, rendering it useless for reactions (see figure 2-5). The final, but perhaps most important conclusion of the work, was that under different operating conditions, the authors believe that different MPL loadings will be optimal.

Song et al. [18] used AC impedance and cyclic voltammetry to explain the results of their study in which they varied MPL composition and loading. Loadings of 1.5, 3.5 and 10.0 mg/cm^2 were used in their study with a PTFE weighting of 30%. Their cyclic voltammetry data showed that the available area of catalyst sites was maximized at 3.5 mg/cm^2. Lower and higher loadings decreased the number of available catalyst sites for reasons unknown to the authors. AC impedance results showed that faradic impedance was at a minimum for 3.5 mg/cm^2, further suggesting that this intermediate loading gives the maximum available surface area for the ORR. Their AC impedance data also showed that at lower loadings, a low frequency arc developed, implying that some kind of mass transfer limitation was present, which is contradictory to the conclusions of other studies.

Unfortunately, the authors did not give an explanation as to why a thinner layer shows larger mass transport losses.

Park et al. [21] varied the loading of a MPL made of 20% PTFE and Acetylene Black, from 0.25 to 2.5 mg/cm^2. Once again an intermediate loading, 0.5 mg/cm^2, gave the best cell performance. The authors suggested that varying the loading of the MPL has a similar effect to varying its PTFE content. An excessive loading causes the CL to flood due to high liquid water flow resistance, similar to the effect of MPLs with a high PTFE composition. An inadequate loading causes water to flood the cathode GDL as it does with MPLs with low PTFE contents. In summary, the authors believe that MPL loading affects the balance of water between the CL and cathode GDL.

In his thesis, Henderson [22] performed a full factorial study in which he examined two levels of MPL loading (1.5 and 4.0 mg/cm^2), and two levels of PTFE weighting (10% and 50%). Using ETEK B1A cloth as a GDL he found that a loading of 1.5 mg/cm^2 with a PTFE content of 10% gave the best performance. Unfortunately, his two-level experiment only allowed for the visualization of linear correlations, meaning that an intermediate loading could be optimal but remain unseen in his statistical analysis. Henderson's study did provide unique insight into how loading and composition affect the adhesion of the CL/MPL and MPL/GDL interfaces. It was his thinking that stronger adhesion correlates with enhanced durability over long and cyclic operating periods. This durability is especially important in Ribbon Cell assemblies where there is no stack compression holding layers together. Henderson found that lower MPL loadings with 30% PTFE gave the best adhesion. One drawback to Henderson's work was that he

didn't validate his theory that better adhesion improved cell durability with experimental data.

2.5 MPL Application and Heat Treatment Techniques.

The method in which the MPL is applied to the GDL can have an effect on performance, but it is commonly overlooked in studies. The most common ways to apply the MPL are spraying, screen printing and tape casting. Spraying is accomplished by using an airbrush and a diluted MPL mixture. In this technique, the MPL is applied in layers, with each layer being allowed to dry before successive layers are added. Although time consuming, this application method provides precise control of MPL loading. In the screen printing method, MPL is forced through a screen onto the GDL with a squeegee. A disadvantage of this method is that the screen porosity and ink viscosity must be carefully monitored to control the MPL loading. Also, the screen must be thoroughly cleaned after every use. Tape casting works best when the application of a single thick MPL is desired. In this process, an excessive amount of MPL is first applied to the GDL. Next, a stencil with a desired thickness is placed around the GDL and a flat blade is run over the stencil to give the desired thickness. A major disadvantage of this method is that it can be difficult to control loading.

Lee et al. [23] explored the effect of MPL application techniques on cell performance. They prepared MPLs with Vulcan XC-72 and 30% PTFE and applied them using spraying, screen printing and rolling methods. The authors found that screen printing produced cells that performed best, as shown in Figure 2-11. They argue that the

different application techniques result in different MPL porosities. Porosity data obtained using mercury porosimetry supported their hypothesis, with MPL porosities of 51, 57 and 61% found for rolling, spraying and screen printing methods respectively. The authors also speculate that sprayed and screen printed MPLs performed better because they had a rougher surface which provided more surface area for CL contact.

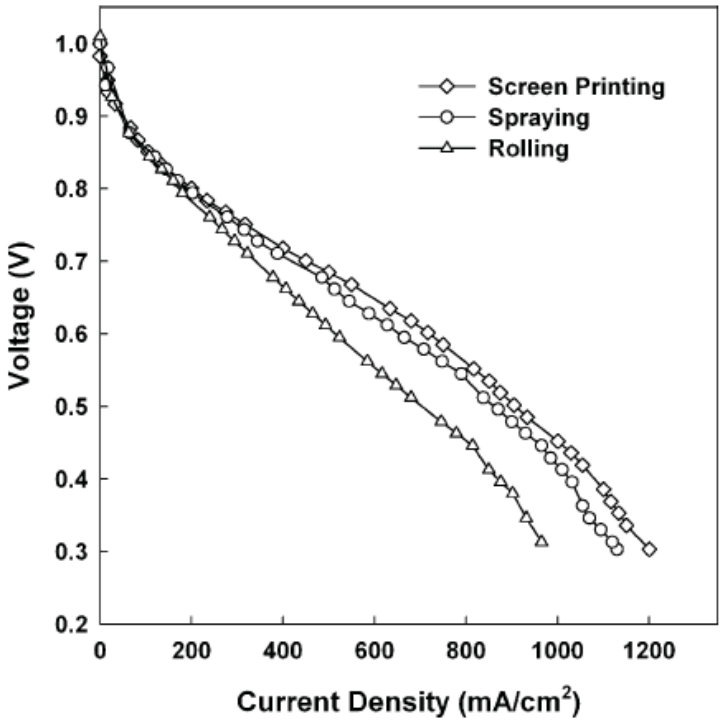

Figure 2-11. Influence of MPL application techniques on cell performance [23].

It is common practice to heat treat the MPL after its application onto the GDL. In most cases the MPL is heated in an oven for 30 minutes at around 100 °C to dry it; then heated at 250 °C for 30 more minutes to evaporate the remaining dispersant (usually iso-propyl alcohol or glycerol). The final step is to sinter the PTFE particles in the MPL by heating at 350 °C for 30 or more minutes. Kong et al. [15] believe that sintering the MPL

improves its water management capabilities by melting the PTFE and transforming it into its fiber phase. This re-dispersion of PTFE during sintering was found to increase the number of micropores in the MPL. Their rather unconventional theory was that an increased number of micropores provides more space for liquid water to occupy, leaving more macropores open and available for gas diffusion. Jordan et al. [17], also observed improved performance in cells with sintered MPLs. The authors believed that sintering provides a more homogeneous covering of PTFE in the layer thus making it more hydrophobic and better at managing water.

2.6 Literature Review Summary

Studies have shown that the MPL plays an important role in conventional PEMFC performance. In conventional cells, its most important function is managing water on the cathode side of the cell. An optimized MPL keeps the electrolyte moist and conductive, while keeping the GDL sub-saturated and thus permeable to reactant gasses. Numerous studies have attempted to find the optimal loading and composition of the MPL, however there is little agreement among researchers as to exactly what these optimal values are. Almost all studies have found that a composition of between 10 and 35%, with a loading of between 1.5 and 4.3 mg/cm^2 yields cells with the best performance. One reason for this lack of consensus is that the cell's operating conditions may play a role in determining the optimal MPL characteristics. For example, a MPL which performs poorly under dry conditions may perform well when reactant gas streams are fully saturated and vice versa. The interaction between loading and composition may be

another reason for the disagreement. Lastly, many believe that the properties of the GDL such as thickness, surface roughness and porosity have an effect on what type of MPL will work best. If this theory is accurate, the lack of GDL standardization among studies could also contribute to the range of optimal values seen in literature.

The work presented herein attempts to find the optimal MPL composition and loading for the high conductivity GDL in the novel Ribbon Fuel Cell architecture. The GDL used in Ribbon Fuel Cells is vastly different from any used in the studies reviewed above. It is composed of large fiber bundles, which are woven into a cloth that is much thicker and rougher than conventional GDLs. In addition, a Ribbon Fuel Cell assembly operates without compression, relying on the MPL to provide adhesion and keep the GDLs and electrolyte in close contact with one another. Few studies have examined the effects of MPL composition and loading on adhesion. Henderson [22] was one of the few to look into the adhesive properties of the MPL, however, the study's design only allowed for linear correlations to be found. Henderson also did not test his specimens in Ribbon Fuel Cell assemblies, nor did he perform durability studies on his samples.

In addition to the adhesive properties of the MPL, Ribbon Fuel Cells rely on a hot press operation to consolidate layers and establish structural integrity. This press operation is referred to in this work as the assembly press, and is performed on the completed Ribbon Cell assembly to bond the anode and cathode GDLs to the electrolyte. A detailed description of the Ribbon Cell assembly process will be presented in the following section. It is common for conventional cells to be pressed together in a similar manner; however no studies have been performed examining the optimal press parameters for cells which operate without external compression, and few have looked

into how the press parameters interact with the MPL to affect adhesion. Henderson [22] was one of the few who examined the interaction between MPL properties and assembly press parameters, but he did so for conventional PEMFC assemblies.

In summary, review of recent MPL literature identified composition and loading as the parameters which most influence fuel cell performance. The findings from these studies for the most part, are not applicable to Ribbon Cells because of the unique GDL and lack of compression inherent in the Ribbon Cell architecture. This work attempts to fill the void of knowledge about the function and optimization of MPLs in planar PEMFCs which operate without compression. To accomplish this, extensive testing of various Ribbon Cells was performed as described in the following experimental procedures section.

3. Experimental Procedures

3.1 Experimental Objectives

The main objective of this research is to optimize the MPL and assembly parameters of Ribbon Fuel Cells in order to improve both their performance and durability. The four parameters being analyzed are the MPL composition, MPL loading, MPL sintering pressure, and cell assembly pressure. To determine the effect of each of these factors on performance and durability, as well as the interactions among factors, an experimental matrix was carefully designed with the help of the statistical software Design Expert® produced by Stat-Ease, Inc.

When deciding on the operating conditions with which to test the Ribbon Cells, the likely applications of the technology were considered. The lightweight design and planar geometry of Ribbon Cells make them ideal for many portable power applications that currently use rechargeable batteries as a power source. In many of these portable applications, it is essential to minimize the weight of not only the Ribbon Cell assembly, but also the weight of the associated system level components. These components include hardware associated with reactant gas storage/humidification as well as those involved in heat and water management. To reduce system complexity and weight, Ribbon Cell assemblies are designed to operate with the cathode side open to the ambient environment. Having this passive cathode eliminates the need for cathode gas supply components (storage bottles, compressors or fans), distribution manifolds and humidification components. In some applications it is likely that even having a

humidification system for the anode gas will cause the Ribbon Cell system to exceed weight limitations. Due to the wide range of operating conditions that could potentially be seen by Ribbon Cell assemblies in various portable power applications, *this work will attempt to find a combination of the aforementioned factors, which will provide the best performance at both high and low reactant gas humidity levels.*

As mentioned previously, because Ribbon Cells do not operate under external mechanical pressure like conventional fuel cell stacks, membrane delamination from MPLs and GDLs is a common failure mode. Preliminary work has shown that Ribbon Cells can sustain their performance for extended operating times at steady conditions (cell temperature, and reactant gas humidity); however, performance drops significantly after only a few on/off or high/low reactant gas RH cycles. For the sake of simplicity, cells which have experienced one or more of these RH cycles will be referred to as "aged samples," while those which have not will be called "un-aged samples." *This work attempts to find a combination of MPL and assembly parameters which minimizes the drop in performance after multiple high and low reactant gas RH cycles.*

Another objective of the research is to explain the observed effect of each of the four factors on Ribbon Cell performance and durability. A number of techniques were used to determine the influence of certain variables on performance including potentiodynamic tests, potentiostatic tests and electrochemical impedance spectroscopy (EIS) tests. In order to provide further insight, data on the adhesion among various layers in the cells was gathered by mechanical testing and analyzed.

This section describes the experimental design used to characterize the aged and un-aged performance of cells constructed with various MPLs and assembly parameters.

The following section goes on to describe the experimental design used for adhesion testing. Next, the procedures used to create Ribbon Cell samples for performance and adhesion testing are outlined, and the methods used to characterize their responses explained.

3.2 Experimental Design for Performance Testing

Since the goal of this work is to determine the MPL and assembly parameters which yield optimal performance, an experimental design which yields correlations with curvature between factors and responses was needed. An experimental design with curvature allows for the prediction of responses between the factor values which were tested. With the need for curvature in mind, three types of experimental designs, full factorial, fractional factorial and central composite were considered for this work.

3.2.1 Experimental Design Exploration. The most basic experimental design considered was a full factorial design. In its simplest form, this design varies each factor between two values which are referred to as high and low levels. Samples are then created for all possible combinations of levels and factors. Figure 3-1 shows a graphical representation of a 2-level, 3-factor full factorial design. This design provides good determination of the interactions among factors, however because only 2-levels are being tested, it is not possible to determine correlations between factors and responses which have curvature. To obtain correlations with curvature, a 3rd level can be added to the design, however this has the effect of adding a large number of runs to the experiment.

For example, a 4-factor, 3-level full factorial design would require at least 81 (3^4) experimental runs. Due to time and material constraints, a 3-level full factorial design was deemed impractical.

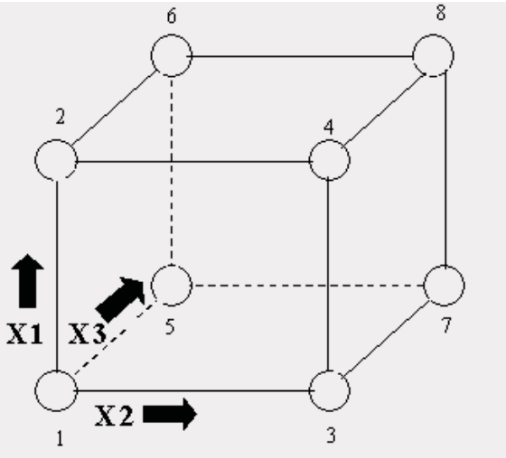

Figure 3-1. Graphical representation of a 2-level, 3-factor (X1, X2, X3) full factorial design [24].

A fractional factorial design can be thought of as a modified full factorial design in which a number of carefully chosen design points are omitted from testing, resulting in a significantly lower number of experimental runs. The most difficult part of designing a fractional factorial experiment is figuring out which design points to leave out. Knowing which points to test and which to leave out requires intimate knowledge of factor interactions and their effect on responses. Since there is little agreement in literature on the optimal level of the factors being analyzed in this work, it would not be prudent to remove certain design points from the experimental design. In addition, the fact that the response of these factors is the performance and durability of a new and relatively unexplored fuel cell design, further reinforced the decision not eliminate design points, and thus not use a fractional factorial design.

The experimental design which was best suited to achieve the goals outlined above was a central composite design (CCD). A CCD can be thought of as a two-level factorial design that is augmented with axial points in order to achieve correlations with curvature. The value of these axial points is determined by the type of CCD used.

In an inscribed central composite design (CCI), factor limits are determined and used as the axial points with the factorial points residing inside these axial points. Figure 3-2 shows a graphical representation of a CCI. The benefit of a CCI is that the designer ensures that he or she does not test factor values that unrealistic or outside the desired factor limits. Unfortunately, the nature of this design causes it to explore a smaller design space and give lower quality predictions over that design space than other CCDs (24).

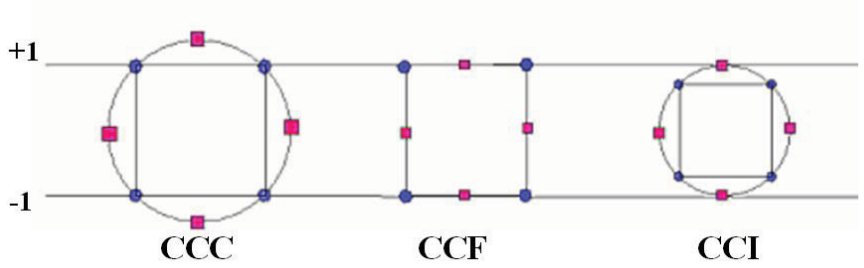

Figure 3-2. Comparison of various CCDs. Factorial points shown in red, axial points shown in blue [24].

A second type of CCD is the face centered design (CCF) in which axial points are located at the center of each face of the factorial design as shown in Figure 3-2. This design provides relatively high quality predictions over the entire design space, however it gives poor precision for estimating pure quadratic coefficients in response correlations (24).

In a circumscribed central composite (CCC) design, the axial points establish new high and low values for each factor and are thus located outside of the factorial design space of the underlying factorial design. Figure 3-2 shows a graphical representation of a 2-factor CCC. The benefits of a CCC are that it explores the largest space of all CCDs, while providing high quality predictions over the entire design space. The drawback of a CCC is that since axial points generate new extremes for all factors, the designer must be careful that the factor settings called for by the axial points are reasonable. After careful consideration, a CCC was chosen for this work because it provides the highest quality predictions over the largest design space of the all the CCDs.

In summary, the experimental design used in this work is a 4 factor circumscribed central composite design consisting of 16 factorial points, 8 axial points and 6 center point replicates which are used for estimation of experimental error. Unfortunately, visualization of a 4 factor design is difficult, however, Figure 3-3 shows a graphical representation of a 3 factor CCC depicting the location of factorial, axial and center point replicates.

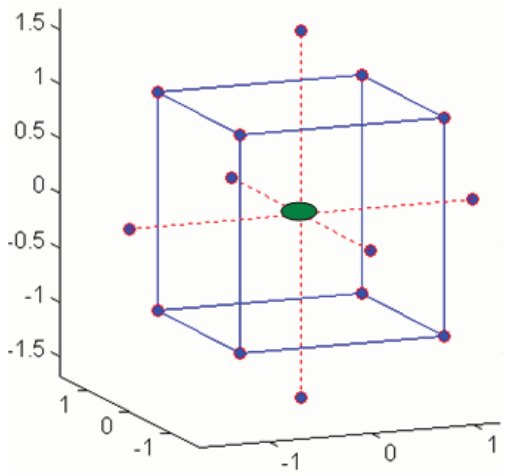

Figure 3-3. Graphical representation of 3-factor CCC showing axial (dotted lines), factorial (solid blue line) and center point replicates (green) [24].

3.2.2 Experimental Design Creation. After deciding which type of experimental design to use, reasonable levels for each factor were determined based on previous Ribbon Cell studies and values cited in literature. Optimal values for MPL composition varied in literature from 10 wt% [22] to 35 wt% PTFE [14]. With these values in mind, factorial levels of 15 wt% and 35 wt% were chosen, with center a point value of 25 wt%. Because Ribbon Cell MPLs have the dual purpose of water management and adhesion, it is possible that the optimal value for the unique Ribbon Cell architecture could be outside the range of optimal values established in literature for conventional cells. With this in mind, axial points were established at 5 wt% and 45 wt% PTFE.

Optimal loading values found in literature varied from 0.625 mg/cm^2 [23] to 4.3 mg/cm^2 [25]. It is important to note that the optimal loading of 0.625 mg/cm^2 found by Park et al. [23], was for a conventional fuel cell using a carbon paper GDL. Carbon paper GDLs have a much smoother and more uniform surface than the high conductivity GDL used in Ribbon Fuel Cells. This difference in surface roughness means that a thin MPL can be used to uniformly cover carbon paper, while a thicker MPL is needed to uniformly cover Ribbon Cell GDLs. Based on the values cited in literature and the unique Ribbon Cell GDL in mind, factorial levels for loading of 2 mg/cm^2 and 4 mg/cm^2 were chosen with a center point value of 3 mg/cm^2. Axial points were then established at 1 and 5 mg/cm^2.

Preliminary work on Ribbon Cell assembly pressure, performed at the Energy Systems Laboratory at Virginia Tech during the summer of 2008, found that cell assemblies pressed between 700 and 1000 psi gave the best performance. Optimal values

for the assembly press found in literature varied from 220 psi [12] to 1000 psi [18]. More importance was given to the optimal value cited in the study at Virginia Tech than those cited in literature, because the Virginia Tech study was performed using Ribbon Cells while studies described in literature were performed with conventional cells which function with external stack pressure. With this in mind, a center point value of 850 psi was chosen with factorial values of 600 and 1100 psi. Lastly, axial points of 350 and 1350 psi were chosen.

In conventional fuel cell stacks it is not common practice to sinter MPLs under pressure; because of this a review of relevant literature yielded no data on the optimal MPL sinter pressure. The reason why MPLs are not sintered under pressure in conventional fuel cells is most likely because it is unnecessary and gives no benefit when compared to sintering without pressure. Ribbon Cells on the other hand, benefit from sintering under pressure because the combination of heat and pressure creates a bond between the MPL and the GDL, which is important for GDL/MEA adhesion. Also, it was found that during the construction of multiple Ribbon Cell assemblies, MPLs which were not sintered under pressure would flake off from the GDL during subsequent construction steps. This observation prompted a preliminary investigation into the effect of sinter pressure on Ribbon Cell performance. The results of this preliminary study showed that cells which had MPLs sintered at pressures above 50 psi performed significantly worse than those containing MPLs sintered at lower pressures. Since performance decreased at sinter pressures above 50 psi, this value was chosen for the high-level axial point. After establishing the upper axial value, a center point pressure of 30 psi was chosen, with factorial points at 20 and 40 psi and a lower axial point of 10 psi.

After choosing the levels for each factor, these values were input to Design Expert® which established appropriate combinations of factors to give axial, factorial and center points[2]. The design points were then placed in a randomized run order to reduce systematic error. Table 3-1 shows the factor values used for each run and the order in which the samples were tested.

Table 3-1. Factor values for the CCC experimental design used in this work, organized by run order.

Run #	wt% PTFE	Loading (mg/cm^2)	Assembly (psi)	Sinter (psi)
1	25	3	1350	30
2	5	3	850	30
3	25	3	850	30
4	35	2	600	40
5	35	4	1100	20
6	25	1	850	30
7	15	2	1100	20
8	15	4	1100	20
9	25	3	850	10
10	15	4	600	40
11	35	4	600	20
12	15	4	600	20
13	25	3	850	30
14	35	2	600	20
15	25	3	850	30
16	25	3	850	30
17	25	3	850	30
18	15	4	1100	40
19	15	2	600	20
20	35	2	1100	40
21	35	2	1100	20
22	45	3	850	30
23	25	5	850	30
24	15	2	600	40
25	25	3	850	30
26	15	2	1100	40
27	35	4	1100	40
28	35	4	600	40
29	25	3	350	30
30	25	3	850	50

[2] Design Expert allows axial points to be input as a certain distance or radius from the center point, or as two specific values, provided that those values are equidistant from the center point. The latter method was used for the experimental design in this work since axial point values were established independently from center or factorial points.

In summary, a 4 factor circumscribed central composite design was created to determine the values for cell assembly pressure, MPL composition, MPL loading and MPL sinter pressure that optimize performance and durability at both high and low reactant gas RHs. Section 3.6 provides a detailed discussion of the responses used to characterize the performance and durability of each of the samples shown in Table 3-1. In the experimental design, MPL composition was varied from 5 wt% to 45 wt% PTFE; loading was varied from 1 mg/cm^2 to 5 mg/cm^2; sinter pressure was varied from 10 psi to 50 psi and cell assembly pressure was varied from 350 psi to 1350 psi.

3.3 Experimental Design for Adhesion Testing.

An experimental design was created to investigate the adhesive properties of the Ribbon Cell samples. It is important to note that the goal of this adhesion study is only to assist in explaining results from the performance and durability study; it is not designed to determine how to maximize MPL adhesion. Maximizing the adhesive properties of the MPL is something which should eventually be explored in Ribbon Cells, but only after the correlation between adhesion and performance is verified and understood at a basic level.

Since the purpose of the adhesion study is to explain the observations from the performance study, it was created after all the performance data was gathered. To minimize the number of experimental runs, factors which did not have a strong influence on the performance were not included in the design. Again, since the purpose of the

study was explanatory, not exploratory, correlations with curvature were not needed, and a simple 3-factor, 2-level factorial design was used. A design with minimal runs was also desired because of the high material cost and preparation time associated with the samples.

Analysis of the performance data suggested that MPL composition, MPL loading and assembly pressure had the strongest influence on both aged and un-aged performance, and these factors were therefore chosen for the adhesion experiment. The high and low values for each factor were chosen to match the corresponding factorial values in the performance study. This matching of factor levels creates similar samples between the two studies, allowing for the accurate comparison of adhesion and performance. With this in mind, the experimental matrix shown in Table 3-2 was created.

Table 3-2. Experimental matrix for adhesion testing.

Run	Composition (wt% PTFE)	Loading (mg/cm^2)	Assembly Press (psi)
1	15	4	600
2	15	4	1100
3	15	2	600
4	15	2	1100
5	35	4	600
6	35	4	1100
7	35	2	600
8	35	2	1100

3.4 Sample Preparation for Performance Testing

The major components that make up a Ribbon Cell are the MPL, high conductivity GDL, and the MEA which consists of catalyzed Nafion®. MPLs and GDLs were constructed in-house, while MEAs were purchased from Ion Power Inc. MEAs consisted of Nafion® (NRE-212) with cathode and anode catalyst layers consisting of 0.4 and 0.05 mg/cm^2 of platinum respectively.

In order to minimize both material cost and sample preparation time, single cell ribbon assemblies were used for testing. A schematic showing the architecture and major components of a single Ribbon Cell is presented in Figure 3-4. The following sub-sections will describe the construction of in-house MPLs and GDLs as well as outline the single cell assembly process.

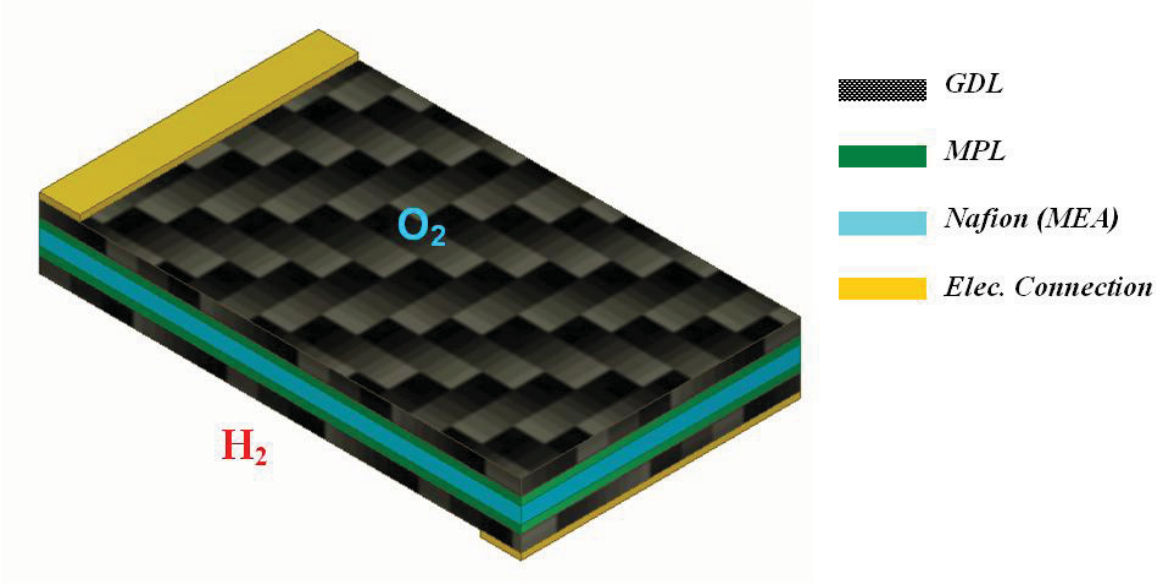

Figure 3-4. Architecture and major components of a single Ribbon Fuel Cell.

3.4.1 Gas Diffusion Layer Preparation. Due to the long conduction pathways associated with the in-plane current conduction in Ribbon Cells, a novel high conductivity GDL created in the ESL at Virginia Tech was used. This high conductivity GDL is a woven cloth, consisting of pitch and PAN based carbon fibers. The pitch based fibers were supplied from Misubishi Chemical of America Inc. with a 2% epoxy sizing which was removed by heat treating at 350°C for 30 minutes after weaving.

After removing the sizing, GDLs were cut into 15 x 10cm sections and wet-proofed by soaking in a PTFE emulsion. Wet-proofing GDLs is a common practice in the construction of a conventional PEMFC, because it enhances the gas transport characteristics of the GDL by reducing the number of pores which can become blocked by liquid water. The majority of literature pertaining to the hydrophobic treatment of GDLs cites an optimal hydrophobic polymer content between 15 – 30% of the total treated GDL mass. A target of 30% PTFE was chosen for the GDLs used in this work because it is thought that this relatively high hydrophobic content will improve Ribbon Cell performance and durability by providing a strong bond between the GDL and MPL that resists delamination.

After trial and error, a soaking time of 60 minutes in a 20% PTFE emulsion in water, was found to produce GDLs with 30% PTFE. The PTFE emulsion was prepared by diluting a homogeneous 60% PTFE emulsion of TFE 30 from ElectroChem Inc. to the desired concentration with de-ionized water. During soaking, the emulsion was agitated using an Ultrasonic Homogenizer from BioLogics Inc. (model 300 V/T) equipped with a 5/32” diameter titanium micro tip set to 20% power to ensure the even dispersion of PTFE particles. Samples were then removed from the emulsion and dried at 90°C in a

low temperature oven to evaporate excess water. The samples were flipped and rotated during the drying process to ensure the even evaporation of excess water and the uniform dispersion of PTFE throughout the GDLs. Hydrophobic samples were then heat treated in a hot press under a pressure of 30 psi at 180°C for 30 minutes to evaporate any remaining water, 280°C for 30 minutes to remove dispersant particles and finally sintered at 350°C for 30 minutes. Next, the weight percentage of PTFE, $wt\%_{PTFE}$, was verified for all GDL samples using Equation 3.1,

$$wt\%_{PTFE} = \frac{m_{\mathrm{GDL\_Total}} - m_{GDL}}{m_{GDL\_Total}} \tag{3-1}$$

where $m_{\mathrm{GDL\_Total}}$ is the total mass of the GDL and PTFE, and m_{GDL} is the mass of the bare GDL before hydrophobic coating. Lastly, the 15 x 10cm GDLs were cut into 4.5 x 3.5cm sections for MPL application.

It is worth noting that in conventional PEMFCs, GDLs are rarely sintered under pressure. However, Ribbon Fuel Cell GDLs perform better when sintered under low pressure, because the process reduces the surface roughness and improves the flexibility of the GDL. Previous Ribbon Cell work has shown that GDLs sintered without pressure had a high surface roughness that made MPL application difficult and sometimes led to shorting as a result of fiber penetration through the MEA. An initial study at the ESL during the Summer of 2008 found that a pressure of 30 psi adequately reduced the GDL surface roughness while still keeping its porosity high enough for sufficient gas diffusion.

3.4.2 Microporous Layer Preparation. MPLs were prepared in various ratios of carbon black to PTFE and suspended in Isopropyl Alcohol (IPA). The ratio of carbon black to PTFE, expressed as a weight percent of PTFE, $wt\%_{PTFE}$, was calculated by

$$wt\%_{PTFE} = \frac{m_{PTFE}}{m_{PTFE} + m_{CB}} \tag{3-2}$$

where, m_{PTFE} is the mass of PTFE, and m_{CB} is the mass carbon black in the MPL. The carbon black used was Vulcan XC-72R manufactured by the Cabot Corporation. The PTFE was introduced as a 60% emulsion of PTFE in water (TFE 30 from ElectroChem Inc.) Mixtures were suspended in IPA to provide a medium in which the carbon and PTFE particles could evenly disperse.

In his work at the ESL, Henderson [22] explored the amount of IPA needed for adequate dispersion of carbon and PTFE particles in MPLs ranging from 10 to 50 wt% PTFE. He found that MPLs below 20 wt% PTFE were most homogeneously dispersed when the mass ratio of IPA to *carbon black* was approximately 33:1[3]. For MPL compositions between 20 and 30 wt% PTFE, he found that holding the ratio of IPA to *PTFE* near 100:1 worked best. Lastly, for MPLs composed of 30 wt% PTFE and higher, the IPA to *PTFE* ratio of around 65:1 was desired. Target values for the mass of carbon black, PTFE and IPA for all the MPL compositions used in this work are shown in Table 3-3.

[3] A ratio of IPA to carbon black of 33:1 translates to a IPA to PTFE ratio of 192:1 for 15 wt% MPLs, and 625:1 for 5 wt% MPLs

Table 3-3. Target values for carbon black, PTFE and IPA for various MPL compositions

MPL Composition (wt% PTFE)	Mass IPA (g)	Mass CB (g)	Mass PTFE (g)
5	25	0.75	0.04
15	25	0.75	0.13
25	25	0.75	0.25
35	25	0.71	0.38
45	25	0.46	0.38

After making each MPL in a 35mL vile, the vile was capped and the solution shaken by hand to provide an initial agitation, and then agitated further with a BioLogics Inc. Ultrasonic Homogenizer equipped with a 5/32" diameter titanium micro tip (model 300 V/T) set to 30% power for 15 minutes. The solutions were then placed in 100mL beaker and reduced on a hot plate until they obtained the consistency of paste. During reduction, solutions were continually mixed with a magnetic stir rod to ensure the even evaporation of IPA, and to maintain the homogeneity of the MPLs. Once reduced to the desired consistency, solutions were placed back in the 35mL vile which was submerged in an ice bath to prevent any further evaporation of IPA. Even though all the MPL samples were reduced for the same amount of time, the difference in PTFE content caused the samples to have very different textures and consistencies. For example, the 5 wt% MPL sample appeared to have a relatively low viscosity and did not clump together, but rather stuck to the sides of the 100mL beaker, making transfer to the 35mL vile difficult; however, the 45 wt% MPL sample appeared much more viscous and clumped together in one large agglomeration, making transfer to the vile extremely easy.

In order to verify the homogeneity of the MPLs, small samples were taken from three different parts of each reduced MPL mixture. The mass of PTFE in each of the three samples was determined using a TA Instruments Q5000 Thermogravimetric

Analyzer (TGA) using air as a purge gas, and compared to one another. The TGA functions by heating the sample while continually measuring the sample's mass. As the temperature increases above the vaporization or degradation temperature of each species in the sample, those constituents are evaporated and the sample mass changes accordingly. This change in mass coupled with knowledge of the vaporization temperature of each species in the sample, allows the mass of each species to be determined. Figure 3-5 shows results from the TGA of two samples taken from different areas of the 35 wt% MPL and a sample of pure PTFE. The figure shows that both samples lost around 35% of their mass around the same temperature that the pure PTFE sample degraded, implying that they each contained approximately 35 wt% PTFE. The similar nature of the MPL curves suggests that PTFE was homogeneously dispersed in the MPL. Since the PTFE was evenly dispersed in this MPL, and all the MPL samples were similarly prepared, it was assumed that the PTFE in the other four MPLs (5, 15, 25 and 45 wt%) was homogeneously dispersed.

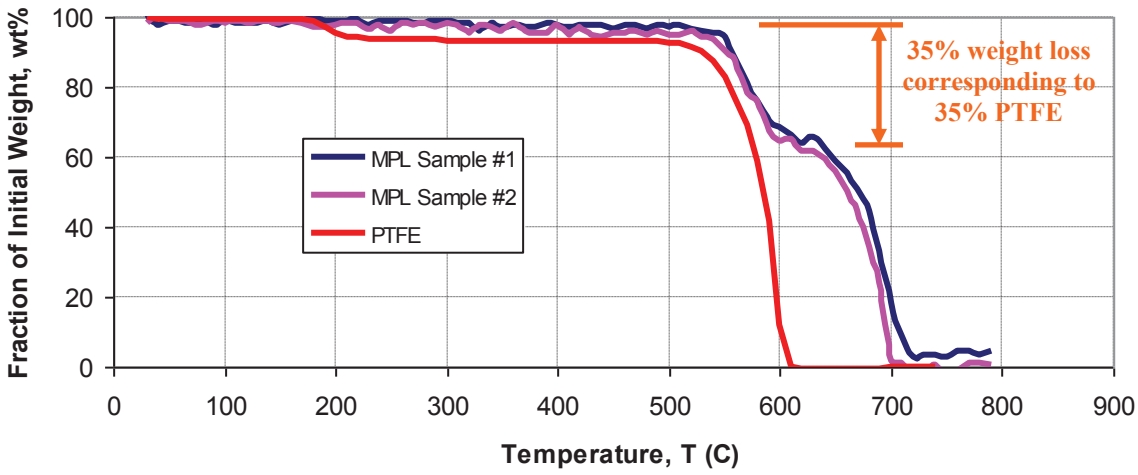

Figure 3-5. TGA results showing the even dispersion of PTFE in 35 wt% MPL

3.4.3 Microporous Layer Application.

There are a number of methods with which to apply MPLs to the GDL, however the two most practical methods for this work were spraying and tape casting. Both of these methods were used successfully in previous work in the ESL; spraying by Henderson [22] and tape casting by Sole [25].

In his work, Henderson used an un-reduced MPL solution with an air brushing technique to precisely control the application of his MPLs onto finely woven GDLs. This method works well when a thin MPL is desired, and the substrate surface is smooth. For this work though, a thick MPL is preferred because the substrate (GDL) has a high surface roughness. Sole used a GDL which was similar to the GDL used in this study, and found that the spraying technique did not work well. During the application, he found that the high porosity of his GDL caused much of the MPL to travel through the GDL instead of depositing onto the fibers. He also observed that the MPL which did deposit on the GDL, followed the rough surface contours of the weave, resulting in a MPL surface that was not smooth. A smooth surface is highly desirable in a MPL because it provides uniform contact with the CL over the entire active area of the fuel cell. Areas with poor CL to MPL contact will exhibit lower localized current densities than areas with good contact. Sole found that a tape casting technique worked much better for his GDL, because it applied a thick and uniform MPL with a smoother surface than did spraying. Because of the similarity of the GDL used in this work to that used in the work of Sole, a tape casting method was chosen to apply the MPLs.

Once the MPLs were reduced, GDLs were cut to a size which left a 0.6cm border of extra material around what would become the cell area. Each GDL was carefully weighed before the application of its MPL. The sample was then placed on a vacuum

plate and a Kapton® template positioned over the sample. The purpose of the template is two-fold. The first is to control the area over which the MPL is applied, and the second is to control the thickness of the applied MPL. After trial and error, template thicknesses were found that produced the desired loading for each MPL composition. After positioning a template of the correct thickness over the sample, a stainless steel frame was placed over its edges to provide compression and ensure the template lay flush against the GDL. Figure 3-6 shows the setup used to apply the MPLs.

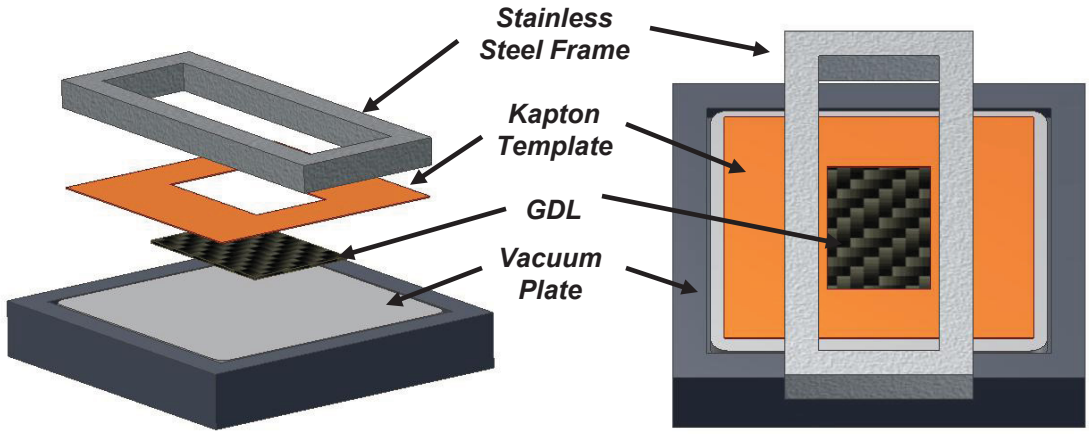

Figure 3-6. Front (right) and exploded (left) views of the setup used to apply MPLs.

The actual application of the MPL was done by placing an excess amount of MPL onto a razor blade which was cut to fit just inside the rectangular steel bar, and carefully dragging the blade across the top of the template. After dragging the blade across the GDL, the deposited MPL was allowed to partially dry for approximately 30 seconds. Allowing the MPL to dry between applications, helps prevent the formation of cracks in the surface of the layer which are undesirable. This process was repeated three more times for a total of four passes before the GDL was placed in an oven at 100°C for 30

minutes to evaporate all the remaining IPA. Samples were then sintered at the pressure prescribed by the experimental design, and with the same heating schedule used to sinter the GDLs. The sintered samples were then weighed, and the average MPL loading, L_{MPL}, was calculated using

$$L_{MPL} = \frac{m_{GDL+MPL} - m_{GDL}}{A_{MPL}} \tag{3.3}$$

where, m_{GDL} is the mass of the bare GDL, $m_{GDL+MPL}$ is the mass of the GDL and MPL and A_{MPL} is the area over which the MPL was applied.

3.4.4 Electrical Connection Application. The lateral current conduction and lack of compression over the active area in Ribbon Cells, create a unique set of challenges in capturing the electrical power produced by the cells. In a conventional stack, current is extracted from the cells via GDL contact with BPPs. Although the area specific contact resistance between these layers may be relatively large, the contact area is also large. This results in a moderate overall contact resistance and manageable ohmic losses associated with current collection. In Ribbon Cells, electrical connections are made over an area that is almost five times smaller than that of a conventional cell of the same size, therefore it is critical for that connection to have a low area specific resistance.

To better facilitate the collection of current, Ribbon Cell assemblies were coated with a conductive paste on opposite ends of the cathode and anode GDLs as shown previously in Figure 3-4. The conductive paste is an electrically conductive heat curing silicone manufactured by Silicone Solutions. It was applied over a 0.5 x 2.2cm area on

the appropriate portion of the anode and cathode GDLs after the sintering of their MPLs. A template made of fiberglass reinforced Teflon was used to ensure the areas over which the paste was applied were identical on every GDL; thus reducing the variation in total resistance associated with the electrical connections of each sample. The coated GDLs were then heat treated at 115°C for 40 minutes to cure the conductive paste and allow it to adhere to the GDL surface. After this heat treatment, the GDLs had both their MPL and electrical connections and were ready for final assembly.

The major drawback of this paste connection is that it relies on collector bar compression to maintain a low resistance. Under inadequate collector bar compression, contact resistances in the connection become high and the overall connection resistance increases. The dependence of the paste electrical connection on compression is discussed further in Section 3.6.1. There are other electrical connection methods which have been successfully used at the ESL which do not rely on compression, and have a lower area specific resistance than the paste connection. A description of these methods, however, is beyond the scope of this work. Despite its drawbacks, a paste electrical connection was chosen for the samples in this work because it is a proven method that is not material or time intensive.

3.4.5 Assembly of Cell Components. It is common practice in conventional fuel cells to perform an assembly press before cells are placed in a stack. This press, along with stack compression, work together to maintain adhesion among layers in the cell. If delamination occurs between any of the layers in the cell, conduction pathways and reaction sites become broken or separated, leading to lower current densities. Because

Ribbon Cells do not operate with stack compression, the adhesion among cell layers must be achieved by the assembly press alone; making the assembly press more critical to performance than in conventional cells.

Cells were assembled by placing anode and cathode GDLs (coated with MPL and conductive paste) on either side of the prefabricated MEA and hot pressing the assembly together. An MEA was cut to 5.0 x 5.0cm, its cathode side marked, and placed accordingly between the anode and cathode GDLs as shown in Figure 3-7. Care was taken to ensure that the cathode side of the MEA, which is loaded more heavily than the anode with platinum catalyst, was placed adjacent to the cathode GDL. The assembly was then placed between two 0.31 cm thick steel dies as shown in Figure 3-8. The purpose of these steel dies is to conduct heat to the cell, and apply pressure over only the active area of the cell. Kapton film was placed between the dies and the cells to prevent ion poisoning of the MEA from the dies or the aluminum platens on the hot press.

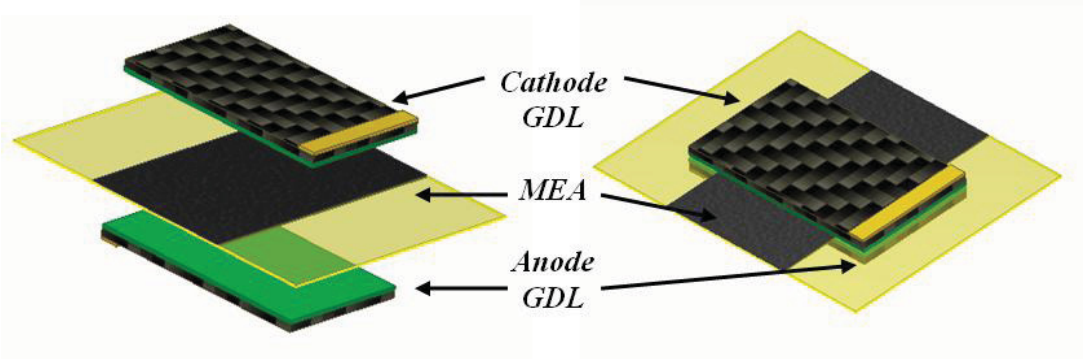

Figure 3-7. Views of the cathode GDL, anode GDL and MEA assembly.

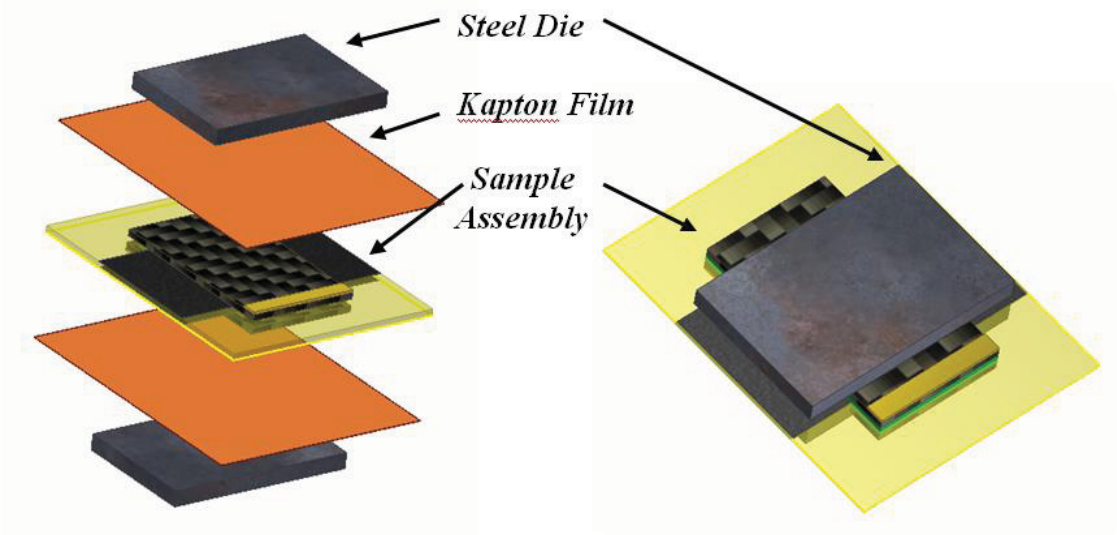

Figure 3-8. Exploded (left) and isometric (right) views of assembly press for adhesion samples. Kapton film not shown in isometric view for purpose of visualization.

The time and temperature of the press were held constant at 3.5 minutes and 145°C respectively for each sample, while the pressure was varied according to the experimental matrix. A 3.5 minute assembly press time was chosen based on the work of Henderson [22], who found that samples which were pressed anywhere between 2 and 8 minutes had the highest performance. A temperature of 145°C was chosen for the press, because it is safely below the degredation temperature of Nafion® while still being high enough to provide a good working bond among cell layers. The exact relationship between adhesion in Ribbon Cells and assembly press temperature is currently unknown, and may be an area of interest for future research.

3.5 Sample Preparation for Adhesion Testing

Sixteen samples were constructed to test the adhesion among various layers in Ribbon Cell assemblies. Twice as many samples were created as runs, because unlike in the performance study, the characterization of the adhesion samples is destructive in nature; therefore, an aged and un-aged sample must be made for each design point. The samples consisted of a cathode GDL, which was prepared, coated and sintered with a MPL in an identical manner to samples constructed for performance testing. Electrical connections were not added to the assemblies. Prepared GDLs were then hot pressed to the cathode side of an Ion Power MEA, which was identical to that used in the performance samples, but cut to a smaller size of 3.2 x 5.0cm. The major architectural difference between adhesion and performance samples is that the former do not have an anode GDL. Figure 3-9 shows the architecture of the adhesion samples. A second difference between adhesion and performance samples is that the pseudo-active area was aligned with the bottom edge of the GDL as opposed to 0.6cm from the edge (compare Figure 3-7 and 3-9). The term "pseudo-active area" is used to describe the area on adhesion samples where the CL of the MEA is hot pressed to the GDL. In a performance sample this would simply be the active area; however, since adhesion samples are never used to generate current, the area is never technically "active."

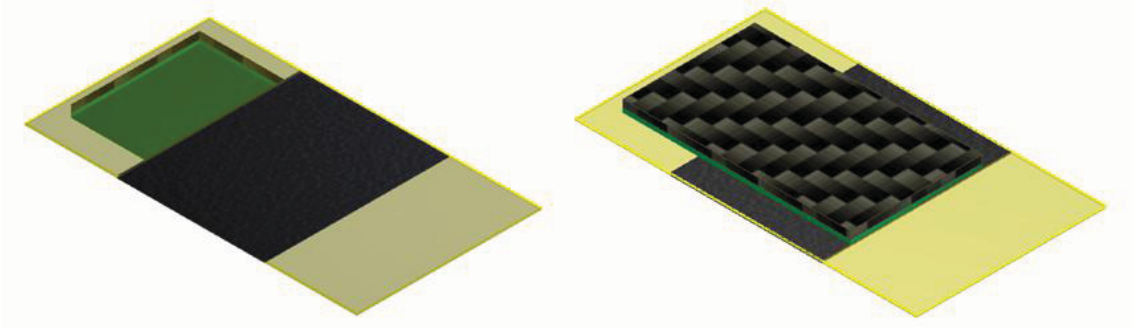

Figure 3-9. Architecture of adhesion study samples. Top and bottom views shown.

Assembly presses for each sample were performed by first aligning the MEA and cathode GDL as shown in Figure 3-9. Steel dies were placed on both sides of the pseudo-active area and pressed as shown in Figure 3-10. The time and temperature of the press were 3.5 minutes and 145°C respectively, while the pressure varied between 600 and 1100psi depending on the sample. Although the prevention of MEA ion poisoning was not critical in adhesion samples, Kapton was still placed between both sides of the dies and samples to serve the purpose of a release film. If a release film such as Kapton was not used during pressing, the steel dies would adhere slightly to the MEA, making them difficult to separate from the sample without destroying the MEA/GDL bond.

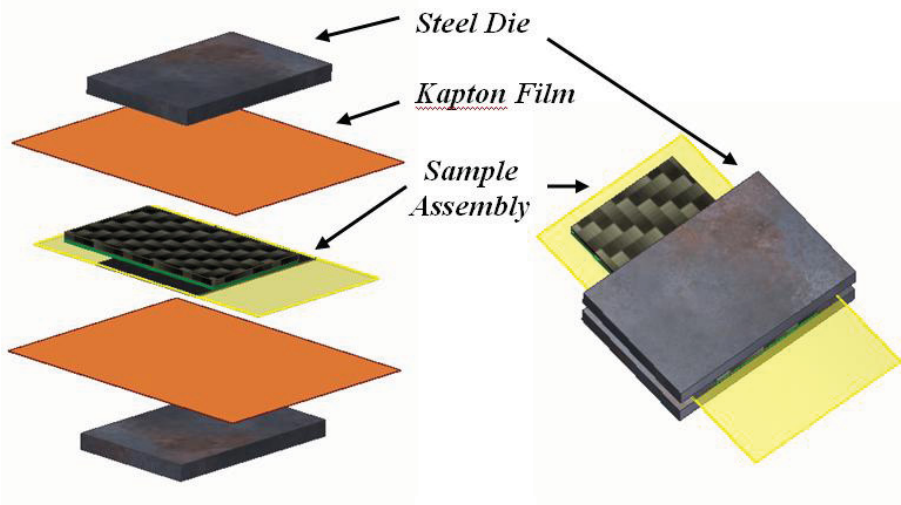

Figure 3-10. Exploded and un-exploded views of assembly press for adhesion samples. Kapton film not shown in un-exploded view for purpose of visualization.

3.6 Performance Study Characterization

The performance of each sample was characterized by its power output at various operating conditions both initially and after a number of wet/dry cycles. The characterization process for each sample began by testing first at wet, then at dry reactant gas conditions. The samples were then aged over 10 wet/dry cycles and re-tested first at wet, then at dry conditions. At each condition, potentiostatic (steady-state) potentiodynamic (polarization) and EIS data were taken. This sub-section first describes the process used to characterize un-aged sample performance. It will then describe the technique used for aging the samples, and finally it will outline the methods used to determine their aged performance.

3.6.1 Initial Performance Characterization. Testing of Ribbon Cell samples was performed using a 5 cm^2 single cell fixture from Fuel Cell Technologies Inc. The

flow fields of the fixtures were modified to accommodate the unique functionality and design of a Ribbon Cell by Sole [25] in his work at the ESL. A picture of a conventional fixture is shown in Figure 3-11. The conventional hardware consists of aluminum end plates which provide a means of clamping the fixture to prevent gas leaks as well as provide appropriate cell compression. Graphite flow fields serve the dual purpose of gas distribution and current collection, while the adjacent gold coated plates provide a connection point for electrical wiring from the cell to an external load.

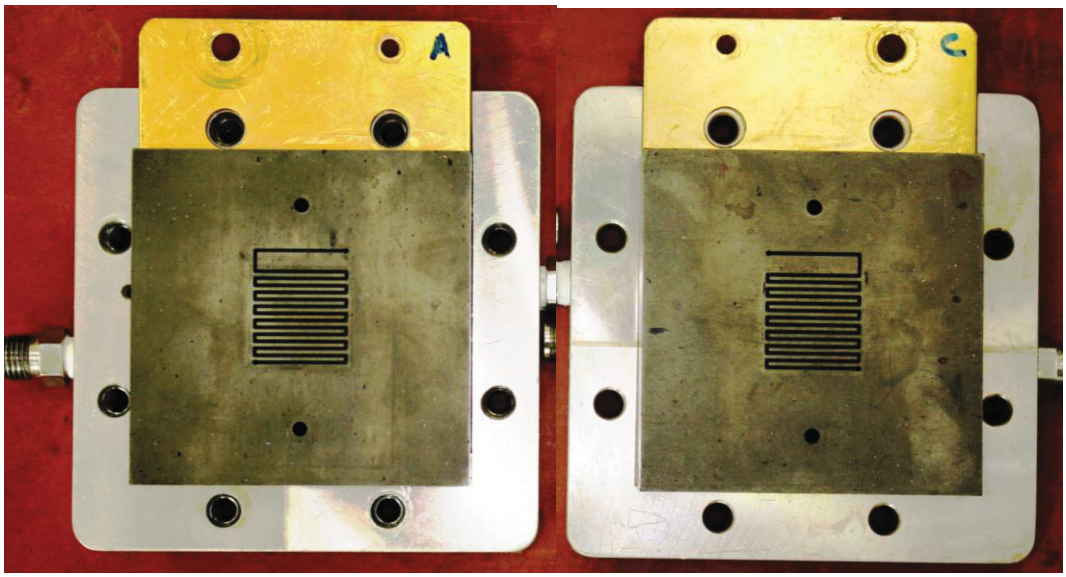

Figure 3-11. Conventional testing fixture for 5cm^2 cell.

Modifications to the conventional fixture involved replacing the graphite flow fields with Teflon blocks containing open flow fields as shown in Figure 3-12. The Teflon provides the electrical insulation needed for planar current conduction and collection, while the open nature of the flow fields mimics the lack of surface compression and the low cathode air velocity that are characteristic of the Ribbon Cell

design. A comparison of an open and a conventional serpentine flow field can be seen in Figure 3-13. The major difference between the two designs is that the serpentine flow channels are replaced with a 2.5mm recess beneath the active area of the cell. The final modification to the fixture was placing stainless steel collector bars flush with the surface of the Teflon blocks as shown in Figure 3-12. Collector bars were positioned so that when both sides of the fixture were clamped together they would make flush contact with the paste coated portion of the cathode and anode GDL.

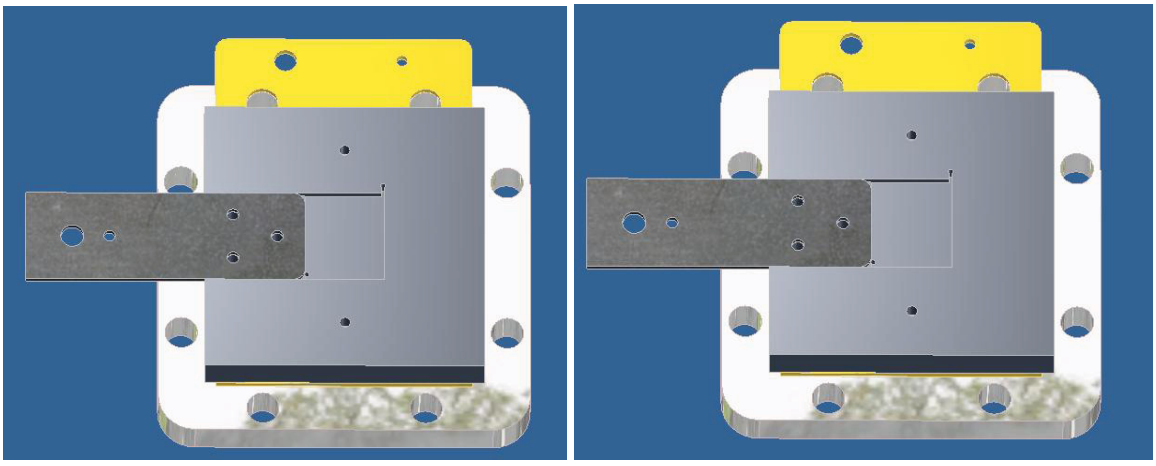

Figure 3-12. Fixture which has been modified for Ribbon Cell testing.

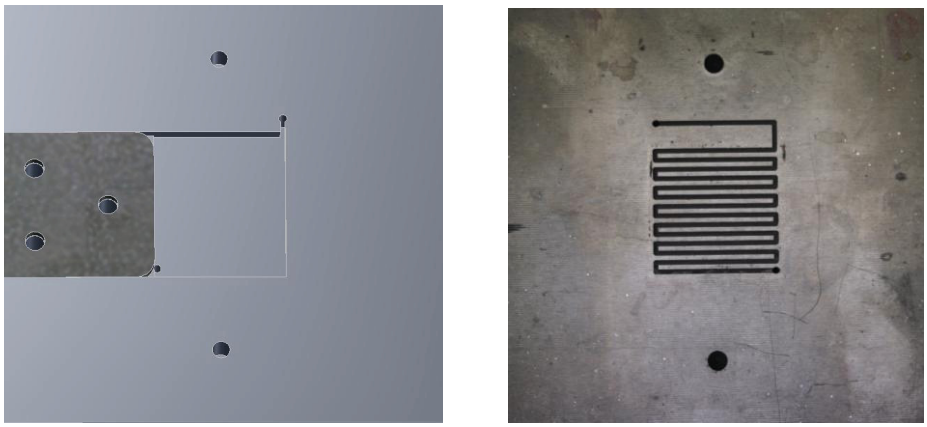

Figure 3-13. Comparison of the open flowfield used in this work (left) and a conventional serpentine flowfield (right).

The first step in the testing process was placing a Ribbon Cell sample in the modified fixture with gaskets on both the anode and cathode sides of the cell as shown in Figure 3-14. Gaskets are commonly used when testing conventional cells to prevent reactant gasses from leaking around the MEA or out of the fixture. Also, by varying the thickness of the gaskets, cell compression can be controlled. In the modified fixture, gaskets made of fiberglass reinforced Teflon film were used to seal the assembly and to control pressure over the electrical connections. Since the resistance of the paste-based electrical connections depends on compression, it is important to use a gasket that is thin enough to allow adequate compression of the stainless steel collector bar against the conductive paste. On the other hand, the gaskets must be thick enough to prevent over-compression of the GDL under the collector bars, which can break fibers or puncture the MEA leading to a short circuit in the cell.

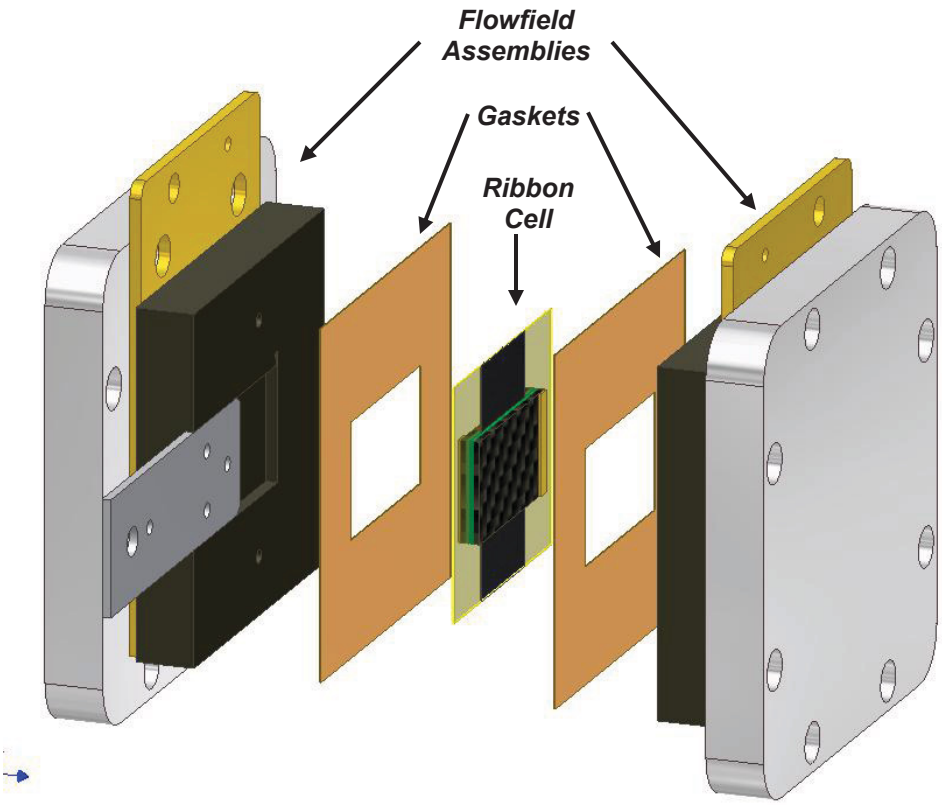

Figure 3-14. Exploded view of open flowfield fixtures with gaskets and Ribbon Cell.

Fueled by knowledge of the relationship between compression and resistance, a brief investigation into the relationship between gasket thickness and the resistance of the paste connections was conducted. In the study, a 550 μm thick GDL with paste connections, was placed in the modified fixture and the gasket thickness was varied while the resistance between the anode and the cathode collector bars measured. The measured resistance was plotted against the gasket thickness for gaskets ranging from 140 to 550 μm. Figure 3-15, shows the results of the study, with gasket thickness expressed as a compression ratio. The compression ratio is simply the ratio of compressed to uncompressed GDL thickness, where the compressed GDL thickness is assumed to be equal to the gasket thickness. A gasket thickness which corresponded to a compression

ratio of 0.5 was chosen for testing because it results in a relatively low connection resistance while not over compressing the GDL.

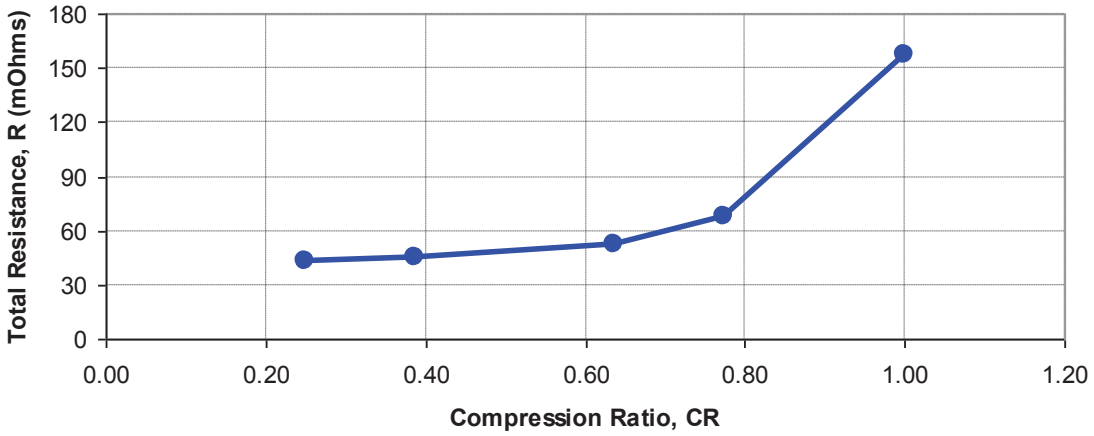

Figure 3-15. Resistance of the paste-coated GDL versus compression ratio.

After placing the Ribbon Cell and its appropriate gaskets in the modified fixture, the assembly was sealed by securing the anode and cathode sides together with eight bolts tightened to 50 in-lbs. The sample was then connected to a dual sided test stand manufactured by Fuel Cell Technologies Inc, which was used to control the reactant gas conditions and cell temperature. The test stand was also equipped with an electronic load cell manufactured by AMREL, which was used to control the operating voltage of the cell as well as measure polarization, steady state and EIS data. Control of all the components of the test stand was accomplished with a LabView interface created by Fuel Cell Technologies Inc.

Samples were heated to a cell temperature of 50 °C and tested under wet reactant gas conditions, before being tested under dry conditions. A cell temperature of 50 °C was used because that is the temperature which 5-Watt Ribbon Cell assemblies reach

during steady state operation without external heating or cooling. Wet and dry reactant gas dew points were chosen to span a wide range of operating conditions and also to mimic extreme environmental conditions which could be experienced by Ribbon Cells in potential portable power applications. For the wet condition, hydrogen with a dew point of 50 °C was supplied at a flow rate of 150 sccm on the anode side, while 30 °C dew point air was supplied at 350 sccm on the cathode side. An anode dew point of 50 °C was used because it represents the wettest condition, (100% RH at 50 °C) that the anode could experience. A cathode dewpoint of 30 °C (46% RH at 50 °C) was chosen because it matches the dew point temperature of the most humid locations on Earth such as Southeast Asia or the Middle East [26]. The dry conditions consisted of hydrogen supplied at a dew point of 25 °C and 150 sccm, with dry air supplied on the cathode side at a flow rate of 350 sccm. A dew point of 25 °C (37% RH at 50 °C) on the anode was chosen because it represents the humidity which could be achieved by flowing the hydrogen through room temperature water. Cathode gas was supplied without water (0 % RH at 50 °C) because it mimics the driest environmental condition which could be seen by a cell operating with an exposed cathode.

After supplying the cell with wet reactant gasses for approximately one minute, an initial polarization curve of the sample was taken. During the polarization curve acquisition, voltage was stepped down from 0.95V to 0.10V and then back up to 0.95V at 0.05V intervals with a dwell time of 30 seconds at each voltage. The current density at each of the voltages was recorded and plotted in order to visualize the cell performance at various operating voltages. All the polarization curves in this work were performed in this manner with identical parameters. Once the initial polarization curve was taken, the

cell voltage was set to 0.5 V and the current density measured until the output reached steady state. A sample was deemed to have reached steady state operation if the change in current density was less than 0.005 A/cm^2 per hour. Depending on the sample, it took between 3 and 30 hours for steady state to be reached. Many of the samples with high power outputs took closer to 30 hours to equilibrate, while poorer performing samples reached steady state much more quickly.

Two polarization curves along with EIS data were taken once the sample reached steady state. EIS is a commonly used method to characterize losses in fuel cells, by measuring the impedance of the cell over a range of frequencies. The method works by applying a small sinusoidal current perturbation (sometimes voltage is perturbed instead of current) and measuring the resulting phase shift and amplitude of the voltage response. This phase shift and amplitude are then broken down into real and imaginary components and plotted on a Nyquist Plot. Each frequency generates a single point on the Nyquist plot, and when a wide range of frequencies are tested and plotted, information about the location of losses in the cell can be determined. Gathering EIS data can be a complicated process, fortunately the test stand used in this work was equipped with an automated AC impedance system controlled by a Labview virtual instrument (VI). The user simply inputs a frequency range, perturbation amplitude and the cell voltage at which the test will be performed; the VI then records and plots EIS data on a Nyquist plot. All EIS tests were conducted at cell voltages of approximately 0.8V and 0.2V, using a frequency range of 10,000 to 0.1 Hz and a perturbation amplitude of 70 mA.

Once polarization and EIS data were obtained, reactant gas humidities were adjusted to their dry levels, and the sample allowed to equilibrate. Dry testing concluded

by taking two polarization curves and EIS data once the sample reached steady state operation. To better understand the un-aged test procedure, a sample test run with data acquisition times is presented in Figure 3-16.

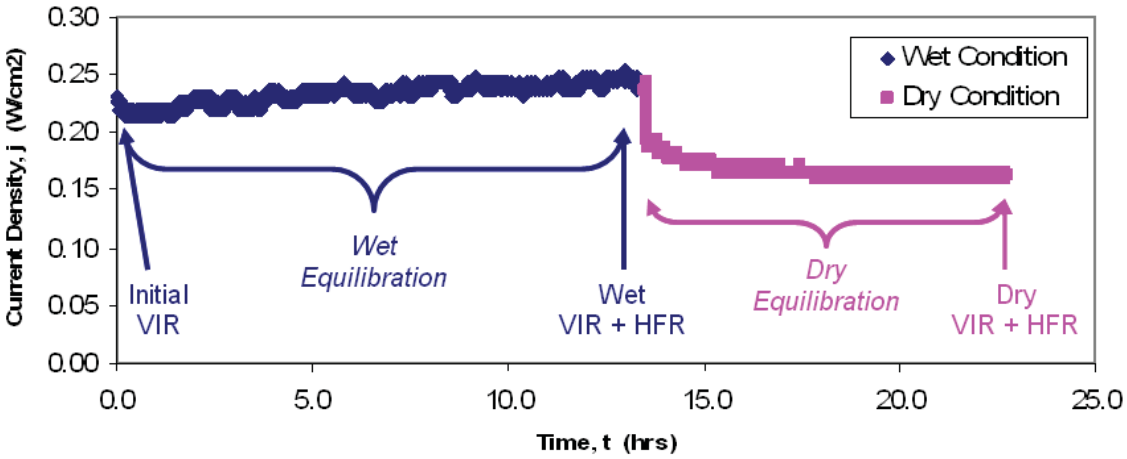

Figure 3-16. Sample test run showing the times at which polarization (VIR) and EIS data were taken for wet and dry operating conditions.

3.6.2 Sample Aging. Following the completion of initial wet and dry testing, samples were carefully removed from their test fixtures and aged using a BT-511 Membrane Conductivity Test System manufactured by BekkTech. The system was designed to measure the in-plane conductivity of electrolyte membranes over a range of relative humidities. At a basic level, the system functions by flowing hydrogen with various moisture contents through a gas tight chamber containing the sample. Conductivity of the sample is continuously measured using a Kiethley 2400 SourceMeter® which is in electrical contact with the sample. Control of flow rate, temperature and RH of the working gas is easily accomplished with a LabView interface

designed by BekkTech. In the aging study, the conductivity measurement feature was not used and only the gas control features were utilized.

Using the environmental control features of the BekkTech system, the samples were aged by humidity cycling *without* power production. To assure that aging with this approach was comparable to aging with power production, two Ribbon Cells were constructed with a 25 wt% MPL, 3 mg/cm^2 loading, 30 psi sinter pressure and an 850 psi assembly pressure. Both cells were first connected to the test stand and allowed to reach equilibrium at wet conditions. One of the cells then underwent simulated aging on the conductivity system, while the other was aged conventionally on the test stand by manually adjusting reactant gas dew points.

For simulated aging (no power production) using the Bekktech environmental control system, the samples were placed in the Teflon chamber shown in Figure 3-17. Flowfield assemblies similar to those used for performance testing, were placed on either side of the chamber and secured with bolts torqued to 50-in lbs. During aging, the chamber temperature was maintained at 80 °C, while air at the same temperature passed through the sample chamber at 500 sccm. The dew point of the air was first set to 80 °C for an hour, and then set to 20 °C for an hour. This cycle was repeated nine more times, so that the sample experienced 10 wet/dry cycles. Since the dew point of the working gas is controlled by the water temperature in the saturator, the response to a set point change was relatively slow, primarily when the dew point was changed from 80 °C to 20 °C. To speed the response of the system when changing from a high to low dew point, fans were used to expedite cooling of the saturator. A plot of both the set point and measured values of RH over 5 cycles is shown in Figure 3.18.

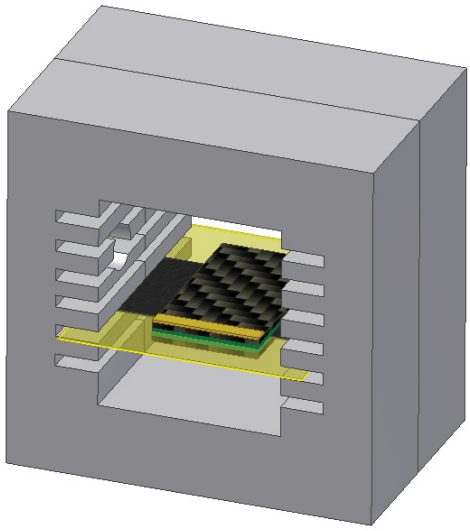

Figure 3-17. Aging chamber used for simulated aging on BT-511. (Flowfield assemblies not shown).

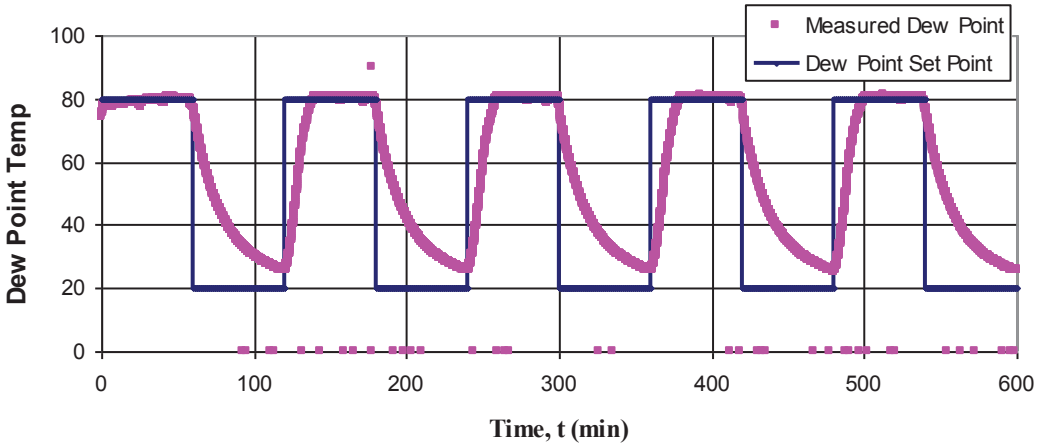

Figure 3-18. Set point and measured values of dew point over 5 wet/dry cycles.

After aging for ten cycles, the sample was placed back in the test fixture and allowed to reach equilibrium at wet conditions before polarization data was taken. Steady state and polarization data were also gathered from the sample which underwent the conventional aging process. The performances of the two aged samples were compared and found to be similar enough to suggest that simulated aging is comparable

to conventional aging (i.e. cell performance decreases primarily because of wet dry reactant gas cycling, and not by electrochemical effects). A comparison of the wet polarization performance of the two samples can be found in Table 3-4.

Table 3-4. Comparison of conventional to simulated aging. Performance expressed as current density at 0.5V

Type of Aging	Initial Performance (A/cm^2)	Aged Performance, 10 Cycles (A/cm^2)	Percent Decrease
Simulated Aging	0.35	0.24	31.4
Conventional Aging	0.27	0.18	34.4

3.6.3 Aged Performance Testing. Characterization of the aged performance of the samples was accomplished using the same test schedule and conditions that were used in the initial performance characterization.

3.7 Adhesion Study

The bond strength among various layers in the adhesion samples was determined by performing peel tests between the MEA and GDL. As described in Section 3.5, two samples were constructed for each design point in the experimental matrix for a total of 16 samples. After construction, one set of samples was tested un-aged, while the other was aged and then tested.

3.7.1 Sample Aging. As with the aging of performance samples, adhesion samples were aged by exposure to cycles of wet and dry air on the Bekktech Membrane Conductivity Test System. In order to make meaningful comparisons with performance

samples, the number of cycles, cycle period and gas conditions were identical to values used for the aging of performance samples. All eight samples were aged at once in the fixture shown in Figure 3-17, and allowed to sit at room temperature conditions for 24 hours before being tested.

3.7.2 Sample Testing. Peel tests of the samples were conducted using a MicroTester™ 5848 manufactured by Instron. The MicroTester™ is well suited for the samples in this work because it is designed for testing small samples and can be equipped with a 50 N load cell. The 50 N load cell is desired because it is able to accurately measure forces similar in magnitude to those observed by Henderson [22] in a comparable adhesion study. In his study, Henderson found that between 1.0 and 0.1 N was required to debond peel test samples similar in size and design to those used in this work.

Scotch® tape was attached to the samples at the un-bonded ends of the MEA and GDL in order to provide gripping surfaces for the MicroTester™. Taped samples were then placed in the MicroTester™ and their GDL secured to the bottom grip. The MEA was then folded 180°, and its tape secured in the upper grip as shown in Figure 3-19. A user interface designed by Bluehill® was used to control the grip movement, and to record the load and grip position during testing. For each test, the grips were moved apart at 7 mm/min and the total grip displacement was 70mm, a distance sufficient to fully debond the MEA from the GDL.

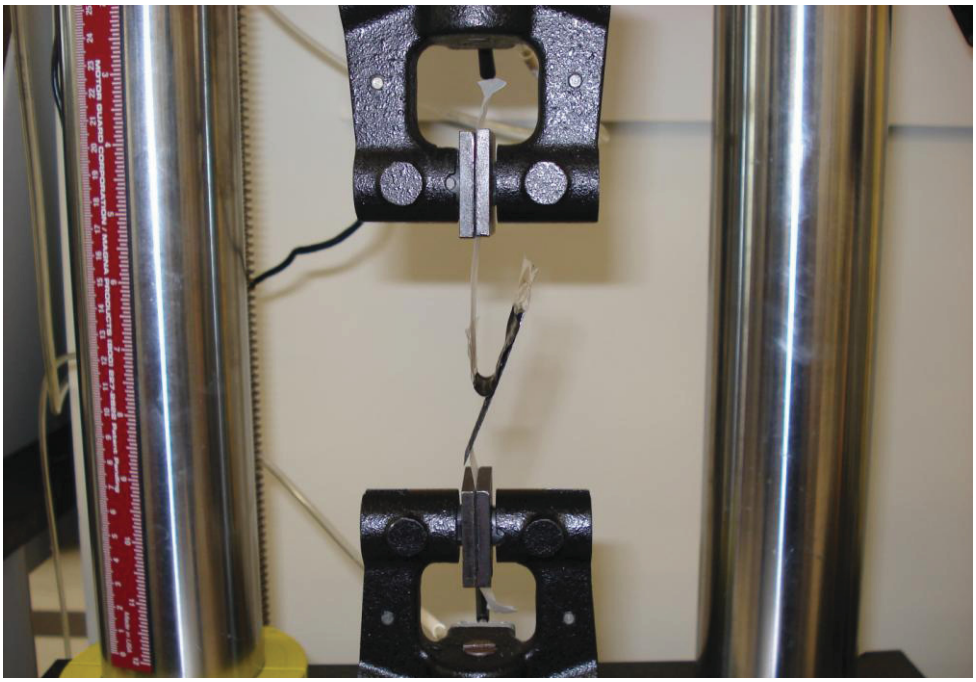

Figure 3-19. Test setup for an adhesion sample in the MicroTester™.

4. Results and Discussion

This section will present and analyze the results of the adhesion and performance studies. First, results from the adhesion study will be presented and location of failure in the samples discussed. The following subsection will show results from the performance study. Next, models for both un-aged and aged performance will be presented and their accuracy validated. Finally, the effects of each factor will be discussed and an optimal design suggested.

4.1 Adhesion Study

4.1.1 Peel Test Results. The strength of the MEA to GDL bond in the peel test samples was quantified by their apparent fracture energy, G_c (J/m^2), which can be thought of as the work required per unit area to debond the samples. To determine G_c from the raw test data, a plot of measured load versus grip displacement was created for each sample. Next, the average force during debonding was calculated and plotted as shown in Figure 4-1. The average debond force was then multiplied by the distance over which it was applied to obtain the work performed during debonding; for all samples this distance was equal to twice the bond length. Finally, the work was divided by the bond area to obtain the apparent fracture energy, G_C for the samples. The equation used to perform the above calculations was

$$G_C = \frac{F_{AVG} \times 2l}{wl} = \frac{F_{AVG} \times 2}{w} \tag{4-1}$$

where, F_{AVG} is the average debond force, l is the bond length and w is the bond width. A sample calculation along with raw data for all the adhesion samples can be found in Appendix B.

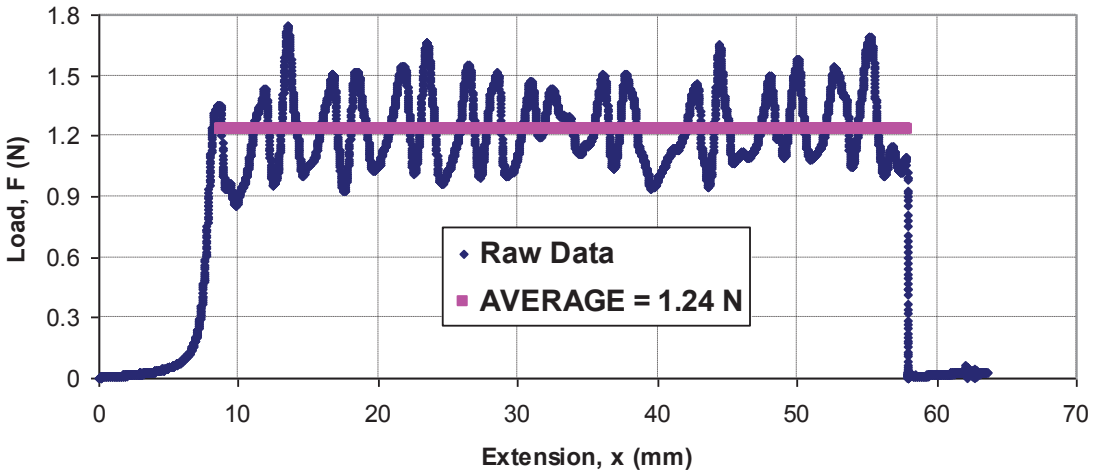

Figure 4-1. Plot of load versus extension for a peel test sample, with the average debond force shown.

The apparent fracture energy for the aged and un-aged samples along with their respective factor levels is presented in Table 4-1. Samples with a 35 wt% MPL had significantly better adhesion than those with a 15 wt% MPL. All of the 15 wt% samples had aged bond strengths that were extremely small; too small to distinguish from experimental noise. In fact, the bond was so weak in the aged 15 wt% samples, that partial delamination of the MEA was visible with the naked eye before the samples were even tested! The 35 wt% samples held up better to aging, however the bond strength still decreased by an average of 50% when compared to the un-aged strength.

Table 4-1. Adhesion Study Results.

Run	Composition (wt% PTFE)	Loading (mg/cm^2)	Assembly Press (psi)	Un-Aged Fracture Energy (J/m^2)	Aged Fracture Energy (J/m^2)
1	15	4	600	4.6	0.0
2	15	4	1100	0.0	0.0
3	15	2	600	6.3	0.0
4	15	2	1100	6.5	0.0
5	35	4	600	73.3	53.8
6	35	4	1100	109.6	55.2
7	35	2	600	70.0	20.3
8	35	2	1100	73.8	41.4

4.1.2 Peel Test Analysis. Analysis of peel test data was performed using the statistical software Design Expert®. This software has the ability to resolve high order models from complex data sets and provides dozens of tools to validate the accuracy of those models. Many of the more complex analysis tools available in the software will be used when modeling data from the performance study, while the more basic functions will be used for analysis of the adhesion study.

The first step in determining the influence of composition, loading and assembly pressure on un-aged adhesion, is to calculate the percent contribution of each of the factors to the response. This is done by dividing the sum of squares for each factor by the total sum of squares and multiplying by 100. The sum of squares is defined as the sum of the difference between each of the measured data points and the mean of the data set due to a particular effect such as composition or loading. The larger the sum of squares, the more influence an effect has on the response. The percent contribution for each of the factors and interaction terms can be seen in the effects table produced by Design Expert®

and displayed in Figure 4-2. The effects table shows that composition has by far the highest percent contribution of all the factors and interaction terms, while loading and assembly pressure have almost no contribution at all to adhesion.

Term	Stdized Effects	Sum of Squares	% Contribution
Intercept			
A-Compostion	77.33	11958.31	91.75
B-Loading	7.72	119.35	0.92
C-Assy Pressure	8.92	159.31	1.22
AB	11.82	279.66	2.15
AC	11.12	247.53	1.90
BC	6.93	95.91	0.74
ABC	9.33	173.91	1.33
Lenth's ME	51.52		
Lenth's SME	123.31		

Figure 4-2. Effects table created by Design Expert® showing the percent contribution of factors and interaction terms for un-aged adhesion.

To obtain another perspective on the relative influence of the factors, a simple model was created with Design Expert®. Each of the three factors was included as a term in the model, and the significance level of those terms analyzed. The significance level of each factor is characterized by its F-value which is used to calculate Prob > F or the p-value. The p-value is defined as the probability of obtaining the measured data while assuming that the spread of that data is completely due to chance. Lower p-values are desired because they mean it is unlikely that the spread of the measured data is due to solely to chance. Models or terms which have low p-values are referred to as *significant,* because they have an influence on the response that cannot be explained by chance. For example, observe Table 4-2, which is the Analysis of Variance (ANOVA) table for un-aged adhesion. The p-value for the composition term is 0.0015, meaning that there is

only a 0.15% chance of obtaining the results measured in the study if composition has no effect on adhesion. For this analysis, any terms with a p-value greater than 0.10 will be considered insignificant. Using this criterion, loading and assembly pressure are insignificant, leaving composition as the only variable which significantly influences adhesion.

Table 4-2. ANOVA table for un-aged adhesion.

Source	Sum of Squares	df	Mean Square	F-Value	p-value
Model	12237	3	4079	20.47	0.0069
A-Composition	11958	1	11958	60.02	0.0015
B-Loading	119	1	119	0.60	0.4822
C-Assy Pressure	159	1	159	0.80	0.4218
Residual	797	4	199		
Cor Total	13034	7			

A similar analysis was performed for aged adhesion, using the percent contribution and p-values to determine the relative influence of factors. As with un-aged adhesion, composition had the highest percent contribution of any factor; however, the contribution of loading increased to 6.32% from an un-aged contribution of 0.92%. Figure 4-3 shows the percent contribution of each term as calculated by Design Expert®. Raw data for the statistical analysis of both aged and un-aged adhesion can be found in Appendix C.

Term	Stdized Effects	Sum of Squares	% Contribution
Intercept			
A-Compostion	42.68	3642.31	82.31
B-Loading	11.83	279.66	6.32
C-Assy Pressure	5.63	63.28	1.43
AB	11.83	279.66	6.32
AC	5.63	63.28	1.43
BC	-4.92	48.51	1.10
ABC	-4.92	48.51	1.10
Lenth's ME	31.76		
Lenth's SME	76.01		

Figure 4-3. Effects table created by Design Expert® showing the percent contribution of factors and interaction terms for aged adhesion.

Although the percent contribution of loading increased to 6.32%, it is unclear from the effects table whether this value represents a significant contribution to aged adhesion. For further analysis, a model containing terms for each of the three factors was created and the significance level of those terms calculated. Table 4-3 shows ANOVA results for the model which were calculated by Design Expert®. Composition is a significant factor with a p-value of 0.0045; however, the 6.32% contribution of loading equated to a p-value of 0.186, which is insignificant. The insignificance of loading was initially surprising, as it was expected that higher loadings would lead to better adhesion, simply because the entire GDL surface would be covered with MPL. Observation of peel test GDLs after MPL coating showed that 2 mg/cm^2 was insufficient to fully cover the GDL surface, leaving areas of exposed fibers. It was predicted that these exposed areas would result in poor local adhesion, decreasing the overall fracture energy. Since the work of Henderson [22], showed that bare GDL does not bond to MEAs, it can be concluded that these exposed areas *did* lower the overall fracture energy, but not to the

point which was detectable by the statistical analysis. In other words, the influence of composition was so large, that it masked the smaller influence of loading.

Table 4-3. ANOVA table for aged adhesion.

Source	Sum of Squares	df	Mean Square	F-Value	p-value
Model	3985	3	1328	12.08	0.0179
A-Composition	3642	1	3642	33.11	0.0045
B-Loading	280	1	280	2.54	0.1860
C-Assy Pressure	63	1	63	0.58	0.4904
Residual	440	4	110		
Cor Total	4425	7			

In summary, results from the peel test coupled with statistical analysis, show that MPL composition has a highly significant influence on aged and un-aged adhesion. Although theory suggests that loadings which do not completely cover the GDL surface will result in poor adhesion, results from the study showed that this effect is not significant when compared to that of composition. Both aged and un-aged peel test results showed that assembly pressure did not significantly influence adhesion.

4.1.3 Investigation of Fracture Location. Investigation into the location of fracture in the samples was conducted in order to determine if improvements in the MPL could increase adhesion. For example, if fracture is occurring between the CL and Nafion®, further improvements in the MPL would not translate to better adhesion. On the other hand, if fracture is occurring between the MPL and adjacent layers, or through the MPL itself, then the possibility exists for improving adhesion by manipulating the MPL.

Inspection of the fractured MEAs and GDLs found that failure was occurring at different locations in 15 wt% and 35 wt% samples, but similarly in aged and un-aged samples of the same composition. Before going further, it should be noted that when a sample is referenced in this subsection, it is the *aged* sample which is being cited. The reason for this is because aged and un-aged samples of the same composition were fracturing similarly. Also, since improving durability is a goal of this work, aged fracture location is more important than un-aged fracture location. More discussion on the relative importance of aged and un-aged data will follow in Section 4.2.3.

Deposits of MPL on the surfaces of debonded CLs and GDLs showed that 15 wt% samples were fracturing through the MPL itself. Images taken on a Nikkon Eclipse LV 100 optical microscope under 50x magnification showed deposits of MPL covering the entire surface of the MEA. To better visualize the surfaces of debonded samples, NIS Elements BR 3.0 Software was used to create a 3-D surface from extended depth of field (EDF) images. Figure 4-4 shows the surface of the MEA from Run #1 (15 wt% MPL) covered by MPL with no CL exposed. Inspection of the corresponding GDL showed the same unbroken surface deposits of MPL. In order to clearly show that a portion of the MPL was removed from the GDL during peel testing, a 3-D surface was created showing the edge of the bond area on the GDL of Run #1. Figure 4-5 shows the non-bonded MPL surface on the left, and the bonded surface (after peel testing) on the right. Although a 50 μm layer has been removed, the GDL is still fully covered by the remaining MPL. These GDL and MEA images were initially surprising, as it was predicted that failure would occur between the CL and MPL interface; the nature of the surface deposits however, clearly show that the MPL was fracturing through its thickness.

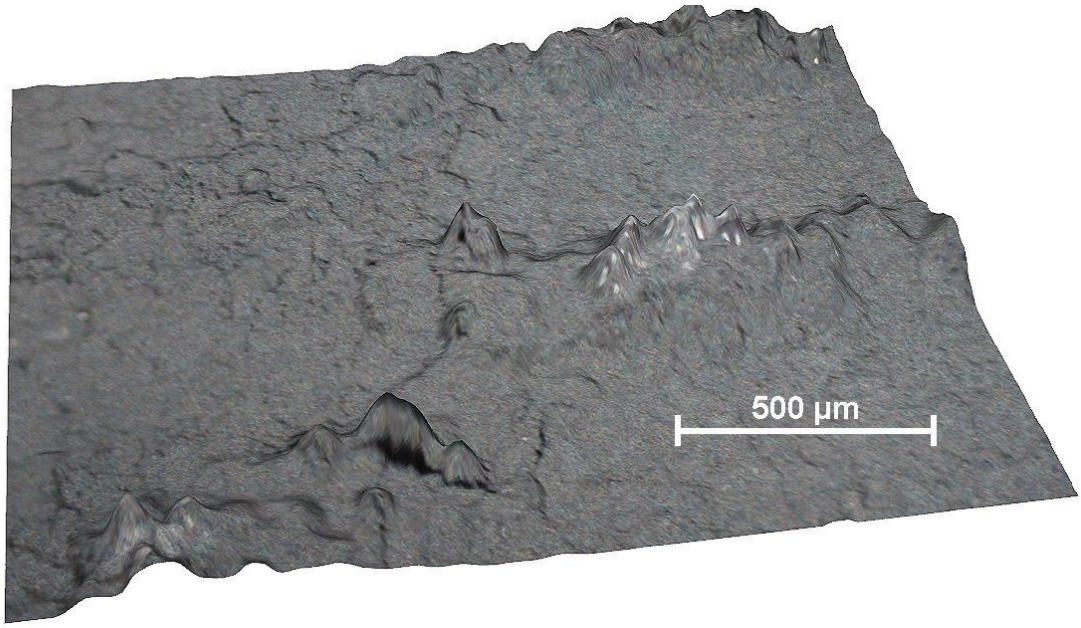

Figure 4-4. MPL Desposits on surface of MEA (above) from 15 wt% Run #1.

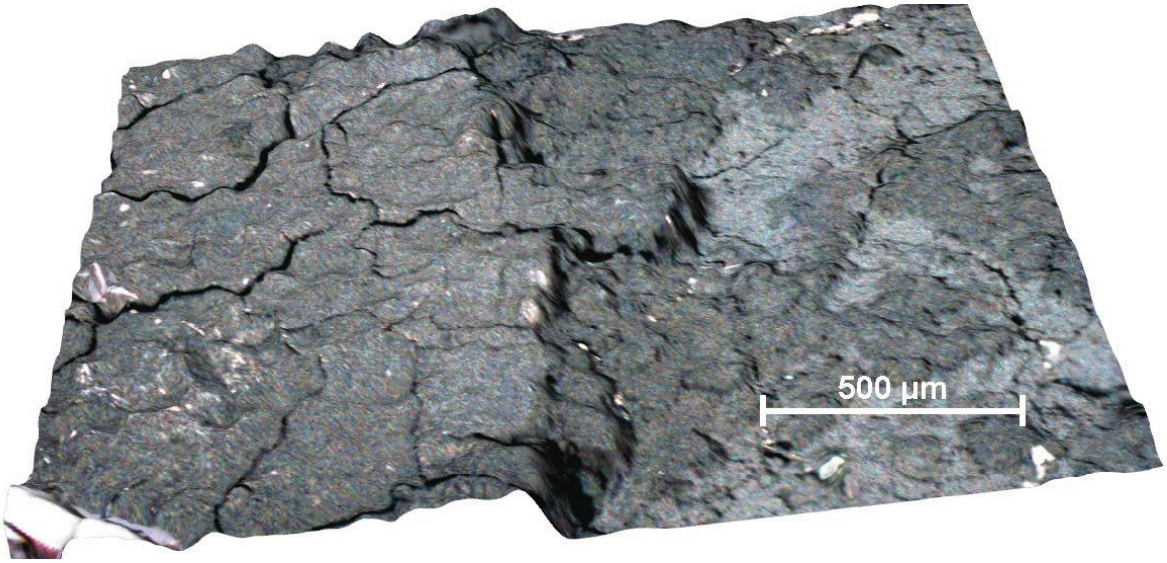

Figure 4-5. 3-D surface image of the bond line on the 15 wt% Run #1 GDL.

For the 35 wt% samples, visual inspection along with magnified images of showed that fracture was occurring at both the GDL / MPL interface, and the MPL / CL interface. Figure 4-6 shows a comparison of a 15 wt% and a 35 wt% GDL after peel

testing. The 35 wt% GDL clearly shows exposed GDL fibers where the MPL has been completely removed, while the 15 wt% GDL still has a complete covering of MPL. Although some GDL fibers are exposed in the 35 wt% sample, others remain covered by MPL that did not debond from the GDL. Upon closer inspection of the images, it became clear that the MPL which had been removed from the GDL was from the valleys or low surface points created by the weave pattern of the GDL. This trend can be explained by the difference in sintering pressure experienced by the MPL on high areas versus low areas of the GDL weave. Since the platen surface is flat, pressing onto the uneven surface of the GDL creates high pressure on the high weave areas and low pressure on the low weave areas. The result is a weak bond between the GDL fibers and MPL in these low lying areas. Figure 4-7 and Figure 4-8 show the surface of the GDL and MEA from Run #6 (35 wt%) magnified 50x. GDL fibers and portions of the CL are shown as lighter recessed areas between the darker MPL deposits.

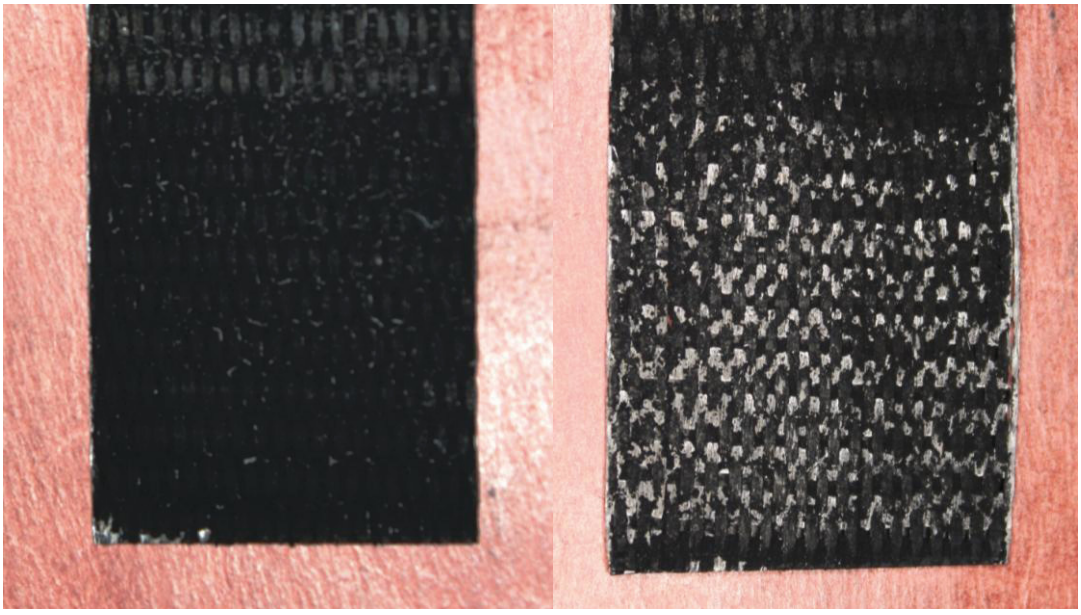

Figure 4-6. Comparison of 15 (left)and 35 wt% (right) MPL fracture. GDLs of Run #1 and Run #6.

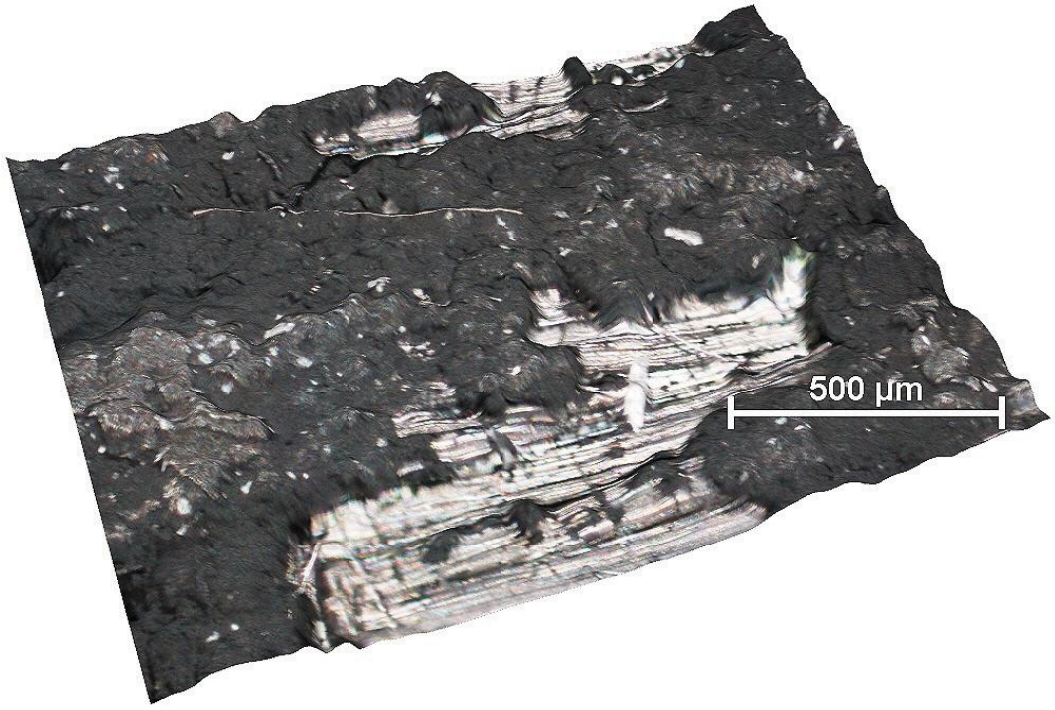

Figure 4-7. Image of the surface of the GDL from Run #6 (35 wt%), showing areas where GDL fibers are exposed.

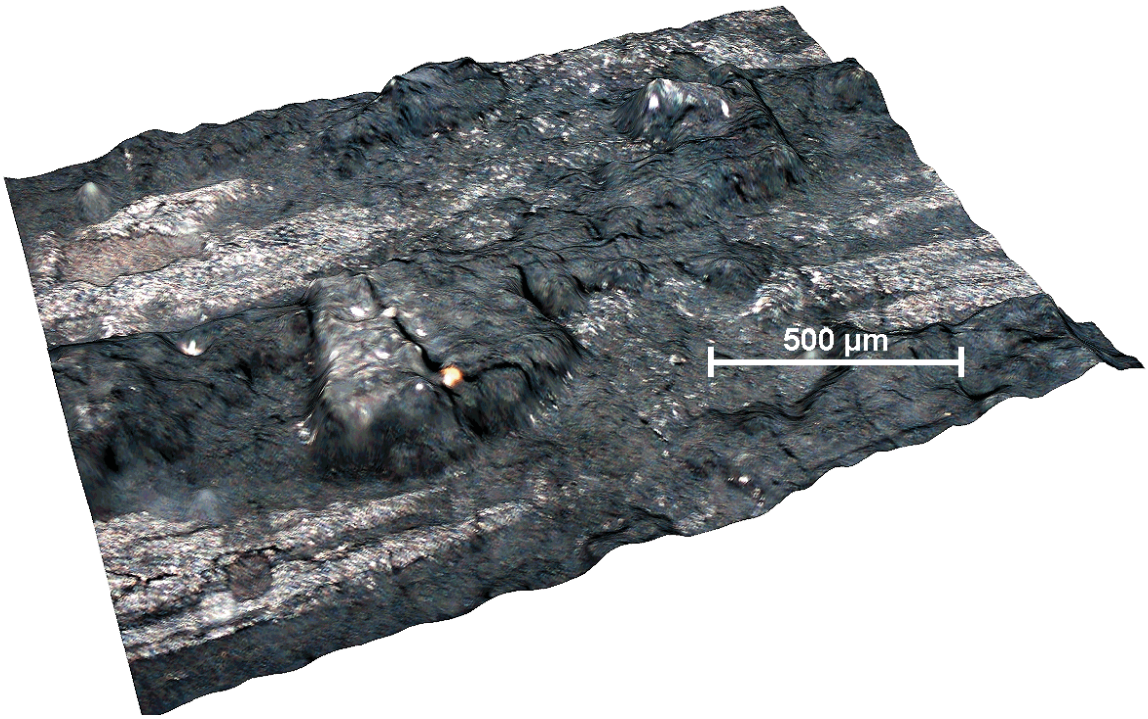

Figure 4-8. Image of the surface of the MEA from Run #6 (35 wt%), showing areas where CL are exposed.

The reason for the difference in fracture location between 15 and 35 wt% samples is likely due to the improved strength of the MPL provided by higher PTFE compositions. During sintering, particles of PTFE in the MPL spread and bond to other PTFE particles, thus increasing the strength of the layer. The result is that MPLs with an inadequate PTFE content form weaker interconnections, making the layer more prone to breaking as seen in the 15 wt% samples. Samples which have MPLs with higher PTFE contents form stronger interconnections that resist breaking. Instead of breaking through the layer itself, these stronger MPLs break away from either the CL or GDL. Since the MPL is not fracturing through its thickness, but instead debonding from the CL or GDL, improvements in bond strength will most likely result from somehow improving these interlayer bonds.

In summary, adhesion test results showed that samples with a 35 wt% MPL had significantly better resistance to delamination than 15 wt% samples both before aging and after aging. Results also showed that the bond strength of aged samples was consistently lower than that of un-aged samples. A statistical analysis was performed to determine the relative influence of composition, loading and assembly pressure on adhesion, and found that composition was by far the most influential. An investigation into the fracture location in the samples was conducted and found that fracture occurred differently in 15 wt% and 35 wt% samples, but at the same location in aged and un-aged samples of the same composition. In the 15 wt% samples, fracture occurred solely through the MPL, while fracture occurred at the MPL / GDL and the MPL / CL interfaces in the 35 wt% samples. The difference in fracture energy and fracture location between 15 and 35 wt% samples, is attributed to the increased strength of the MPL created by increased PTFE

compositions. The location of fracture suggests that increasing the strength of the MPL further will likely have diminishing improvements on adhesion. Since high PTFE samples fractured at the interfaces on either side of the MPL, increased adhesion is only likely to be realized with improvements in these interlayer bonds.

4.2 Performance Study

This sub-section will present and analyze the results obtained from the performance study. First, un-aged performance data will be presented and the overall trends discussed. Next, a statistical model for un-aged performance will be shown and its accuracy validated. Aged performance results will then be presented, followed by an analysis of the aged statistical model.

4.2.1 Un-Aged Performance Results. Un-aged performance of each of the 30 Ribbon Cells shown in Table 3-1 was characterized by polarization and steady state performance at wet and dry conditions. Results from the study are shown in Table 4-4 ordered from highest to lowest wet steady state performance, with the center point replicates highlighted in yellow. It is important to note that both polarization and steady state performance are expressed as a current density at a cell voltage of 0.5V. Raw data for all 30 cells can be found in Appendix A, shown in the form of polarization and steady state plots. In addition to polarization and steady state data, EIS data was also taken for each cell, and can be found in Appendix A.

Table 4-4. Un-aged performance results ordered from highest to lowest wet steady state current density.

Run #	Composition (wt% PTFE)	Loading (mg/cm^2)	Assembly Pressure (psi)	Sinter Pressure (psi)	Wet Polarization (A/cm^2)	Dry Polarization (A/cm^2)	Wet Lifetime (A/cm^2)	Dry Lifetime (A/cm^2)
15	25	3	850	30	0.43	0.37	0.42	0.37
22	45	3	850	30	0.43	0.36	0.42	0.36
25	25	3	850	30	0.42	0.39	0.41	0.39
10	15	4	600	40	0.42	0.36	0.40	0.36
17	25	3	850	30	0.39	0.33	0.37	0.34
9	25	3	850	10	0.38	0.37	0.35	0.39
13	25	3	850	30	0.36	0.32	0.34	0.30
16	25	3	850	30	0.34	0.37	0.34	0.36
23	25	5	850	30	0.37	0.29	0.34	0.33
3	25	3	850	30	0.37	0.31	0.33	0.30
28	35	4	600	40	0.35	0.35	0.32	0.33
29	25	3	350	30	0.35	0.31	0.32	0.30
21	35	2	1100	20	0.34	0.28	0.31	0.28
27	35	4	1100	40	0.32	0.32	0.30	0.30
4	35	2	600	40	0.31	0.33	0.30	0.32
5	35	4	1100	20	0.34	0.35	0.29	0.32
30	25	3	850	50	0.33	0.32	0.29	0.31
14	35	2	600	20	0.31	0.26	0.28	0.25
11	35	4	600	20	0.30	0.31	0.26	0.28
12	15	4	600	20	0.25	0.16	0.24	0.16
19	15	2	600	20	0.25	0.27	0.23	0.26
20	35	2	1100	40	0.27	0.32	0.23	0.30
18	15	4	1100	40	0.25	0.22	0.23	0.22
8	15	4	1100	20	0.24	0.18	0.22	0.17
26	15	2	1100	40	0.20	0.13	0.21	0.12
6	25	1	850	30	0.21	0.12	0.20	0.11
1	25	3	1350	30	0.21	0.21	0.19	0.20
24	15	2	600	40	0.19	0.11	0.18	0.11
7	15	2	1100	20	0.18	0.13	0.16	0.12
2	5	3	850	30	0.11	0.08	0.13	0.08

Because of the nature of the experimental design used for the performance study, it is difficult to draw precise conclusions from the data in Table 4-4 without the assistance of statistical software; general trends and overall conclusions however, can be made. Comparison of Run #2 to Run #22 allows for the influence of composition to be observed because the other three factors are at identical values while composition varies from 5 to 45 wt% PTFE. The large difference in performance between Run #2 (0.13 A/cm^2) and Run #22 (0.42 A/cm^2), suggests that the PTFE content of the MPL has a profound influence on performance. The difference in performance is most likely due to increased adhesion between various layers in the cell provided by a MPL with a high

PTFE content, a trend shown by the adhesion study. Better adhesion translates to a lower contact resistance and thus lower ohmic losses. High frequency resistance data supports this conclusion as the area specific resistance of the cells increased from 0.29 Ω-cm^2 in Run #22 to 0.50 Ω-cm^2 in Run #2 at wet conditions. Further analysis of the impact of MPL composition on performance will be presented during the discussion of the statistical performance model.

Comparison of Run #6 (0.20 A/cm^2) to Run #15 (0.42 A/cm^2) allows for the influence of MPL loading to be determined since loading varies from 1 to 3 mg/cm^2 while other factor levels remain the same. Inspection of the MPL on the GDLs of Run #6 revealed that a loading of 1 mg/cm^2 was insufficient to provide a continuous covering of the GDL. The GDL of Run #15 however, had a smooth and continuous MPL covering its entire surface. Data from these two runs suggests that even if a MPL has an adequate PTFE content, the loading must be high enough to smoothly cover the entire GDL surface for its beneficial adhesive and water management properties to be realized.

Assembly pressure and sinter pressure appeared to have a weak influence on performance, however it is difficult to determine their exact relationship without the aid of statistical analysis. The final point which can be made about the data is that there is some variation in the performance of the center point replicates which can be attributed to a number of factors including MEA variation and electrical connection variation. The most significant source of error though, is likely caused by inconsistent GDLs. Although care was taken to produce identical GDLs for all samples, the inherent variation associated with hand weaving the GDLs, likely resulted in weaves which were non-uniform. This variation in weaving translates to variations in conductivity among GDLs

which leads to the variation in performance seen among the center point replicates. In addition to the GDL variation which is unique to Ribbon Cells, results from other PEMFC studies suggest that there is a relatively large amount of variation in most PEMFCs constructed by hand. For example, the polarization performance of the four center point replicates of the conventional cells tested by Henderson [22] varied between 1.27 and 0.82 A/cm^2 at 0.5 V. In comparison, the seven un-aged center points in this study varied between 0.43 and 0.37 A/cm^2 at 0.5 V during polarization testing. The following subsection will use statistical analysis to provide a more in-depth analysis of the un-aged performance data.

4.2.2 Un-Aged Performance Models. Separate statistical models were created for all four un-aged responses (wet polarization, wet steady state, dry polarization and dry steady state) using Design Expert®. Since the process used to create each of these models was extensive yet similar, only the wet steady state model will be presented and validated in this section. Statistical data for the other three un-aged responses can be found in Appendix C.

In addition to determining the influence of each factor and their interactions on performance, statistical models were created to predict the performance of future Ribbon Cell assemblies as well as to determine the factor levels which lead to optimal performance. The first step towards creating such a model is determining which order model to use (linear, quadratic, cubic etc.). To assist in model selection, Design Expert® provides a comparison of models from a constant value (mean) up to a sixth order polynomial, as shown in Table 4-5. Each row in the table determines the significance of

adding model terms of the next highest order to the previous lower order model. The best model for the data is the highest order polynomial where the additional terms are significant and the model is not aliased. An aliased model simply means that there were not enough design points in the experimental matrix to independently estimate the highest order terms in that model. With these criteria in mind, a quadratic model was selected because it is the highest order model that is not aliased, in which additional terms are significant (p-value = 0.0060).

Table 4-5. Fit summary table for un-aged wet steady state performance[4].

Source (model type)	Sum of Squares	df	Mean Square	F-Value	p-value	
Mean vs Total	2.1451	1	2.1451			
Linear vs Mean	0.1202	4	0.0300	5.94	0.0017	***Suggested***
2FI vs Linear	0.0152	6	0.0025	0.43	0.8483	
Quadratic vs 2FI	0.0665	4	0.0166	5.55	0.0060	***Suggested***
Cubic vs Quadratic	0.0316	8	0.0040	2.09	0.1737	***Aliased***
Quartic vs Cubic	0.0063	2	0.0031	2.23	0.2028	***Aliased***
Fifth vs Quartic	0.0000	0				***Aliased***
Sixth vs Fifth	0.0000	0				***Aliased***
Residual	0.0070	5	0.0014			
Total	2.3918	30	0.0797			

Once the type model was chosen, the next step was to determine which terms to include in the model and which to exclude. The decision of which terms to include is slightly more complicated than simply including all model terms with a significant p-value. In addition to the significance of each term, the fit of the model to the data must be considered. A number of tools are available in Design Expert® to asses the fit of a

[4] 2FI model is a 2 factor interaction model including terms AB, AC, AD etc. in addition to the linear and intercept terms.

model, the most universal however, are R^2, adjusted R^2 and predicted R^2. Most scientists are familiar with R^2, which is simply the measure of variation in a data set that is explained by a particular model; but they are unfamiliar with adjusted R^2 and predicted R^2 which are in fact more important. Since R^2 increases with the addition of terms, even if those terms are insignificant, it is not a sound metric in determining the best model for a data set. Adjusted R^2 corrects this issue by adjusting for the number of terms in the model. The result is that the value of adjusted R^2 decreases when additional terms are added to the model, if those terms do not add value to the model. Predicted R^2 is a measure of how well the model predicts a response value, and is important to maximize if the model will be used for the prediction of future design points[5].

Keeping in mind the importance of maximizing adjusted R^2 and predicted R^2, a backwards selection method was used to incrementally remove terms with the highest p-values. The method works by allowing the user to input a cutoff p-value. Any terms that have a p-value above the cutoff are automatically removed from the model. This process was performed for p-value cutoff points of 0.50, 0.25, 0.10 and 0.05 and the values for adjusted R^2 and predicted R^2 recorded. Table 4-6 shows R^2 values as well as the model terms which were *excluded* at various cutoff levels.

[5] Predicted R^2 is calculated using the Predicted Residual Sum of Squares for the model, which is a measure of how well a particular model fits each point in the design. The coefficients for the model are calculated without the first point. This new model is then used to estimate the first point and calculate the residual for point one. This is done for each data point and the squared residuals are summed.

Table 4-6. R^2 values for various cutoff levels of the un-aged wet steady state model[6].

Variables Excluded:	R^2	Adj. R^2	Pred R^2
None	0.79	0.58	-0.06
Terms > 0.5 (BC)	0.78	0.60	0.06
Terms > 0.25 (BC, AD, CD, AC)	0.74	0.61	0.21
Terms > 0.1 (BC, AD, CD, AC, D^2, AB, BD)	0.66	0.57	0.26
Terms > 0.05 (BC, AD, CD, AC, D^2, AB, BD)	0.66	0.57	0.26

A cutoff level of 0.1 was chosen for the model even though it is not the model with the highest adjusted R^2 value, because it is the model which achieves the highest combination of adjusted R^2 and predicted R^2. This selection process was performed for each of the four responses. The resulting un-aged model equations are shown in Table 4-7 along with R^2 values.

Table 4-7. Model equations and R^2 values for un-aged responses.

Response	Model	Adj. R^2	Pred R^2
Wet Polarization	$j = -0.50 + 0.02*(A) + 0.18*(B) + 6.56E\text{-}4*(C) - 3.07E\text{-}4*(A^2) - 0.03*(B^2) - 4.37E\text{-}7*(C^2)$	0.65	0.39
Dry Polarization	$j = -0.65 + 0.02*(A) + 0.25*(B) + 5.62E\text{-}4*(C) - 3.19E\text{-}4*(A^2) - 0.04*(B^2) - 3.73E\text{-}7*(C^2)$	0.73	0.67
Wet Steady State	$j = -0.49 + 0.02*(A) + 0.18*(B) + 7.32E\text{-}4*(C) - 2.55E\text{-}4*(A^2) - 0.03*(B^2) - 4.82E\text{-}7*(C^2)$	0.57	0.26
Dry Steady State	$j = -0.66 + 0.02*(A) + 0.23*(B) + 6.54E\text{-}4*(C) - 3.35E\text{-}4*(A^2) - 0.03*(B^2) - 4.29E\text{-}7*(C^2)$	0.69	0.58

A number of common trends exist among all four un-aged response models, most notably that they all include the same terms: A, B, C, A^2, B^2 and C^2. Sinter pressure was found to be insignificant for each of the models, meaning that between the factorial levels

[6] In table 4-6, variables are coded as follows: A = composition, B = loading, C = assembly pressure and D = sinter pressure (note, the full quadratic model contains terms: Intercept, A, B, C, D, AB, AC, AD, BC, BD, CD, A^2, B^2, C^2 and D^2).

of 20 and 40 psi sinter pressure did not significantly influence performance. That's not to say sinter pressure does not need to be controlled. In fact, previous Ribbon Cell work has found that sinter pressures above 50 psi result in decreased power output because the GDL becomes compacted, lowering its porosity which leads to large diffusive losses. Previous work also found that MPLs which were not sintered under pressure often detached from the GDL during subsequent Ribbon Cell construction steps. These previous conclusions coupled with results from the performance study suggest that *MPL sinter pressure should be controlled between 20 and 40 psi for optimal performance.*

Although more trends can be harvested from inspection of the model equations, their true value lies in their ability to determine factor levels which lead to optimal performance. Fortunately, Design Expert® makes this process relatively simple with its numerical optimization tools. The software allows the user to input either a single response or multiple responses which are to be maximized, and calculates the factor levels which lead to maximum response values. This process was first used to maximize each of the four individual responses (wet polarization, dry polarization, wet steady state and dry steady state). It was then utilized to determine what factor levels would lead to the highest power output at both wet and dry steady state operating conditions (denoted at "Wet + Dry Steady State" response in Table 4-8). Table 4-8 shows the optimal factor values as determined by Design Expert® for each of the individual responses as well as for the combined response of wet and dry steady state performance. The maximum current density predicted by the models is also shown.

Table 4-8. Factor values which maximize current density at various conditions. Maximum current density as predicted by the models for each response are also shown.

Responses	Composition (wt% PTFE)	Loading (mg/cm^2)	Assembly Pressure (psi)	Sinter Pressure (psi)	Current Density (A/cm^2)
Wet Polarization	33.25	3.59	750	30	0.41
Dry Polarization	34.83	3.43	752	30	0.39
Wet Steady State	33.05	3.52	759	30	0.38
Dry Steady State	33.79	3.51	763	30	0.38
Wet + Dry Steady State	33.45	3.52	760	30	0.38*

*Wet and dry current densities were both 0.38 A/cm^2

Optimal factor levels were nearly identical for each response; 34 wt% PTFE, 3.5 mg/cm^2, 750 psi assembly pressure and 30 psi sinter pressure. To better visualize an optimal MPL, a contour plot showing the influence of loading and composition on wet steady state performance is displayed in Figure 4-9. Assembly pressure and sinter pressure are held at 750 and 30 psi respectively in the plot. The figure shows a hot spot between 25 and 40 wt% PTFE and from 2.5 to 4.5 mg/cm^2 where performance above 0.35 A/cm^2 is predicted. Areas of poor performance are predicted for low loading and low composition.

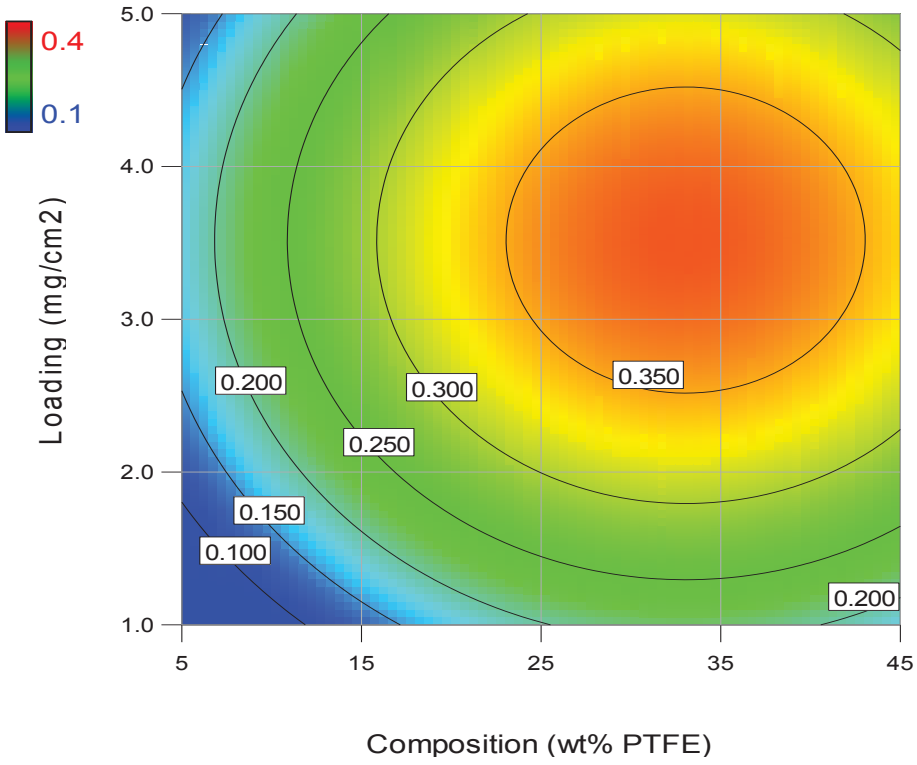

Figure 4-9. Contour plot showing the influence of loading and composition on un-aged wet steady state performance.

A PTFE content around 34 wt% in the MPL leads to high performance because it translates to a strong MPL which resists fracture during membrane shrink/swell cycles as shown by the adhesion study. Although the un-aged performance samples have not experienced as many MEA shrinking and swelling cycles as aged samples, they still experience at least one cycle. The first contraction and expansion cycle of the MEA occurs during wet performance testing, when the membrane which has been dried during the assembly press (145 °C for 3.5 minutes), swells as humid reactant gasses and product water hydrate it. It is believed that during this initial swelling cycle certain areas in lower PTFE content MPL samples fracture. Localized debonding results in areas with a high contact resistance, leading to lower overall power output from the cell. High frequency

resistance data support this theory, with 35 wt% cells averaging 0.31 Ω–cm^2 and 15 wt% cells averaging 0.36 Ω–cm^2 at wet conditions. A second benefit of having a high PTFE content is that the MPL retains more water adjacent to the MEA, keeping the Nafion® moist and its ionic conductivity high.

A loading around 3.5 mg/cm^2 leads to optimal performance because it is high enough to provide a smooth uniform layer over the rough surface of the high conductivity GDL used in Ribbon Cells. Observation of MPL coated GDLs has found that MPL loadings below 2.5 mg/cm^2 were insufficient to completely coat the GDL. Figure 4-10 shows GDLs which have a MPL coating of 2 and 4 mg/cm^2. The insufficiently loaded MPL leaves GDL fibers exposed at high spots in the weave. Exposed areas such as these do not benefit from the water management capabilities provided by the MPL, leading to drying of the Nafion® or flooding of the GDL, resulting in higher ohmic and mass transfer losses respectively. A second drawback is that exposed fiber areas will have poor adhesion to the CL, creating a high localized contact resistance. Although the performance penalty for over-loading, is not as severe as for under-loading, cell performance will decrease with a MPL that is too thick. The thick layer reduces the overall porosity of the MPL increasing mass transfer losses. A thicker layer also means longer electron transfer pathways between the GDL and CL. Longer pathways lead to higher ohmic losses, especially in MPLs with high PTFE contents.

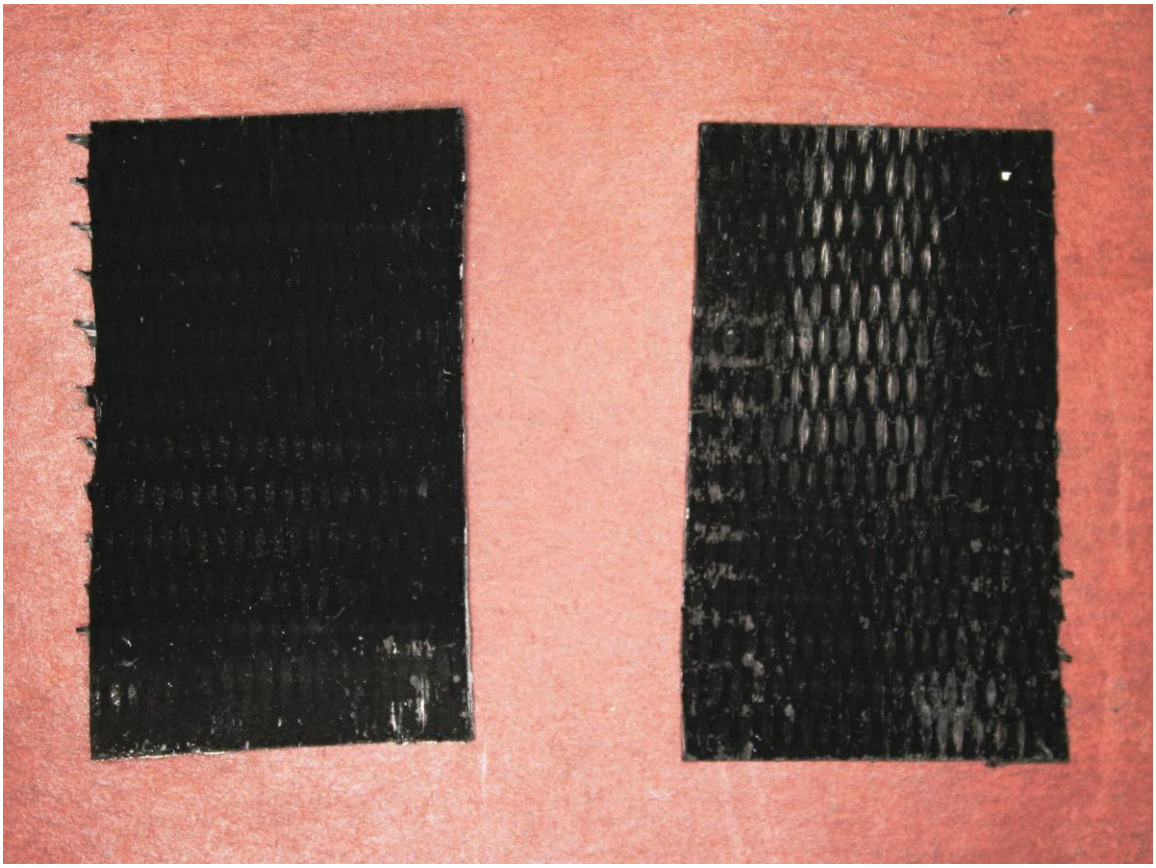

Figure 4-10. GDLs coated with 4 mg/cm^2 (left) and 2 mg/cm^2 (right). Note exposed GDL fibers on 2 mg/cm^2 MPL.

Prior to adhesion testing, it was believed that the optimal pressure of the assembly press needed to be high enough to provide adhesion but not so high as to over-compress the GDL and reduce its porosity. Adhesion tests however, showed that assembly pressures between 600 and 1100 psi did not have a significant influence on the bond strength between the MPL and CL. Since low assembly pressures do not result in poor adhesion, the conclusion can be made that low assembly pressures do not translate to poor performance. Figure 4-11, which shows the influence of assembly pressure on wet steady state performance, depicts this trend. The figure also shows that there is a significant drop in performance as assembly pressure increases above the optimal level of

750 psi. Inspection of Ribbon Cells assembled at various pressures found that cells pressed at 1100 psi were slightly thinner than those pressed at 600 psi. Since GDLs and MEAs used in the cells were the same thickness prior to assembly, the difference in overall cell thickness must have been caused by the assembly press. These findings suggest that high assembly pressures permanently compress GDLs, reducing their porosity and increasing mass transfer losses.

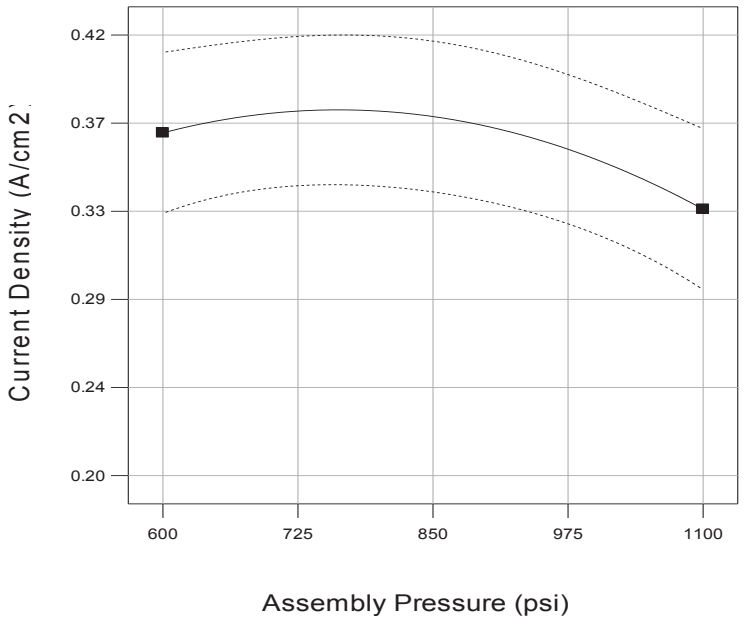

Figure 4-11. One factor plot showing influence of assembly pressure on wet steady state performance. (Composition = 35 wt%, Loading = 3.5 mg/cm^2, Sinter Pressure = 30 psi).

A comparison of the optimal MPL composition and loading found in this work, to the values found in the study performed by Henderson [22], show that Ribbon Cells require a MPL that is far different from that required by conventional cells. Henderson found that the optimal composition and loading for his MPLs were 10 wt% PTFE and 1.5 mg/cm^2. If these values are plotted on Figure 4-9, they are in the region where the worst

performance is predicted! Low loading worked well for Henderson's conventional cells because only a thin layer was required to completely coat his smooth and uniform GDLs. A high PTFE content was also not necessary in his MPLs, because Henderson's cells relied on external stack compression, not the MPL itself, to hold cell layers together. The difference in the results of this study and that performed by Henderson show that conclusions about the MPL of conventional cells do not transfer well to the MPL of Ribbon Cells.

In summary, results from the un-aged performance study showed that MPL composition, MPL loading and assembly pressure had a significant influence on performance. Sinter pressure was not found to be a significant variable in any of the response models, implying that sinter pressures anywhere between 20 and 40 psi will lead to optimal performance. Optimization of the response models found that a 34 wt% MPL yielded cells with highest power output. Results from the adhesion study and HFR data suggest that a high PTFE content is desired in the MPL because it translates to a strong layer that resists breaking during the initial swelling of the MEA. A loading around 3.5 mg/cm^2 leads to optimal performance because it translates to a MPL that completely covers the rough surface of the GDL without being thick enough to incur large mass transfer and ohmic losses. Response models also calculated that an assembly press of 750 psi led to optimal performance. Assembly pressures above 750 psi pay a more severe performance penalty than lower pressures because they compress the GDL reducing porosity and incurring large mass transfer losses. Lastly, a comparison of the optimal MPL found by Henderson to that found in this work, suggests that Ribbon Cells require a MPL that is far different from that of conventional fuel cells.

4.2.3 Aged Performance Results. Aged performance results from the 30 samples will be presented and analyzed in the same manner as was un-aged performance in the previous section. Before proceeding, it is important to note the relative importance of the aged and un-aged results. Since Ribbon Cell assemblies are being designed primarily for portable power applications, they will be functioning much as a rechargeable battery would function, with many on/off cycles. Therefore, aged performance data is much more valuable than un-aged performance data; just as the power output of a rechargeable battery after a number of discharge/recharge cycles is more important than its initial power output. The un-aged performance results are not completely moot however, because they can be used to calculate the percent decrease in performance after aging. Un-aged results are also valuable because they represent the upper limit of aged performance that can be achieved with perfect durability. With that said, the aged performance results are presented in Table 4-9, ordered from highest to lowest wet steady state performance. Center point replicates are highlighted in yellow, and the percent decrease from un-aged performance is also shown for each sample. Raw data for the aged performance of each sample can be found in Appendix A.

Table 4-9. Aged performance results ordered by highest to lowest wet steady state performance. Percent decrease from un-aged performance is also shown.

Run #	Composition (wt% PTFE)	Loading (mg/cm^2)	Assembly Pressure (psi)	Sinter Pressure (psi)	Aged Wet Polarization (A/cm^2)	Aged Dry Polarization (A/cm^2)	Aged Wet Lifetime (A/cm^2)	Aged Dry Lifetime (A/cm^2)	Wet Polarization % Diff	Dry Polarization % Diff	Wet Lifetime % Diff	Dry Lifetime % Diff
22	45	3	850	30	0.42	0.32	0.42	0.32	1.6	11.0	-1.2	9.3
25	25	3	850	30	0.38	0.28	0.35	0.28	10.1	28.0	14.0	27.4
17	25	3	850	30	0.38	0.29	0.34	0.29	3.8	13.3	7.6	14.5
9	25	3	850	10	0.35	0.33	0.32	0.32	6.1	12.0	9.1	16.4
28	35	4	600	40	0.33	0.29	0.30	0.27	7.1	17.5	7.2	19.4
13	25	3	850	30	0.33	0.25	0.30	0.24	10.2	21.0	13.5	19.7
14	35	2	600	20	0.29	0.23	0.27	0.22	7.4	9.4	4.6	13.3
3	25	3	850	30	0.29	0.23	0.26	0.22	21.6	26.8	21.6	26.4
21	35	2	1100	20	0.30	0.24	0.26	0.23	11.5	14.2	15.0	18.4
27	35	4	1100	40	0.28	0.24	0.26	0.22	12.9	23.1	14.4	27.1
16	25	3	850	30	0.28	0.26	0.25	0.25	19.1	30.3	27.1	31.6
5	35	4	1100	20	0.29	0.24	0.25	0.22	15.3	31.2	16.3	31.3
30	25	3	850	50	0.28	0.25	0.24	0.24	14.4	22.8	16.7	23.2
15	25	3	850	30	0.27	0.17	0.24	0.18	38.7	53.4	43.8	53.1
11	35	4	600	20	0.28	0.21	0.23	0.19	8.3	31.7	11.2	32.5
4	35	2	600	40	0.25	0.28	0.22	0.27	20.7	15.9	24.7	14.6
29	25	3	350	30	0.24	0.19	0.22	0.17	31.8	39.7	31.7	42.6
10	15	4	600	40	0.22	0.18	0.20	0.18	46.5	49.6	49.8	49.9
20	35	2	1100	40	0.24	0.17	0.20	0.17	13.6	44.9	15.2	44.5
23	25	5	850	30	0.21	0.20	0.18	0.20	44.0	28.9	46.5	39.4
8	15	4	1100	20	0.18	0.13	0.17	0.13	23.3	25.1	22.5	23.5
19	15	2	600	20	0.16	0.13	0.15	0.13	35.8	50.9	36.8	51.0
18	15	4	1100	40	0.14	0.10	0.13	0.09	45.1	55.9	43.6	56.5
12	15	4	600	20	0.13	0.11	0.12	0.10	47.6	35.4	49.4	36.2
2	5	3	850	30	0.13	0.08	0.12	0.07	-20.4	2.5	6.3	12.0
1	25	3	1350	30	0.12	0.10	0.12	0.10	42.0	51.5	38.5	51.3
6	25	1	850	30	0.11	0.09	0.10	0.09	50.0	24.8	50.0	25.4
7	15	2	1100	20	0.10	0.08	0.10	0.08	45.1	38.3	41.4	34.8
26	15	2	1100	40	0.10	0.08	0.09	0.08	53.4	39.4	57.9	39.5
24	15	2	600	40	0.09	0.07	0.09	0.07	51.4	40.9	52.0	40.0

Initial inspection of aged performance data shows that many of the poor performing samples had MPLs with 15 wt% PTFE and below, while better performing cells had MPLs with 25 wt% PTFE and above. Closer inspection reveals that the best performing cell (Run #22, 0.42 A/cm^2) had a 45 wt% MPL and the three poorest performers (Run #7, #26 and #24, 0.10, 0.09 and 0.09 A/cm^2 respectively) had a 15 wt% MPL with a loading of 2 mg/cm^2. In fact, no cell with a 15 wt% MPL performed better than 0.20 A/cm^2, and no cell with a 35 wt% MPL performed worse than 0.20 A/cm^2. These observations strongly suggest that the composition of the MPL heavily influences aged Ribbon Cell performance, with higher PTFE contents leading to better performance than lower PTFE contents. This trend can be explained by the increased bond strength of MPLs with higher PTFE weightings. Recall that aged peel test samples with 15 wt% MPLs had extremely low fracture energies, and exhibited MEA debonding prior to testing that was clearly visible with the naked eye. Further discussion on the cause of poor durability, as well as the correlation between aged performance and aged adhesion results will be presented in the following subsection.

It is difficult to determine the influence of the other three factors without the assistance of statistical analysis, in part because the influence of composition is so great, and also because of the complex nature of the experimental design. The final conclusion which can be made from inspection of the data in Table 4-9, is that if Ribbon Cells are not constructed correctly they will exhibit very poor durability. Results show that 15 of the 30 samples had a decrease in dry steady state performance of over 30% after just 10 wet/dry cycles!

4.2.4 Aged Performance Models. Aged performance models were created and analyzed in the same manner as un-aged performance models. Because of the similarity between the two processes some of the details and statistical tables that were presented in the un-aged performance model section will be omitted from this section. Complete statistical tables and other relevant information can be found in Appendix C.

Quadratic models were used for aged responses because they were the highest order model for which additional terms were significant without being aliased. A backwards elimination process was used to determine which terms to include in the model. As with un-aged model selection, terms were included that yielded the highest combination of adjusted R^2 and predicted R^2. The final model equations along with their respective R^2 values for each of the four responses are shown in Table 4-10.

Table 4-10. Model equations and R^2 values for aged responses (A = Composition, B = Loading, C = Assembly Pressure, D = Sinter Pressure).

Response	Model	Adj. R^2	Pred R^2
Wet Polarization	$j = -0.61 + 0.01*(A) + 0.23*(B) + 9.62E\text{-}4*(C) - 6.01E\text{-}3*(D) + 1.67E\text{-}3*(B)*(D) - 1.40E\text{-}4*(A^2) - 0.04*(B^2) - 6.02E\text{-}7*(C^2)$	0.85	0.78
Dry Polarization	$j = -0.63 + 0.01*(A) + 0.16*(B) + 9.34E\text{-}4*(C) + 2.78E\text{-}4*(D) + 1.35E\text{-}3*(B)*(D) - 5.70E\text{-}6*(C)*(D) - 1.58E\text{-}4*(A^2) - 0.03*(B^2) - 4.86E\text{-}7*(C^2)$	0.81	0.74
Wet Steady State	$j = -0.44 + 6.41E\text{-}3*(A) + 0.20*(B) + 8.44E\text{-}4*(C) - 6.36E\text{-}3*(D) + 1.81E\text{-}3*(B)*(D) - 0.04*(B^2) - 5.30E\text{-}7*(C^2)$	0.82	0.73
Dry Steady State	$j = -0.68 + 0.01*(A) + 0.16*(B) + 9.97E\text{-}4*(C) + 1.19E\text{-}3*(D) + 1.14E\text{-}3*(B)*(D) - 5.98E\text{-}6*(C)*(D) - 1.61E\text{-}4*(A^2) - 0.03*(B^2) - 5.17E\text{-}7*(C^2)$	0.80	0.70

A major difference between aged and un-aged model equations is that sinter pressure is included as a term. The linear sinter pressure term (D) was included in the models even though it was not significant, in order to maintain hierarchy. Since interaction terms involving sinter pressure were found to be significant, the linear sinter pressure term must be included; otherwise predicted responses from the model could be inaccurate. The aged models fit the raw data well, as shown by their adjusted R^2 values which are all 0.80 and above. Predicted R^2 values are also relatively high, meaning that these models predict performance accurately.

Optimization of the aged models was performed for each individual response and for the combined response of wet and dry steady state performance. Table 4-11 shows the factor levels which lead to optimal performance for each of the responses. The response labeled "Wet + Dry Steady State" denotes the factor levels which lead to the maximum combination of dry and wet steady state performance. Essentially it gives the recipe for a Ribbon Cell which will perform well at a wide range of reactant gas conditions. A contour plot is presented in Figure 4-12 in order to visualize the MPL composition and loading which lead to the best steady state performance at wet conditions.

Table 4-11. Factor values which maximize current density at various conditions. Maximum current density as predicted by the models for each response are also shown

Responses	Composition (wt% PTFE)	Loading (mg/cm^2)	Assembly Pressure (psi)	Sinter Pressure (psi)	Current Density (A/cm^2)
Wet Polarization	45.00	3.05	800	20	0.41
Dry Polarization	45.00	3.55	726	40	0.33
Wet Steady State	45.00	3.01	796	20	0.41
Dry Steady State	43.55	3.47	733	40	0.31
Wet + Dry Steady State	45.00	3.05	827	20	0.41* / .31**

*Wet current density
**Dry current density

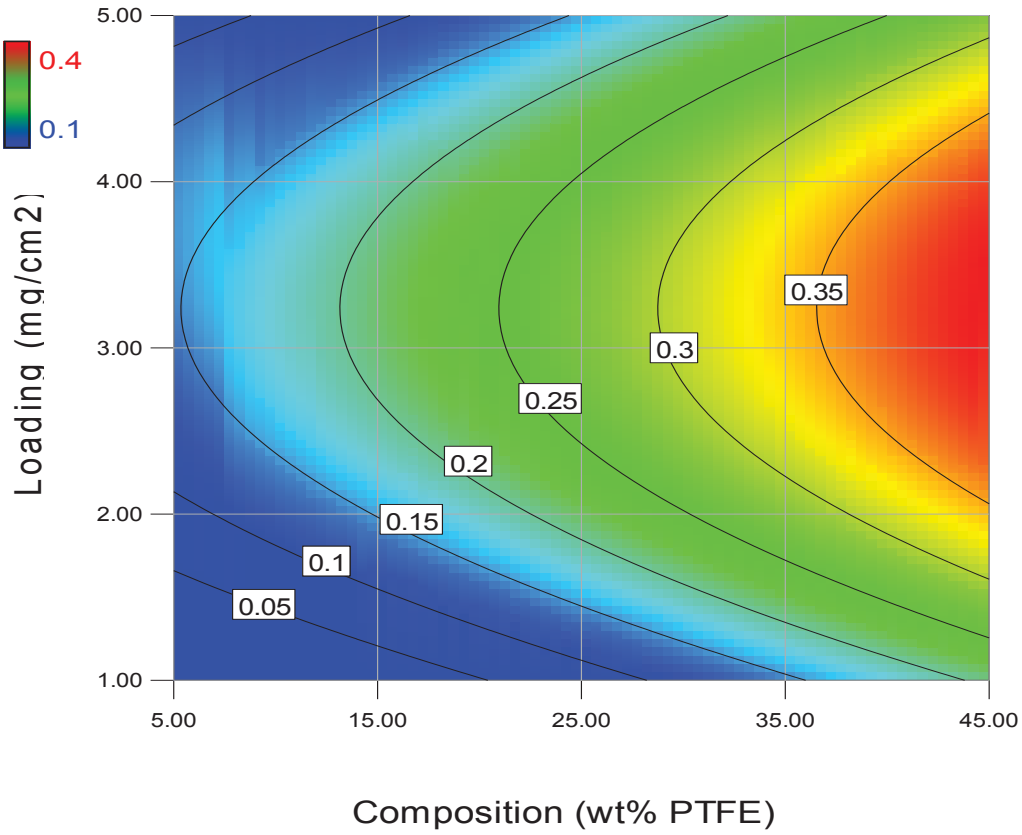

Figure 4-12. Contour plot showing the influence of loading and composition on aged wet steady state performance.

Optimization data in Table 4-11 and Figure 4-12 show that a 45 wt% MPL yields the best performance at both wet and dry conditions. Before going further with this analysis, the reason for extrapolating outside of the factorial points (15 – 35 wt% PTFE) will be justified. Statisticians often warn about the dangers of using a model to predict responses for factor values which are outside the factorial design space, because those predictions may be inaccurate. Since Run #22 (45 wt%, 3 mg/cm^2) is a data point at the levels of composition and loading being extrapolated to, it was used verify the accuracy of the model's prediction. Comparison of the model prediction to measured data showed that the wet and dry steady state performance predicted by the model (0.41 A/cm^2 wet, 0.31 A/cm^2 dry) was extremely close the performance measured for Run #22 (0.42 A/cm^2, 0.31 A/cm^2 dry); therefore the predictions in Table 4-11 and Figure 4-12 were deemed to be accurate.

A PTFE content of 45 wt% in the MPL leads to high performance because it results in a strong bond between cell layers caused by the increased strength of the layer itself. A robust bond between cell layers is needed to achieve high *initial* performance, but it becomes even more essential in achieving high *aged* performance after multiple expansion/contraction cycles of the MEA. Since the MEA is bonded to the relatively rigid MPL / GDL assembly, its swelling and shrinking creates stress at the interlayer bonds, as well as in the MPL itself. If the MPL does not have a high PTFE content it will not be strong enough to withstand these stresses, and will fracture. In areas where fracture has occurred, current density will plummet because the electron pathways between the GDL and reaction sites in the CL will be broken. Increasing the PTFE content in the MPL strengthen the layer to the point where it will not fracture as the MEA

swells and shrinks, thus keeping contact resistances low. High frequency resistance data supports this theory with Run #22 (45 wt%) having an area specific resistance of 0.29 Ω–cm^2, 35 wt% cells averaging 0.39 Ω–cm^2 and 15 wt% cells averaging 0.47 Ω–cm^2 at wet conditions.

Observations and data from the adhesion study support this debonding theory. In the study, it was observed that samples containing MPLs with 15 wt% PTFE showed significant debonding between the MEA and GDL after aging. Inspection of debonded MEAs and GDLs found that a uniform layer of MPL existed on both components, suggesting that the MPL itself fractured as the MEA expanded and contracted. Inspection of 35 wt% samples found that increasing the PTFE content strengthened the MPL to the point where it did not fracture during aging. Peel test data however, showed that even in samples containing a high PTFE content, aged bonds were only about half as strong as they were prior to aging. This decrease in bond strength caused by aging is likely why the 35 wt% performance samples showed a slight decrease in power output after aging. The reason why the performance of Run #22 which had a 45 wt% MPL, did not decrease after aging is because the higher PTFE content strengthened the MPL even further, to the point where almost no debonding occured. To verify this theory, an adhesion sample was constructed with a 45 wt%, 4 mg/cm^2 MPL and aged. Data from the peel test showed that this 45 wt% aged sample had a 12% higher fracture energy than the aged 35 wt% aged sample with the same loading (61.6 J/m^2 compared to 55.2 J/m^2).

It is possible that increasing the MPL PTFE content above 45 wt% will increase the aged bond strength and thus result in more durable Ribbon Cells; however this may not be the case. There are drawbacks to having a MPL with an excessively high PTFE

content. The most significant is that the conductivity of the MPL will decrease as the ratio of conductive carbon black to non-conductive PTFE is decreased. Increasing the PTFE content also reduces the porosity of the MPL which increases mass transfer losses. Performance would likely further decrease because the extremely hydrophobic MPL will hold an excessive amount of water adjacent to the MEA resulting in the blocking of reaction sites due to flooding of the CL. Because of these drawbacks it is not prudent to assume that PTFE contents above 45 wt% will lead to better aged performance. Further adhesion and performance data must be gathered before conclusions about MPLs with PTFE contents above 45 wt% can be made.

MPLs with loadings between 3 and 3.5 mg/cm^2 are predicted to produce the best performing cells by the statistical models. The optimal loading range for aged performance is similar to the range in which un-aged performance is optimal. The justification for why this range is optimal is the same for aged samples as for un-aged samples. Loadings below this range are not sufficient to fully cover the GDL surface resulting in poor local contact resistance, while loadings above the range result in a MPL which is too thick and incurs ohmic as well as mass transfer losses. Figure 4-13 presents a one-factor plot showing the optimal value for loading, as well as the performance penalties for over or under loading the MPL. From the figure, it can be seen that under-loading results in a larger performance decrease than over-loading. The reason for this trend is because the drawbacks of having exposed fibers are more severe than the drawbacks associated with the ohmic and mass transfer losses incurred by a thick MPL.

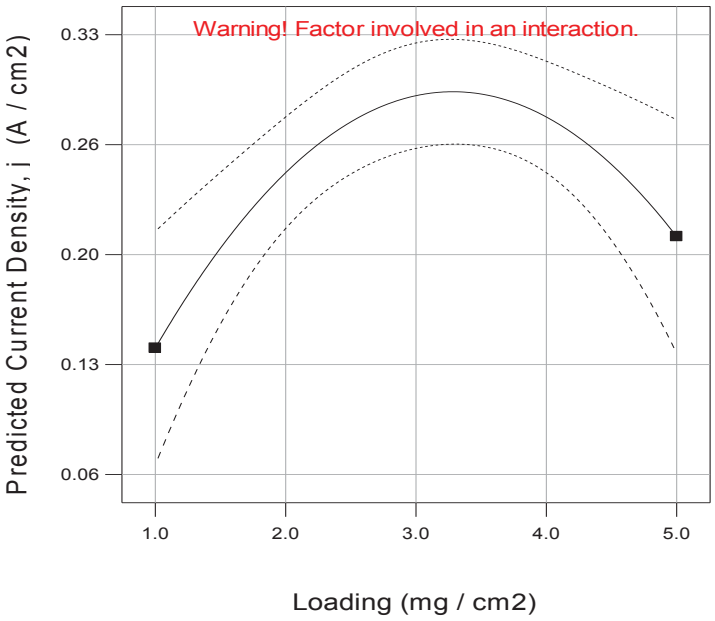

Figure 4-13. One factor plot showing the influence of loading on aged dry steady state performance. (Composition = 35 wt%, Assy Press = 750 psi, Sinter = 30 psi).

Assembly pressures between 700 and 850 psi were calculated to be optimal for aged performance. As with un-aged performance, assembly pressures above this range compress the GDL, reducing porosity and lowering performance. Assembly pressures below this range do not pay as severe a performance penalty because adhesion does not decrease as assembly pressure decreases. See Appendix C for one-factor plots of assembly pressure, sinter pressure, loading and composition for aged performance.

In summary, a cell with a MPL containing 45 wt% PTFE, loaded at 3.5 mg/cm^2, sintered between 20 and 40 psi, and hot pressed together at 750 psi will yield optimal aged performance. A PTFE content of 45 wt% is rarely, if ever found in the MPL of conventional cells because of the large mass transfer and ohmic losses associated with high PTFE to carbon ratios. In Ribbon Cells however, a 45 wt% MPL provides benefits which far outweigh the ohmic and mass transfer losses which high PTFE compositions

incur. The chief benefit is that a high PTFE content strengthens the MPL to the point where it does not fracture from the expansion and contraction of the MEA caused by wet and dry operating cycles. A Ribbon Cell formulated with these optimal MPL parameters and assembly pressure should produce around 0.4 A/cm^2 at wet operating conditions and 0.3 A/cm^2 at dry conditions after ten wet/dry cycles.

5. Conclusions and Recommendations

5.1 Conclusions

Results from the performance study show that MPL characteristics and assembly parameters have a dramatic influence on the performance of Ribbon Fuel Cells. For both aged and un-aged performance, composition was the most influential variable, followed by loading, then assembly pressure, and finally sinter pressure was shown to have no significant influence. Before going further, the relative importance of aged and un-aged results should be briefly reiterated. Since aged data is far more important than un-aged data in determining the construction of future Ribbon Cell assemblies, the majority of the discussion in this section will center on the parameters which optimize aged performance.

Comparison of aged to un-aged data confirmed that Ribbon Cell performance decreases significantly after experiencing just 10 wet/dry reactant gas cycles. Results from the adhesion study correlated well with data from the performance study. Samples with 15 wt% MPLs showed poor aged performance and poor aged adhesion, while 35 wt% samples had improved adhesion and improved aged performance. Also, the cell with the highest aged performance (Run #22, 45 wt% MPL) had the highest aged adhesion. The clear correlation between aged performance and aged adhesion, suggests that the reason why certain Ribbon Cells show such poor durability, is because their MPL provides poor adhesion between the MEA and GDL. Without external compression holding cell layers together, poorly formed MPLs fracture as the MEA expands and contracts during cell operation. In order to construct a Ribbon Cell with improved structural integrity during aging and thus has improved aged performance, the following

variable levels should be used: *Composition – 45 wt% PTFE, Loading – 3.5 mg/cm^2, Assembly Pressure – 750psi and Sinter Pressure – between 20 and 40psi.*

Statistical analysis of aged Ribbon Cell performance showed that a MPL with 45 wt% PTFE yielded cells with the best performance and durability among those constructed in this study. It is highly uncommon for conventional PEMFCs to be constructed with MPLs containing this high a PTFE content, because of the associated ohmic and mass transfer losses. The reason why a 45 wt% MPL is optimal for Ribbon Cells, can be explained by results from the adhesion study, which showed that increasing the PTFE content of the MPL reduced the susceptibility of the MPL to fracture. Magnified images of the debonded surfaces of aged MEAs and GDLs revealed that 15 wt% samples were fracturing through the MPL itself, while 35 wt% samples were fracturing at the MPL / GDL and MPL / CL interfaces. This difference in fracture location suggests that increasing the PTFE content, increases the strength of the MPL. Higher MPL strength translates to higher performance, especially after aging, because the MPL resists fracture during MEA expansion and contraction. If the MPL does not contain enough PTFE, it will fracture as the MEA expands, creating areas with high contact resistances and low local current densities. High frequency resistance data taken during performance testing supports this theory, with cells containing 35 wt% MPLs having a lower area specific ohmic resistances than those with 15 wt% MPLs. It is unclear if MPLs with PTFE contents above 45 wt% will lead to better aged performance because it was the highest composition tested in this work.

A MPL loading of approximately 3.5 mg/cm^2 produces cells with the highest aged performance because it is sufficient to fully cover the GDL, while not being too thick to

incur significant mass transfer and ohmic penalties. The optimal loading value found in this work is on the high end of optimal loading values for conventional fuel cells. The reason for this high optimal loading value is that the GDL used in Ribbon Cells has a higher surface roughness than almost all conventional GDLs; therefore, it requires a greater amount of MPL to fully cover the GDL fibers and create a smooth surface. Exposed GDL fibers mean poor contact with the CL and poor water management, leading to high local contact resistance and ohmic losses due to membrane drying. It is also likely that areas where fibers are exposed have poor adhesion between the GDL and MEA; however, this appears to be contradicted by results from the adhesion study, which found that only composition had a significant influence on adhesion. The reason for this apparent contradiction may be that composition had such a strong influence on adhesion, the effects of loading may have been masked. Future adhesion studies are needed to confirm this theory.

Statistical models found that an assembly pressure around 750 psi produces Ribbon Cells that have the highest aged performance. Pressures which are significantly above this value will compress the GDL, reducing its porosity and increasing mass transfer losses. Assembly pressures which are significantly below 750psi will incur a less severe performance penalty; however, it is unclear exactly why this is the case. Initial speculation was that lower assembly pressures result in poorer adhesion, but results from the adhesion study showed assembly pressure did not have a significant influence on adhesion. Since assembly pressure is the variable with the second lowest influence on response, understanding exactly why lower pressures leads to lower performance is not critical for Ribbon Cell construction, but could be an area of future exploration.

Sinter pressure was not found to have a significant influence on aged performance in the pressure range investigated. This does not mean that sinter pressure does not need to be controlled; rather that between 20 and 40 psi sinter pressure does not affect cell performance. Upper and lower limits on sinter pressure do exist, and were found in previous Ribbon Cell work at the ESL. Previous studies found that if MPLs were not sintered under at least small pressure, they would debond from the GDL during subsequent Ribbon Cell Assembly steps. Sintering above 50 psi compresses the GDL to the point where mass transfer losses become severe. Results from previous studies coupled with results from this work lead to the conclusion that sinter pressure should be controlled between 20 and 40 psi to produce Ribbon Cells with optimal aged performance.

5.2 Recommendations

Although this work answered many questions about the relationship between the construction and performance of Ribbon Cells, it also raised a number of questions which should be addressed in future studies. The most important question left unanswered by this work is whether or not Ribbon Cells, constructed with the aforementioned optimal parameters, will show a significant decrease in performance after more than 10 wet/dry aging cycles. To answer this question, Ribbon Cells should be constructed at the optimal variable levels, aged for more than 10 cycles and tested as described in Section 3. The number of aging cycles will depend on the potential application of the Ribbon Cell. If it will be used as a portable power supply for a laptop, then hundreds or even thousands of

aging cycles would likely be required. On the other hand if the application is a low cost unmanned aerial vehicle that will only be used a handful of times, then 10 aging cycles may be sufficient.

The fact that the highest composition tested (45 wt%) was found to be optimal raises the question of whether improved durability can be achieved with MPLs containing even more PTFE. For this to be the case, losses associated with high PTFE MPLs must be balanced by improved aged adhesion. A second possibility for improving the MEA / GDL bond is by altering the amount of PTFE in the GDL. Since higher strength MPLs were failing mostly at the GDL / MPL interface, increasing the PTFE content of the GDL may improve this interfacial bond. Again, the benefits in adhesion must be weighed against the increased ohmic losses which GDLs with high PTFE contents will incur. Further improvements in the GDL / MPL bond may be realized by sintering the MPL and GDL in one step, instead of in two separate steps as was done in this work. Care should be taken in these future studies to design an experiment that allows for curvature as well as for the meaningful comparison of adhesion and performance results.

5.3 Closing Remarks

Ribbon Fuel Cells have many beneficial characteristics such as their low profile planar geometry, and lightweight design, that make them desirable for portable power applications. This work has found that when constructed correctly, Ribbon cells can produce between 0.4 and 0.3 A/cm^2 (depending on their operating conditions) at 0.5 V after ten wet/dry or on/off cycles. This performance is comparable to other fuel cell

designs vying for the portable power niche; however, durability of the Ribbon Cell design is still a concern. Improvements of Ribbon Cell performance after longer term aging is the next step in the development and commercialization of this technology.

References

1. Ballard Power Systems, “http://www.ballard.com.” 3/2/2009.

2. O’Hayre, R., Cha S.W., Colella, W. and Prinz, F.B. (2006). *Fuel Cell Fundamentals*. New Jersey: John Wiley & Sons, Inc.

3. University of Deleware Fuel Cell Research Laboratory, “http://www.me.udel.edu/research_groups/prasad/proj/piv.html.” 2/27/2009.

4. Larminie, J., and Dicks, A. (2003). *Fuel Cell Systems Explained.* West Sussex, England: John Wiley & Sons Ltd.

5. Yu, X., and Ye, S. (2007). “Recent advances in activity and durability enhancement of Pt/C catalytic cathode in PEMFC: Part I. Physico-chemical and electronic interaction between Pt and carbon support, and activity enhancement of Pt/C catalyst.” *Journal of Power Sources*, 172(1), 133-134.

6. Fuel Cell Energies, “http://www.futureenergies.com.” 3/2/2009.

7. M. Ellis and D. Dillard, “VTIP Disclosure No. 03.-129, ‘Novel PEM Fuel Cell Architectures,’” 2001.

8. Heinzel, A., Nolte, R., Ledjeff-Hey, K., and Zedda, M. (1998). “Membrane fuel cells – concepts and system design.” *Electrochimica Acta*, 43(24), 3817-3820.

9. Jiang, R., and Chu, D. (2001). “Stack design and performance of polymer electrolyte membrane fuel cells.” *Journal of Power Sources*, 93(1-2), 25-31.

10. Weber, A.Z., and Newman, J. (2005). “Effects of microporous layers in polymer electrolyte fuel cells.” *Journal of the Electrochemical Society*, 152(4), A677-A688.

11. Nitta, I., Himanen, O., and Mikkola, M. (2008). “Contact resistance between gas diffusion layer and catalyst layer of PEM fuel cell.” *Electrochemical Communications*, 10(1), 47-51.

12. Park, S., Lee, J. W., and Popov, B. N. (2008). “Effect of PTFE content in microporous layer on water management in PEM fuel cells.” *Journal of Power Sources*, 177(2), 457-463.

13. Li, H., Tang, Y., Wang, Z., Shi, Z., Wu, S., Song, D., Zhang, J., Fatih, K., Zhang, J., Wang, H., Liu, Z., Abouatallah, R., and Mazza, A. (2008). “A review of water

flooding issues in the proton exchange membrane fuel cell." *Journal of Power Sources*, 178(1), 103-117.

14. Qi, Z., and Kaufman, A. (2002). "Improvement of water management by a microporous sublayer for PEM fuel cells." *Journal of Power Sources*, 109(1), 38-46.

15. Kong, C. S., Kim, D. Y., Lee, H. K., Shul, Y. G., and Lee, T. H. (2002). "Influence of pore-size distribution of diffusion layer on mass-transport problems of proton exchange membrane fuel cells." *Journal of Power Sources*, 108(1-2), 185-191.

16. Passalacqua, E., Squadrito G., Lufrano F., Patti, A., and Giorgi, L. (2001). "Effects of the diffusion layer characteristics on the performance of polymer electrolyte fuel cell electrodes." *Journal of Applied Electrochemistry*, 31(4), 449-454.

17. Jordan, L. R., Shukla, A. K., Behrsing T., Avery, N. R., Muddle, B. C., and Forsyth, M. (2000). "Diffusion layer parameters influencing optimal fuel cell performance." *Journal of Power Sources*, 86(1-2), 250-254.

18. Song, J. M., Cha, S. Y., and Lee, W. M. (2001). "Optimal composition of polymer electrolyte fuel cell electrodes determined by the AC impedance method." *Journal of Power Sources*, 94(1), 78-84.

19. Giorgi, L., Antolini E., Pozio, A., and Passalacqua E. (1998). "Influence of the PTFE content in the diffusion layer of low-Pt loading electrodes for polymer electrolyte fuel cells." *Electrochimica Acta*, 43(24), 3675-3680.

20. Velayutham, G., Kaushik, J., Rjalakshmi, N., and Dhathathreyan, K. S. (2007). "Effect of PTFE content in gas diffusion media and microlayer on the performance of PEMFC tested under ambient pressure." *Fuel Cells*, 7(4), 314-318.

21. Park, S., Lee, J. W., Popov, B. N. (2006). "Effect of carbon loading in microporous layer on PEM fuel cell performance." *Journal of Power Sources*, 163(1), 357-363.

22. Henderson, K. (2005). Evaluation of the Effect of Microporous Sublayer Design and Fabrication on Performance and Adhesion in PEM Fuel Cell Assemblies. Masters Thesis, Virginia Polytechnic Institute and State University.

23. Lee, H. K., Park, J. H., Kim, D. Y., and Lee, T. H. (2004). "A study on the characteristics of the diffusion layer thickness and porosity of the PEMFC." *Journal of Power Sources*, 131(1-2), 200-206.

24. Engineering Statistics Handbook, "http://itl.nist.gov/div898/handbook/pri/section3/pri333.htm" 3/15/2009.

25. Sole, J. (2005). Investigation of Novel Gas Diffusion Media for Application in PEM Fuel Cell Ribbon Assemblies. Masters Thesis, Virginia Polytechnic Institute and State University.

26. Relative Humidity and Dew Points Explained, "http://www.shorstmeyer.com/wxfaqs/humidity/humidity.html" 3/25/2009.

Appendix A: EIS, Polarization and Steady State Data

Table A-1. High frequency resistance data from EIS ordered by lowest to highest Aged Wet HFR

					Un-Aged		Aged	
Run #	wt% PTFE	Loading (mg/cm^2)	Assembly (psi)	Sinter (psi)	Wet HFR (Ω-cm2)	Dry HFR (Ω-cm2)	Wet HFR (Ω-cm2)	Dry HFR (Ω-cm2)
22	45	3	850	30	0.29	0.44	0.29	0.45
28	35	4	600	40	0.28	0.38	0.30	0.44
9	25	3	850	10	0.27	0.39	0.32	0.45
25	25	3	850	30	0.28	0.41	0.32	0.52
17	25	3	850	30	0.35	0.49	0.35	0.52
20	35	2	1100	40	0.30	0.44	0.35	0.53
30	25	3	850	50	0.33	0.42	0.35	0.59
4	35	2	600	40	0.30	0.43	0.37	0.52
19	15	2	600	20	0.31	0.46	0.37	0.52
3	25	3	850	30	0.29	0.50	0.38	0.57
5	35	4	1100	20	0.32	0.42	0.38	0.57
27	35	4	1100	40	0.33	0.41	0.38	0.51
11	35	4	600	20	0.28	0.40	0.39	0.53
15	25	3	850	30	0.30	0.40	0.39	0.68
23	25	5	850	30	0.29	0.43	0.39	0.60
13	25	3	850	30	0.29	0.46	0.40	0.57
16	25	3	850	30	0.28	0.38	0.40	0.53
1	25	3	1350	30	0.34	0.47	0.41	0.53
8	15	4	1100	20	0.43	0.60	0.41	0.60
10	15	4	600	40	0.29	0.40	0.41	0.64
7	15	2	1100	20	0.40	0.63	0.43	0.69
29	25	3	350	30	0.32	0.44	0.43	0.63
2	5	3	850	30	0.50	0.80	0.46	0.82
12	15	4	600	20	0.27	0.43	0.46	0.52
21	35	2	1100	20	0.35	0.49	0.46	0.69
14	35	2	600	20	0.35	0.50	0.47	0.68
26	15	2	1100	40	0.40	0.64	0.52	0.78
24	15	2	600	40	0.41	0.68	0.57	0.94
6	25	1	850	30	0.43	0.84	0.58	1.19
18	15	4	1100	40	0.35	0.52	0.60	0.87

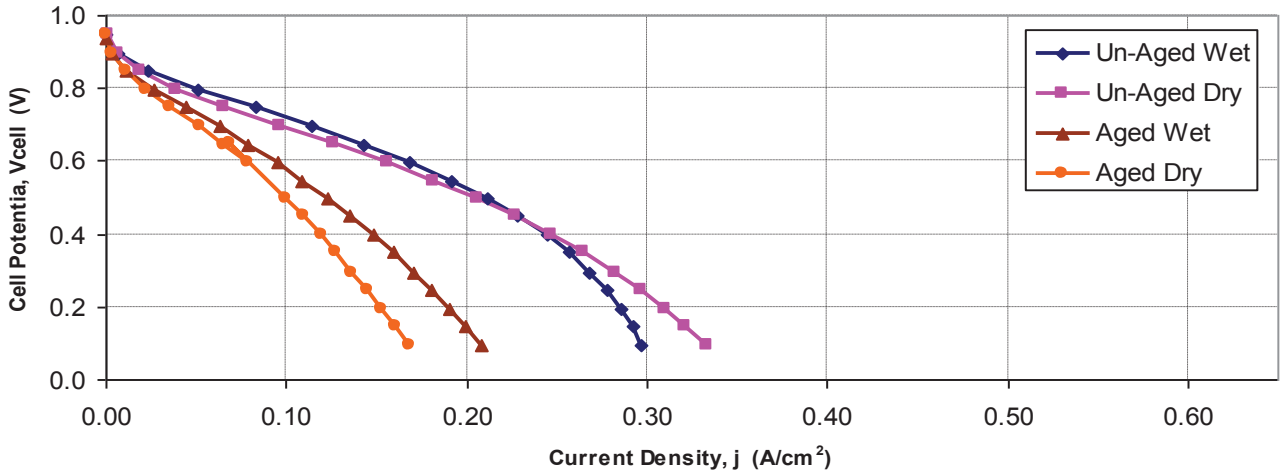

Figure A-1. Polarization data for design point 1 (25% PTFE, 3mg/cm^2, 1350psi Assy, 30psi Sinter)

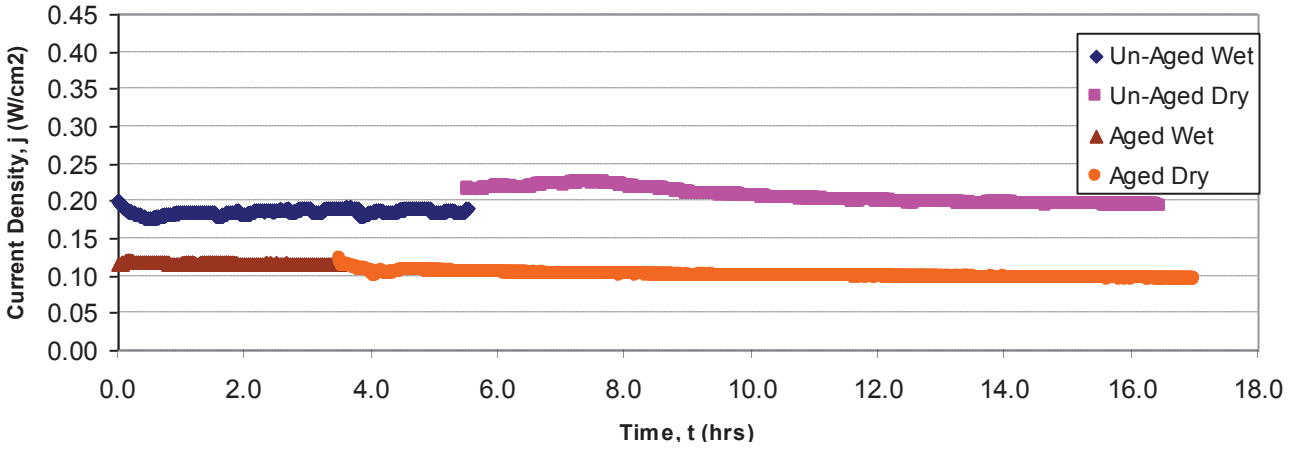

Figure A-2. Steady state data for design point 1 (25% PTFE, 3mg/cm^2, 1350psi Assy, 30psi Sinter)

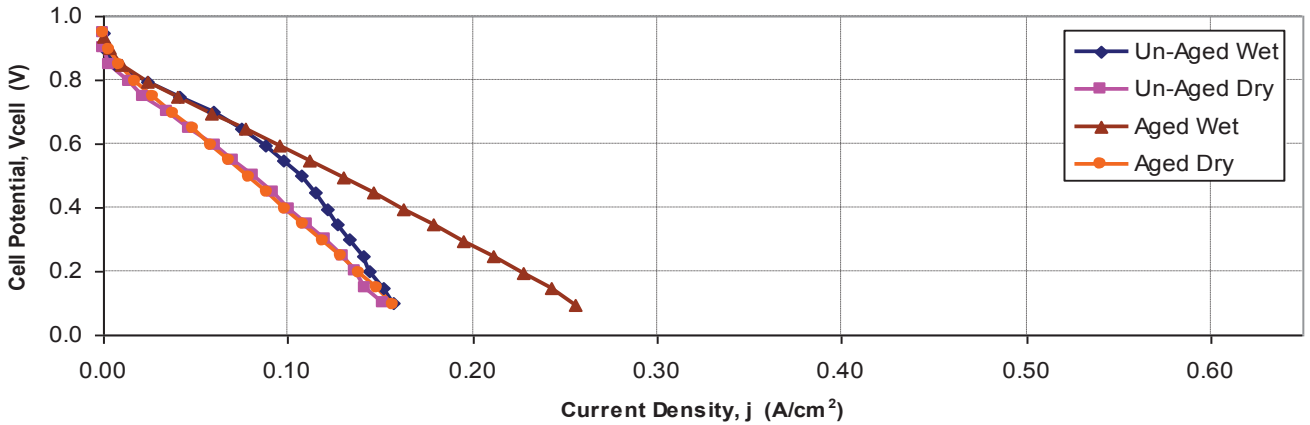

Figure A-3. Polarization data for design point 2 (5% PTFE, 3mg/cm^2, 850psi Assy, 30psi Sinter)

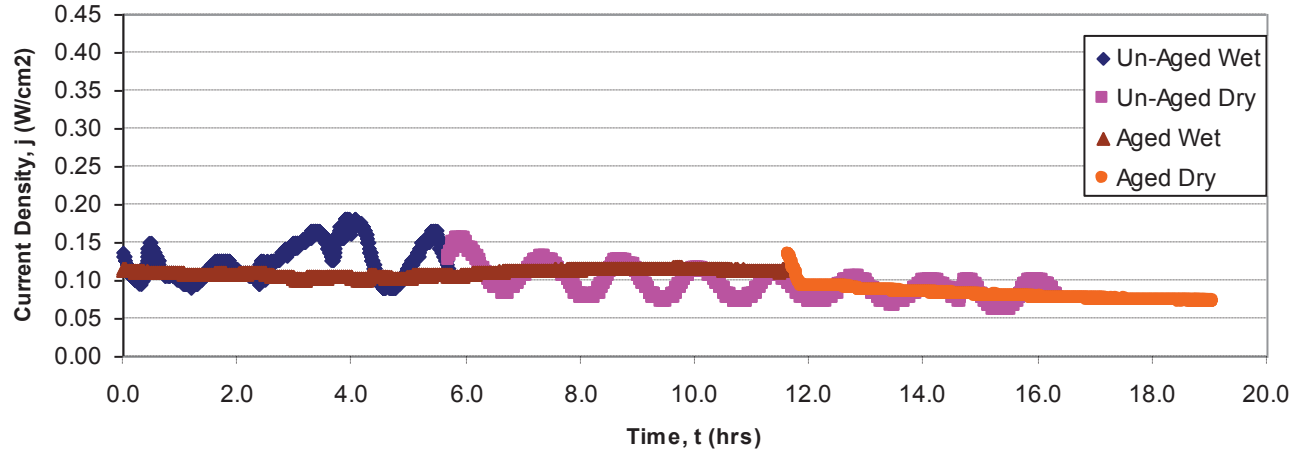

Figure A-4. Steady state data for design point 2 (5% PTFE, 3mg/cm^2, 850psi Assy, 30psi Sinter)

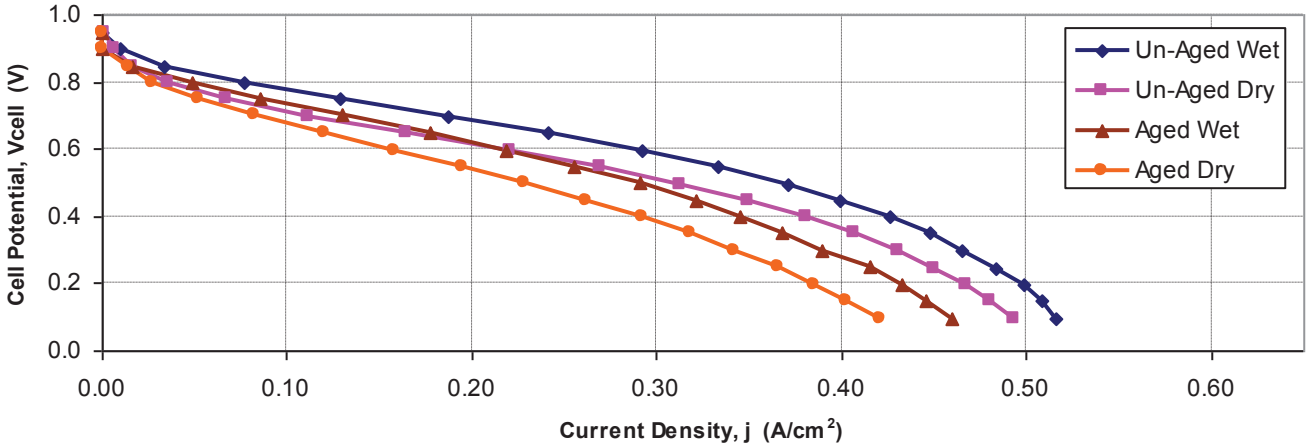

Figure A-5. Polarization data for design point 3 (25% PTFE**,** 3mg/cm^2, 850psi Assy, 30psi Sinter)

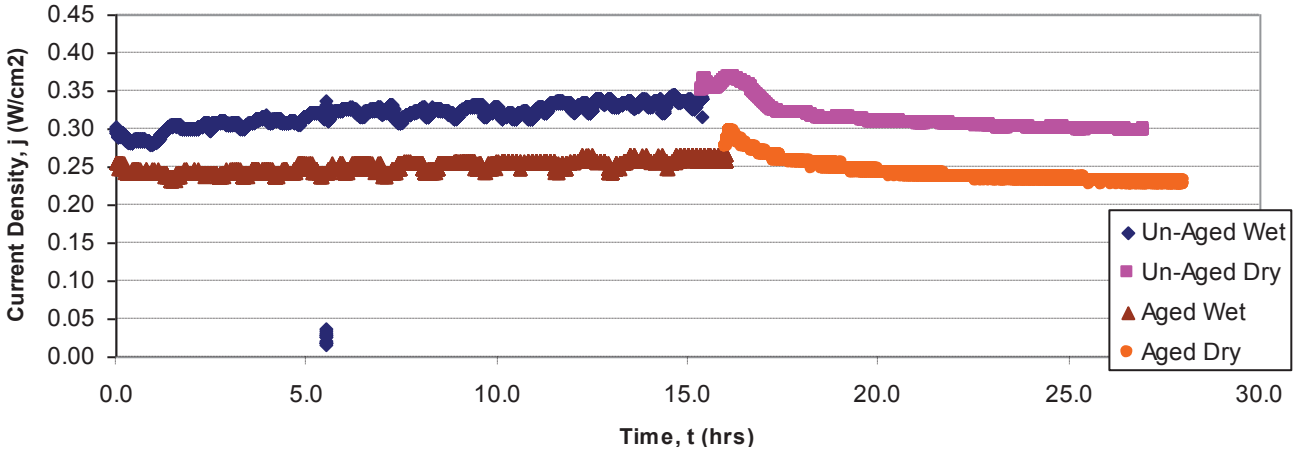

Figure A-6. Steady state data for design point 3 (25% PTFE**,** 3mg/cm^2, 850psi Assy, 30psi Sinter)

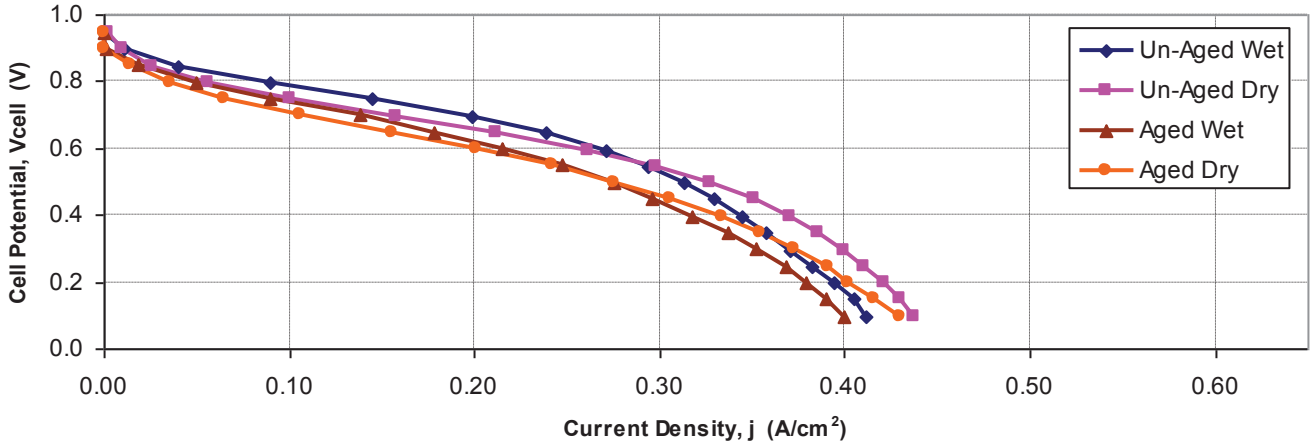

Figure A-7. Polarization data for design point 4 (35% PTFE, 2mg/cm^2, 600psi Assy, 40psi Sinter)

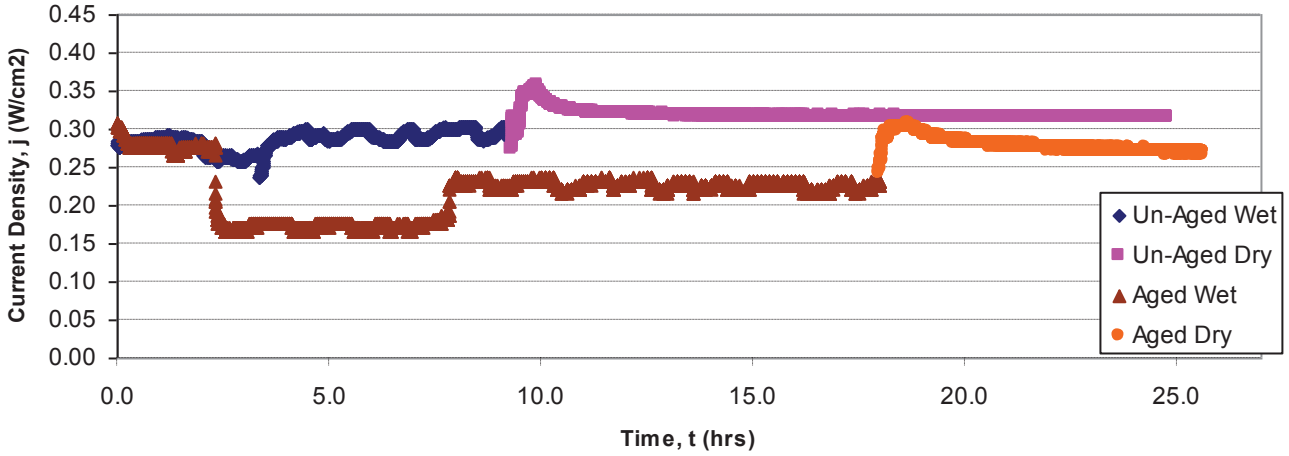

Figure A-8. Steady state data for design point 4 (35% PTFE, 2mg/cm^2, 600psi Assy, 40psi Sinter)

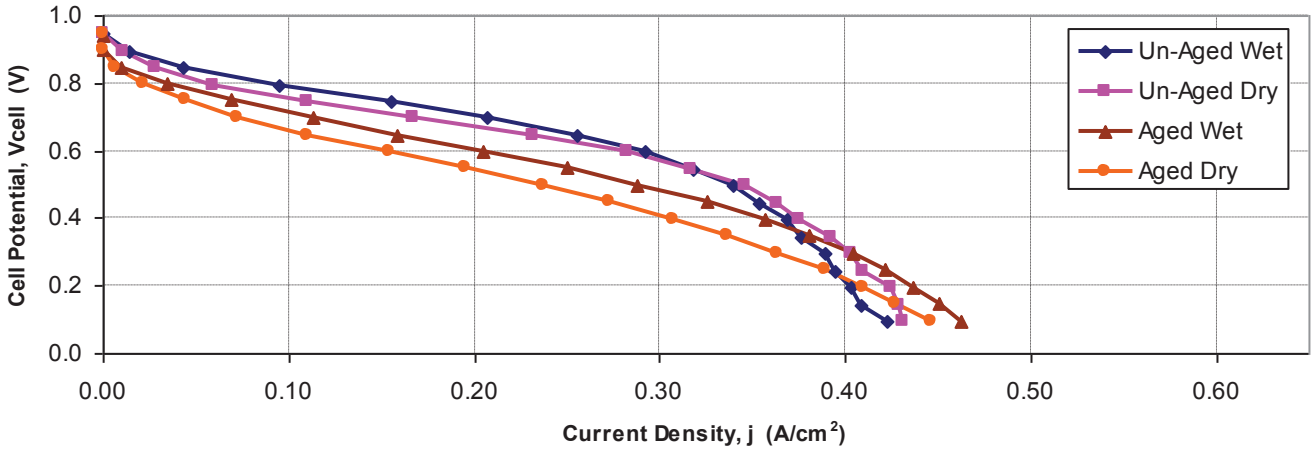

Figure A-9. Polarization data for design point 5 (35% PTFE, 4mg/cm^2, 1100psi Assy, 20psi Sinter)

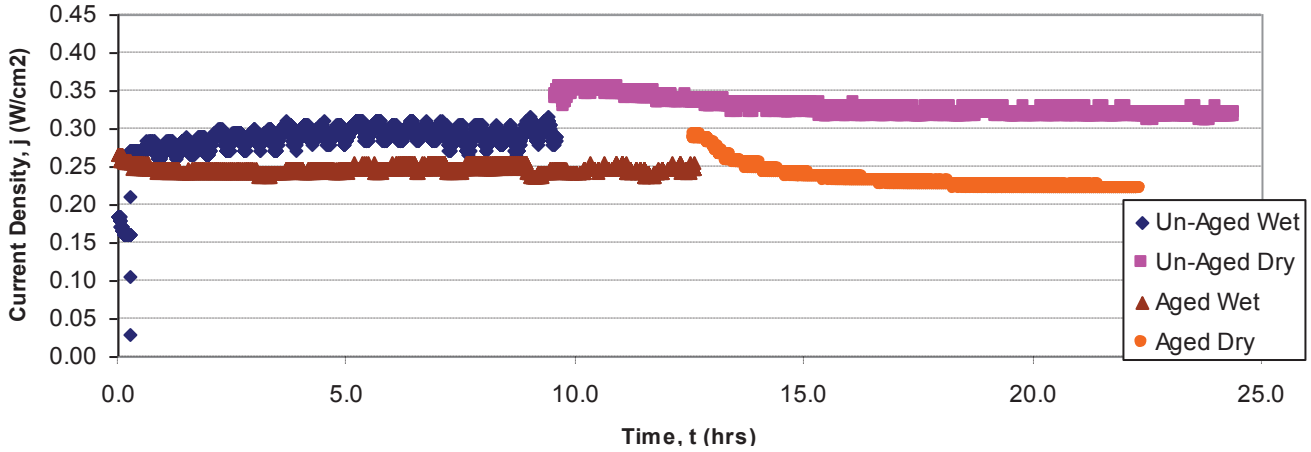

Figure A-10. Steady state data for design point 5 (35% PTFE, 4mg/cm^2, 1100psi Assy, 20psi Sinter)

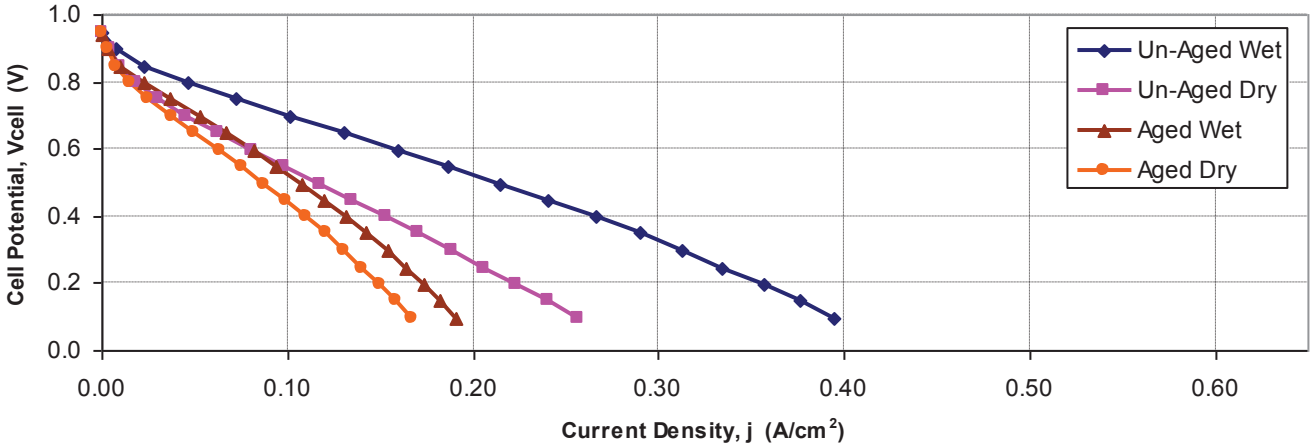

Figure A-11. Polarization data for design point 6 (25% PTFE, 1mg/cm^2, 850psi Assy, 30psi Sinter)

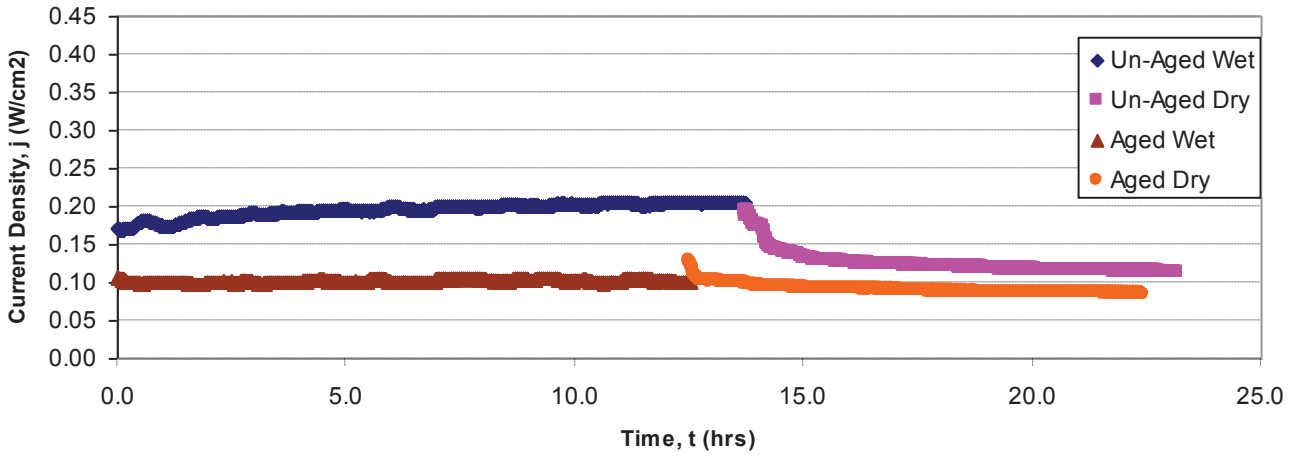

Figure A-12. Steady state data for design point 6 (25% PTFE, 1mg/cm^2, 850psi Assy, 30psi Sinter)

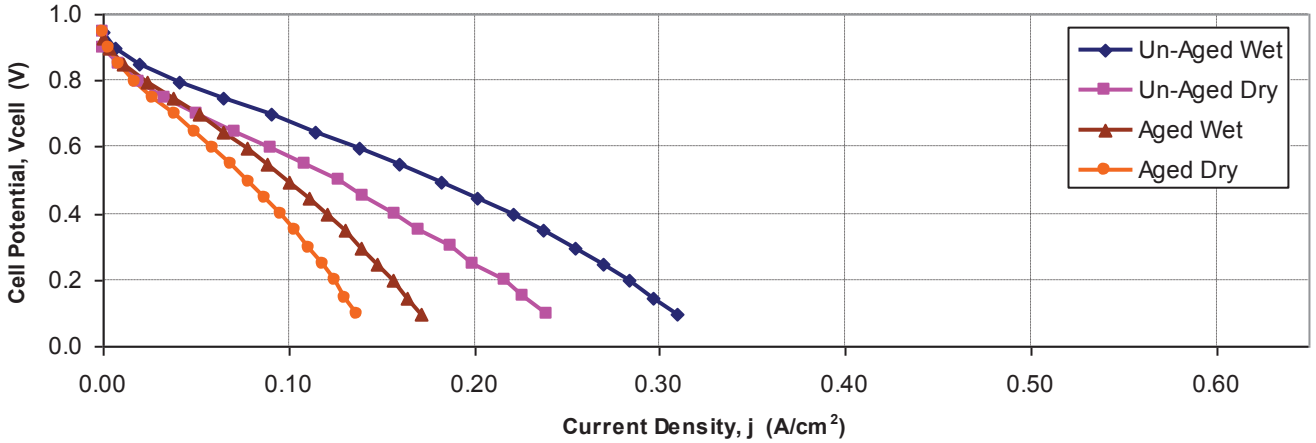

Figure A-13. Polarization data for design point 7 (15% PTFE, 2mg/cm^2, 1100psi Assy, 20psi Sinter)

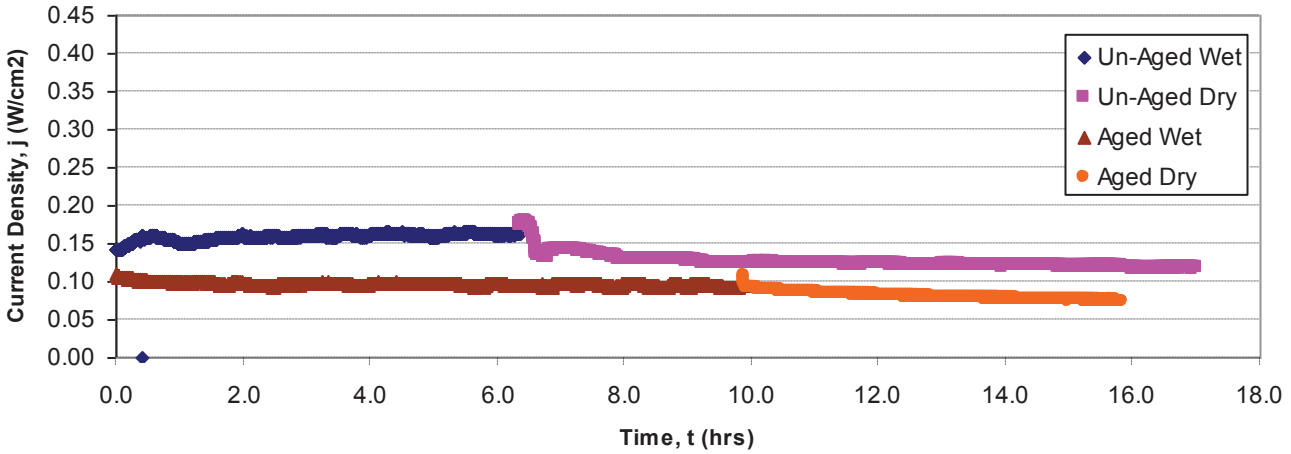

Figure A-14. Steady state data for design point 7 (15% PTFE, 2mg/cm^2, 1100psi Assy, 20psi Sinter)

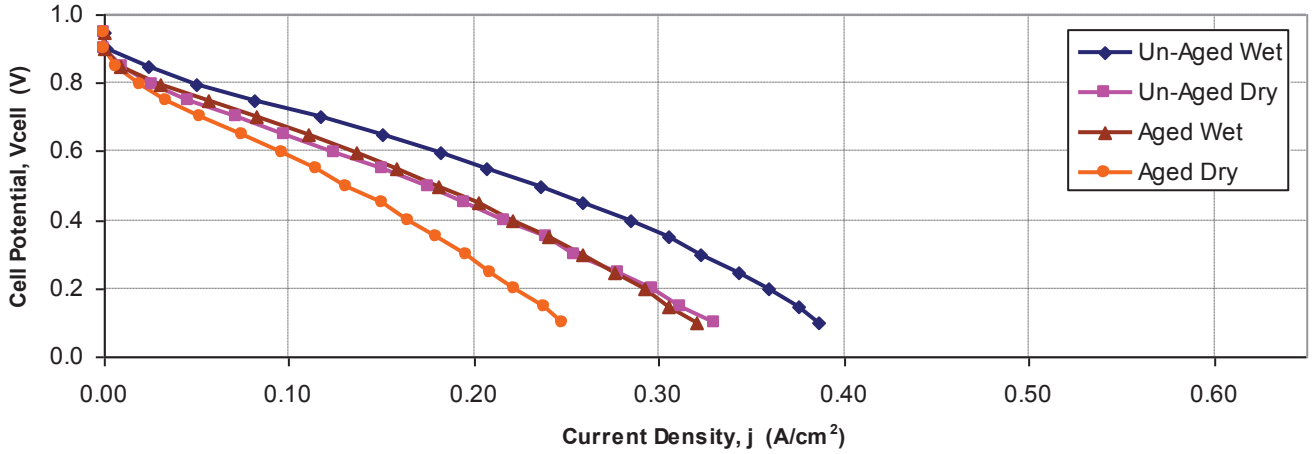

Figure A-15. Polarization data for design point 8 (15% PTFE**,** 4mg/cm^2, 1100psi Assy, 20psi Sinter)

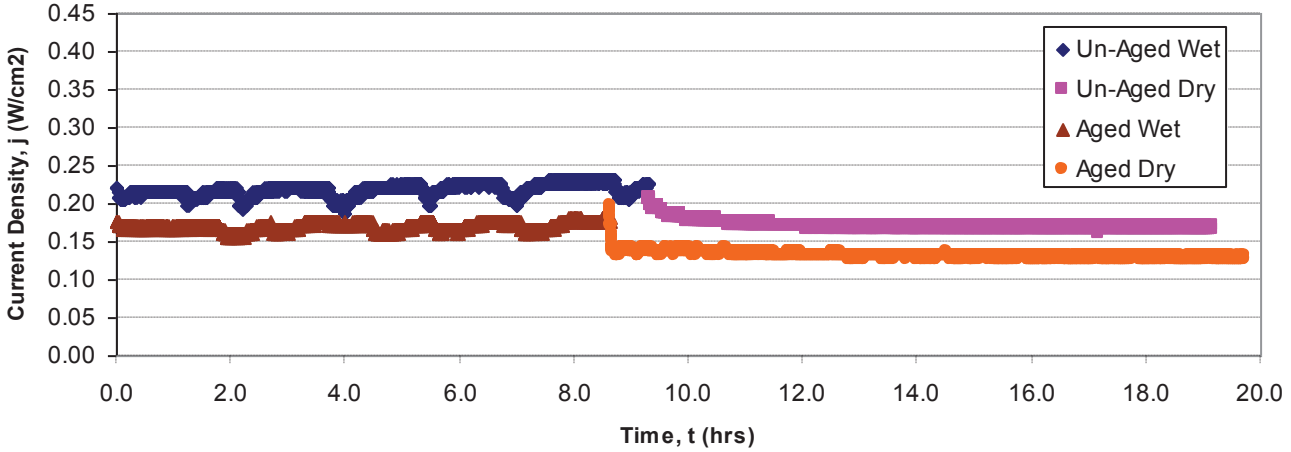

Figure A-16. Steady state data for design point 8 (15% PTFE**,** 4mg/cm^2, 1100psi Assy, 20psi Sinter)

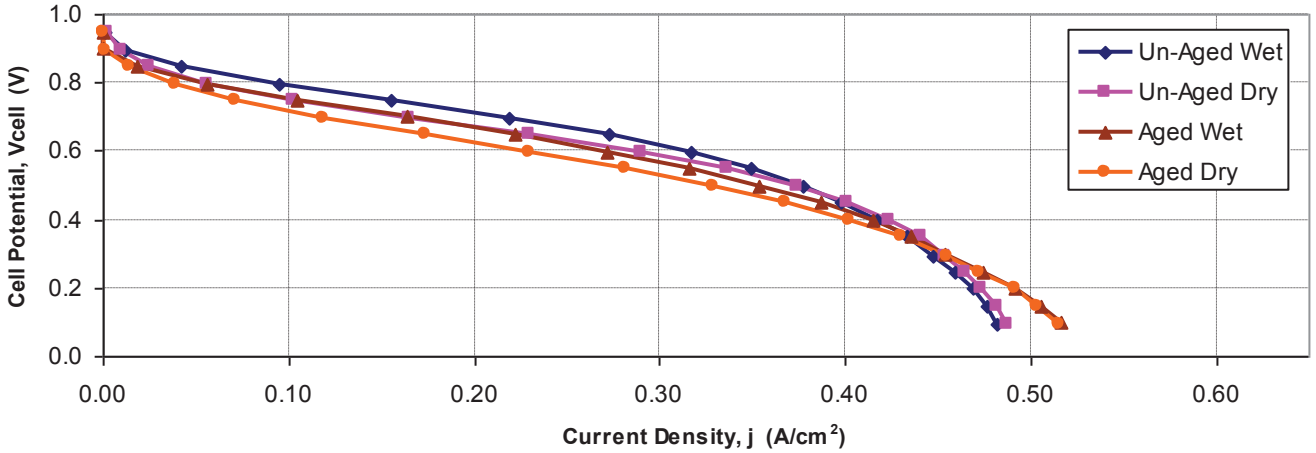

Figure A-17. Polarization data for design point 9 (25% PTFE, 3mg/cm^2, 850psi Assy, 10psi Sinter)

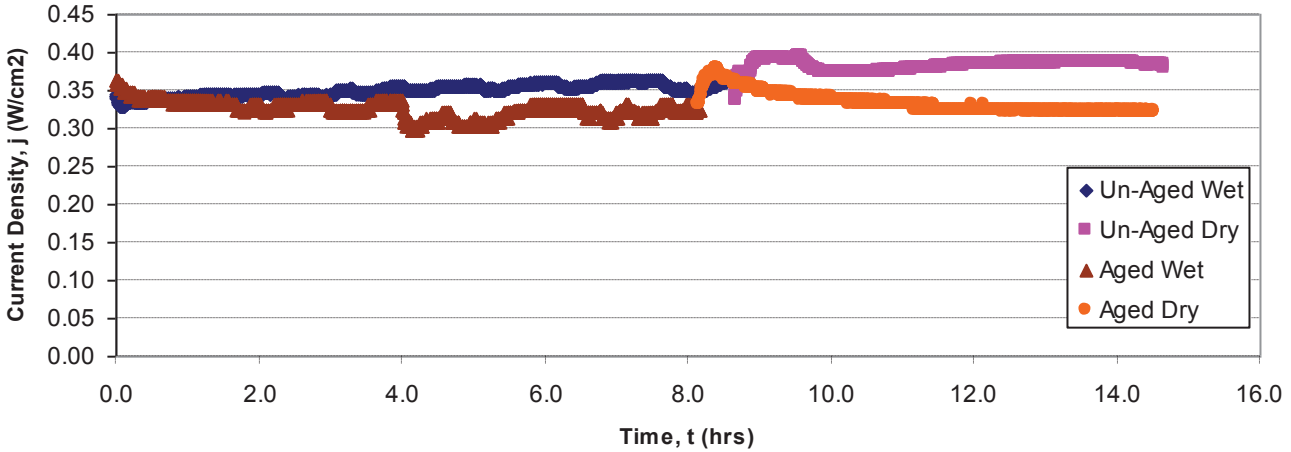

Figure A-18. Steady state data for design point 9 (25% PTFE, 3mg/cm^2, 850psi Assy, 10psi Sinter)

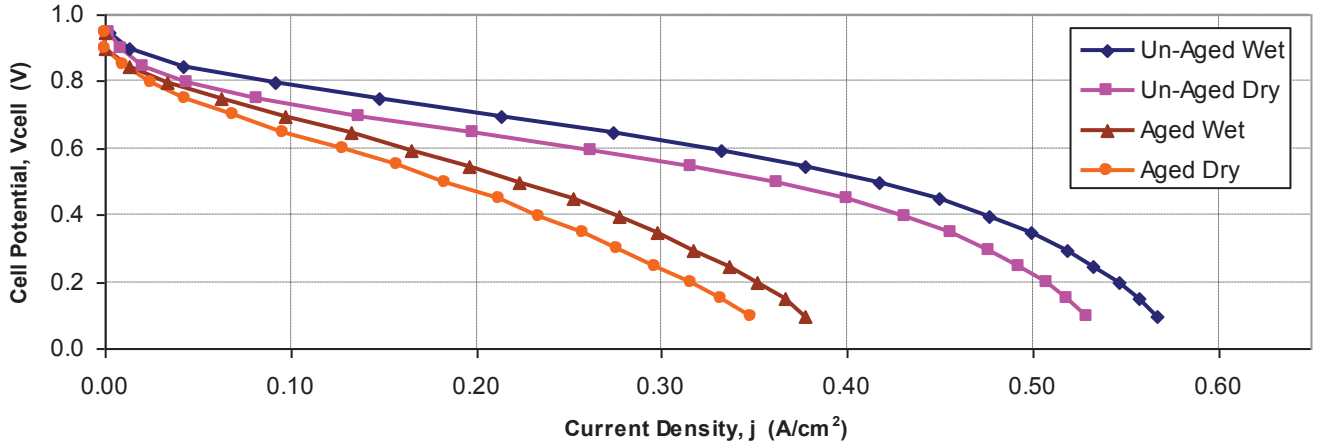

Figure A-19. Polarization data for design point 10 (15% PTFE**,** 4mg/cm^2, 600psi Assy, 40psi Sinter)

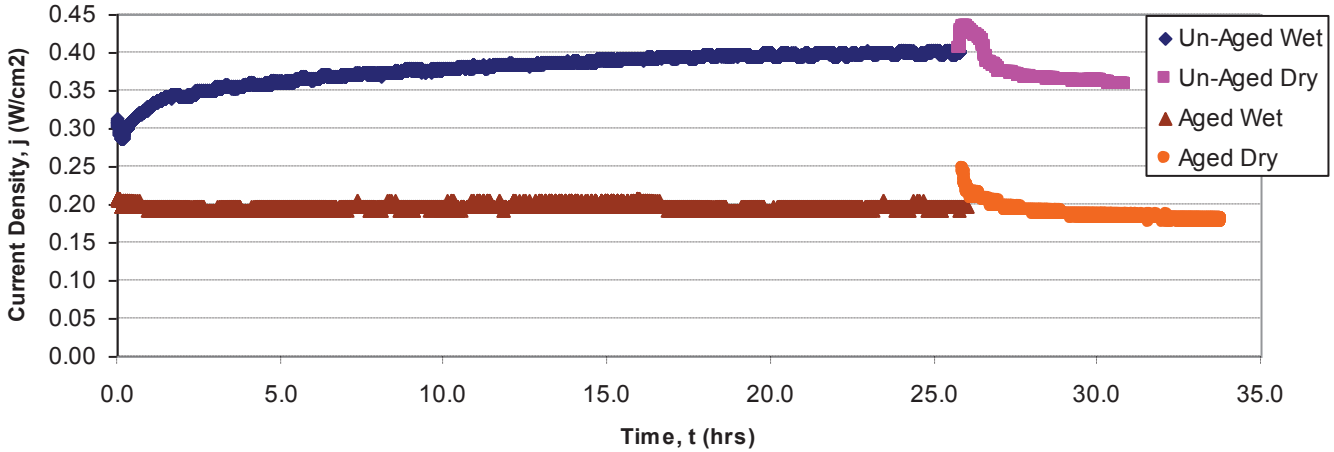

Figure A-20. Steady state data for design point 10 (15% PTFE**,** 4mg/cm^2, 600psi Assy, 40psi Sinter)

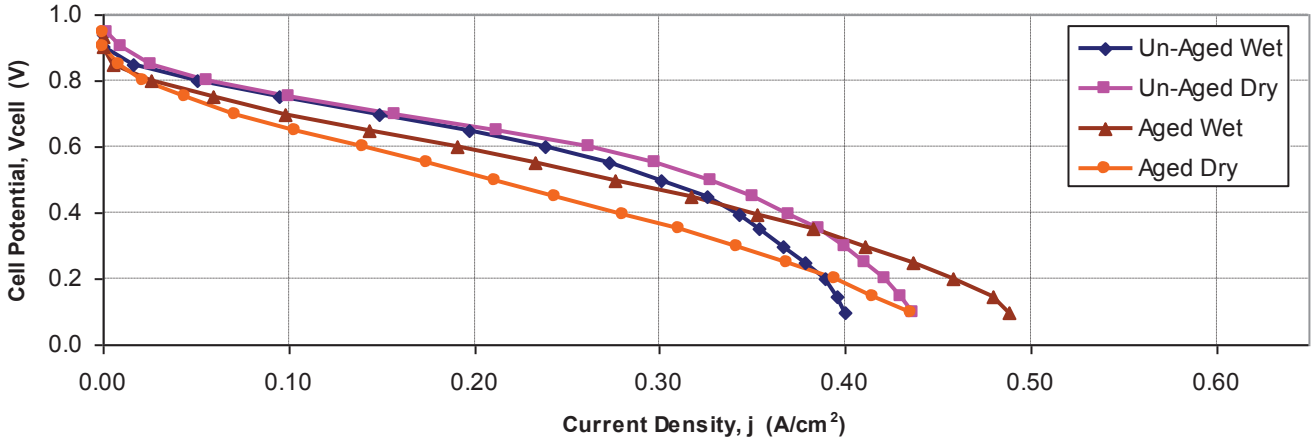

Figure A-21. Polarization data for design point 11 (35% PTFE, 4mg/cm^2, 600psi Assy, 20psi Sinter)

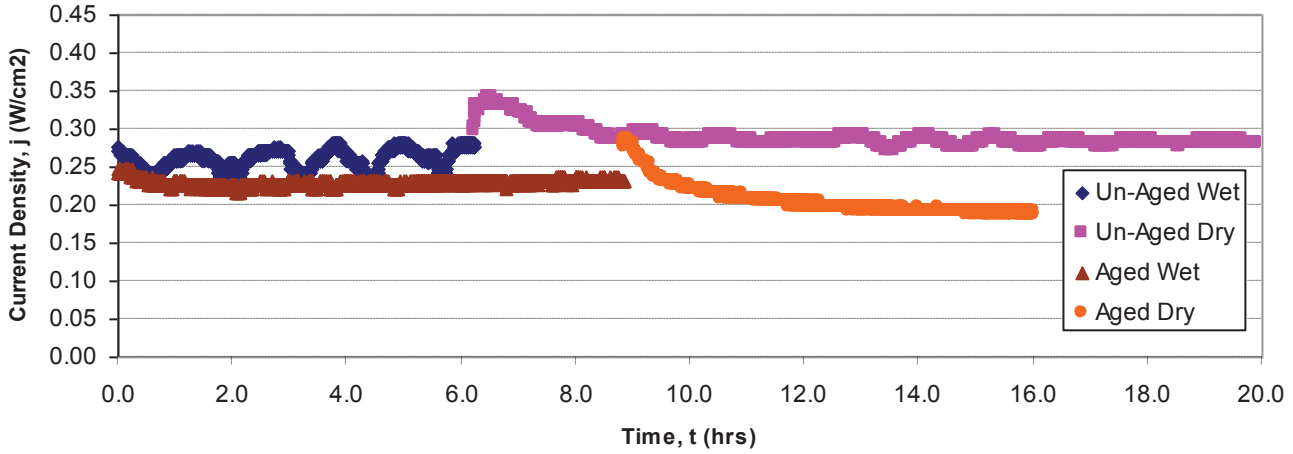

Figure A-22. Steady state data for design point 11 (35% PTFE, 4mg/cm^2, 600psi Assy, 20psi Sinter)

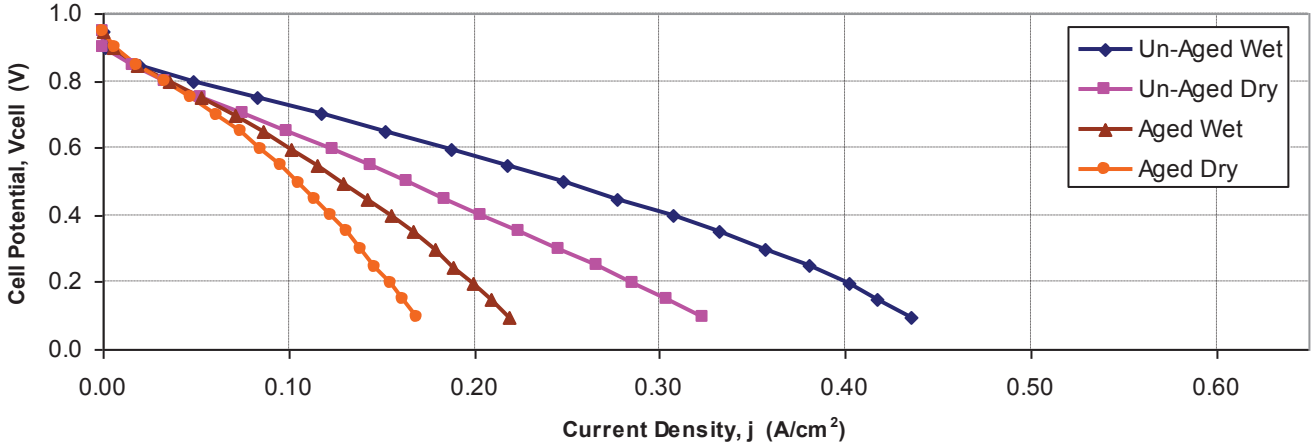

Figure A-23. Polarization data for design point 12 (15% PTFE, 4mg/cm^2, 600psi Assy, 20psi Sinter)

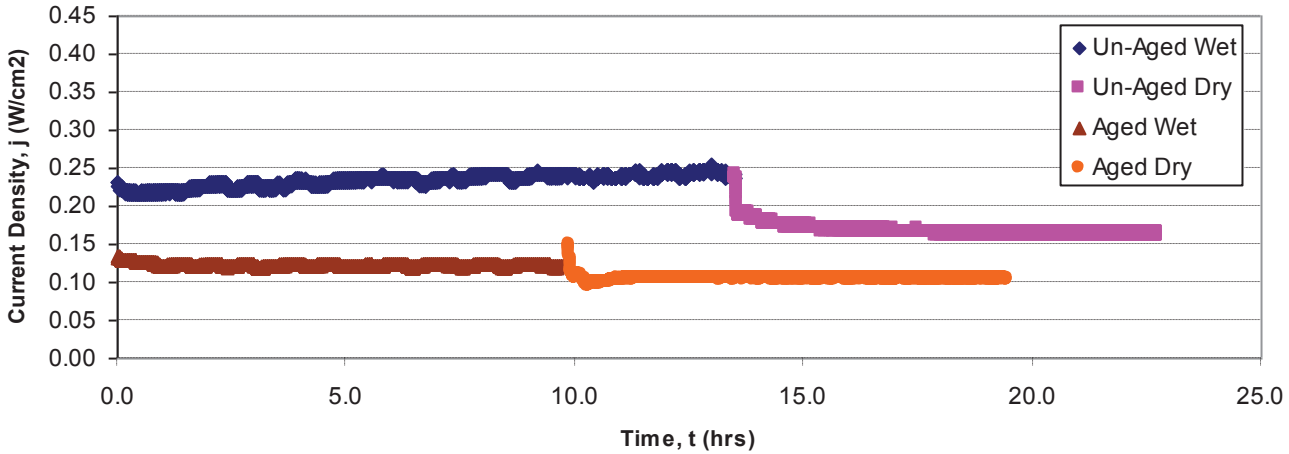

Figure A-24. Steady state data for design point 12 (15% PTFE, 4mg/cm^2, 600psi Assy, 20psi Sinter)

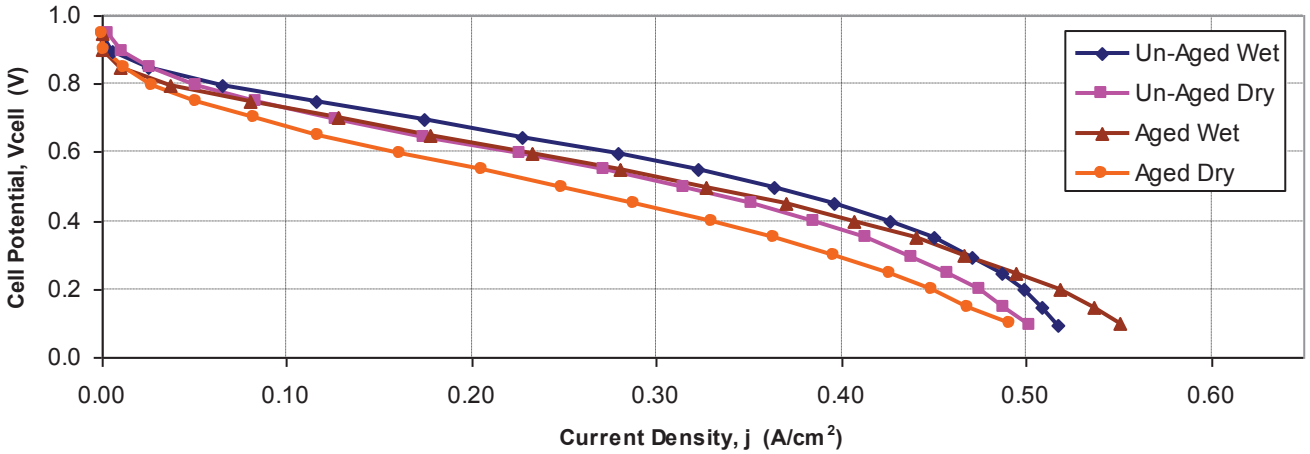

Figure A-25. Polarization data for design point 13 (25% PTFE**,** 3mg/cm^2, 850psi Assy, 30psi Sinter)

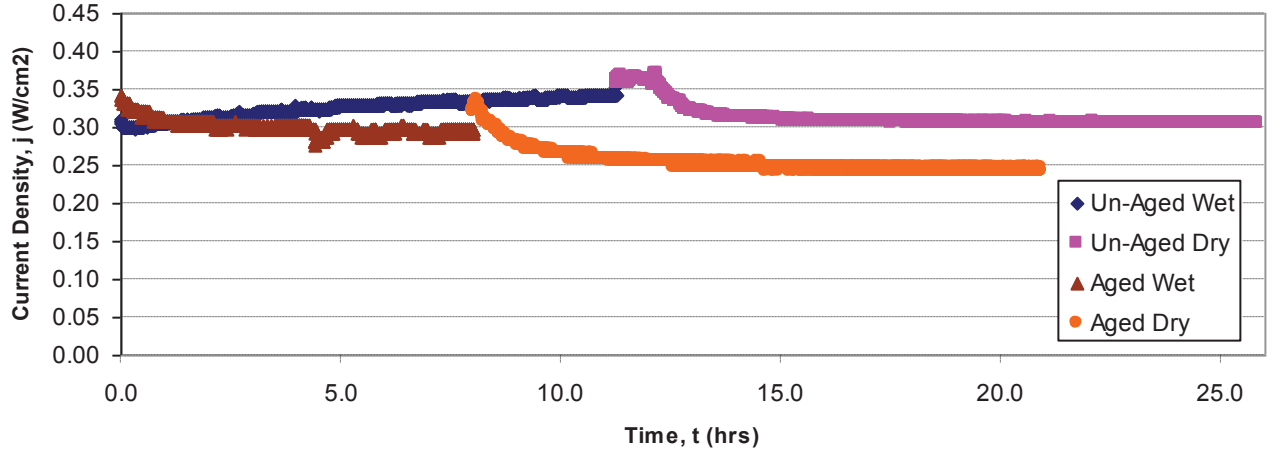

Figure A-26. Steady state data for design point 13 (25% PTFE**,** 3mg/cm^2, 850psi Assy, 30psi Sinter)

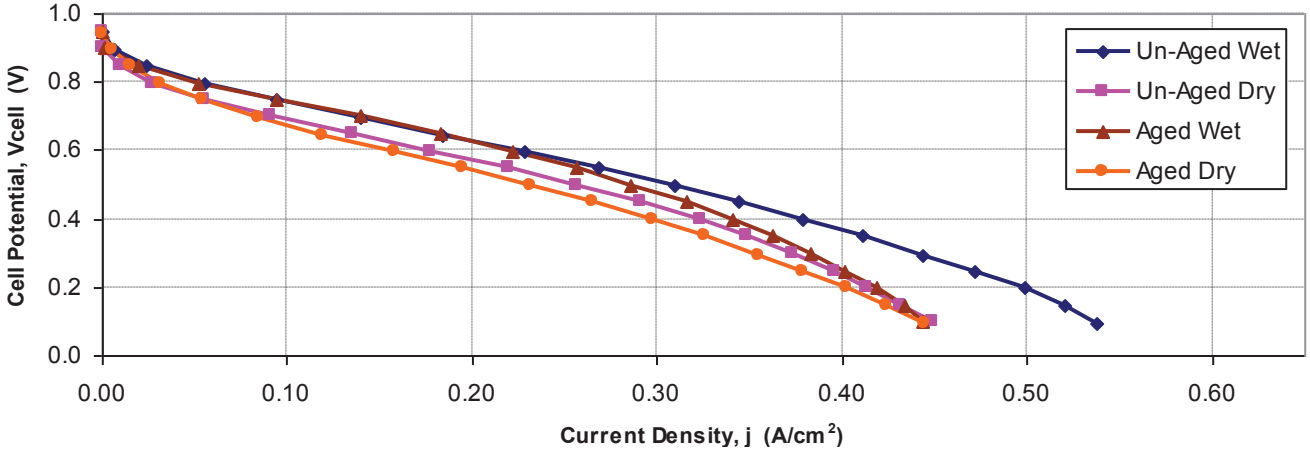

Figure A-27. Polarization data for design point 14 (35% PTFE, 2mg/cm^2, 600psi Assy, 20psi Sinter)

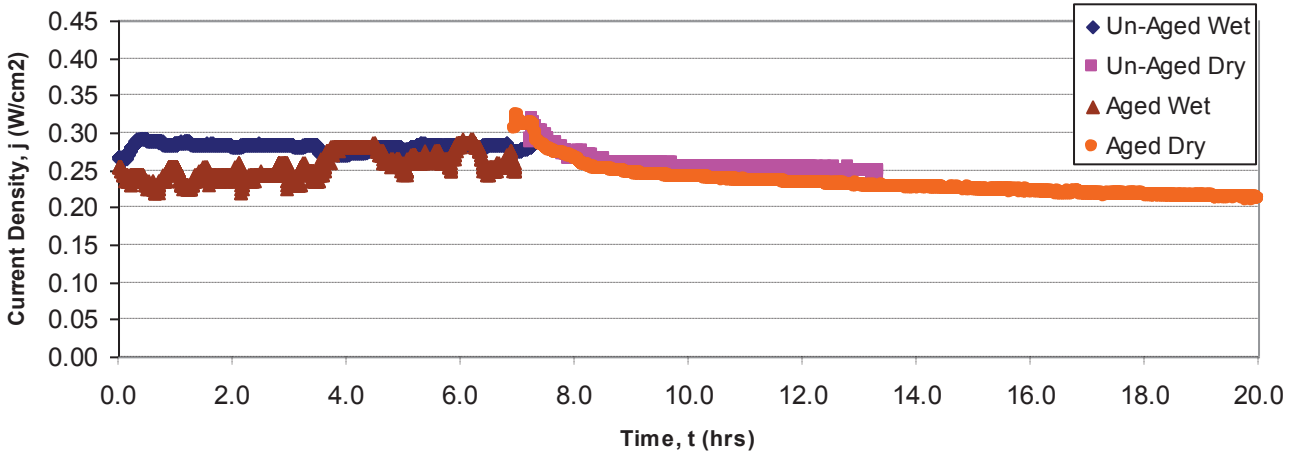

Figure A-28. Steady state data for design point 14 (35% PTFE, 2mg/cm^2, 600psi Assy, 20psi Sinter)

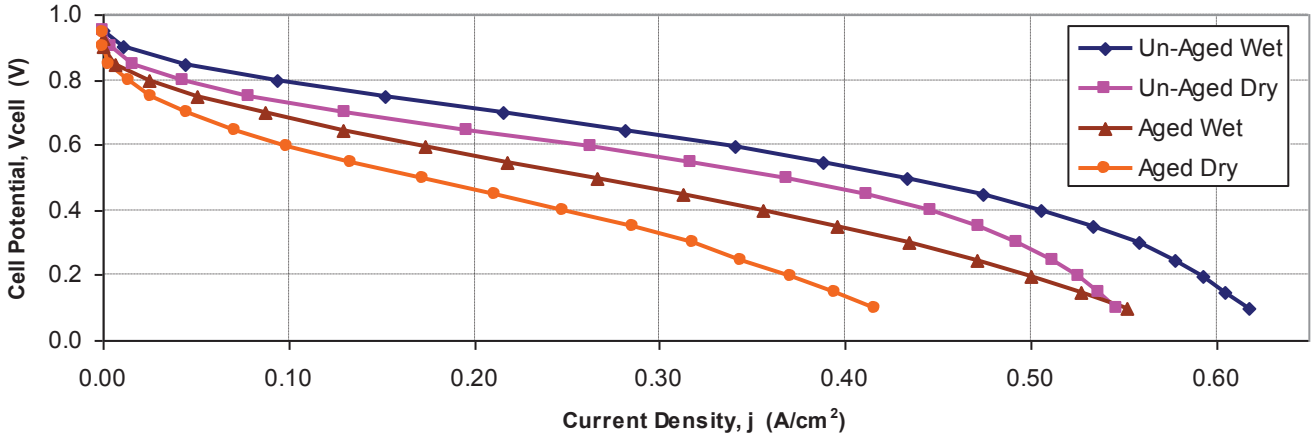

Figure A-29. Polarization data for design point 15 (25% PTFE, 3mg/cm^2, 850psi Assy, 30psi Sinter)

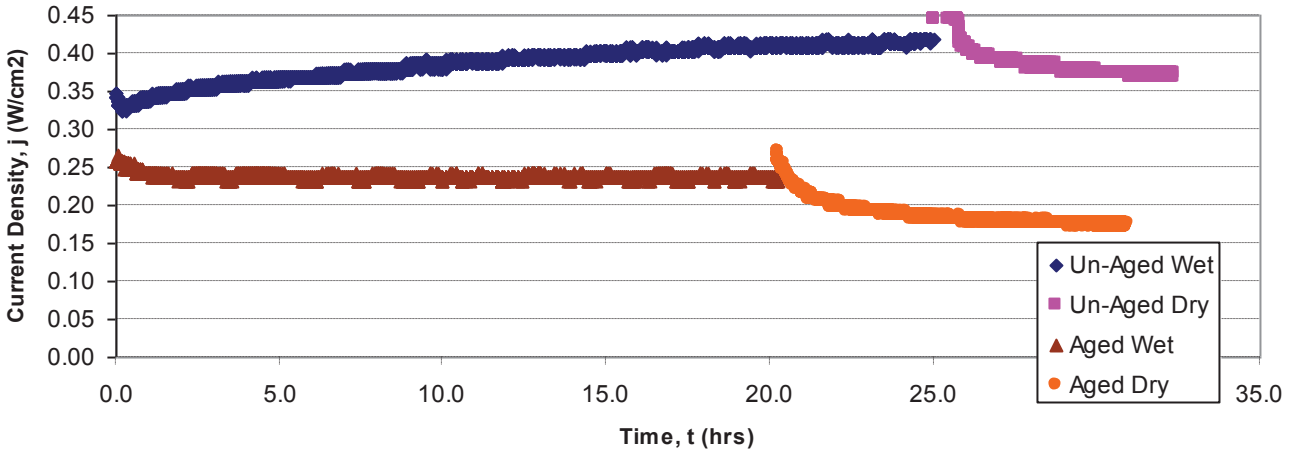

Figure A-30. Steady state data for design point 15 (25% PTFE, 3mg/cm^2, 850psi Assy, 30psi Sinter)

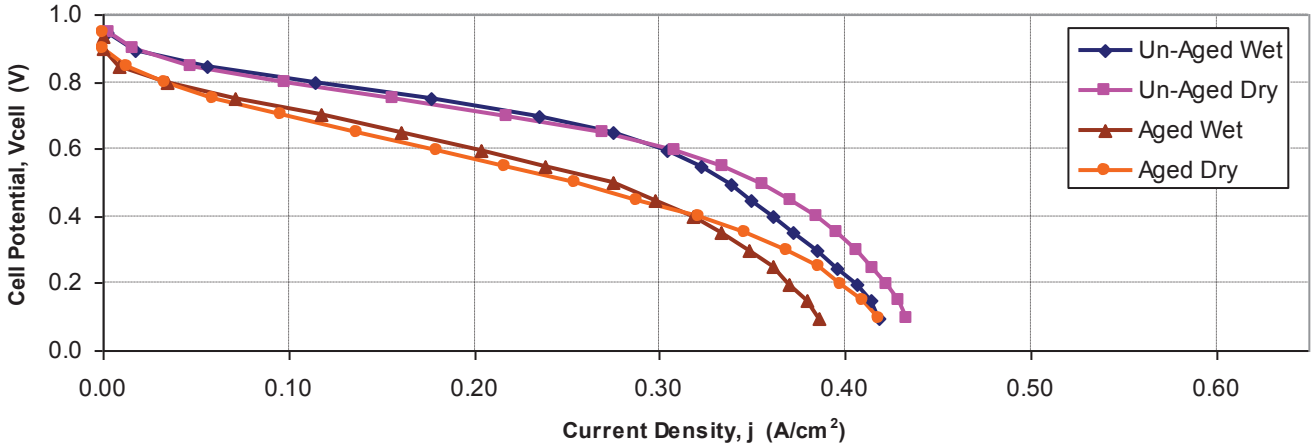

Figure A-31. Polarization data for design point 16 (25% PTFE, 3mg/cm^2, 850psi Assy, 30psi Sinter)

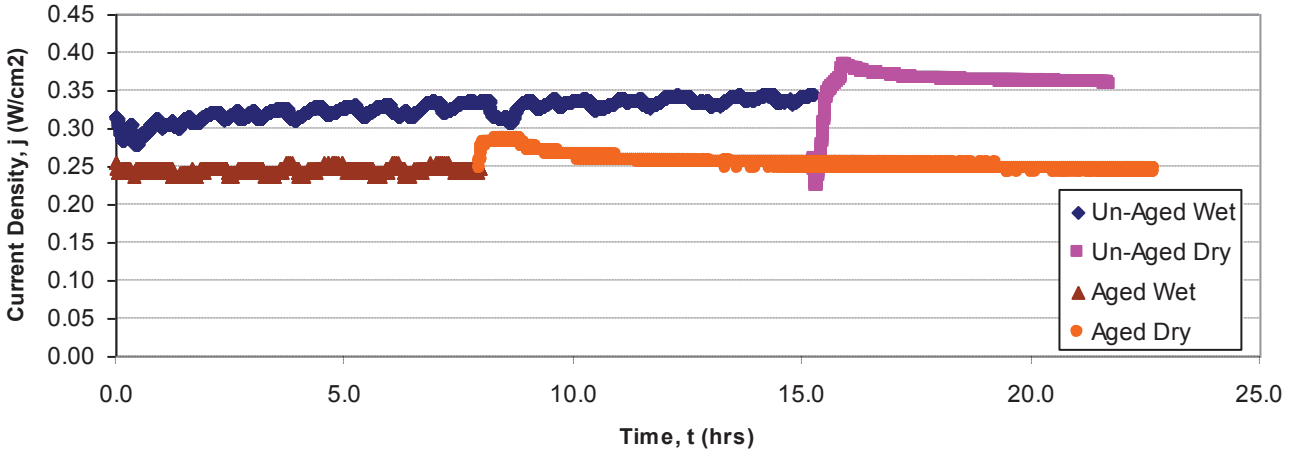

Figure A-32. Steady state data for design point 16 (25% PTFE, 3mg/cm^2, 850psi Assy, 30psi Sinter)

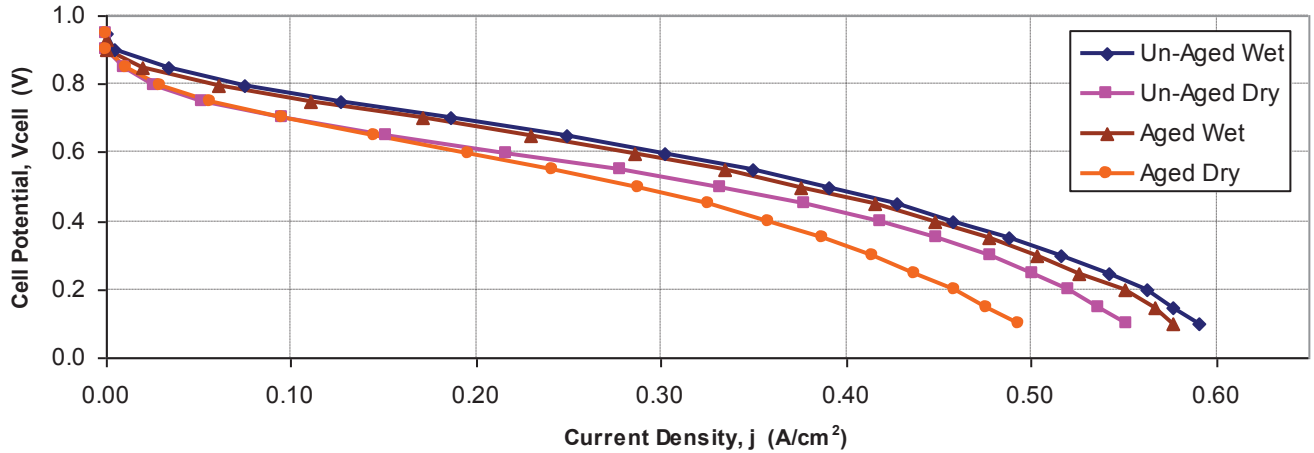

Figure A-33. Polarization data for design point 17 (25% PTFE, 3mg/cm^2, 850psi Assy, 30psi Sinter)

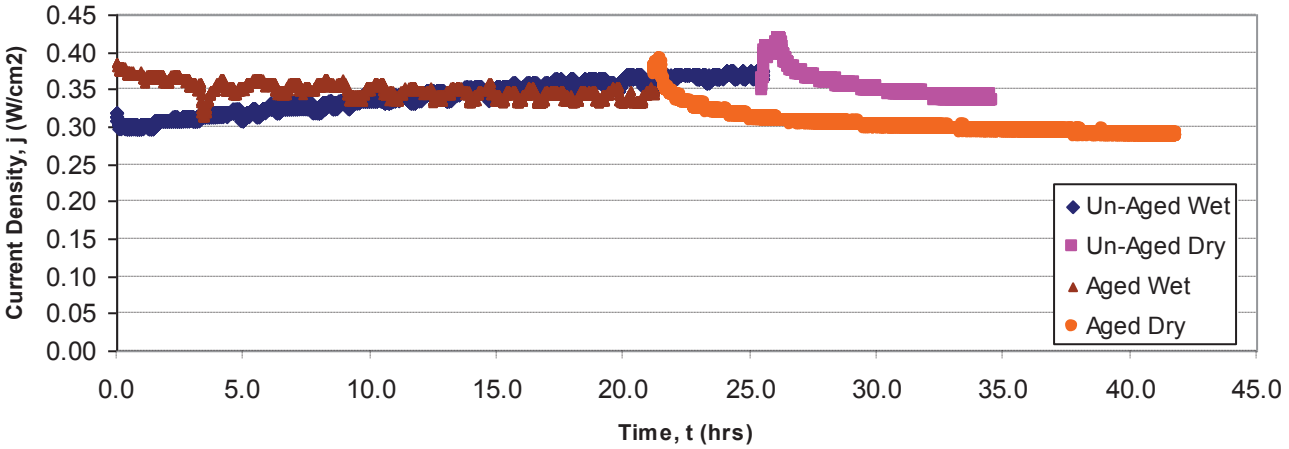

Figure A-34. Steady state data for design point 17 (25% PTFE, 3mg/cm^2, 850psi Assy, 30psi Sinter)

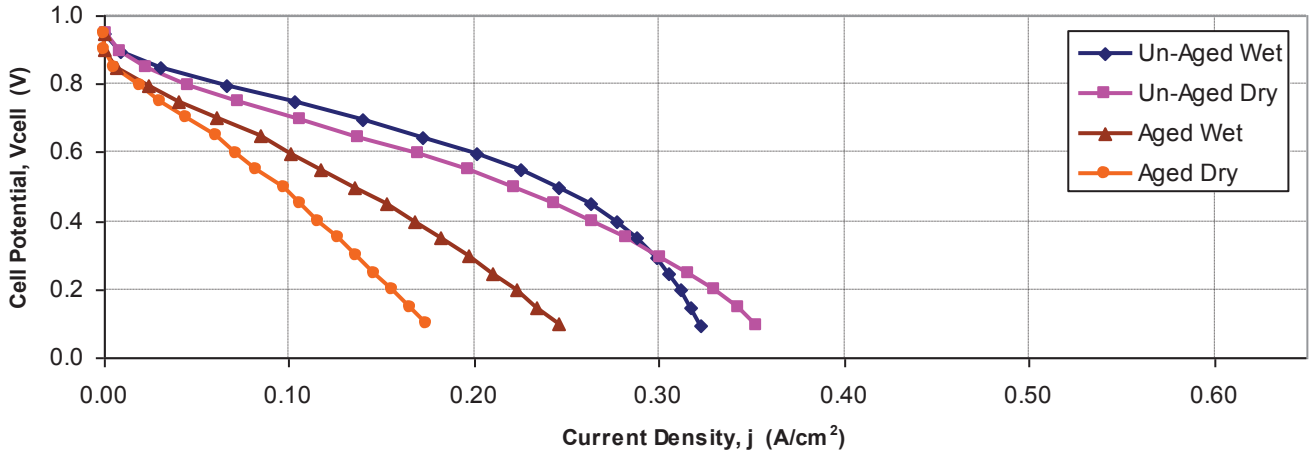

Figure A-35. Polarization data for design point 18 (15% PTFE, 4mg/cm^2, 1100psi Assy, 40psi Sinter)

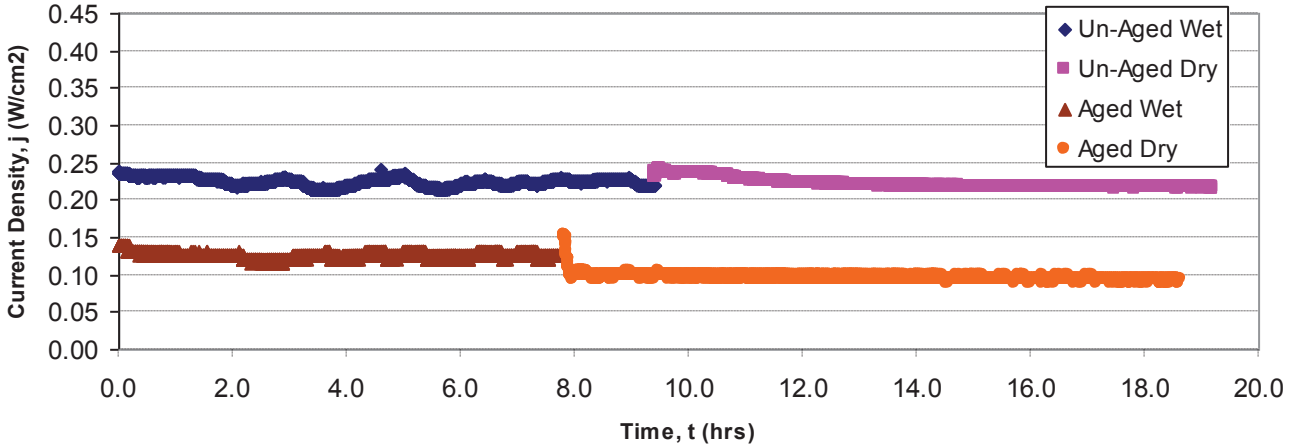

Figure A-36. Steady state data for design point 18 (15% PTFE, 4mg/cm^2, 1100psi Assy, 40psi Sinter)

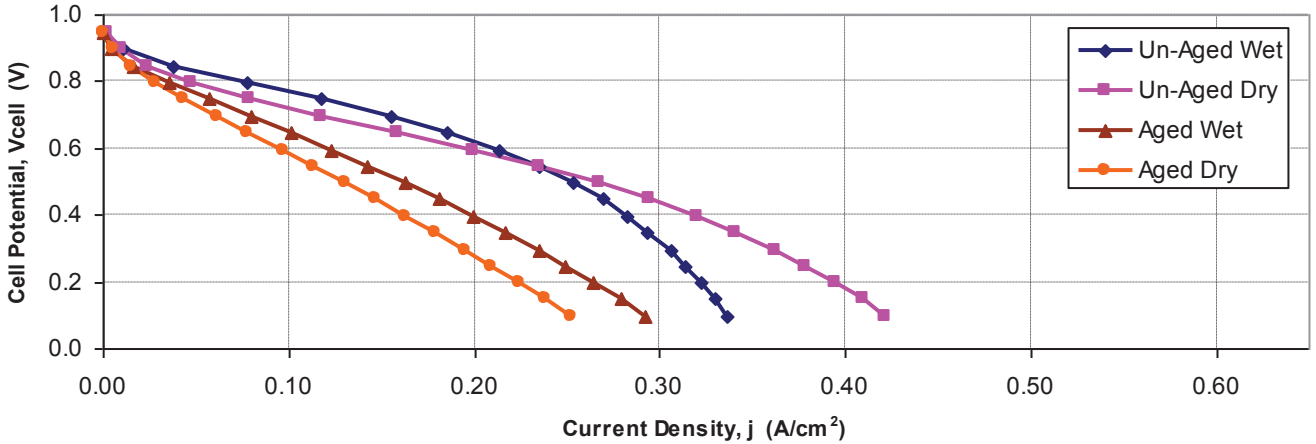

Figure A-37. Polarization data for design point 19 (15% PTFE**,** 2mg/cm^2, 600psi Assy, 20psi Sinter)

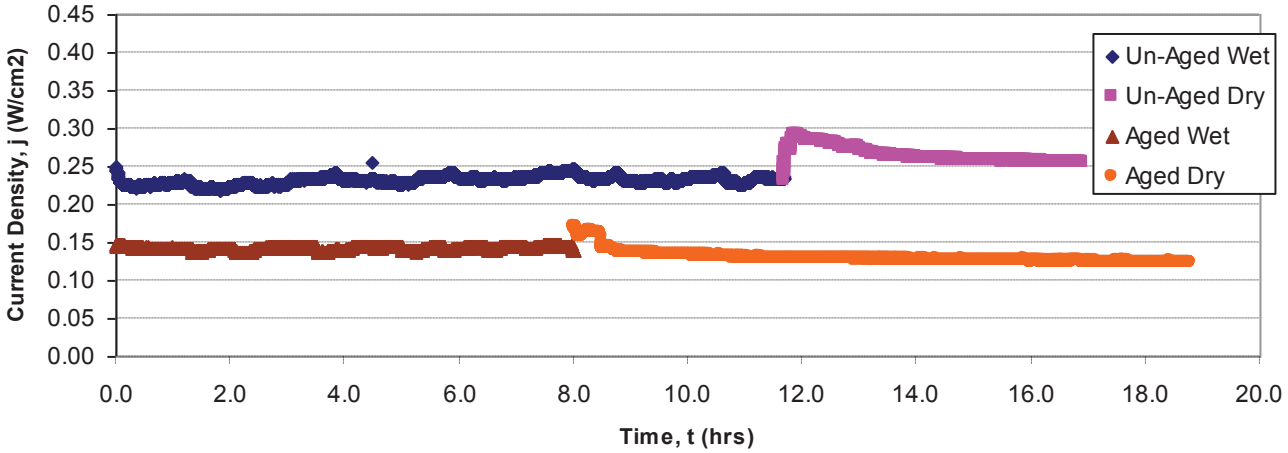

Figure A-38. Steady state data for design point 19 (15% PTFE**,** 2mg/cm^2, 600psi Assy, 20psi Sinter)

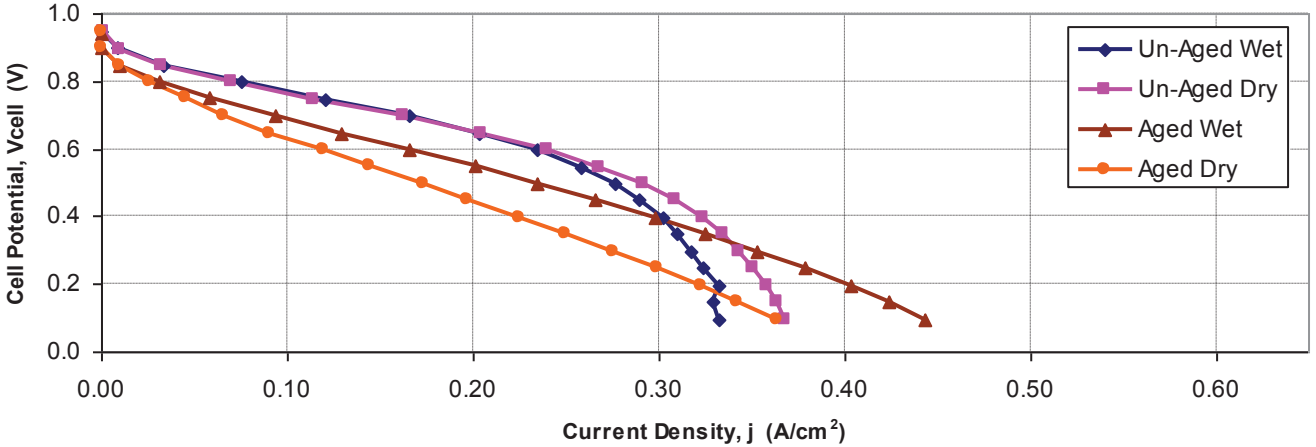

Figure A-39. Polarization data for design point 20 (35% PTFE, 2mg/cm^2, 1100psi Assy, 40psi Sinter)

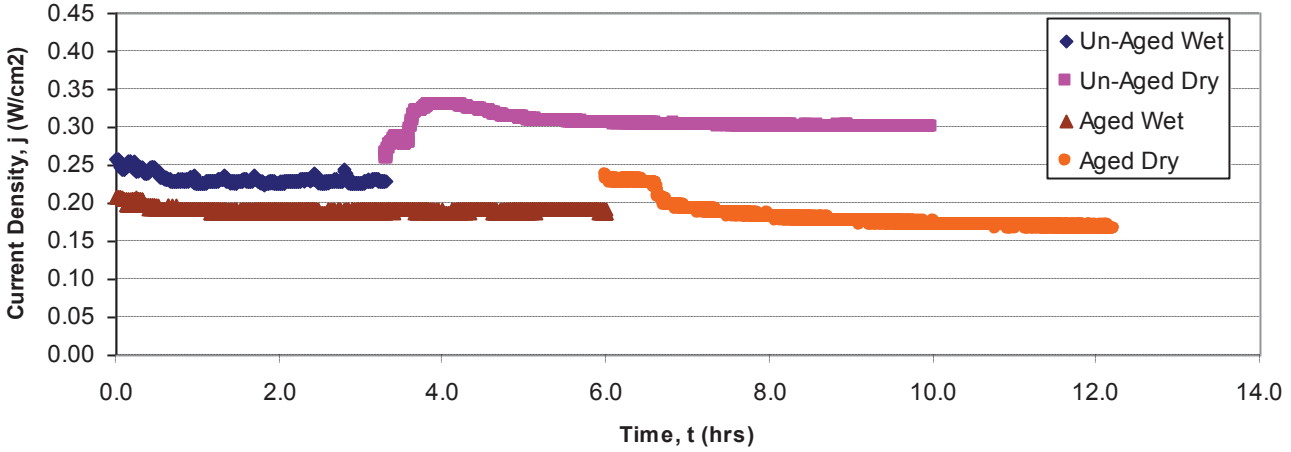

Figure A-40. Steady state data for design point 20 (35% PTFE, 2mg/cm^2, 1100psi Assy, 40psi Sinter)

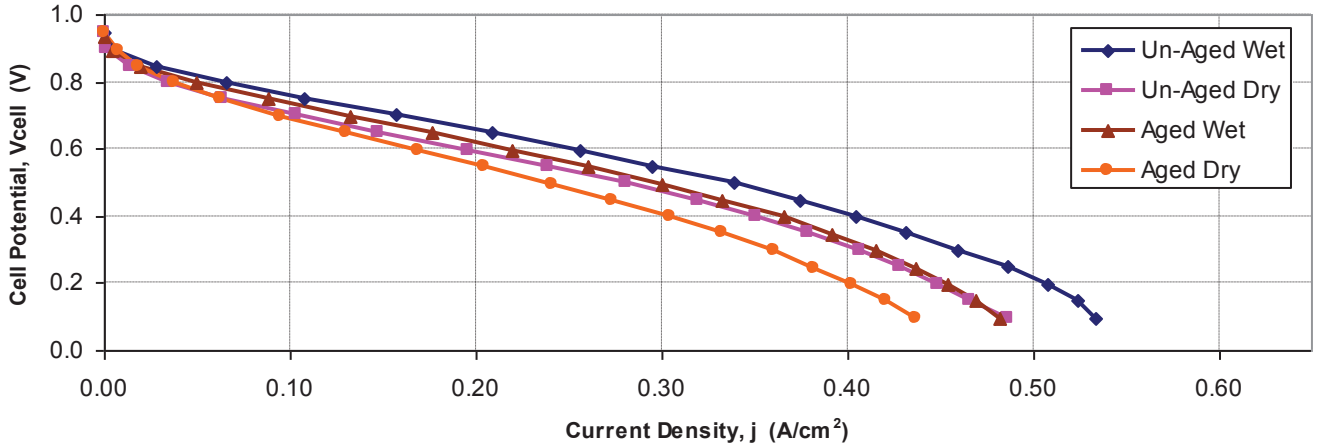

Figure A-41. Polarization data for design point 21 (35% PTFE**,** 2mg/cm^2, 1100psi Assy, 20psi Sinter)

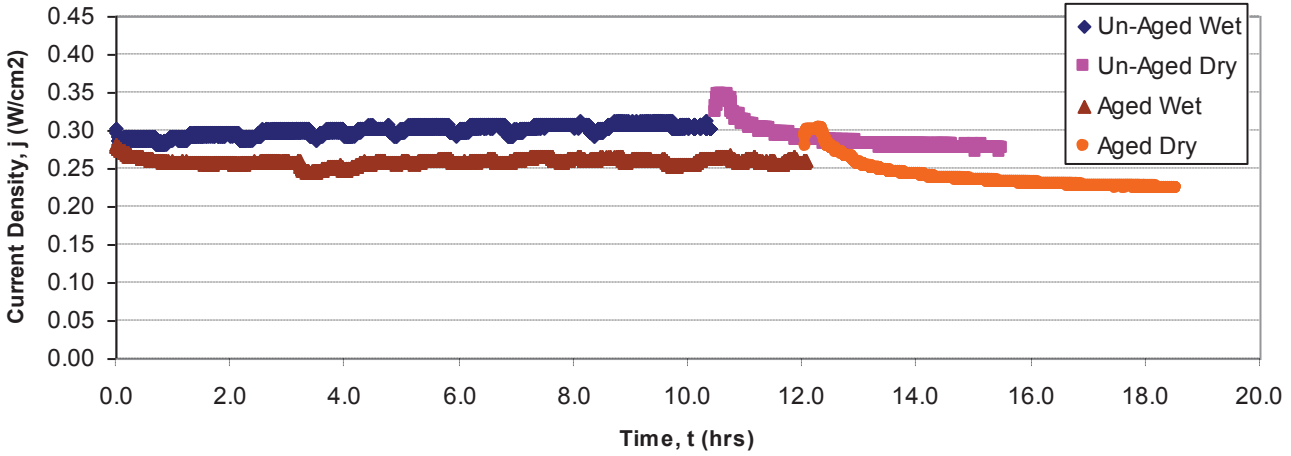

A-42. Steady state data for design point 21 (35% PTFE**,** 2mg/cm^2, 1100psi Assy, 20psi Sinter)

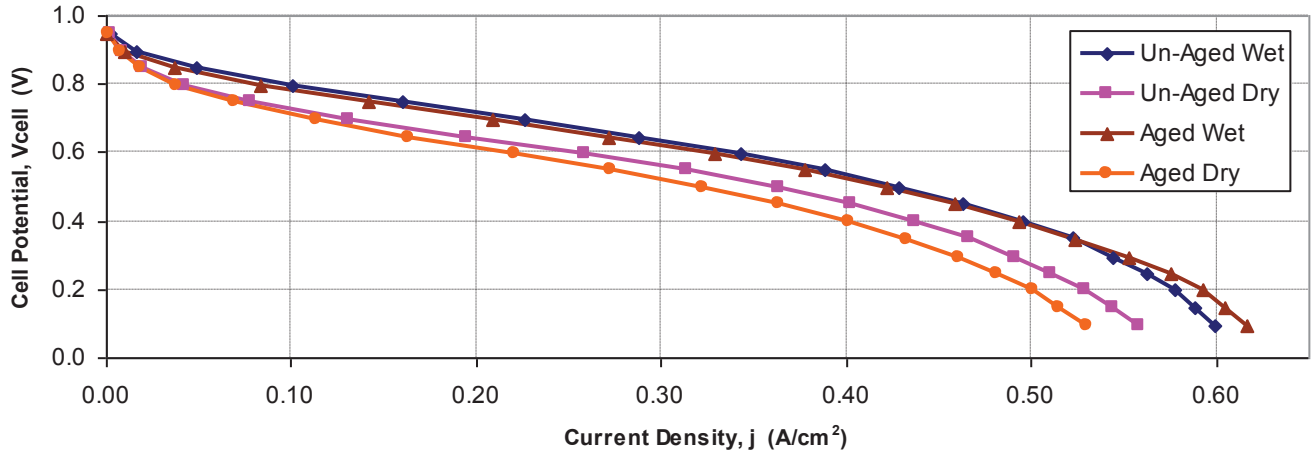

Figure A-43. Polarization data for design point 22 (45% PTFE, 3mg/cm^2, 850psi Assy, 30psi Sinter)

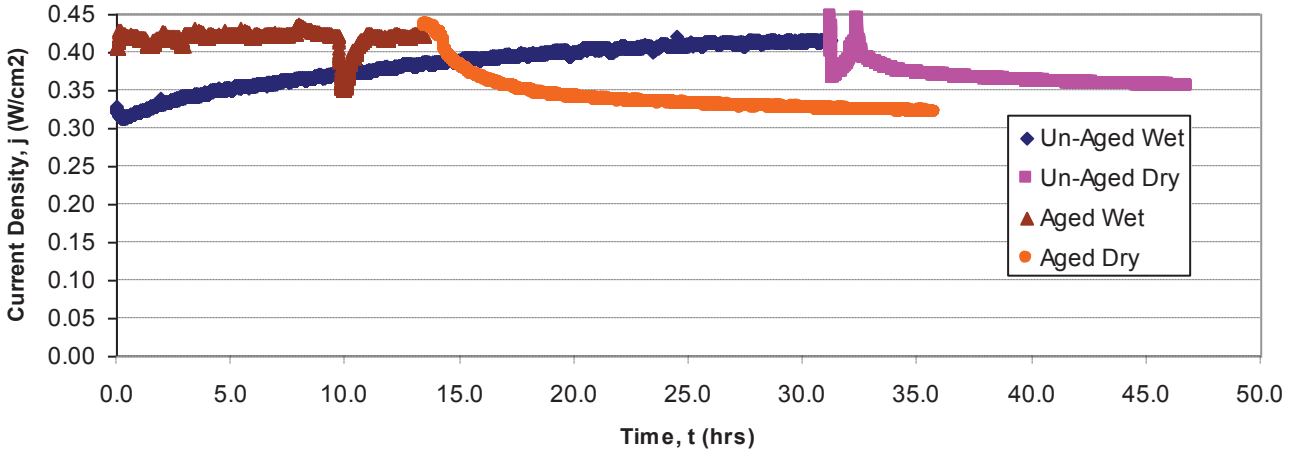

Figure A-44. Steady state data for design point 22 (45% PTFE, 3mg/cm^2, 850psi Assy, 30psi Sinter)

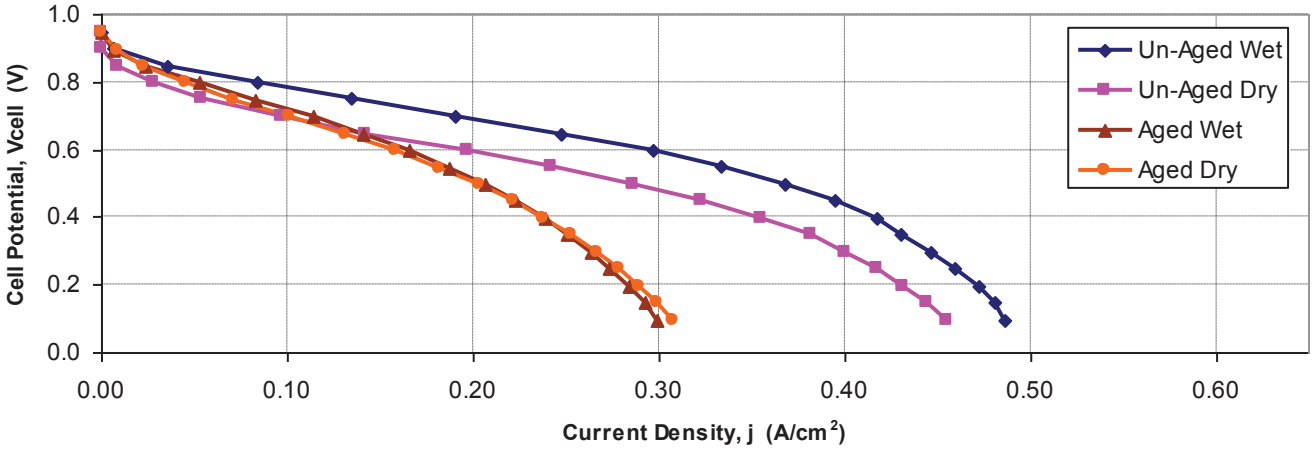

Figure A-45. Polarization data for design point 23 (25% PTFE**,** 5mg/cm^2, 850psi Assy, 30psi Sinter)

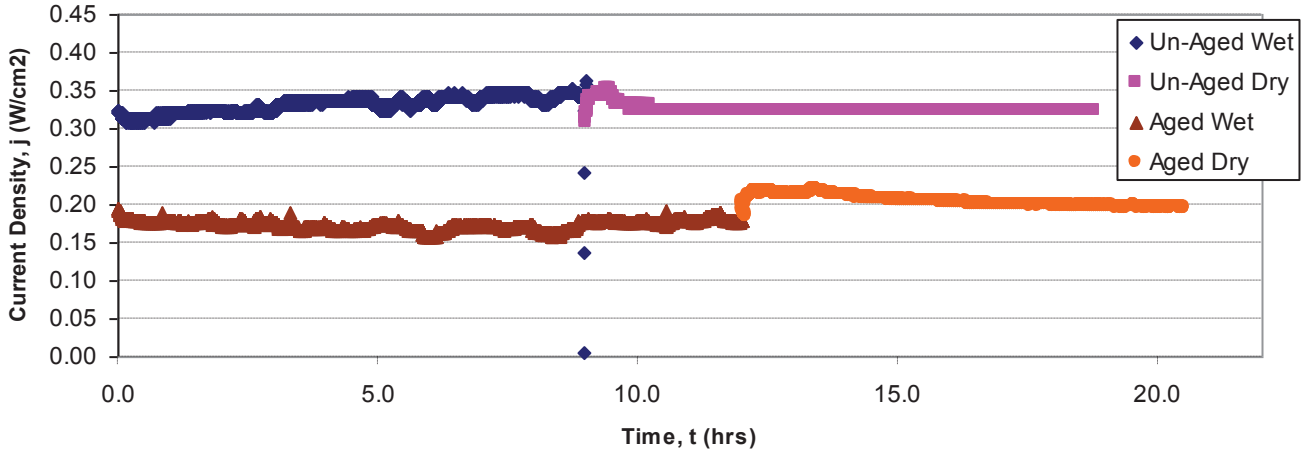

Figure A-46. Steady state data for design point 23 (25% PTFE**,** 5mg/cm^2, 850psi Assy, 30psi Sinter)

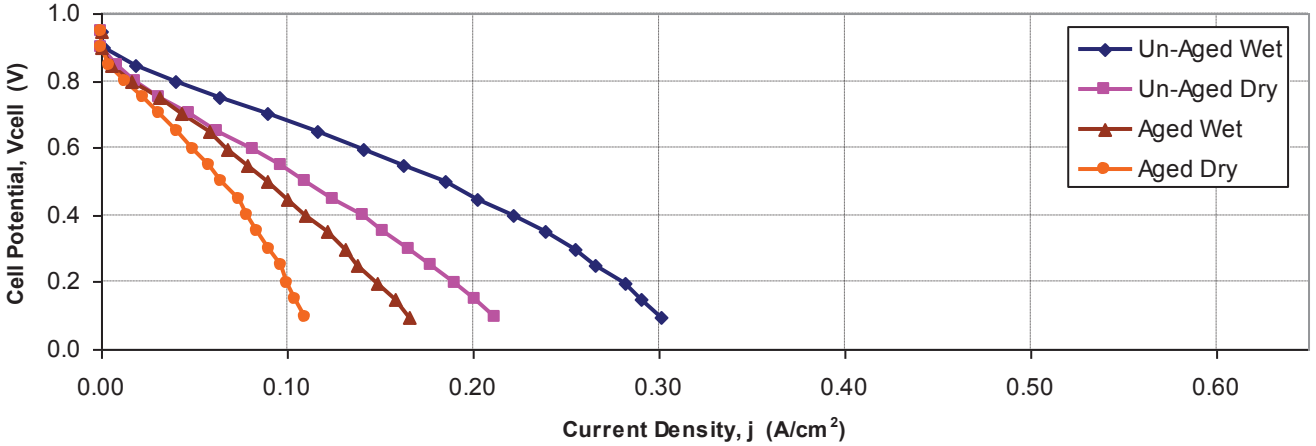

Figure A-47. Polarization data for design point 24 (15% PTFE, 2mg/cm^2, 600psi Assy, 40psi Sinter)

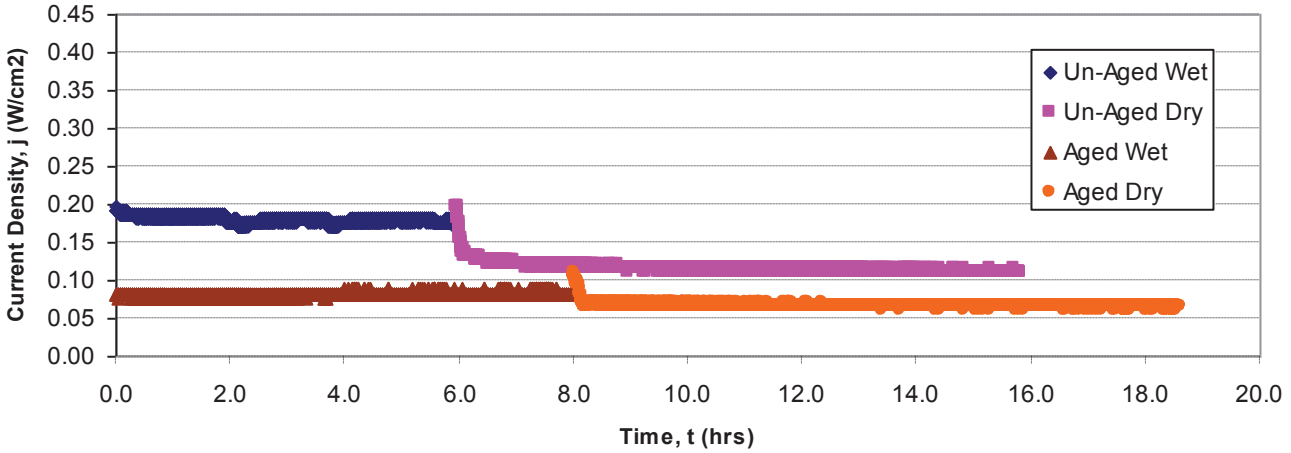

Figure A-48. Steady state data for design point 24 (15% PTFE, 2mg/cm^2, 600psi Assy, 40psi Sinter)

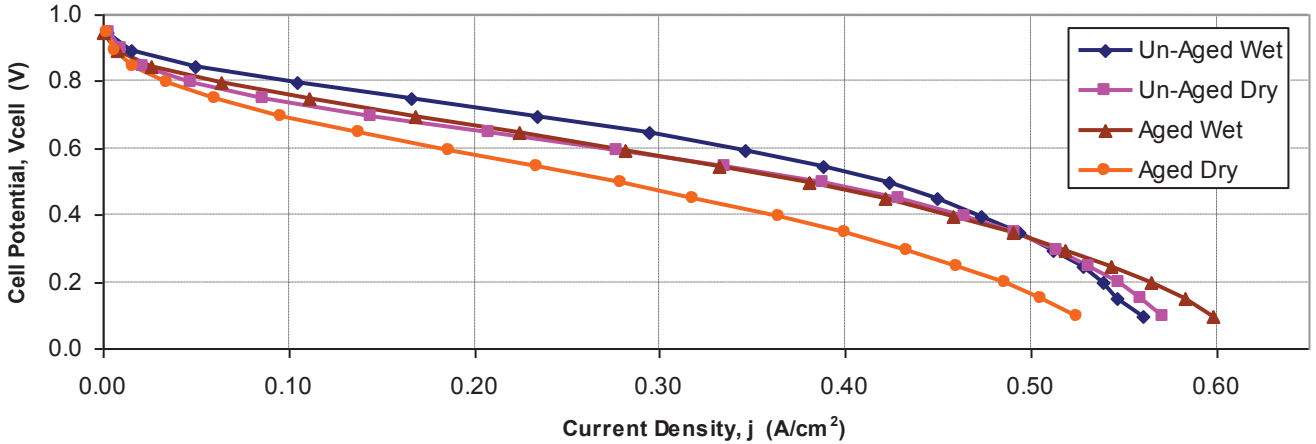

Figure A-49. Polarization data for design point 25 (25% PTFE, 3mg/cm^2, 850psi Assy, 30psi Sinter)

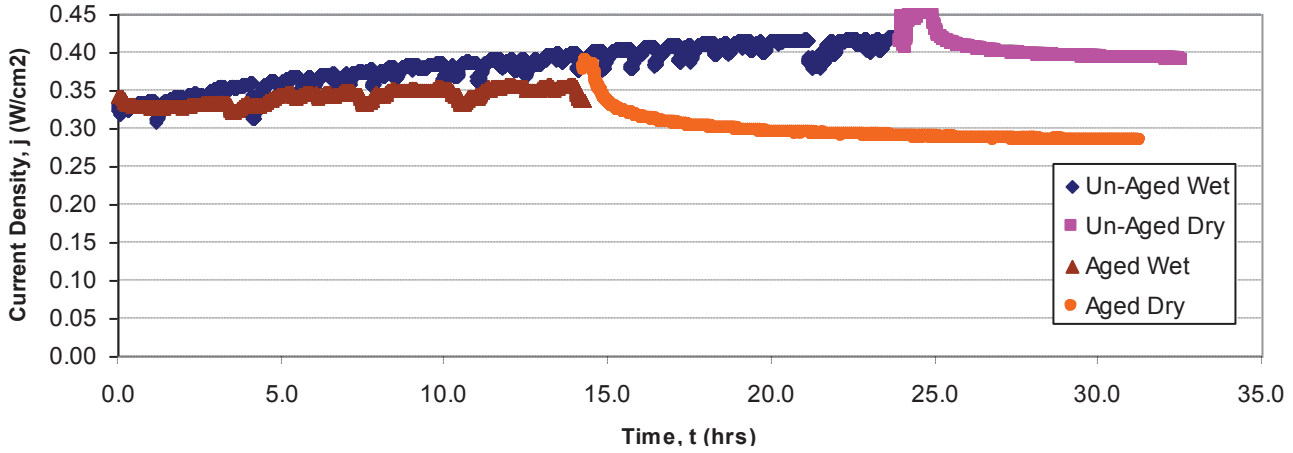

Figure A-50. Steady state data for design point 25 (25% PTFE, 3mg/cm^2, 850psi Assy, 30psi Sinter)

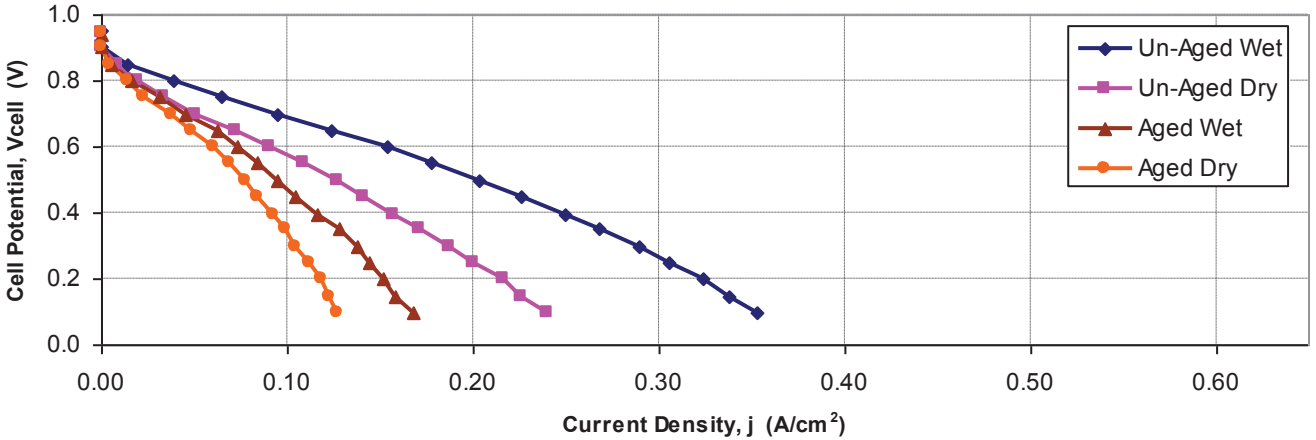

Figure A-51. Polarization data for design point 26 (15% PTFE, 2mg/cm^2, 1100psi Assy, 40psi Sinter)

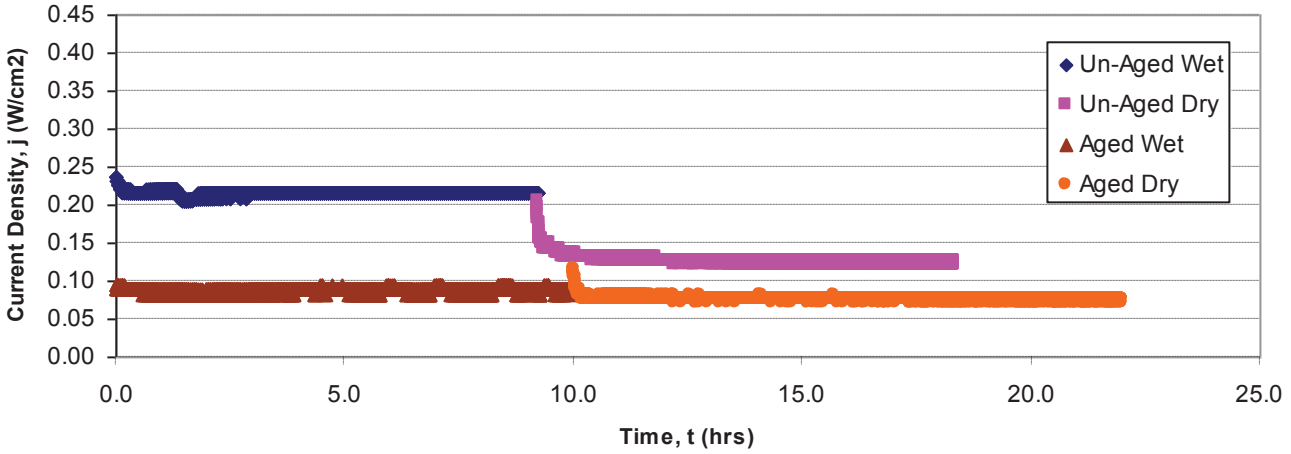

Figure A-52. Steady state data for design point 26 (15% PTFE, 2mg/cm^2, 1100psi Assy, 40psi Sinter)

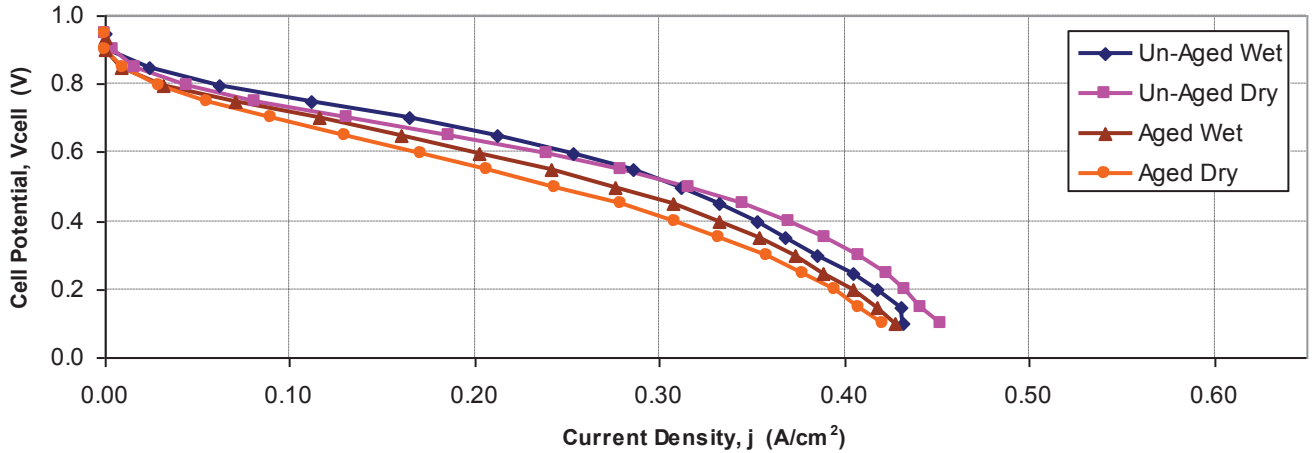

Figure A-53. Polarization data for design point 27 (35% PTFE, 4mg/cm^2, 1100psi Assy, 40psi Sinter)

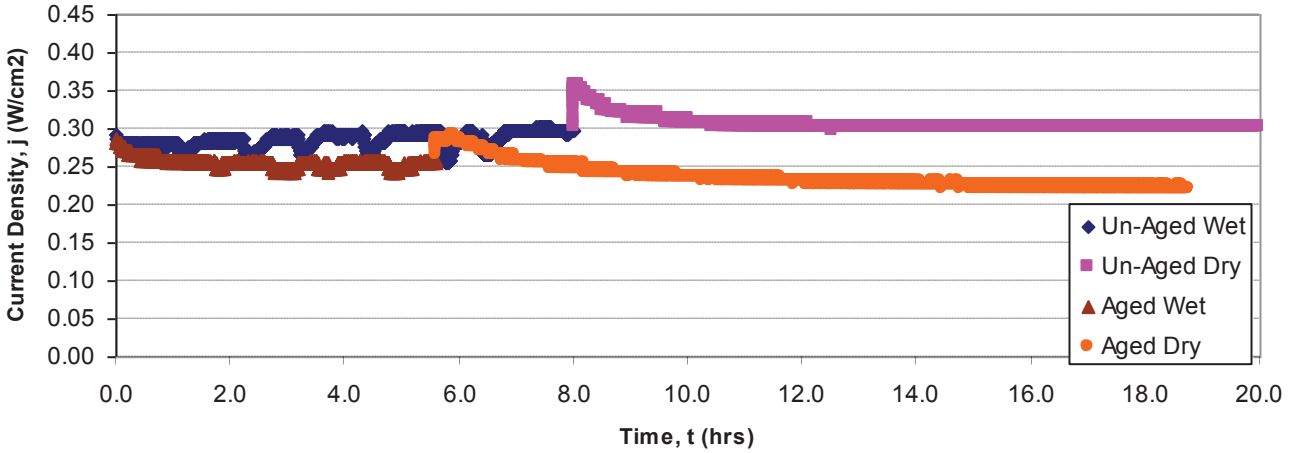

Figure A-54. Steady state data for design point 27 (35% PTFE, 4mg/cm^2, 1100psi Assy, 40psi Sinter)

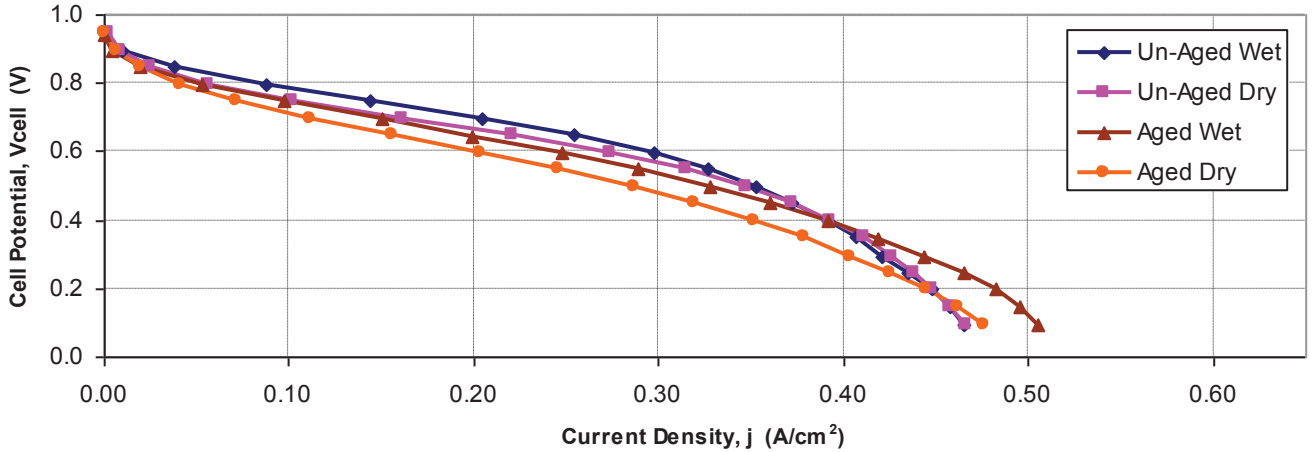

Figure A-55. Polarization data for design point 28 (35% PTFE**,** 4mg/cm^2, 600psi Assy, 40psi Sinter)

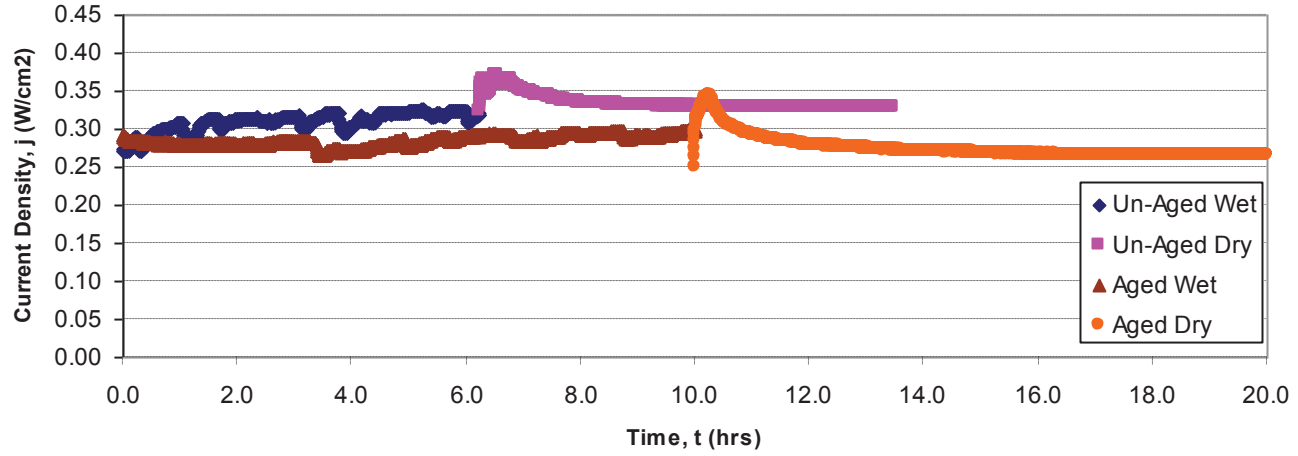

Figure A-56. Steady state data for design point 28 (35% PTFE**,** 4mg/cm^2, 600psi Assy, 40psi Sinter)

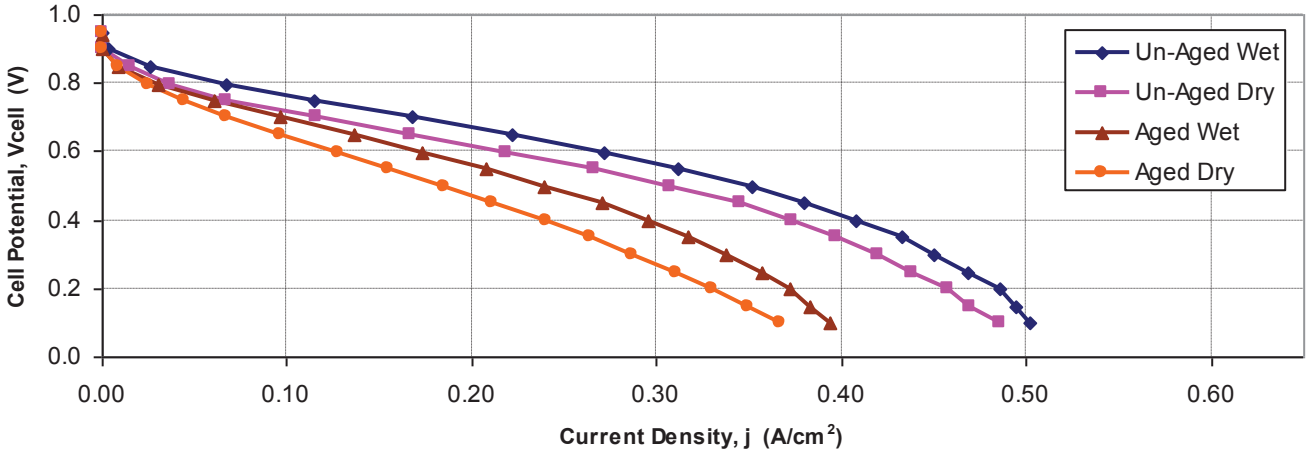

Figure A-57. Polarization data for design point 29 (25% PTFE**,** 3mg/cm^2, 350psi Assy, 30psi Sinter)

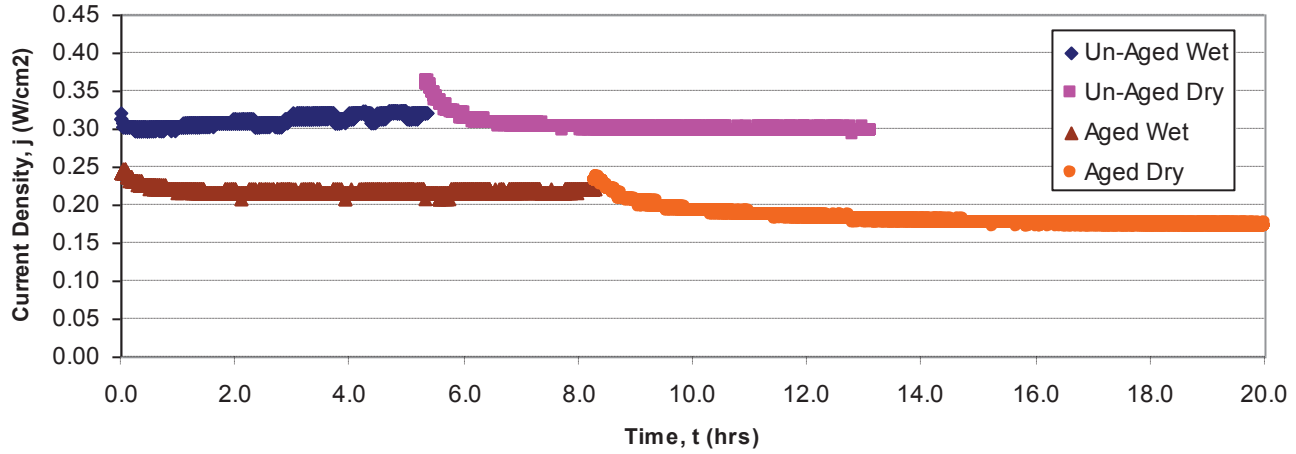

Figure A-58. Steady state data for design point 29 (25% PTFE**,** 3mg/cm^2, 350psi Assy, 30psi Sinter)

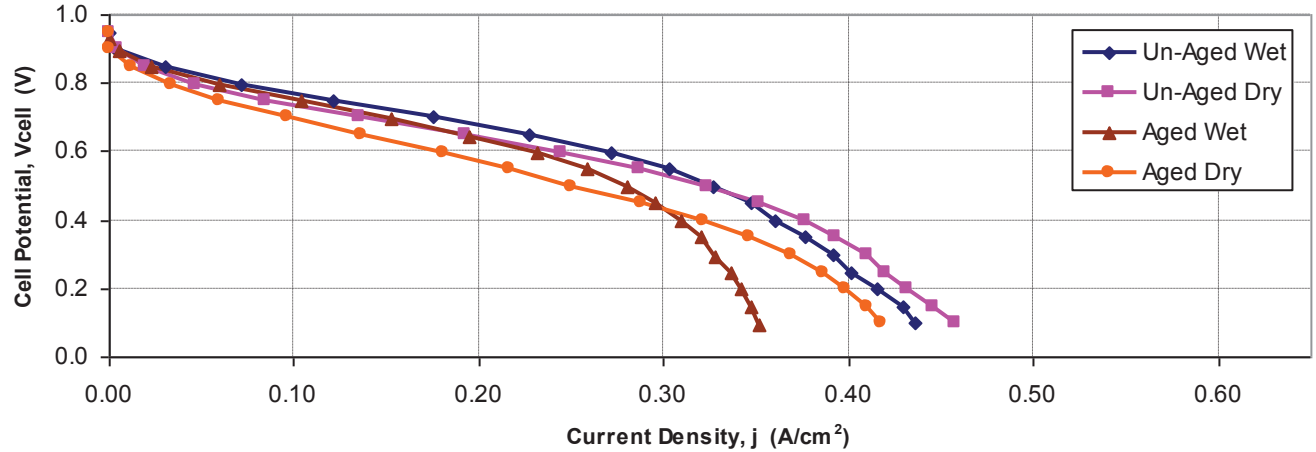

Figure A-59. Polarization data for design point 30 (25% PTFE, 3mg/cm^2, 850psi Assy, 50psi Sinter)

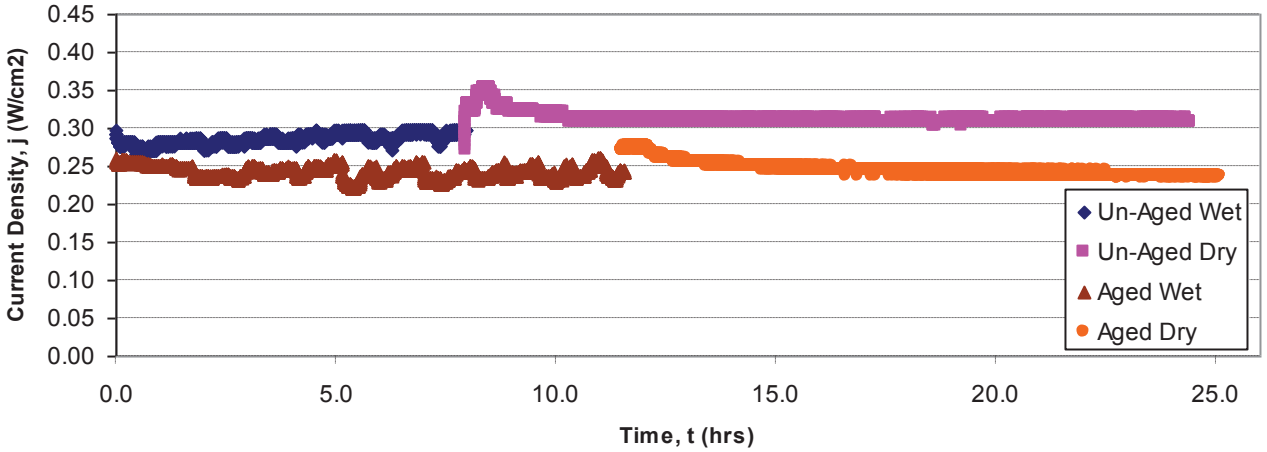

Figure A-60. Steady state data for design point 30 (25% PTFE, 3mg/cm^2, 850psi Assy, 50psi Sinter)

Appendix B: Adhesion Study Data

Sample Calculation for Fracture Energy:

Given:

$F_{AVG} = 1.23N$ *(Average debond force in Newtons)*

$l = 0.0225m$ *(Sample length in meters)*

$w = 0.0225m$ *(Sample width in meters)*

$D_{GRIPS} = 2 \times l$ *(Distance traveled by the grips equals twice the bond length)*

Solution:

$$G_C = \frac{Work}{Area}$$ *(Governing equation for fracture energy)*

$$Area = w \times l$$
$$Work = F_{AVG} \times D_{GRIPS} = F_{AVG} \times 2l$$ *(Equations for area and work)*

$$G_C = \frac{F_{AVG} \times 2l}{wl}$$ *(Plugging in equations for Area and Work)*

$$G_C = \frac{2 \times F_{AVG}}{w}$$ *(Canceling like terms)*

$$G_C = \frac{2 \times 1.23N}{.0225m}$$ *(Plugging in known values)*

$$G_C = 190.3 \frac{J}{m^2}$$ *(Solving and converting units)*

Plots of Raw Data: Un-Aged Samples

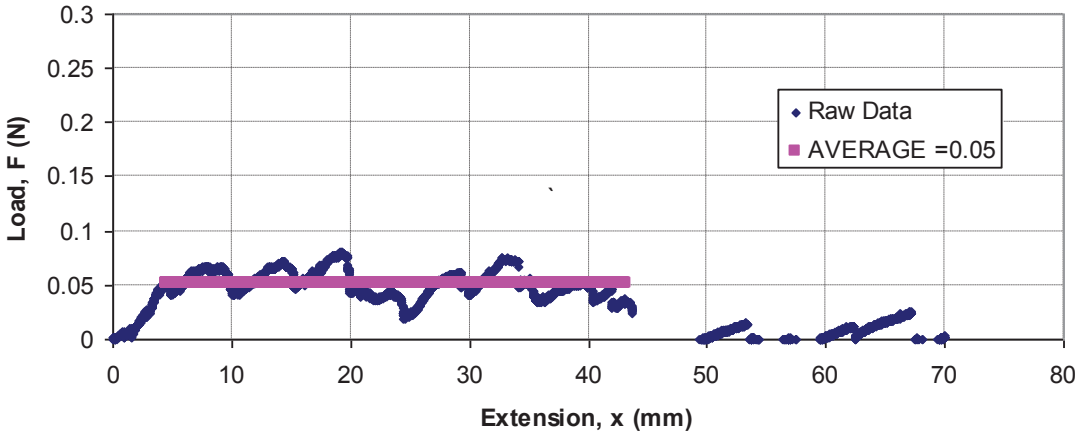

Figure B-1. Peel test data for Un-Aged Run #1 (15 wt%, 4mg/cm^2, 600psi)

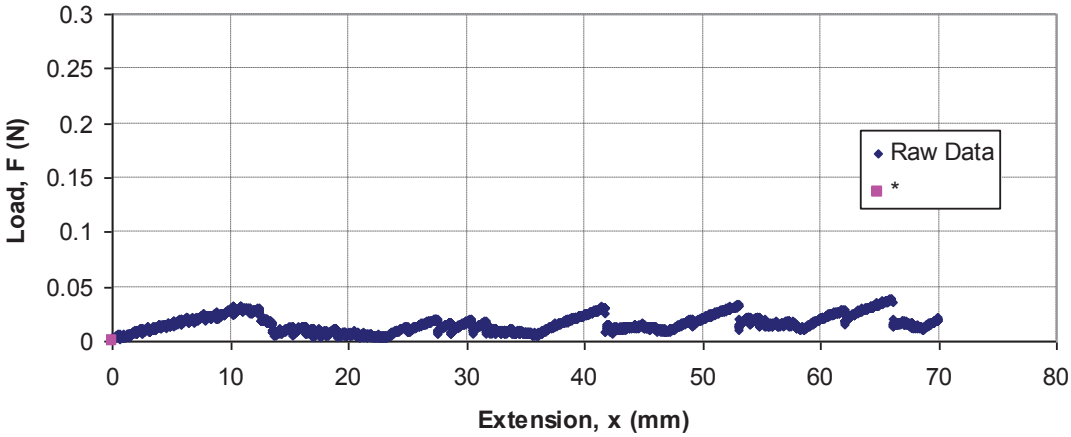

Figure B-2. Peel test data for Un-Aged Run #2 (15 wt%, 4mg/cm^2, 1100psi)
* Bond force indistinguishable from noise.

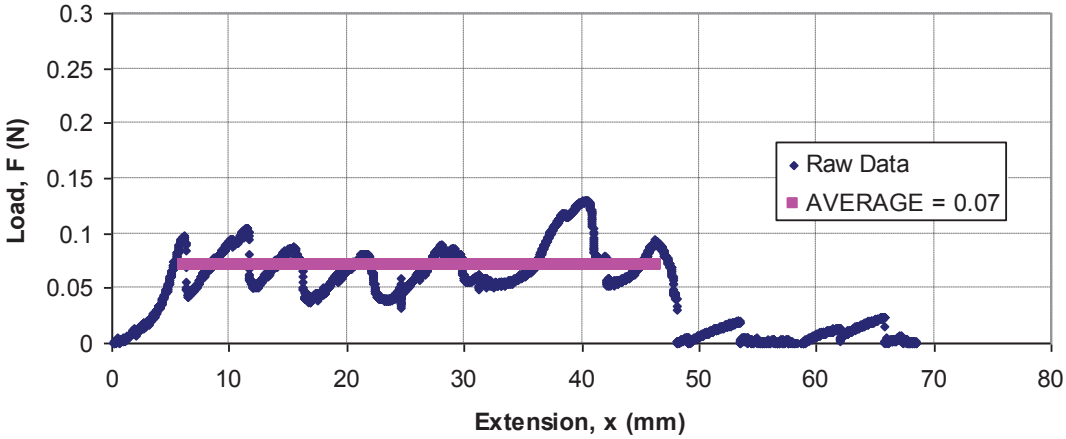

Figure B-3. Peel test data for Un-Aged Run #3 (15 wt%, 2mg/cm^2, 600psi)

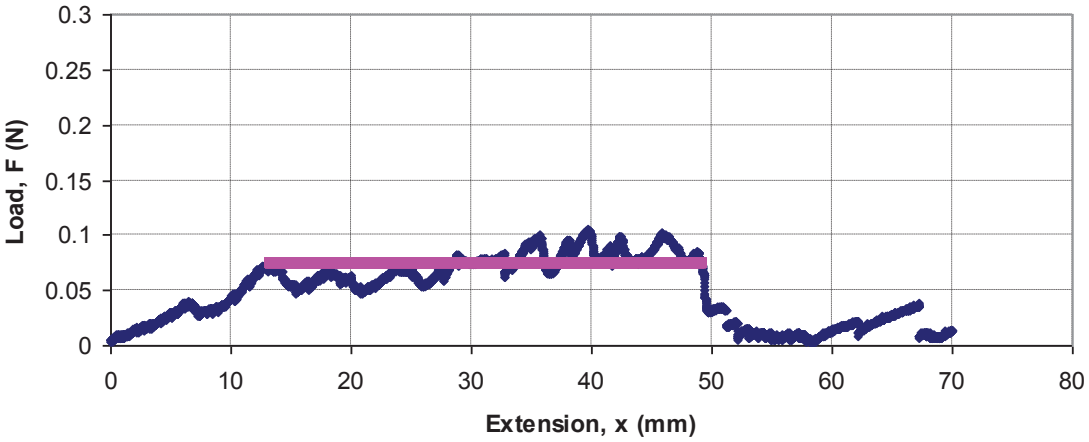

Figure B-4. Peel test data for Un-Aged Run #4 (15 wt%, 2mg/cm^2, 1100psi)

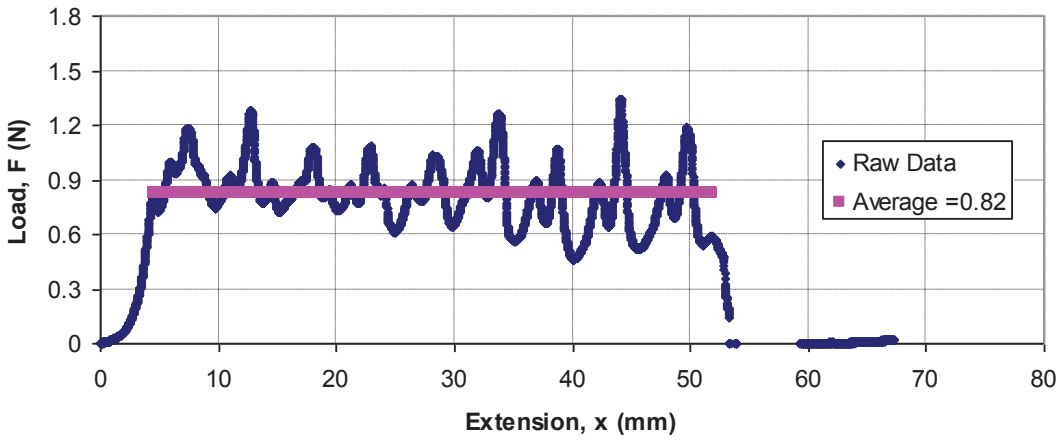

Figure B-5. Peel test data for Un-Aged Run #5 (35 wt%, 4mg/cm^2, 600psi)

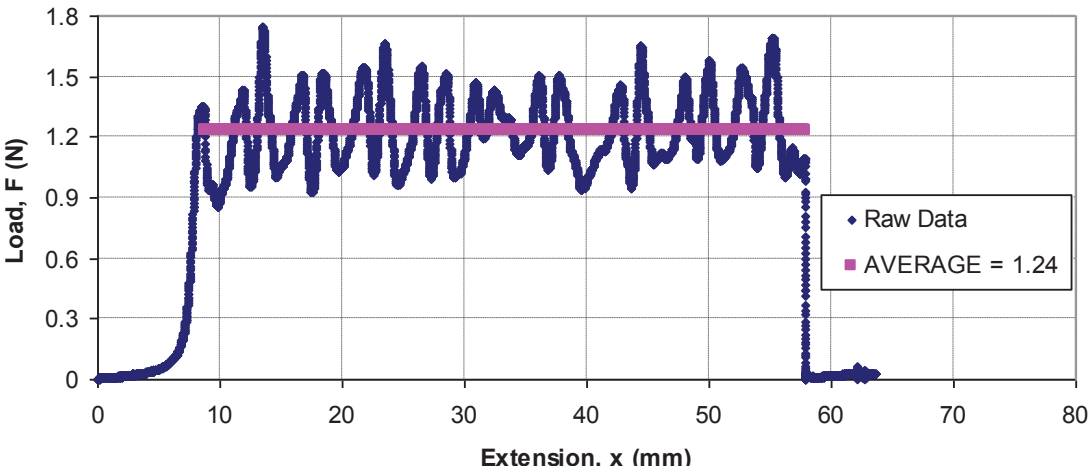

Figure B-6. Peel test data for Un-Aged Run #6 (35 wt%, 4mg/cm^2, 1100psi)

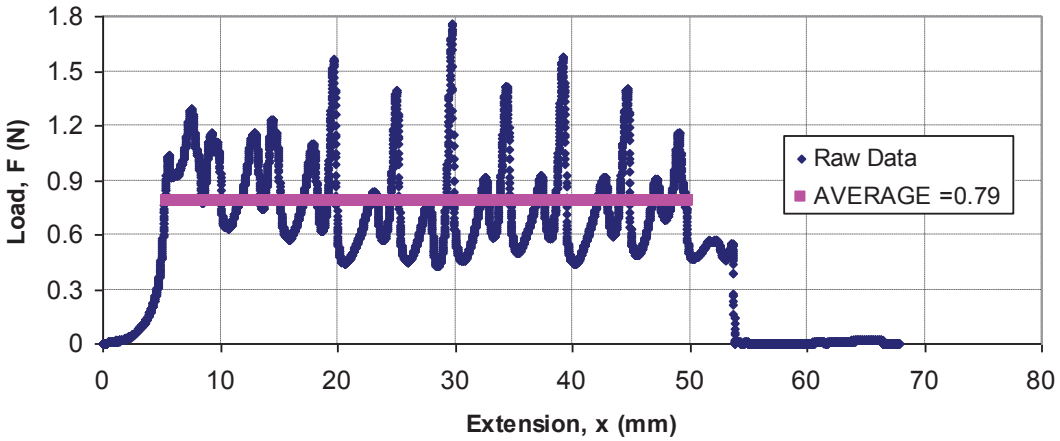

Figure B-7. Peel test data for Un-Aged Run #7 (35 wt%, 2mg/cm^2, 600psi)

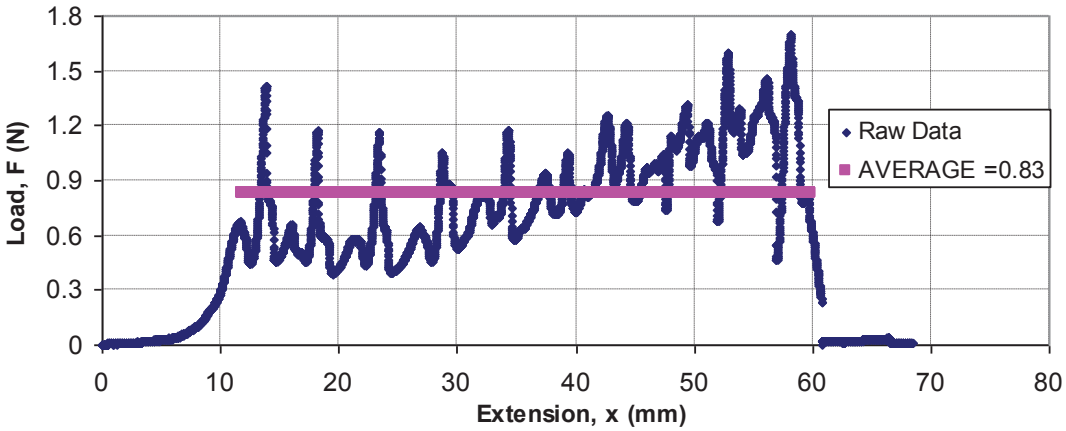

Figure B-8. Peel test data for Un-Aged Run #8 (35 wt%, 2mg/cm^2, 1100psi)

Aged Samples

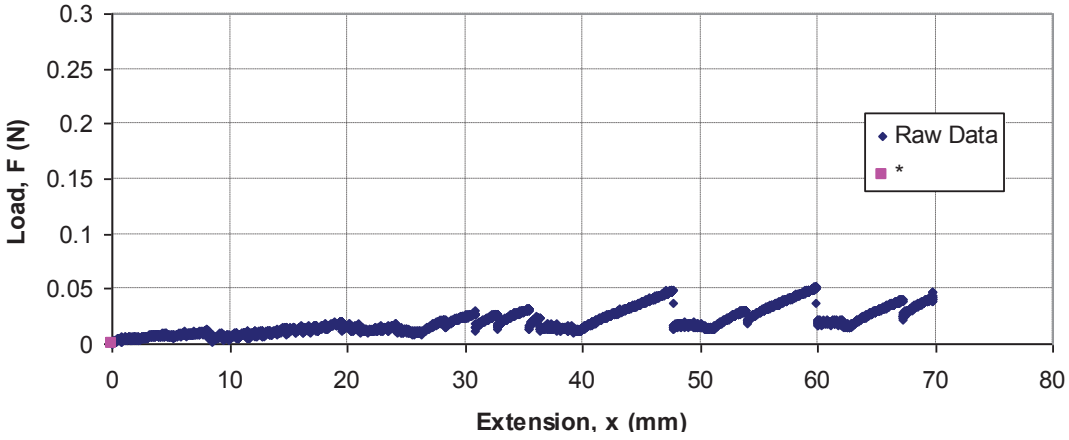

Figure B-9. Peel test data for Aged Run #1 (15 wt%, 4mg/cm^2, 600psi)
*Bond force indistinguishable from noise.

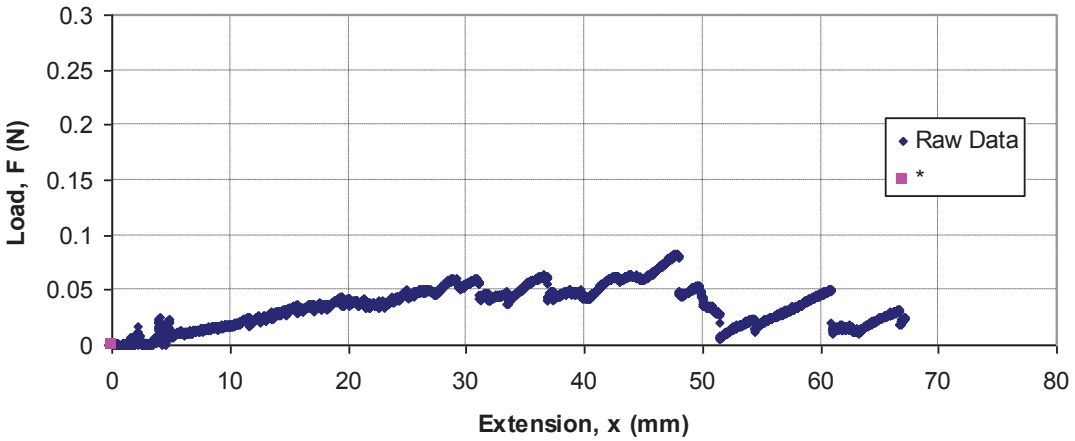

Figure B-10. Peel test data for Aged Run #2 (15 wt%, 4mg/cm^2, 1100psi)
*Bond force indistinguishable from noise.

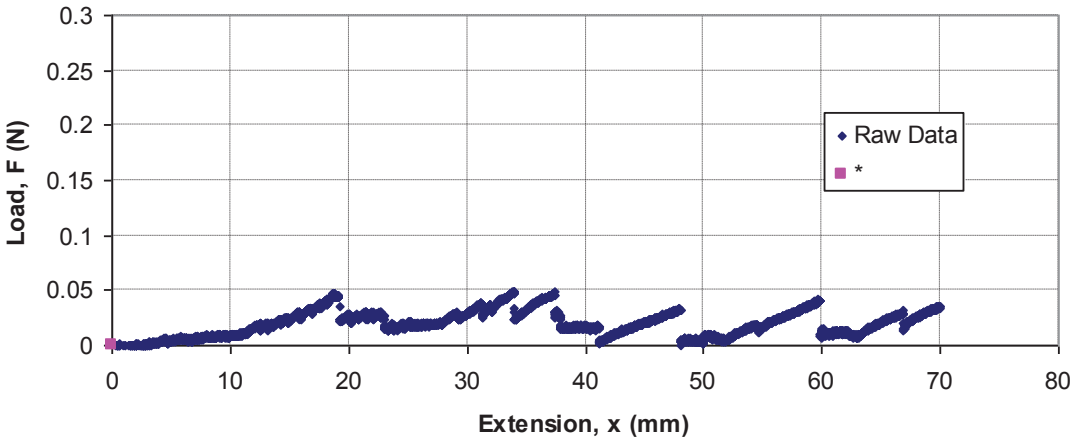

Figure B-11. Peel test data for Aged Run #3 (15 wt%, 2mg/cm^2, 600psi)
*Bond force indistinguishable from noise.

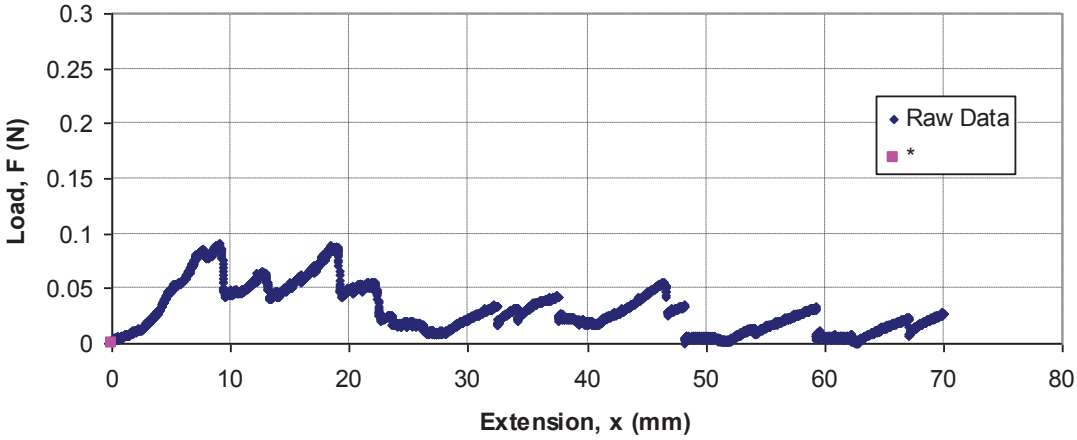

Figure B-12. Peel test data for Aged Run #4 (15 wt%, 2mg/cm^2, 1100psi)
*Bond force indistinguishable from noise.

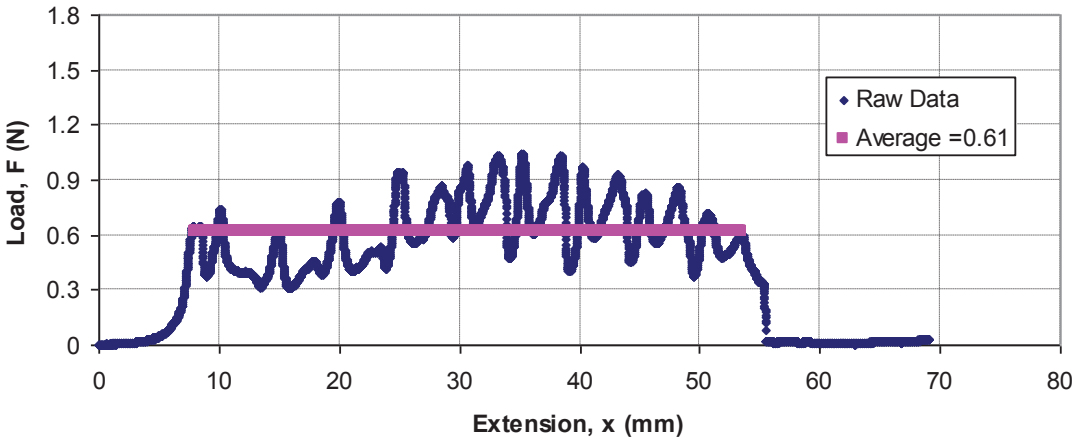

Figure B-13. Peel test data for Aged Run #5 (35 wt%, 4mg/cm^2, 600psi)

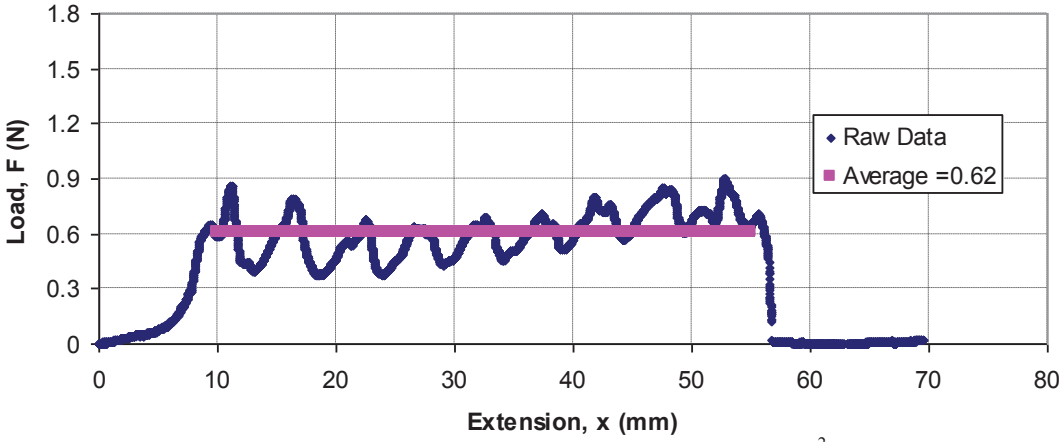

Figure B-14. Peel test data for Aged Run #6 (35 wt%, 4mg/cm^2, 1100psi)

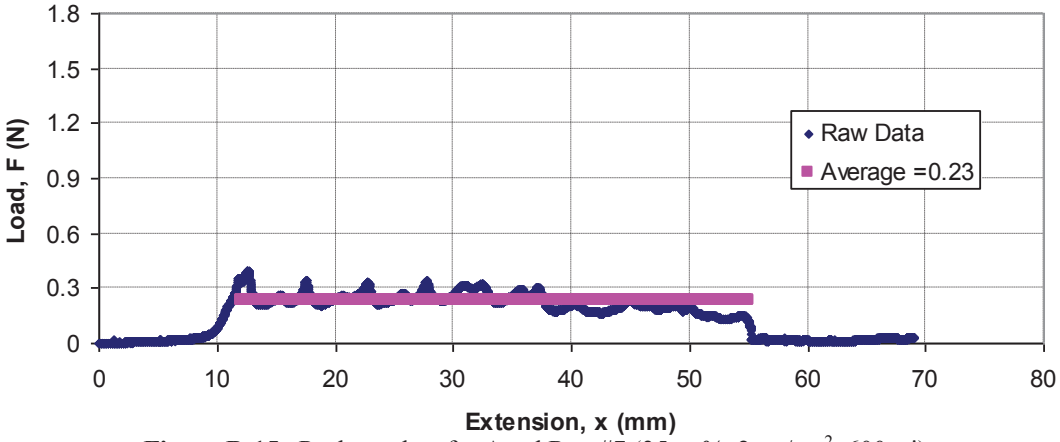

Figure B-15. Peel test data for Aged Run #7 (35 wt%, 2mg/cm^2, 600psi)

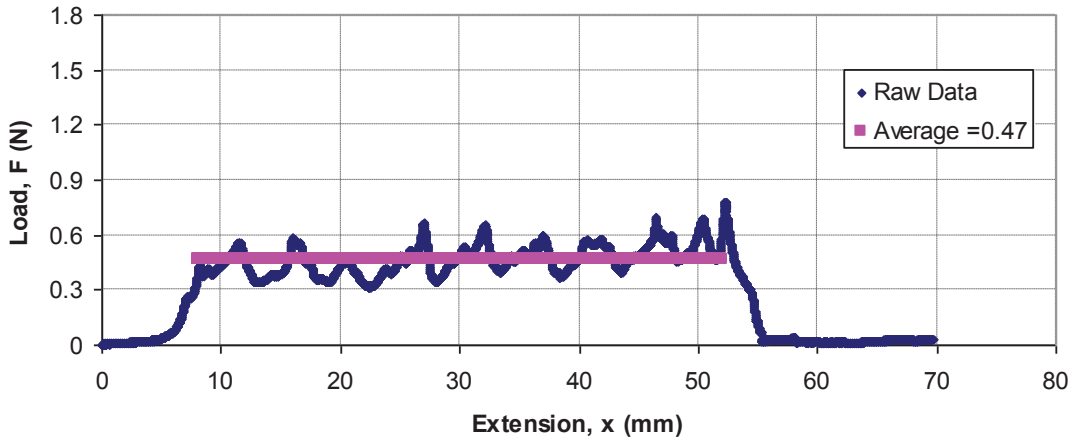

Figure B-16. Peel test data for Aged Run #8 (35 wt%, 2mg/cm^2, 1100psi)

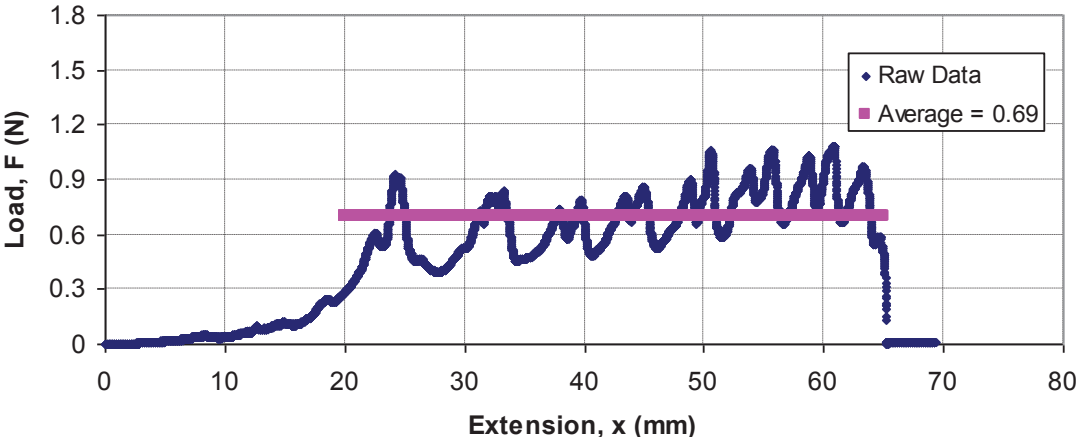

Figure B-17. Peel test data for Aged Sample with 45 wt%, 4mg/cm^2, 1100psi.

Appendix C: Statistical Analysis for Adhesion and Performance Study

I. Adhesion Study.

A. Un-Aged Fracture Energy

1. *Model Analysis*

Source	Sum of Squares	df	Mean Square	F Value	p-value Prob > F
Model	12236.97	3	4078.99	20.47	0.0069
A-Composition	11958.31	1	11958.31	60.02	0.0015
B-Loading	119.35	1	119.35	0.60	0.4822
C-Assy Pressure	159.31	1	159.31	0.80	0.4218
Residual	797.01	4	199.25		
Cor Total	13033.99	7			

Std. Dev.	14.12	R-Squared	0.9389
Mean	43.01	Adj R-Squared	0.8930
C.V. %	32.82	Pred R-Squared	0.7554
PRESS	3188.06	Adeq Precision	9.415

Factor	Coefficient Estimate	df	Standard Error	95% CI Low	95% CI High
Intercept	43.01	1	4.99	29.16	56.87
A-Compostion	38.66	1	4.99	24.81	52.52
B-Loading	3.86	1	4.99	-9.99	17.72
C-Assy Pressure	4.46	1	4.99	-9.39	18.32

Final Equation in Terms of Coded Factors:

Un-Aged Adhesion = 43.01 + 38.66*A + 3.86*B + 4.46*C

Final Equation in Terms of Actual Factors:

Un-Aged Adhesion = -80.40375 + 3.86625*Composition + 3.86250*Loading
+ 0.017850*Assy Pressure

2. *Influence of Composition*

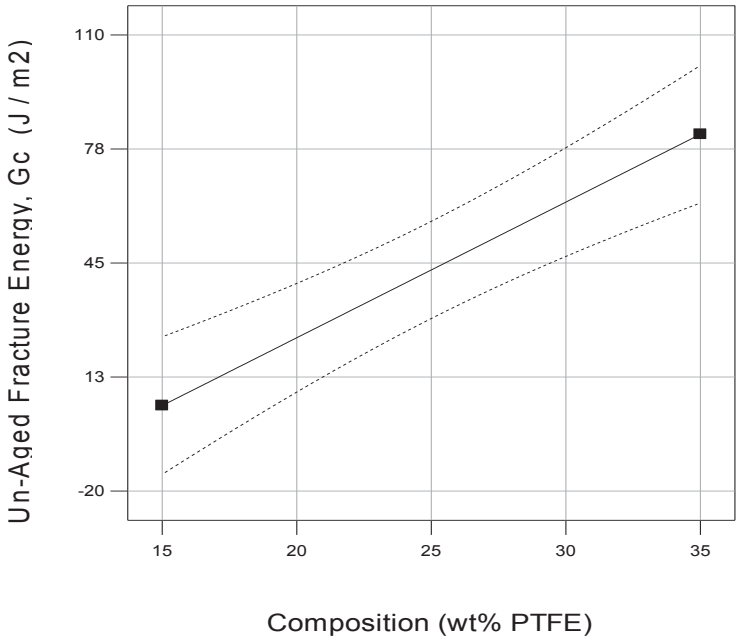

Figure C-1. Once factor plot showing the influence of composition on Un-aged Adhesion (Loading =3 mg/cm^2, Assy Pressure = 850 psi).

B. *Aged Fracture Energy*

1. *Model Analysis*

Source	Sum of Squares	df	Mean Square	F Value	p-value Prob > F
Model	3985.25	3	1328.42	12.08	0.0179
A-Composition	3642.31	1	3642.31	33.11	0.0045
B-Loading	279.66	1	279.66	2.54	0.1860
C-Assy Pressure	63.28	1	63.28	0.58	0.4904
Residual	439.96	4	109.99		
Cor Total	4425.22	7			

Std. Dev.	10.49	R-Squared	0.9006
Mean	21.34	Adj R-Squared	0.8260
C.V. %	49.15	Pred R-Squared	0.6023
PRESS	1759.86	Adeq Precision	8.108

Factor	Coefficient Estimate	df	Standard Error	95% CI Low	95% CI High	
Intercept	21.34	1	3.71	11.04	31.63	
A-Compostion	21.34	1	3.71	11.04	31.63	B-
Loading	5.91	1	3.71	-4.38	16.21	C-
Assy Pressure	2.81	1	3.71	-7.48	13.11	

Final Equation in Terms of Coded Factors:

Aged Adhesion = 21.34 + 21.34*A + 5.91*B + 2.81*C

Final Equation in Terms of Actual Factors:

Aged Adhesion = -59.30625 + 2.13375*Composition + 5.91250*Loading
+ 0.011250*Assy Pressure

2. Influence of Composition

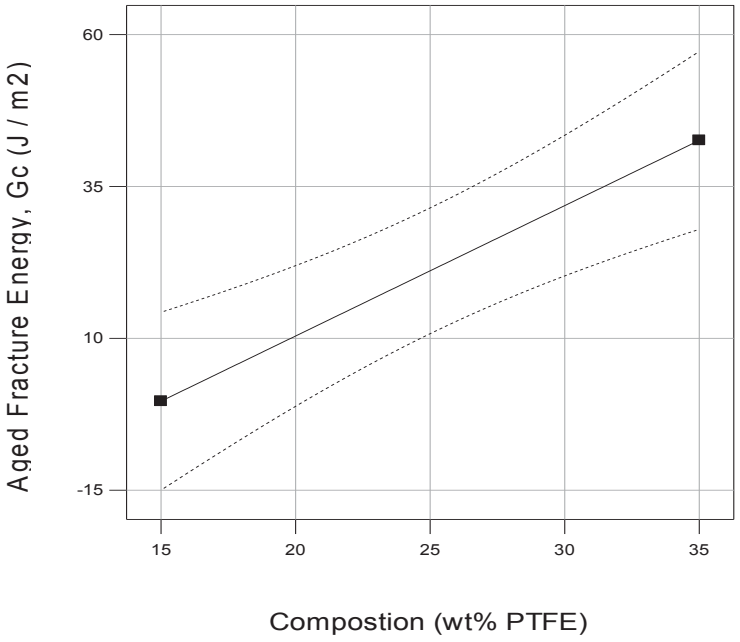

Figure C-2. Once factor plot showing the influence of composition on Aged Adhesion (Loading =3 mg/cm^2, Assy Pressure = 850 psi).

II. Performance Study.

A. Un-Aged Performance

1. Wet Polarization Model Analysis

Source	Sum of Squares	df	Mean Square	F Value	p-value Prob > F
Model	0.15	6	0.024	9.93	< 0.0001
A-Composition	0.062	1	0.062	25.11	< 0.0001
B-Loading	0.021	1	0.021	8.50	0.0078
C-Assembly Press	0.011	1	0.011	4.69	0.0410
A^2	0.026	1	0.026	10.78	0.0033
B^2	0.018	1	0.018	7.19	0.0133
C^2	0.021	1	0.021	8.54	0.0077
Residual	0.056	23	2.449E-3		
Lack of Fit	0.050	18	2.764E-3	2.10	0.2107
Pure Error	6.581E-3	5	1.316E-3		
Cor Total	0.20	29			

Std. Dev.	0.049	R-Squared	0.7215
Mean	0.31	Adj R-Squared	0.6488
C.V. %	16.09	Pred R-Squared	0.3934
PRESS	0.12	Adeq Precision	10.161

Factor	Coefficient Estimate	df	Standard Error	95% CI Low	95% CI High
Intercept	0.37	1	0.017	0.34	0.41
A-Composition	0.051	1	0.010	0.030	0.072
B-Loading	0.029	1	0.010	8.560E-003	0.050
C-Assembly Press	-0.022	1	0.010	-0.043	-9.771E-004
A^2	-0.031	1	9.353E-3	-0.050	-0.011
B^2	-0.025	1	9.353E-3	-0.044	-5.733E-003
C^2	-0.027	1	9.353E-3	-0.047	-7.983E-003

Table C-1. R^2 values for various cutoff levels of Un-Aged Wet Polarization Model

Variables Excluded:	R^2	Adj. R^2	Pred R^2	(Pred R^2)- (Adj. R^2)
None	0.90	0.82	0.66	0.15
Terms > 0.5 (BC, AD, AC, D^2)	0.90	0.85	0.77	0.08
Terms > 0.25 (BC, AD, AC, D^2, AB, CD)	0.89	0.85	0.78	0.07
Terms > 0.1 (BC, AD, AC, D^2, AB, CD)	0.89	0.85	0.78	0.07
Terms > 0.05 (BC, AD, AC, D^2, AB, CD)	0.89	0.85	0.78	0.07

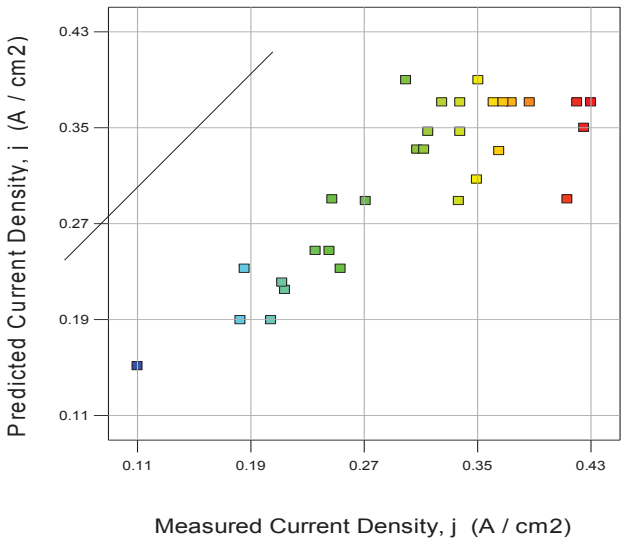

Figure C-3. Predicted response by the model vs. measured response for Un-Aged Wet Polarization.

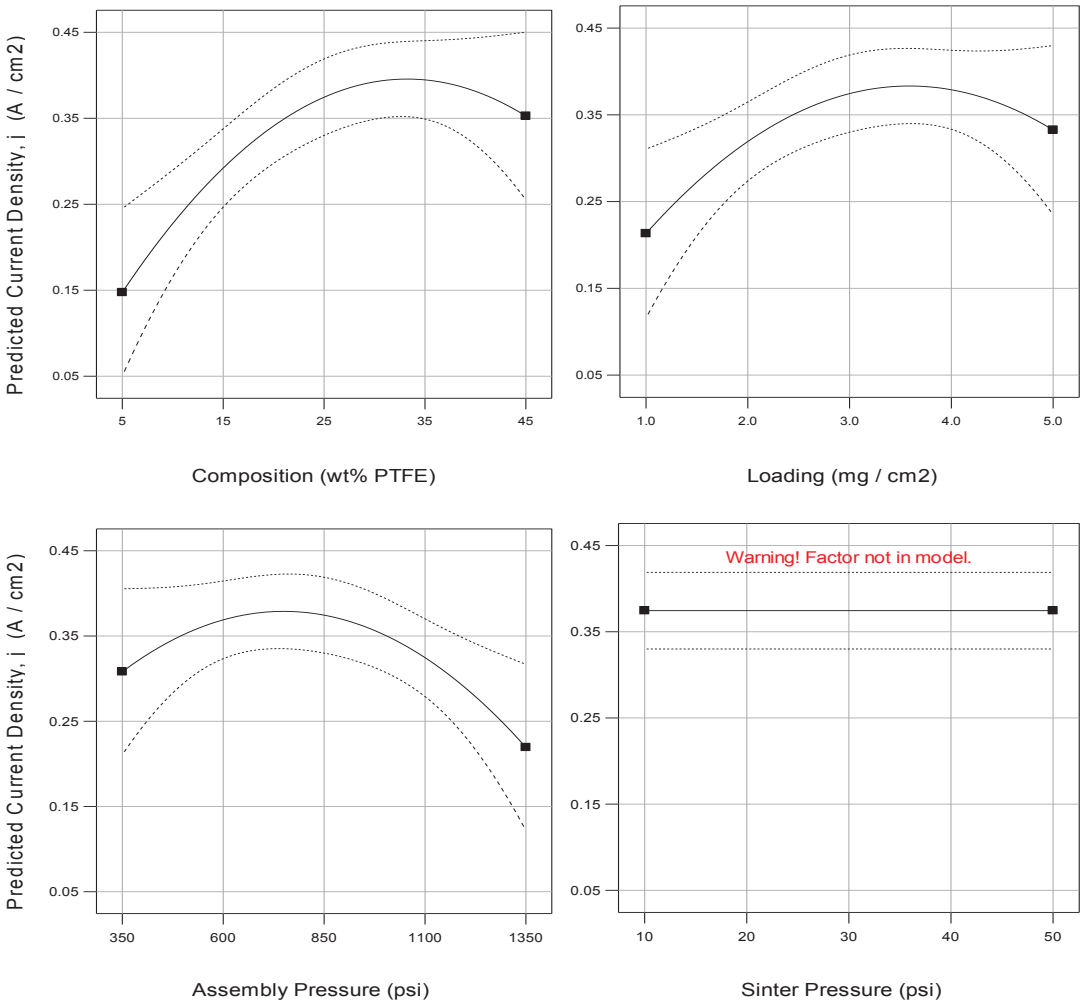

Figure C-4. One factor plots showing the influence of Composition (top left), Loading (top right), Assembly Pressure (lower left) and Sinter Pressure (lower right) on Un-aged Wet Polarization.

2. Dry Polarization Model Analysis

Source	Sum of Squares	df	Mean Square	F Value	p-value Prob > F
Model	0.19	6	0.032	14.12	< 0.0001
A-Composition	0.095	1	0.095	41.39	< 0.0001
B-Loading	0.025	1	0.025	10.79	0.0032
C-Assembly Press	7.921E-3	1	7.921E-3	3.46	0.0757
A^2	0.029	1	0.029	12.48	0.0018
B^2	0.038	1	0.038	16.70	0.0005
C^2	0.015	1	0.015	6.65	0.0168
Residual	0.053	23	2.289E-3		
Lack of Fit	0.048	18	2.647E-3	2.64 0	.1433
Pure Error	5.013E-3	5	1.003E-3		
Cor Total	0.25	29			

Std. Dev.	0.048	R-Squared	0.7864
Mean	0.27	Adj R-Squared	0.7307
C.V. %	17.51	Pred R-Squared	0.6692
PRESS	0.082	Adeq Precision	11.869

Factor	Coefficient Estimate	df	Standard Error	95% CI Low	95% CI High
Intercept	0.35	1	0.017	0.31	0.38
A-Composition	0.063	1	9.767E-3	0.043	0.083
B-Loading	0.032	1	9.767E-3	0.012	0.052
C-Assembly Press	-0.018	1	9.767E-3	-0.038	2.037E-3
A^2	-0.032	1	9.042E-3	-0.051	-0.013
B^2	-0.037	1	9.042E-3	-0.056	-0.018
C^2	-0.023	1	9.042E-3	-0.042	-4.616E-3

Table C-2. R^2 values for various cutoff levels of Un-Aged Dry Polarization Model

Variables Excluded:	R^2	Adj. R^2	Pred R^2	(Pred R^2)- (Adj. R^2)
None	0.84	0.69	0.16	0.53
Terms > 0.5 (D^2, BC, AD, CD)	0.84	0.75	0.57	0.18
Terms > 0.25 (D^2, BC, AD, CD, AB)	0.83	0.75	0.62	0.13
Terms > 0.1 (D^2, BC, AD, CD, AB, D, AC, BD)	0.79	0.73	0.67	0.06
Terms > 0.05 (D^2, BC, AD, CD, AB, D, AC, BD)	0.79	0.73	0.67	0.06

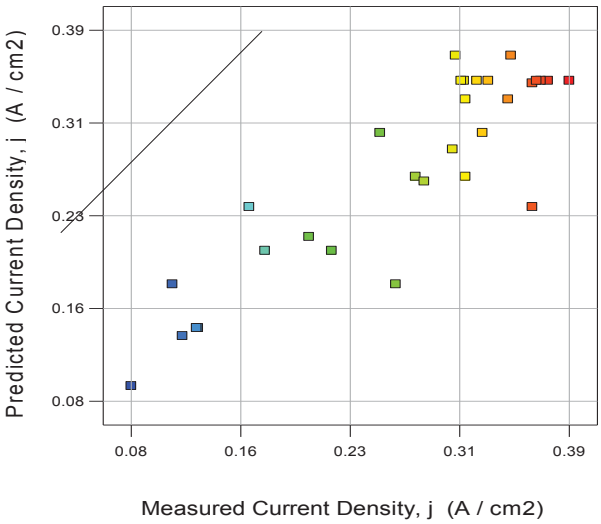

Figure C-5. Predicted response by the model vs. measured response for Un-Aged Dry Polarization.

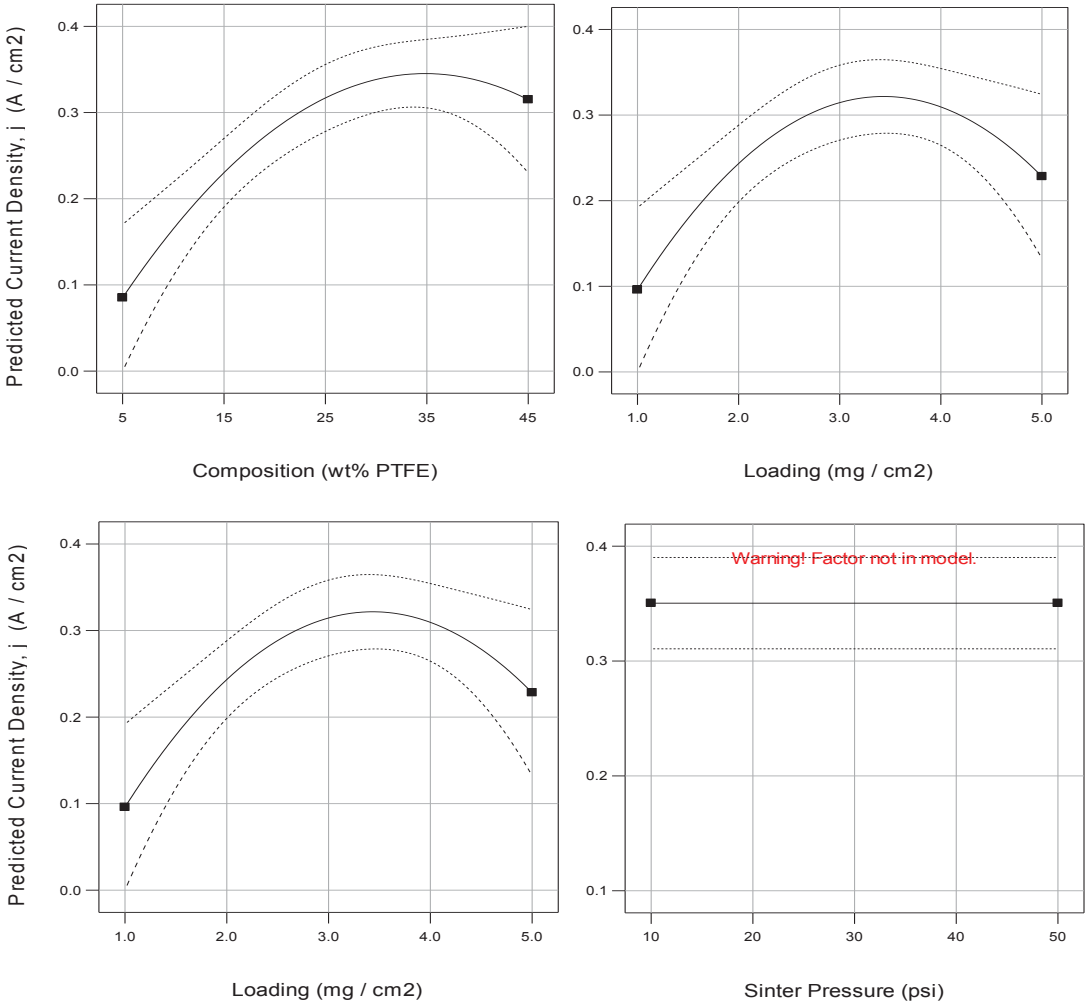

Figure C-6. One factor plots showing the influence of Composition (top left), Loading (top right), Assembly Pressure (lower left) and Sinter Pressure (lower right) on Un-aged Dry Polarization performance.

3. Wet Steady state Model Analysis

Source	Sum of Squares	df	Mean Square	F Value	p-value Prob > F
Model	0.12	6	0.020	7.47	0.0002
A-Composition	0.041	1	0.041	15.36	0.0007
B-Loading	0.017	1	0.017	6.31	0.0195
C-Assembly Press	0.012	1	0.012	4.37	0.0478
A^2	0.018	1	0.018	6.91	0.0150
B^2	0.018	1	0.018	6.84	0.0154
C^2	0.025	1	0.025	9.64	0.0050
Residual	0.061	23	2.638E-3		
Lack of Fit	0.053	18	2.972E-3	2.07	0.2158
Pure Error	7.180E-003	5	1.436E-3		
Cor Total	0.18	29			

Std. Dev.	0.051	R-Squared	0.6608
Mean	0.29	Adj R-Squared	0.5723
C.V. %	17.88 P	red R-Squared	0.2560
PRESS	0.13	Adeq Precision	7.760

Factor	Coefficient Estimate	df	Standard Error	95% CI Low	95% CI High
Intercept	0.35	1	0.018	0.32	0.39
A-Composition	0.041	1	0.010	0.019	0.063
B-Loading	0.026	1	0.010	4.646E-3	0.048
C-Assembly Press	-0.022	1	0.010	-0.044	-2.296E-4
A^2	-0.026	1	9.706E-3	-0.046	-5.440E-3
B^2	-0.025	1	9.706E-003	-0.045	-5.315E-003
C^2	-0.030	1	9.706E-003	-0.050	-0.010

Table C-3. R^2 values for various cutoff levels of Un-Aged Wet Steady state Model

Variables Excluded:	R^2	Adj. R^2	Pred R^2	(Pred R^2)- (Adj. R^2)
None	0.79	0.58	-0.06	0.65
Terms > 0.5 (BC)	0.78	0.60	0.06	0.54
Terms > 0.25 (BC, AD, CD, AC)	0.74	0.61	0.21	0.40
Terms > 0.1 (BC, AD, CD, AC, D^2, AB, BD)	0.66	0.57	0.26	0.32
Terms > 0.05 (BC, AD, CD, AC, D^2, AB, BD)	0.66	0.57	0.26	0.32

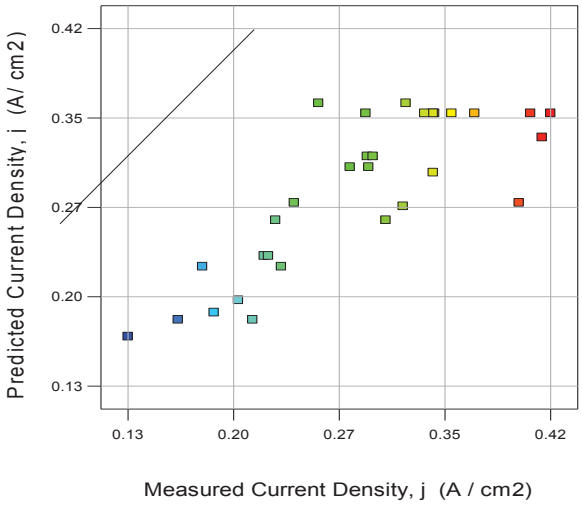

Figure C-7. Predicted response by the model vs. measured response for Un-Aged Wet Steady state.

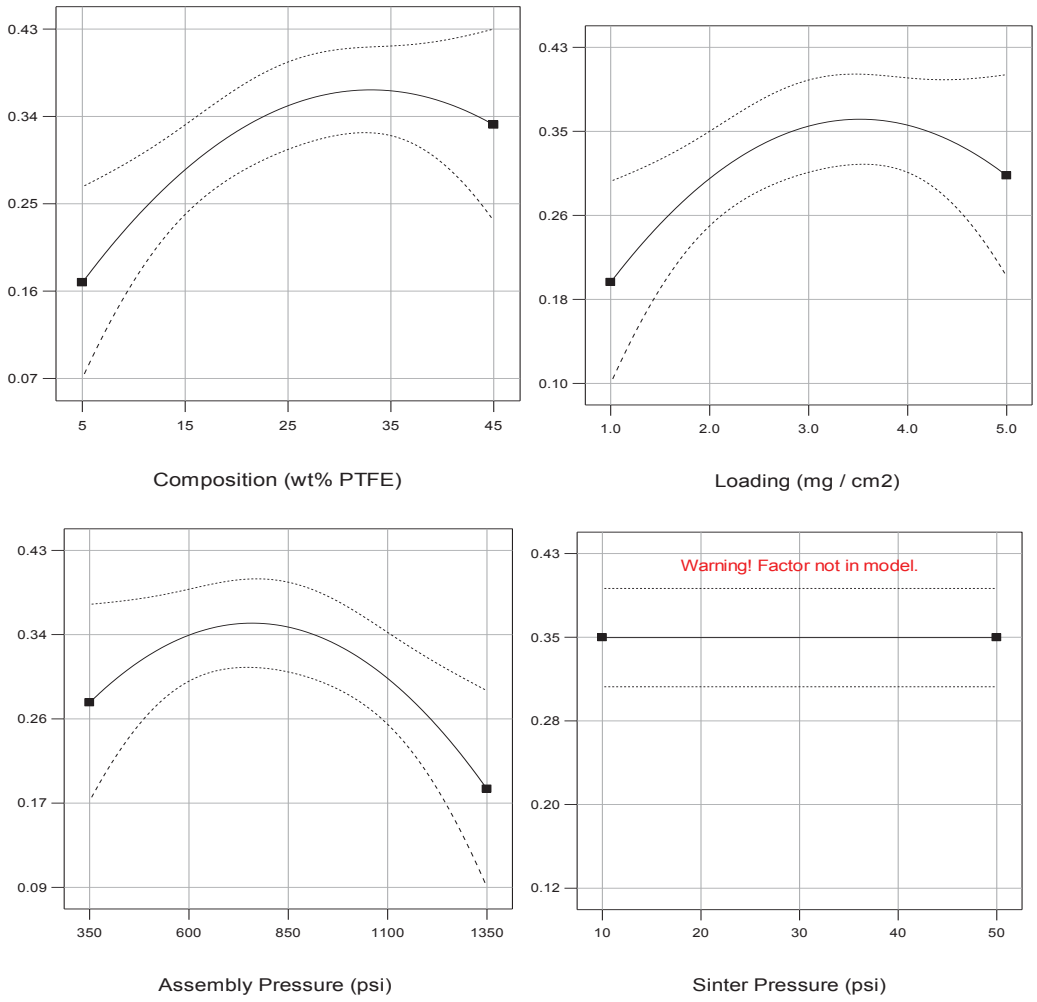

Figure C-8. One factor plots showing the influence of Composition (top left), Loading (top right), Assembly Pressure (lower left) and Sinter Pressure (lower right) on Un-aged Wet Steady state performance.

4. Dry Steady state Model Analysis (ANOVA)

Source	Sum of Squares	df	Mean Square	F Value	p-value Prob > F
Model	0.12	6	0.020	7.47	0.0002
A-Composition	0.041	1	0.041	15.36	0.0007
B-Loading	0.017	1	0.017	6.31	0.0195
C-Assembly Press	0.012	1	0.012	4.37	0.0478
A^2	0.018	1	0.018	6.91	0.0150
B^2	0.018	1	0.018	6.84	0.0154
C^2	0.025	1	0.025	9.64	0.0050
Residual	0.061	23	2.638E-3		
Lack of Fit	0.053	18	2.972E-3	2.07	0.2158
Pure Error	7.180E-3	5	1.436E-3		
Cor Total	0.18	29			

Std. Dev.	0.051	R-Squared	0.6608
Mean	0.29	Adj R-Squared	0.5723
C.V. %	17.88	Pred R-Squared	0.2560
PRESS	0.13	Adeq Precision	7.760

Factor	Coefficient Estimate	df	Standard Error	95% CI Low	95% CI High
Intercept	0.35	1	0.018	0.32	0.39
A-Composition	0.041	1	0.010	0.019	0.063
B-Loading	0.026	1	0.010	4.646E-3	0.048
C-Assembly Press	-0.022	1	0.010	-0.044	-2.296E-4
A^2	-0.026	1	9.706E-3	-0.046	-5.440E-3
B^2	-0.025	1	9.706E-3	-0.045	-5.315E-3
C^2	-0.030	1	9.706E-3	-0.050	-0.010

Table C-4. R^2 values for various cutoff levels of Un-Aged Dry Steady state Model.

Variables Excluded:	R^2	Adj. R^2	Pred R^2	(Pred R^2)- (Adj. R^2)
None	0.82	0.65	0.07	0.57
Terms > 0.5 (D^2, BC, AD, CD)	0.81	0.72	0.50	0.22
Terms > 0.25 (D^2, BC, AD, CD, AB)	0.80	0.72	0.53	0.18
Terms > 0.1 (D^2, BC, AD, CD, AB, D, AC, BD)	0.75	0.69	0.58	0.11
Terms > 0.05 (D^2, BC, AD, CD, AB, D, AC, BD)	0.75	0.69	0.58	0.11

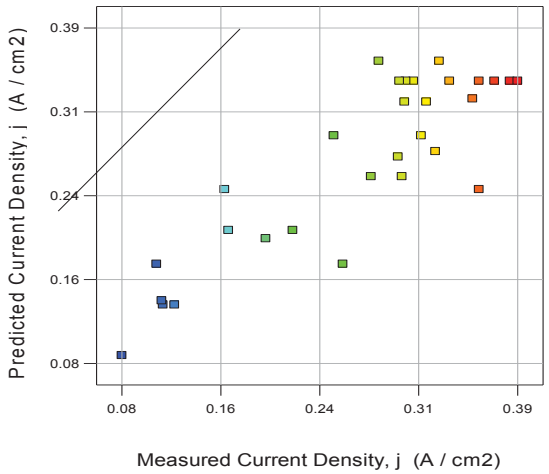

Figure C-9. Predicted response by the model vs. measured response for Un-Aged Dry Steady state.

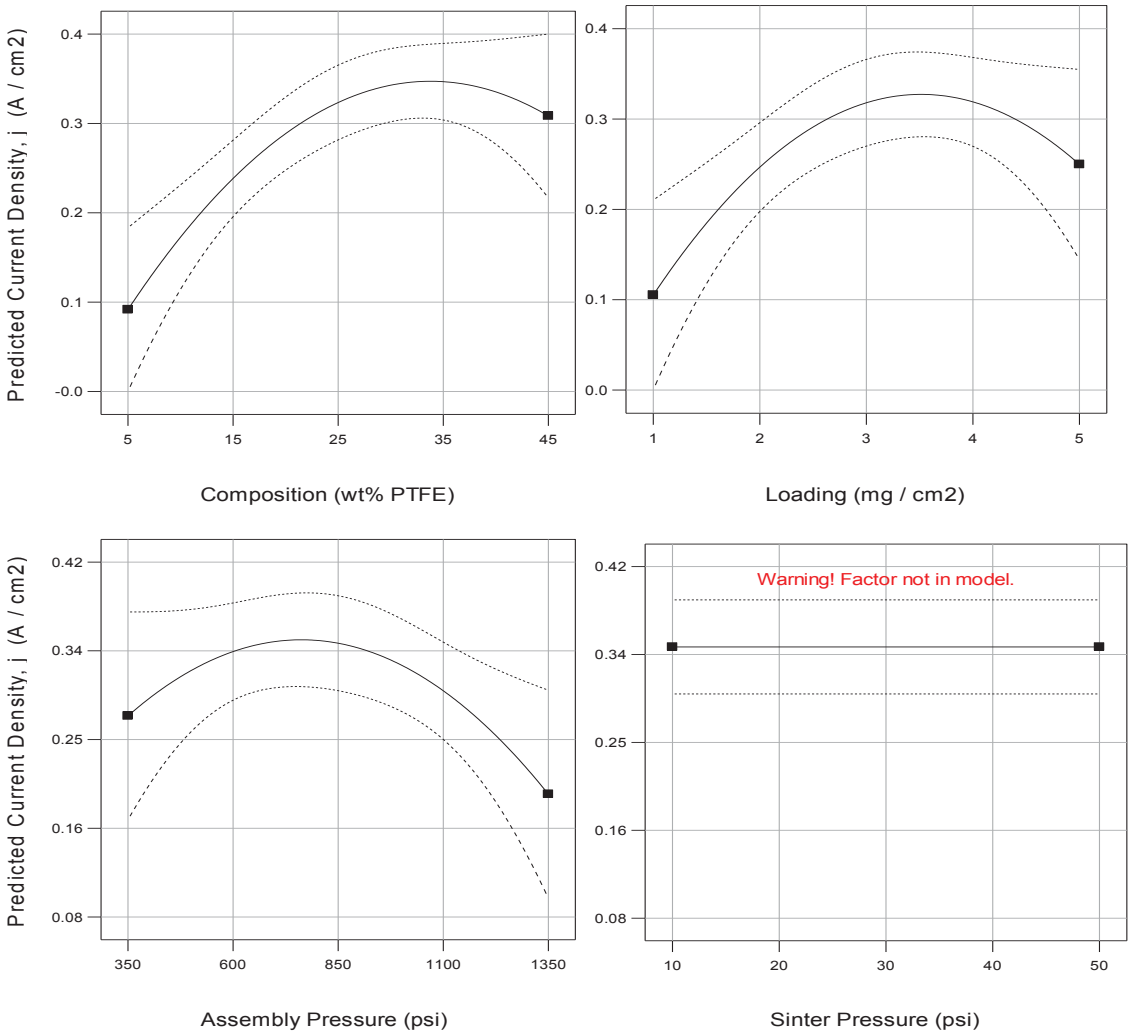

Figure C-10. One factor plots showing the influence of Composition (top left), Loading (top right), Assembly Pressure (lower left) and Sinter Pressure (lower right) on Un-aged Dry Steady state performance.

B. Aged Performance

1. Wet Polarization Model Analysis

Source	Sum of Squares	df	Mean Square	F Value	p-value Prob > F
Model	0.23	8	0.029	21.49	< 0.0001
A-Composition	0.12	1	0.12	91.01	< 0.0001
B-Loading	0.011	1	0.011	8.37	0.0087
C-Assembly Press	5.673E-3	1	5.673E-3	4.26	0.0515
D-Sinter Press	2.420E-3	1	2.420E-3	1.82	0.1919
BD	4.456E-3	1	4.456E-3	3.35	0.0815
A^2	5.495E-3	1	5.495E-3	4.13	0.0550
B^2	0.054	1	0.054	40.52	< 0.0001
C^2	0.040	1	0.040	29.80	< 0.0001
Residual	0.028	21	1.331E-3		
Lack of Fit	0.015	16	9.610E-4	0.38	0.9349
Pure Error	0.013	5	2.515E-3		
Cor Total	0.26	29			

Std. Dev.	0.036	R-Squared	0.8912
Mean	0.24	Adj R-Squared	0.8497
C.V. %	15.35	Pred R-Squared	0.7755
PRESS	0.058	Adeq Precision	15.827

Factor	Coefficient Estimate	df	Standard Error	95% CI Low	95% CI High
Intercept	0.31	1	0.013	0.29	0.34
A-Composition	0.071	1	7.447E-3	0.056	0.087
B-Loading 0.022	1	7.447E-003	6.055E-3	0.037	
C-Assembly Press	-0.015	1	7.447E-3	-0.031	1.115E-4
D-Sinter Press	-0.010	1	7.447E-3	-0.026	5.445E-3
BD	0.017	1	9.120E-3	-2.280E-3	0.036
A^2	-0.014	1	6.894E-3	-0.028	3.288E-4
B^2	-0.044	1	6.894E-3	-0.058	-0.030
C^2	-0.038	1	6.894E-3	-0.052	-0.023

Table C-5. R^2 values for various cutoff levels of Aged Wet Polarization Model.

Variables Excluded:	R^2	Adj. R^2	Pred R^2	(Pred R^2)- (Adj. R^2)
None	0.90	0.82	0.66	0.15
Terms > 0.5 (BC, AD, AC, D^2)	0.90	0.85	0.77	0.08
Terms > 0.25 (BC, AD, AC, D^2, AB, CD)	0.89	0.85	0.78	0.07
Terms > 0.1 (BC, AD, AC, D^2, AB, CD)	0.89	0.85	0.78	0.07
Terms > 0.05 (BC, AD, AC, D^2, AB, CD)	0.89	0.85	0.78	0.07

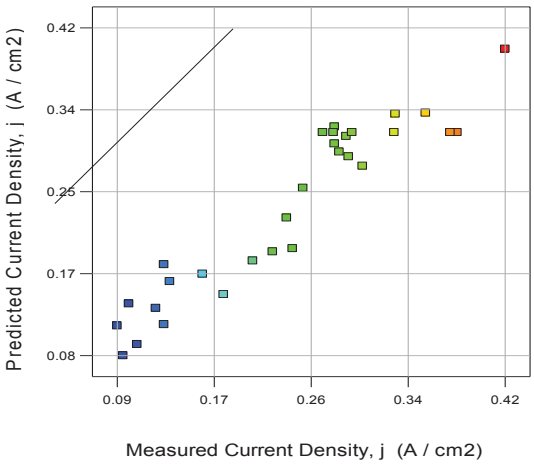

Figure C-11. Predicted response by the model vs. measured response for Aged Wet Polarization.

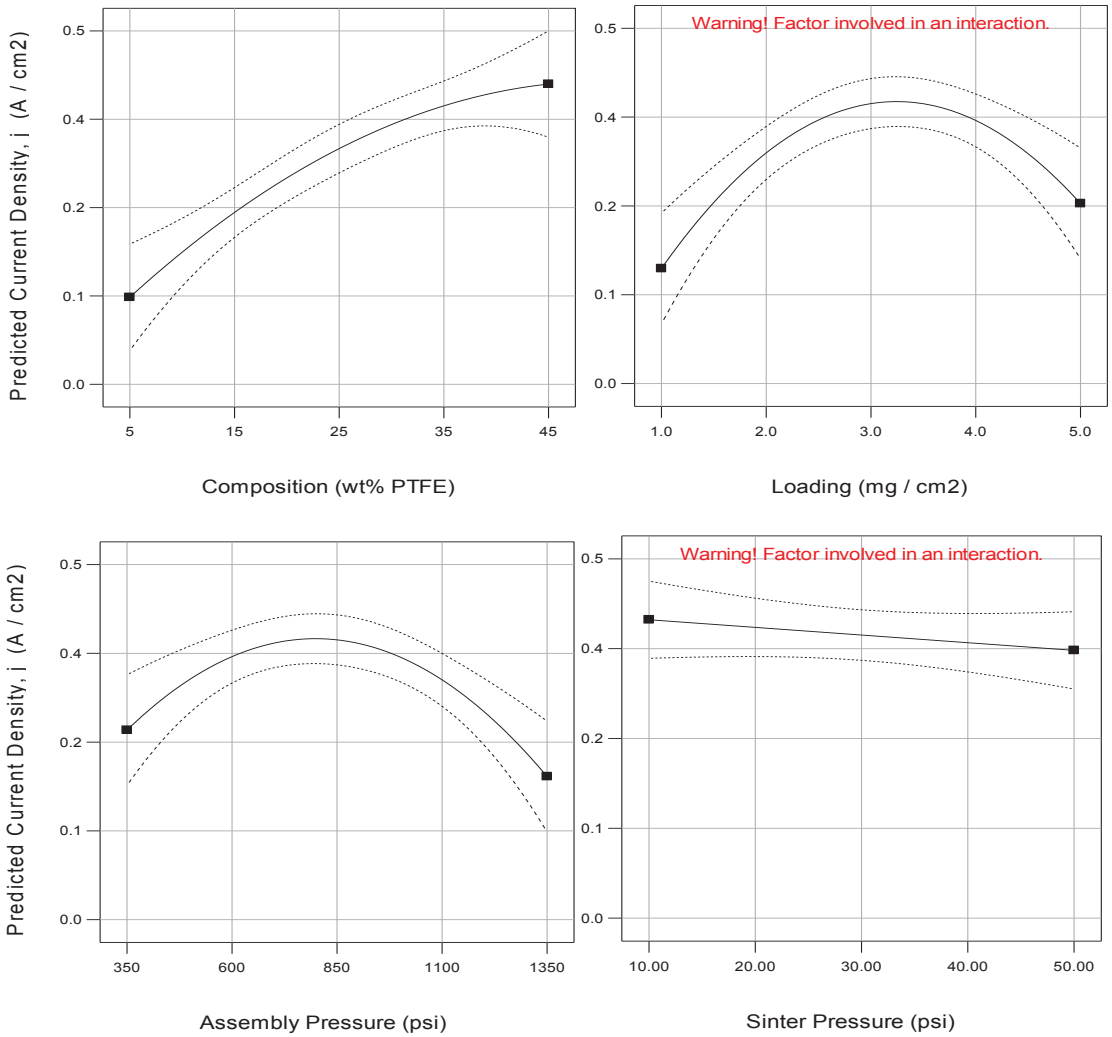

Figure C-12. One factor plots showing the influence of Composition (top left), Loading (top right), Assembly Pressure (lower left) and Sinter Pressure (lower right) on Aged Wet Polarization performance.

2. Dry Polarization Model Analysis

Source	Sum of Squares	df	Mean Square	F Value	p-value Prob > F
Model	0.16	9	0.018	15.23	< 0.0001
A-Composition	0.096	1	0.096	80.10	< 0.0001
B-Loading	8.588E-3	1	8.588E-3	7.15	0.0146
C-Assembly Press	6.017E-3	1	6.017E-3	5.01	0.0368
D-Sinter Press	6.407E-4	1	6.407E-4	0.53	0.4738
BD	2.916E-3	1	2.916E-3	2.43	0.1350
CD	3.249E-3	1	3.249E-3	2.70	0.1158
A^2	6.962E-3	1	6.962E-3	5.79	0.0259
B^2	0.024	1	0.024	20.30	0.0002
C^2	0.026	1	0.026	21.52	0.0002
Residual	0.024	20	1.202E-3		
Lack of Fit	0.015	15	1.018E-3	0.58	0.8103
Pure Error	8.774E-3	5	1.755E-3		
Cor Total	0.19	29			

Std. Dev.	0.035	R-Squared	0.8727
Mean	0.19	Adj R-Squared	0.8154
C.V. %	17.92	Pred R-Squared	0.7390
PRESS	0.049	Adeq Precision	13.503

Factor	Coefficient Estimate	df	Standard Error	95% CI Low	95% CI High
Intercept	0.25	1	0.012	0.23	0.28
A-Composition	0.063	1	7.076E-3	0.049	0.078
B-Loading	0.019	1	7.076E-3	4.155E-3	0.034
C-Assembly Press	-0.016	1	7.076E-3	-0.031	-1.072E-3
D-Sinter Press	-5.167E-3	1	7.076E-3	-0.020	9.595E-3
BD	0.014	1	8.667E-3	-4.579E-3	0.032
CD	-0.014	1	8.667E-3	-0.032	3.829E-3
A^2	-0.016	1	6.552E-3	-0.029	-2.102E-3
B^2	-0.030	1	6.552E-3	-0.043	-0.016
C^2	-0.030	1	6.552E-3	-0.044	-0.017

Table C-6. R^2 values for various cutoff levels of Aged Dry Polarization Model.

Variables Excluded:	R^2	Adj. R^2	Pred R^2	(Pred R^2)- (Adj. R^2)
None	0.89	0.78	0.56	0.23
Terms > 0.5 (AD, AC, BC)	0.88	0.81	0.67	0.14
Terms > 0.25 (AD, AC, BC, AB, D^2)	0.87	0.82	0.74	0.08
Terms > 0.1 (AD, AC, BC, AB, D^2, D, BD, CD)	0.84	0.79	0.74	0.05
Terms > 0.05 (AD, AC, BC, AB, D^2, D, BD, CD)	0.84	0.79	0.74	0.05

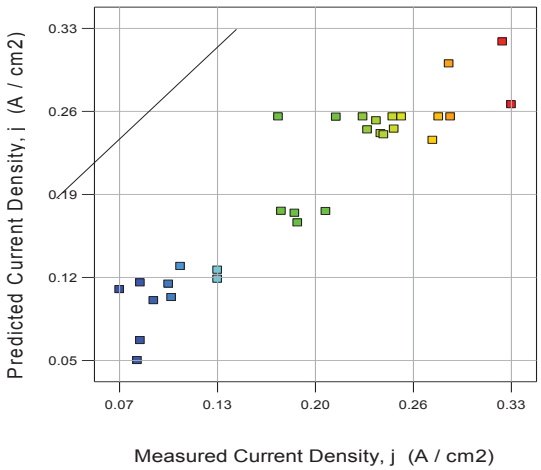

Figure C-13. Predicted response by the model vs. measured response for Aged Dry Polarization.

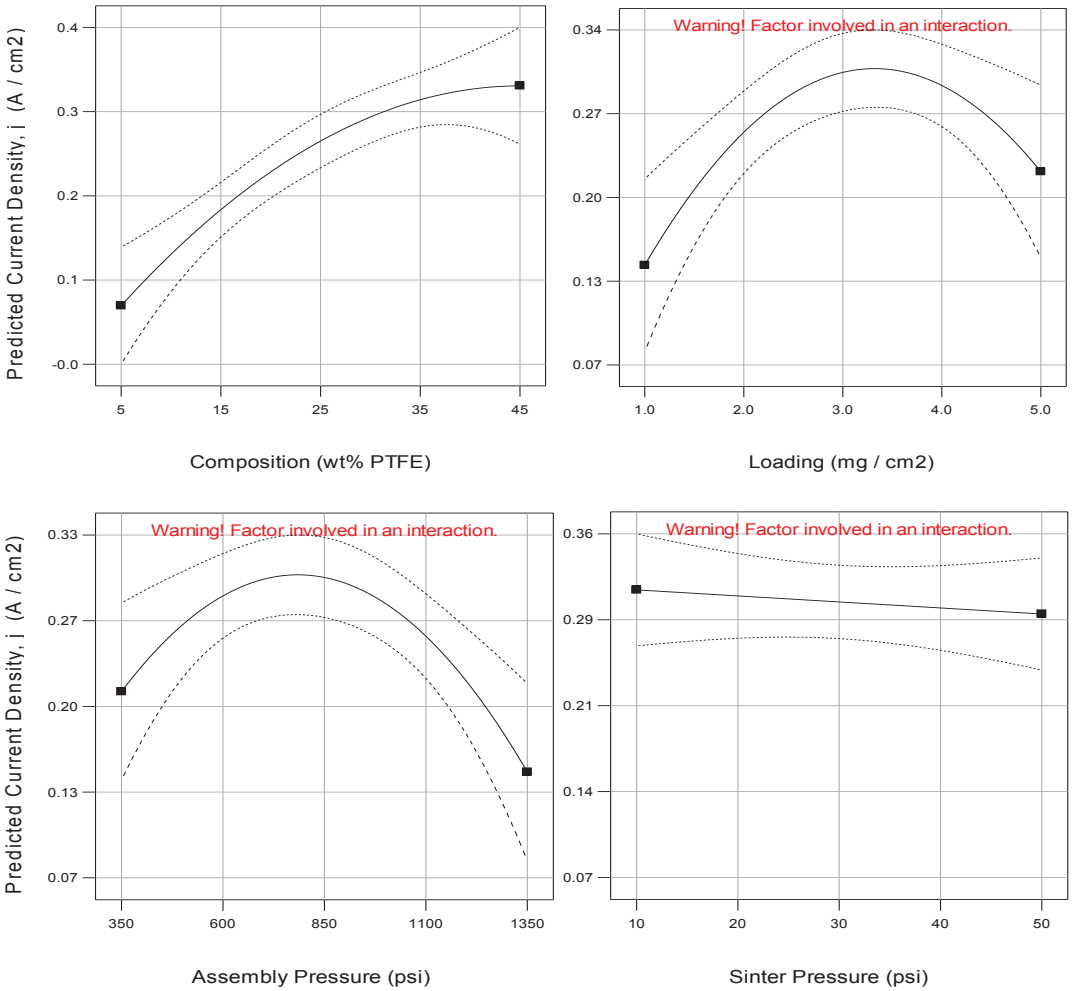

Figure C-14. One factor plots showing the influence of Composition (top left), Loading (top right), Assembly Pressure (lower left) and Sinter Pressure (lower right) on Aged Dry Polarization performance.

3. Wet Steady state Model Analysis

Source	Sum of Squares	df	Mean Square	F Value	p-value Prob > F
Model	0.19	7	0.027	19.76	< 0.0001
A-Composition	0.099	1	0.099	73.00	< 0.0001
B-Loading	8.325E-3	1	8.325E-3	6.16	0.0212
C-Assembly Press	4.902E-3	1	4.902E-3	3.63	0.0700
D-Sinter Press	2.109E-3	1	2.109E-3	1.56	0.2248
BD	5.220E-3	1	5.220E-3	3.86	0.0622
B^2	0.044	1	0.044	32.45	< 0.0001
C^2	0.031	1	0.031	23.12	< 0.0001
Residual	0.030	22	1.352E-3		
Lack of Fit	0.018	17	1.062E-3	0.45	0.8983
Pure Error	0.012	5	2.340E-3		
Cor Total	0.22	29			

Std. Dev.	0.037	R-Squared	0.8628
Mean	0.22	Adj R-Squared	0.8191
C.V. %	17.04	Pred R-Squared	0.7299
PRESS	0.059	Adeq Precision	17.124

Factor	Coefficient Estimate	df	Standard Error	95% CI Low	95% CI High
Intercept	0.27	1	0.011	0.25	0.30
A-Composition	0.064	1	7.506E-3	0.049	0.080
B-Loading	0.019	1	7.506E-3	3.060E-3	0.034
C-Assembly Press	-0.014	1	7.506E-3	-0.030	1.274E-3
D-Sinter Press	-9.375E-3	1	7.506E-3	-0.025	6.190E-3
BD	0.018	1	9.192E-3	-1.001E-3	0.037
B^2	-0.039	1	6.894E-3	-0.054	-0.025
C^2	-0.033	1	6.894E-3	-0.047	-0.019

Table C-7. R^2 values for various cutoff levels of Aged Wet Steady state Model.

Variables Excluded:	R^2	Adj. R^2	Pred R^2	(Pred R^2)- (Adj. R^2)
None	0.89	0.78	0.58	0.20
Terms > 0.5 (AD, AC, BC)	0.89	0.82	0.68	0.13
Terms > 0.25 (AD, AC, BC, AB, D^2, CD)	0.87	0.82	0.71	0.11
Terms > 0.1 (AD, AC, BC, AB, D^2, CD, A^2)	0.86	0.82	0.73	0.09
Terms > 0.05 (AD, AC, BC, AB, D^2, CD, A^2, BD, D)	0.83	0.79	0.71	0.08

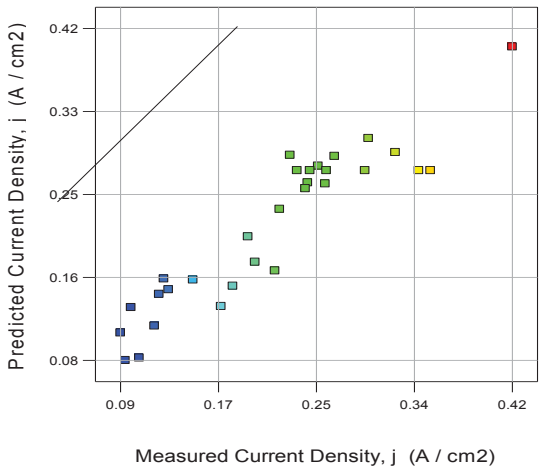

Figure C-15. Predicted response by the model vs. measured response for Aged Wet Steady state.

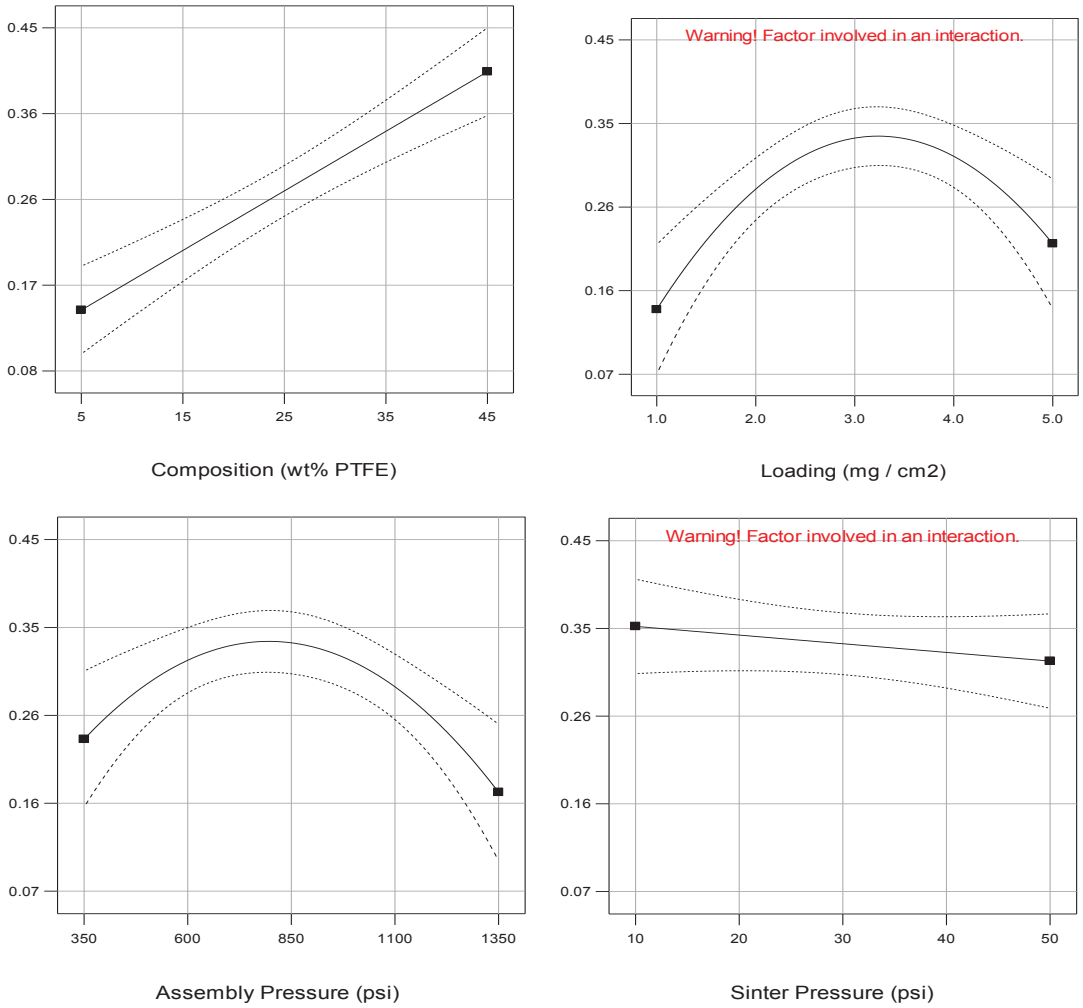

Figure C-16. One factor plots showing the influence of Composition (top left), Loading (top right), Assembly Pressure (lower left) and Sinter Pressure (lower right) on Aged Wet Steady state performance.

4. Dry Steady state Model Analysis

Source	Sum of Squares	df	Mean Square	F Value	p-value Prob > F
Model	0.15	9	0.017	13.58	< 0.0001
A-Composition	0.085	1	0.085	67.12	< 0.0001
B-Loading	7.038E-003	1	7.038E-003	5.55	0.0288
C-Assembly Press	5.551E-003	1	5.551E-003	4.38	0.0493
D-Sinter Press	5.134E-004	1	5.134E-004	0.40	0.5318
BD	2.093E-003	1	2.093E-003	1.65	0.2135
CD	3.570E-003	1	3.570E-003	2.82	0.1089
A^2	7.224E-003	1	7.224E-003	5.70	0.0270
B^2	0.026	1	0.026	20.13	0.0002
C^2	0.029	1	0.029	23.06	0.0001
Residual	0.025	20	1.268E-003		
Lack of Fit	0.016	15	1.093E-003	0.61	0.7906Pure
Error	8.967E-003	5	1.793E-003		
Cor Total	0.18	29			

Std. Dev.	0.036	R-Squared	0.8594
Mean	0.19	Adj R-Squared	0.7961
C.V. %	19.12	Pred R-Squared	0.7009
PRESS	0.054	Adeq Precision	12.467

Factor	Coefficient Estimate	df	Standard Error	95% CI Low	95% CI High
Intercept	0.25	1	0.012	0.22	0.27
A-Composition	0.060	1	7.268E-3	0.044	0.075
B-Loading	0.017	1	7.268E-3	1.964E-3	0.032
C-Assembly Press	-0.015	1	7.268E-3	-0.030	-4.779E-5
D-Sinter Press	-4.625E-3	1	7.268E-3	-0.020	0.011
BD	0.011	1	8.901E-3	-7.130E-3	0.030
CD	-0.015	1	8.901E-3	-0.034	3.630E-3
A^2	-0.016	1	6.729E-3	-0.030	-2.027E-3
B^2	-0.030	1	6.729E-3	-0.044	-0.016
C^2	-0.032	1	6.729E-3	-0.046	-0.018

Table C-8. R^2 values for various cutoff levels of Aged Dry Steady state Model.

Variables Excluded:	R^2	Adj. R^2	Pred R^2	(Pred R^2)- (Adj. R^2)
None	0.87	0.76	0.49	0.27
Terms > 0.5 (AD, AC, BC)	0.87	0.79	0.62	0.17
Terms > 0.25 (AD, AC, BC, D^2, AB)	0.86	0.80	0.70	0.10
Terms > 0.1 (AD, AC, BC, D^2, AB, D, BD, CD)	0.83	0.78	0.71	0.07
Terms > 0.05 (AD, AC, BC, D^2, AB, D, BD, CD)	0.83	0.78	0.71	0.07

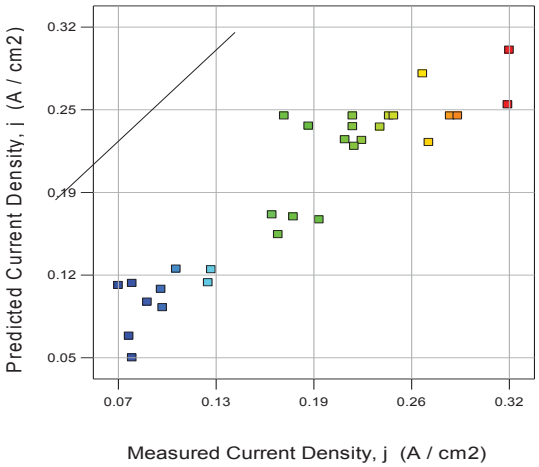

Figure C-17. Predicted response by the model vs. measured response for Aged Dry Steady state.

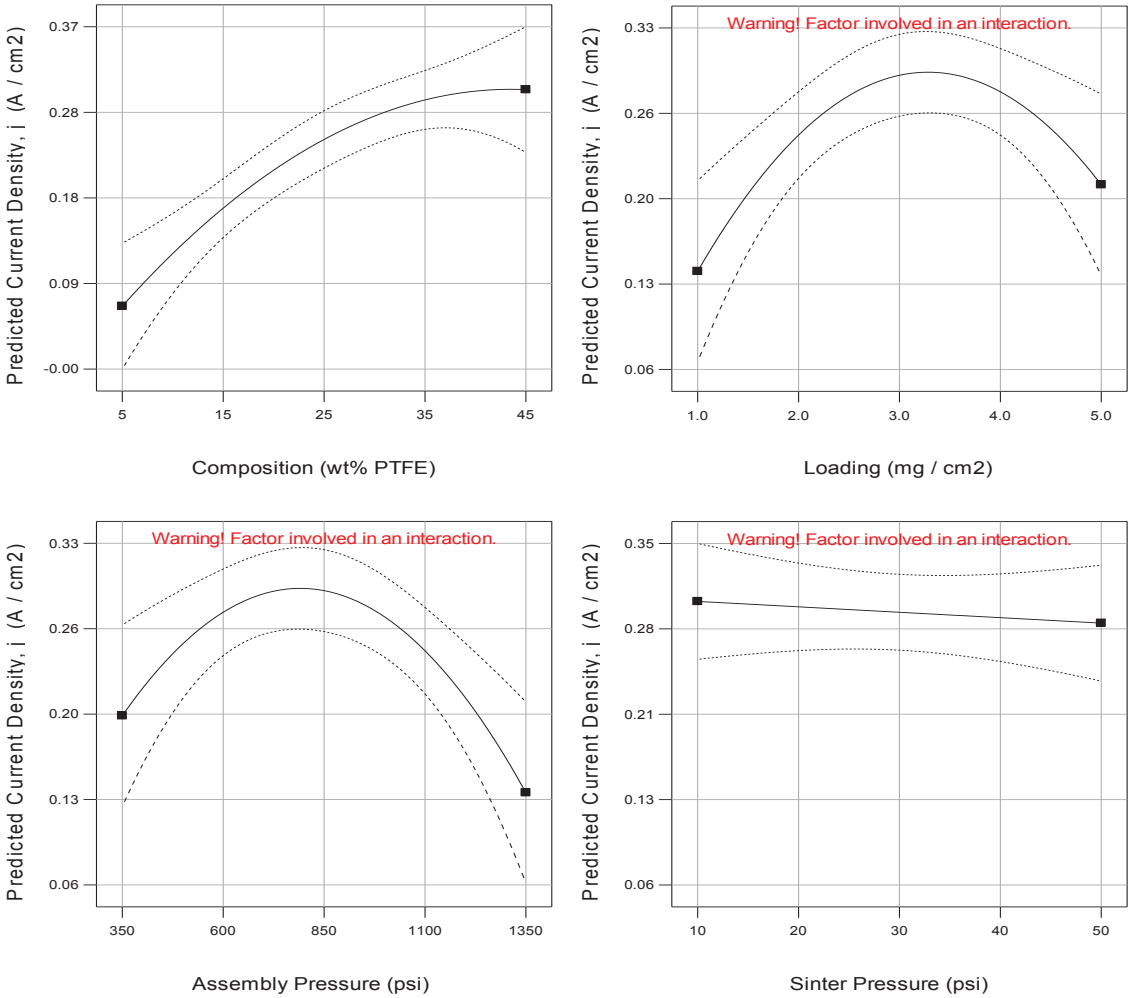

Figure C-18. One factor plots showing the influence of Composition (top left), Loading (top right), Assembly Pressure (lower left) and Sinter Pressure (lower right) on Aged Dry Steady state performance.